Improvements in Electrospray Ionization Source Design and Advances in Tandem Mass Spectrometry

Jared M. Bushey

A dissertation submitted to the faculty of the University of North Carolina at Chapel Hill in partial fulfillment of the requirements for the degree of Doctor of Philosophy in the Department of Chemistry

Chapel Hill

2008

Approved by:

Advisor: Professor Gary L. Glish

Professor Tomas Baer

Professor James Jorgenson

Professor Mark Schoenfisch

Professor Muhammad Yousaf

Abstract

Jared M. Bushey

Improvements in Electrospray Ionization Source Design
and Advances in Tandem Mass Spectrometry
(Under the direction of Dr. Gary L. Glish)

Mass spectrometry (MS) is an analytical tool that is widely used to identify the mass-to-charge ratio and abundance of components within a sample. However, without fragmentation the only information that can be garnered from a typical mass spectrum is the mass-to-charge ratio of the intact ion. Knowing only the mass-to-charge ratio of the intact ion is typically not descriptive enough for an accurate identification. To overcome the disadvantage of limited fragmentation, the intact ion can be activated through one of a number of processes to induce dissociation. The process of inducing the dissociation of a specific ion is referred to as tandem mass spectrometry (MS/MS).

The work described in this dissertation has involved the development and modification of instrumentation for the purposes of operating a multi-sprayer nESI source and for improving the amount and quality of information from MS/MS Experiments. The mass spectrometers used for the various MS/MS experiments are linear ion trap / time-of-flight (LIT/TOF) and quadrupole Fourier transform ion cyclotron resonance (Q-FTICR) instruments. The LIT/TOF and Q-FTICR instruments used for the projects described in the subsequent chapters are commercially available mass spectrometers that were modified either to perform a unique MS/MS experiment or an established MS/MS method on an instrument for the first time. Examples of unique MS/MS experiments include the implementation of iterative accumulation multiplexing (IAM) on the Q-FTICR and the development of simultaneous electron capture dissociation, collision induced dissociation, ECD+CID, on the LIT/TOF. The LIT/TOF and Q-FTICR instruments are unique in that they represent the only mass spectrometers commercially available to-date capable of performing ECD. ECD results acquired for different analytes from both instruments will be presented. Other MS/MS experiments that will be

discussed include the first demonstration of electron detachment dissociation (EDD) and activated ion (AI)-ECD in the LIT/TOF.

The work described in this dissertation demonstrates improvements in the information content of MS/MS experiments. Overall, the goal was to increase the amount of information acquired about the parent ion(s) through tandem mass spectrometry.

Acknowledgements

I would like to thank my wife for her unending support and immeasurable sacrifice throughout the course of my graduate work. Mandy, I could not have done any of this if it were not for you. Thank you for making every day worth it.

I would like to thank my parents and my brothers for everything they have done for me. Their encouragement and ability to keep me grounded even during the tough times has been invaluable. Mom and dad, thank you for instilling in me the idea that any goal is possible and teaching me the work ethic needed to reach those goals.

I would like to thank Dr. Gary L. Glish for showing me how to think critically, for having the patience to allow me to think through problems on my own, for continually pushing me to achieve the next step, and for advising me, both professionally and personally, during my time at Chapel Hill.

I would like to thank Dr. Takashi Baba for his willingness to teach under any circumstance and for showing me the merit of slowing myself down from time-to-time.

Thank you to all of the Glish lab members, past and present. It has been a great privilege getting to know all of you.

Table of Contents

List of Tables

List of Figures

List of Abbreviations and Symbols

A	ampere
AI-ECD	activated ion electron capture dissociation
Au	gold
B	magnetic field
BaF_2	barium fluoride
BIRD	blackbody infrared radiative dissociation
BNC	Bayonet Neill Concelman connector (used with coaxial cable connections)
B sector	magnetic sector
C	carbon
C_α	the carbon in a polypeptide backbone to which an amino acid side chain is bound
CE	capillary electrophoresis
C_{ext}	capacitor in a resistor-capacitor network external to an integrated circuit
CID	collision induced dissociation
CI	chemical ionization
CO_2	carbon dioxide
Coll. Eff.	collection efficiency
Cu	copper
Cys	cysteine
ºC	temperature in degrees Celsius
D	dissociation
Da	Dalton
dc	direct current
dia.	diameter
e	elementary charge (1.602×10^{-19} Coulombs $mole^{-1}$)
EC	electron capture
ECD	electron capture dissociation
ECD_{LIT}	linear ion trap within the nanoFrontier mass spectrometer where ECD is performed

ECD+CID	simultaneous electron capture dissociation and collision induced dissociation
ECD→IR	AI-ECD where ion activation is done with IR photons after ECD
E_{com}	maximum energy fraction converted to internally energy during ion-neutral collisions
EDD	electron detachment dissociation
EDD_{LIT}	linear ion trap within the nanoFrontier mass spectrometer where EDD is performed
EI	electron ionization
E_{lab}	ion kinetic energy in laboratory frame of reference
ESI	electrospray ionization
ε_0	critical energy for dissociation
eV	electron volt
E sector	electric sector
Fe	iron
f.l.	focal length
FOCL2	focusing lens 2 in the Bruker Q-FTICR-MS instrument
Frag. Eff.	fragmentation efficiency
FTICR	Fourier transform ion cyclotron resonance
h2	collision / external accumulation hexapole in the Bruker Q-FTICR-MS instrument
HECD	high energy (hot) electron capture dissociation
HPLC	high performance liquid chromatography
hv	photon energy (*h* = Planck's constant, 6.63×10^{-34} J sec; *v* = frequency, s^{-1})
HV	high voltage
Hz	hertz
i	electrical current (in amperes)
IAM	iterative accumulation multiplexing
ICR	ion cyclotron resonance
I.D.	inner diameter
IR	infrared
IR→ECD	AI-ECD where ion activation is done with IR photons before ECD

IRMPD	infrared multiphoton dissociation
IVR	intramolecular vibrational energy redistribution
K	one thousand (e.g., 512 K data points for ICR detection)
kcal mol^{-1}	kilo calories per mole (unit of energy per Avogadro's number)
$k_{dissociation}$	rate constant for dissociation
keV	kilo electron volt ($1x10^3$ eV)
kHz	kilo hertz ($1x10^3$ Hz)
kΩ	kilo Ohm
LC	liquid chromatography
LIT	linear ion trap (two-dimensional quadrupole linear ion trap)
LMCO	low mass cut off
LOD	limit of detection
m	mass
MALDI	matrix assisted laser desorption ionization
m_d^+	product ion
m_n	neutral fragment
m_p^+	parent ion
μA	microampere ($1x10^{-6}$ ampere)
μF	microFarad ($1x10^{-6}$ Farad)
μL	microliter ($1x10^{-6}$ liter)
μM	micromolar concentration ($1x10^{-6}$ molar concentration)
μm	micrometer ($1x10^{-6}$ meter)
μs	microseconds ($1x10^{-6}$ seconds)
MCP	multi-channel plate
M_i	mass of ion
mm	millimeter ($1x10^{-3}$ meter)
MMA	mass measurement accuracy
MΩ	mega Ohm ($1x10^6$ ohms)

mol	Avogadro's number (6.02×10^{23} entities per mole)
m_p^{+*}	activated ion
M_r	molecular weight of neutral analyte
MS	mass spectrometry
ms	milliseconds (1×10^{-3} seconds)
MS/MS	tandem mass spectrometry
MS/MS Eff.	MS/MS efficiency
M_t	mass of target gas
m/z	mass-to-charge ratio
n	number of protons added to or subtracted from a molecule, M ($\mathbf{[M+nH]^{n+}}$, $\mathbf{[M-nH]^{n-}}$)
N	number of degrees of freedom
N	nitrogen
N_2	molecular nitrogen
nA	nanoampere (1×10^{-9} ampere)
nESI	nano-electrospray ionization
Ω	ohm (unit for electrical resistance)
ω	observed frequency of ion motion within the ECD_{LIT} / EDD_{LIT}
ω_c	ion cyclotron frequency
ω_0	frequency of the applied supplemental dipolar waveform in the ECD_{LIT}
ω_q	ion secular frequency
O_2	molecular oxygen
pA	picoampere (1×10^{-12} ampere)
PA	proton affinity
PEG	polyethylene glycol
pF	picoFarad (1×10^{-12} Farad)
φ(x,y,t)	quadrupolar potential
PPA	protonated phthalic anhydride
PPG	polypropylene glycol

ppm	parts per million
PTM	post translational modification
q	quadrupole device used as a collision cell for CID experiments
Q	quadrupole mass filter
Qh	section of Bruker Q-FTICR-MS comprised of the Q and collision hexapole
QIT	quadrupole ion trap
QITMS	three-dimensional quadrupole ion trap mass spectrometer
Q-FTICR-MS	quadrupole-Fourier transform ion cyclotron resonance-mass spectrometer
QUIPS	quarupole user interface power supply (part of the Bruker Q-FTICR-MS)
rf	radio frequency
r_0	inscribed radious of linear ion trap rod array
RC	resistor-capacitor network
RRKM	Rice-Rampsberger-Kassel-Marcus theory for unimolecular dissociations
R_T	external resistor
s	seconds
σ	sigma, electron capture cross-section
S/N	signal-to-noise ratio
SNAP2	peak picking algorithm used by Bruker Daltonics data analysis software
SORI-CID	sustained off-resonance irradiation collision induced dissociation
SWIM	stored waveform ion modulation
Σ	sigma, indicating the summation of what follows (e.g., Σ(product ion abundances))
TOF	time of flight
TA-IRMPD	thermally assisted infrared multiphoton dissociation
torr	unit of pressure (1 torr = 1 mmHg = 1.33 mbar = 133.3 Pascal)
t	time
T	tesla, measure of magnetic field strength (1 T = 1 kg A^{-1} s^{-2})
TCNQ	7,7,8,8-tetracyanodiquinodimethane
TTL	transistor-transistor logic

t_w	pulse width
U	dc potential
V	voltage or volts
%v	percent by volume
$V_{0\text{-}p}$	amplitude (zero-to-peak) of an electrodynamic voltage
W	watt, measurement of power (1 W = 1 N m s^{-1})
z	charge
ZnSe	zinc selenide (focusing lens for IR radation)

Chapter 1

Introduction to Tandem Mass Spectrometry (MS/MS)

1.1 Mass spectrometry as a rapid, sensitive technique for structural analysis

Mass spectrometry (MS) is a technique that has gained widespread use due to its speed of analysis (on the order of 100 ms)[1], sensitivity, and limit of detection (zeptomole detection limits have been reported when chromatographic separations are used before MS analysis).[2] MS has been employed to study analyte structure, complex mixtures, solid surfaces, tissue imaging, and environmental conditions. For a sample to be analyzed by MS it must be ionized in the gas phase and possess a net charge (either positive or negative). MS provides information on the mass-to-charge ratio and abundance of analytes present in a sample

Over the past century since MS was first practiced by J. J. Thomson, advances in instrumentation have increased the breadth of applications and users in the MS field. This is particularly due to the development of different ionization sources that allow analytes representing a range of volatilities to be studied. Initial MS experiments required samples to be highly volatile due to the commonly used electron ionization (EI) source. In addition to ionizing the gaseous sample, the EI process often results in the fragmentation of the molecular ion. The fragments can then be used to determine structural information which aids in the identification of the intact analyte, much in the same way as the pieces of a jigsaw puzzle complete the image of the intact picture. However, EI is only applicable for samples with sufficiently high volatility to be in the gas phase prior to ionization. In general, as analyte size increases volatility decreases. Several schemes have been developed to provide a means of transferring non-volatile species into the gas phase with ionization occurring either during or after the transfer. Matrix assisted laser desorption (MALDI) and electrospray ionization (ESI) are two methods that were developed to ionize large, non-volatile samples for MS

analysis. The advent of MALDI[3, 4] and ESI[5] allowed MS to enter the areas of biological research. ESI has become widely used for biomolecule analysis because molecules can be sampled directly from solution, allowing ESI to be coupled to analytical separation techniques (i.e., liquid chromatography, LC and capillary electrophoresis, CE).[6]

ESI is referred to as a “soft” ionization technique.[6, 7] While “soft” carries little analytical information, the term is used to indicate that little or no fragmentation of the intact analyte is observed from the ionization process itself. The lack of fragmentation has the advantage of simplifying the mass spectra that are acquired. However, without fragmentation the only information that can be garnered from a typical ESI spectrum is the mass-to-charge ratio of the intact ion. Knowing only the mass-to-charge ratio of the intact ion is typically not descriptive enough for an accurate identification because there are frequently a multitude of ways to combine the constituent atoms in the molecule that would result in the same nominal mass-to-charge ratio. To overcome the disadvantage of limited fragmentation in ESI, the intact ion can be activated through one of a number of processes to induce dissociation. The process of inducing the dissociation of a specific ion is referred to as tandem mass spectrometry (MS/MS). The term tandem mass spectrometry is used because two stages of MS analysis are required. First, the ion that is being activated (referred to as the parent ion) is isolated based on an intrinsic property (e.g., kinetic energy or mass-to-charge ratio). Second, the ions that result from parent ion dissociation (referred to as product ions) are mass analyzed to generate the product ion spectrum. Tandem mass spectrometry makes it possible to use ESI to obtain structural information for large, non-volatile molecules (e.g., peptides and proteins).

Several different methods of parent ion activation exist for performing MS/MS experiments. The choice of which method to use depends on the structure of the parent ion, the gas-phase chemistry the parent ion may participate in, and the design of the mass spectrometer intended to be used for the MS/MS experiment. Different mass spectrometers are capable of performing different types of ion activation. Also, mass spectrometers can employ different ways of detecting ions based on their mass-to-charge ratios, i.e. mass analysis. Some forms of mass analysis offer higher mass resolving power (i.e., the ability to differentiate two peaks of similar mass-to-charge in a mass spectrum) than others and different mass analyzers operate on different experimental time scales. In

general, no one mass analyzer is the best for all situations where MS/MS analyses are performed. By coupling different mass analyzers together into one mass spectrometer, a more versatile instrument for MS/MS experiments can be constructed.

The most common mass-to-charge analyzers are listed in Table 1.1 along with the ion kinetic energies at which they each operate. In sector instruments the ion kinetic energy is in the kilo electron volt (keV) region while for quadrupole mass filters ion kinetic energy is < 50 eV. The differences in kinetic energies associated with each mass spectrometer are a result of the method by which each is operated. For example, the sensitivity of multi-channel plates (MCPs) typically used to detect ions in time-of-flight (TOF) mass analyzers increases with the kinetic energy of the incident ions. Conversely, in a quadrupole mass filter (Q) lower ion kinetic energies result in more resolved ion isolation because the ions are exposed to more cycles of the rf potential. Specific mass analyzers are often chosen to be coupled together to take advantage of their individual characteristics. Using the Q and TOF analyzers as an example, a quadrupole mass filter can isolate a parent ion with unit resolution. The isolated ion can then be made to undergo dissociation and the product ions detected with a TOF mass analyzer. The TOF detection offers resolving power in the tens of thousands and mass measurement accuracies of less than 50 parts per million. Higher resolving power allows for more information to be obtained from one spectrum because overlapping peaks can be clearly

Table 1.1 Ion kinetic energies associated with common mass analyzers used in mass spectrometry.

Mass spectrometer (type of mass analyzer)	Ion kinetic energy range
Time-of-flight (TOF)	1 – 30 keV
Sectors (Electric, E or Magnetic, B)	2 – 10 keV
Quadrupole mass filter (Q)	< 50 eV
3-D quadrupole ion trap (QITMS)	< 10 eV
Fourier Transform ion cyclotron resonance (FTICR)	< 10 eV

differentiated into unique mass-to-charge values. The mass measurement accuracy is a metric used to describe the accuracy with which a mass analyzer detects ions by comparing an experimentally determined mass-to-charge ratio to a theoretical value using a standard. The implementation of a QTOF would thus allow sensitive parent ion isolation and provide accurate mass product ion

information resulting in improved MS/MS results over using either the quadrupole mass filter or the TOF mass analyzer alone.[8]

Along the same line of thinking that led to the creation of the QTOF mass spectrometers, FTICR-MS instruments have now been coupled to quadrupole mass filters for external ion isolation and accumulation. The main motivation behind developing external accumulation was to overcome the difficulties associated with trapping ions generated from an external, continuous source (e.g., ESI) at the ultralow pressures of the ICR cell. Such difficulties created problems for coupling liquid phase chromatographic separations to the FTICR mass analyzer. The first report of external ion accumulation implemented with FTICR-MS was published in 1997.[9] In this setup, ions were trapped in an rf-only octapole thus no mass selective isolation could be performed. However, external accumulation resulted in an improved duty cycle (near 100 %), enhanced signal-to-noise ratios (S/N), and increased mass resolving power. Given the success of external accumulation coupled to an FTICR-MS instrument, research continued in an effort to add improved sensitivity to the previously mentioned benefits of the technique. By incorporating a quadrupole mass filter before an accumulation multipole device, mass-selective external accumulation could be performed (i.e., Q-FTICR-MS.[10] Researchers have shown that by using ion selection prior to external accumulation an order of magnitude increase in dynamic range results from only a 6-fold increase in accumulation time and a ~10 zmol (~600 molecules) limit of detection (LOD) can be obtained.[10]

The use of a Q-FTICR-MS instrument has been reported for MS/MS experiments for the top-down analysis of intact proteins.[11] This hybrid instrument offers the previously described advantages associated with external ion accumulation. For example, a 7.5-fold improvement in S/N was obtained by mass-selectively isolating a parent ion rather than passing ions in rf-only mode through the mass resolving quadrupole. Most unique to this specific Q-FTICR-MS instrument is its incorporation of several different methods of ion activation. Specifically, infrared multiphoton dissociation (IRMPD) and electron capture dissociation (ECD) can be performed in the ICR cell and collision induced dissociation (CID) can be done in the external accumulation region. Each one of these MS/MS methods will be described in Section 1.2. By coupling mass-selective parent ion isolation with the highest resolving power offered by any mass spectrometer currently (i.e., the FTICR

mass analyzer) the Q-FTICR-MS capitalizes on the benefits of its constituent mass analyzers. In addition, the incorporation of a variety of MS/MS methods on the Q-FTICR-MS creates a more versatile instrument for MS/MS experiments.

1.2 Tandem mass spectrometry (MS/MS)

Tandem mass spectrometry allows ion structural information to be acquired which aids in analyte identification.[12, 13] As mentioned, MS/MS requires two stages of MS. The isolation of the parent ion is performed in the first stage. In the second stage, dissociation of the isolated parent ion is induced through some form of ion activation and the resultant product ions are mass analyzed. Various methods of MS/MS exist and they are named according to type of ion activation they employ. The type of ion activation (i.e., MS/MS method) used is dependent upon what information is required from the MS/MS experiment and which methods of activation are available on a given mass spectrometer.

1.2.1 *General description*

In general, an MS/MS experiment can be represented by Equation 1.1 where $\boldsymbol{m_p}^+$ represents the parent ion, and $\boldsymbol{m_d}^+$ and $\boldsymbol{m_n}$ are the product ion and neutral fragment, respectively.

$$m_p^+ \rightarrow m_d^+ + m_n \qquad \text{(Equation 1.1)}$$

If $\boldsymbol{m_p}^+$ is multiply charged, as from ESI, then $\boldsymbol{m_n}$ may not be neutral but could also carry a charge. In Equation 1.1, $\boldsymbol{m_d}^+$ is referred to as a first generation product ion. In some mass spectrometers $\boldsymbol{m_d}^+$ could be isolated and dissociated to generate second generation product ions. The process of performing sequential MS/MS experiments is referred to as MS^n, where the dissociation of $\boldsymbol{m_d}^+$ would be an example of MS^3. In addition to providing structural information about the parent ion, MS/MS is also useful for mixture analysis.[14]

The reaction in Equation 1.1 is a unimolecular dissociation which occurs at a rate that can be described by RRKM theory (Rice-Ramsberger-Kassel-Marcus).[15] For such dissociations, product ion formation is dependent upon overcoming the critical energy for dissociation (ε_0). As shown in Figure 1.1, ε_0 is the relative difference in potential energy between the internal energy before activation and the barrier to dissociation. MS/MS experiments differ in the type of ion activation used to overcome the critical energy barrier.

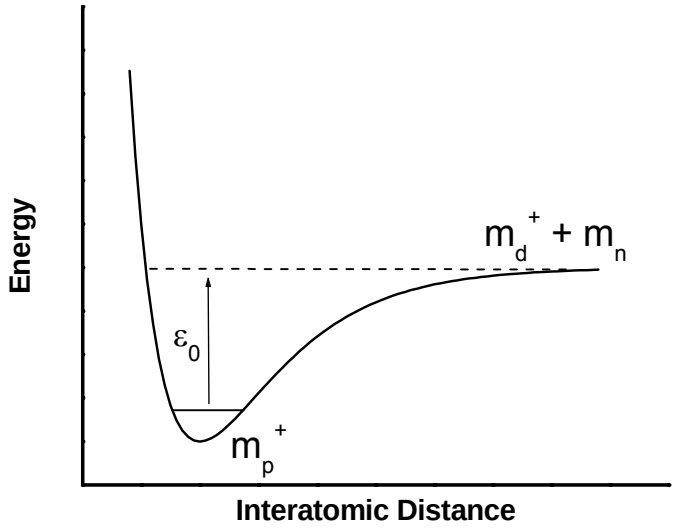

Figure 1.1 Generic potential energy diagram illustrating the critical energy of dissociation.

1.2.2 *Types of MS/MS used in this dissertation*

Tandem mass spectrometry has been reviewed in the literature.[16, 17] For the work discussed in this dissertation, all of the analytes that have been studied and subjected to MS/MS analysis have been peptide and protein ions. One goal behind performing MS/MS on such samples is to determine their amino acid sequence. Determination of their sequence allows peptides and proteins to be unambiguously identified. Knowing the sequence can also provide structural information about the analyte. Shown in Figure 1.2 is a generic peptide sequence where the amino acid side chains are labeled as R-groups. By cleaving the peptide backbone at different locations,

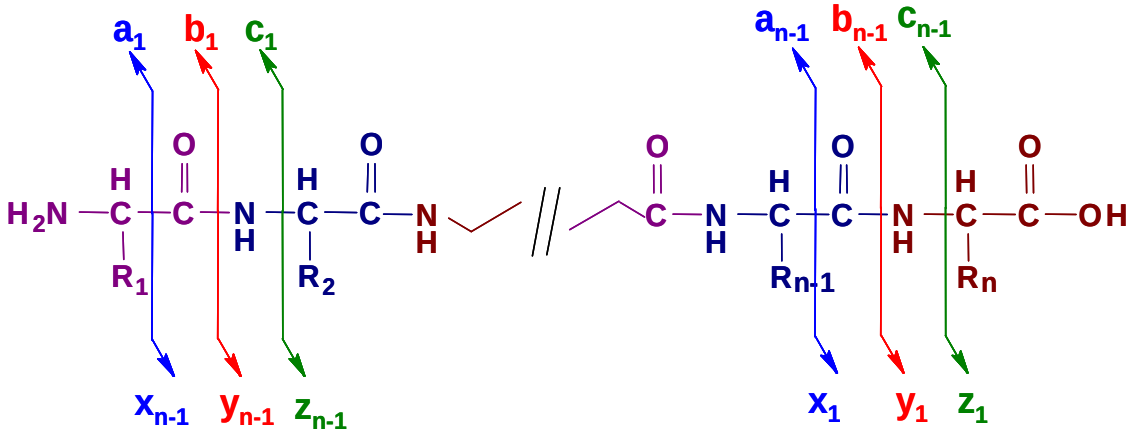

Figure 1.2 Annotation of peptide and protein MS/MS data. CID and IRMPD result in **b** / **y** formation, ECD produces mainly **c** / **z** ions, and EDD gives **a** / **x** ions.

different types of product ions can be formed. For example, cleavage of the N-C_α bond could result in the formation of a **c** or **z** ion, or both if the parent ion is multiply charged. If the charge remains on the N-terminus, then a **c** ion is formed. Which **c** ion is formed is denoted by the number of the residue, with the numbering beginning at the N-terminal end of the peptide. Conversely, if the charge were to remain on the C-terminus, then the product ion would be a **z** ion where now the numbering begins from the C-terminal end. The type of product ions (i.e., **b**/**y**, **c**/**z**, or **a**/**x**) generated depends upon the type of activation method employed. Four different MS/MS methods that have been studied and will be addressed in this dissertation are collision induced dissociation (CID), infrared multiphoton dissociation (IRMPD), electron capture dissociation (ECD), and electron detachment dissociation (EDD). Each one of these will be explained over the next few sections.

To quantitatively compare different types of tandem mass spectrometry to each other as well as to compare one MS/MS method on two different instruments, the metrics of fragmentation, collection, and MS/MS efficiency can be used. Fragmentation efficiency indicates the percentage of the total ion abundance in the MS/MS spectrum that corresponds to product ions:

$$\text{Fragmentation Efficiency: } \frac{\sum(\text{product ion abundance})}{\sum(\text{product ion abundance}) + (\text{remaining parent ion abundance})}$$

(Equation 1.2.)

In Equation 1.2, the product ion abundance includes the abundance of any mass-to-charge ratios that are detected, whether or not they can be identified, and have a different mass-to-charge ratio than the parent ion. The remaining parent ion abundance is the abundance of the isolated parent ion mass-to-charge ratio that is remaining following activation. To determine what percentage of the parent ion signal can be accounted for following ion activation, the collection efficiency can be calculated as shown in Equation 1.3:

$$\text{Collection Efficiency: } \frac{\sum(\text{product ion abundance}) + (\text{remaining parent ion abundance})}{(\text{initial parent ion abundance})} \quad \text{(Equation 1.3)}$$

In Equation 1.3 the denominator represents the abundance of the parent ion acquired in the isolation spectrum. The collection efficiency provides a measure of ion loss between different stages of MS.

Finally, the complete analysis of an MS/MS experiment is given by the MS/MS efficiency, which is defined in Equation 1.4:

$$\text{MS/MS Efficiency: } \frac{\sum(\text{product ion abundance})}{(\text{initial parent ion abundance})} \quad \text{(Equation 1.4).}$$

The MS/MS efficiency indicates how effectively the isolated parent ion has been dissociated into product ions and how well those product ions have been detected. Considering Equations 1.2—1.4 it can be seen that the MS/MS efficiency is the product of the fragmentation and collection efficiencies.

1.2.2.1 *Collision induced dissociation (CID)*

Collision induced dissociation (CID) is most commonly used for MS/MS experiments.[18-20] In CID experiments, a parent ion undergoes collisions with a neutral gas or molecule to convert some of the ion's kinetic energy into internal energy. Once enough internal energy has been deposited into vibrational modes of the parent ion to overcome the critical energy for dissociation, the parent ion dissociates into product ions. Because the total amount of energy and momentum in the system must be conserved, it can be shown that the maximum amount of translational energy that can be converted into internal energy (E_{com}) is given by:

$$E_{com} = E_{lab} \frac{M_t}{M_i + M_t} \qquad \text{(Equation 1.5).}$$

Where M_i is the ion mass, M_t is the mass of the target (or collision) gas or molecule, and E_{lab} is the ion kinetic energy in the laboratory frame of reference.[2, 20] Different collision gases have been used but the most common are helium, nitrogen, and argon due to their inertness and their relative inability to distribute any energy into internal modes within themselves.

From Equation 1.5 it can be seen that the CID process depends upon the relative masses of the two colliding species. The conservation of energy dictates that if the relative translational energies of M_t and M_i change by a specific amount, that same amount of energy must appear as internal energy.[16] Consequently, an increase in M_t would result in a larger E_{com} and a concomitant increase in the amount of parent ion internal energy. For this reason, heavier collision gases are preferred. However, the benefit of increased conversion of translational energy to internal energy can be offset by increased ion scattering leading to a decrease in sensitivity.

In addition to changing the mass of the target (collision) gas, the kinetic energy of the parent ion can be increased. Two general classes of CID exist: low and high energy collisions. As described in reference [16] low-energy collisions (1—100 eV) are common in quadrupole devices, and QqQ and FTICR-MS instruments. Conversely, high-energy collisions (100 – 1000eV) are typically used for sector and TOF/TOF mass spectrometers.

Under low energy CID conditions, parent ion excitation is mostly vibrational.[16] As a consequence, the internal energy imparted to the ion can be redistributed throughout the vibrational modes of the molecule. This process is referred to as intramolecular vibrational energy redistribution (IVR). Because of this redistribution multiple ion-neutral collisions are required in this energy regime to overcome the critical energy barrier for dissociation. Another consequence of IVR is that as the internal energy of the parent ion increases and gets redistributed throughout the ion, the weakest bonds in the parent ion are broken first. Consequently, for polypeptide analytes CID results in the facile loss of labile moieties (e.g., post translational modifications, PTMs) and the preferential formation of **b** and **y** ions.[20]

1.2.2.2 *Infrared multiphoton dissociation (IRMPD)*

As an alternative to CID, the internal energy of a parent ion can be increased by vibrational excitation through the absorption of IR photons. If the internal energy is increased enough to overcome the critical energy for dissociation the parent ion will go on to form product ions and the process is referred to infrared multiphoton dissociation (IRMPD).[21, 22] IRMPD utilizes continuous-wave CO_2 lasers of 10.6 μm wavelength and laser powers below 100 W. Irradiation times of tens to hundreds of milliseconds are typical.[16] Ion trapping instruments like three- and two-dimensional quadrupole ion traps (QIT and LIT) mass spectrometers and FTICR-MS are most conducive for IRMPD work because the absorption of multiple IR photons is required for product ion formation.

In general, photodissociation can be viewed as occurring through Equation 1.6:

$$m_p^+ \xrightarrow{nhv} m_p^{+*} \xrightarrow{k_{dissociation}} m_d^+ + m_n \qquad \text{(Equation 1.6).}$$

The number of absorbed photons is given by n, hv is the photon energy, and $k_{dissociation}$ is the rate constant for dissociation.[16] As the parent ion absorbs IR photons into IR-active modes, the gained

internal energy is redistributed over all internal vibrational degrees of freedom. This redistribution is the same process that occurs during multiple collision events of low energy CID. Both CID and IRMPD result in a statistical internal energy distribution, consequently IRMPD and CID typically provide similar product ions.

One significant difference between CID and IRMPD is the effect collisional cooling has on the latter. In CID, the parent ion is resonantly excited allowing the parent ion internal energy to increase from sequential ion-neutral collisions. In most experiments, IRMPD is not a resonant process and as the internal energy of an ion is increased through the absorption of IR photons the ion is still undergoing collisions with the neutral bath gas. Note that the bath gas has the same chemical composition as the collision gas in CID, but because the activation of the ion through collisions is not the intent during IRMPD the gas is referred to as the bath gas. The effect of the IR activated ion ($\boldsymbol{m_p}^{+*}$) colliding with the bath gas is that some of the parent ion internal energy goes into increasing the kinetic energy of the bath gas molecule. As a result, the rate of collision cooling is in competition with the rate of dissociation resulting from IR absorption. This competition is especially important in mass analyzers where there is a significant bath gas pressure (e.g., QIT and LIT mass spectrometers) and is less important in the ultrahigh vacuum conditions of an FTICR-MS instrument. Different strategies have been implemented to reduce the effect of collisional cooling for the improvement of IRMPD in ion trapping instruments. Reducing the helium bath gas pressure[16], using pulsed introduction of the helium bath gas,[23] and heating the bath gas to raise its average kinetic energy in a process referred to as thermally assisted (TA)-IRMPD[24] have all proven successful.

1.2.2.3 *Electron capture dissociation (ECD)*

Electron capture dissociation (ECD) involves the capture of a low kinetic energy, free electron by a multiply charged cation ($\mathbf{[M+nH]^{n+}}$), where the multiply charged cation is typically formed from ESI.[25] The electron capture results in the formation of the charge-reduced species, $\mathbf{[M+nH]^{(n-1)+\bullet}}$. For polypeptide ions, the odd-electron intermediate then undergoes extensive dissociation to form primarily **c'** and **z•** ions from cleavage of the (N-C_α) bond and to a lesser extent **a•** and **y'** ions, through the reactions proposed in Equations 1.7 –1.9.[26] The prime and radical notation

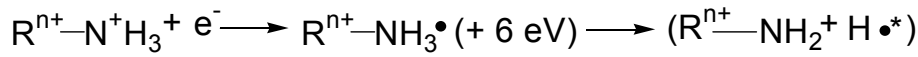

(Equation 1.7)

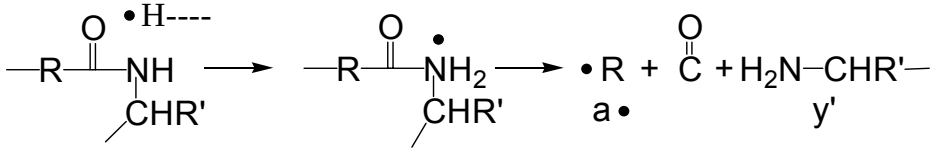

(Equation 1.8)

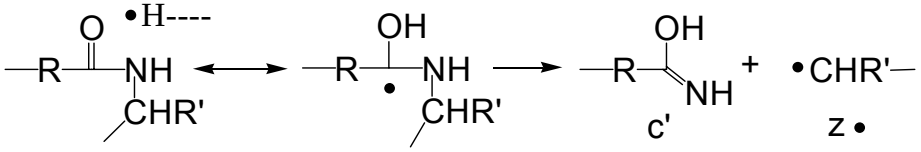

(Equation 1.9)

distinguishes product ions that differ by one H-atom and is used to indicate which product ion contains the neutralized proton resulting from electron capture. During ECD experiments of polypeptide ions, it is possible to form **c•** and **z'** ions, which has been proposed to be the result of H-atom abstraction from the **c**-ion backbone or side chains by the alpha-carbon radical on the **z•** ion.[27, 28] In a later report, the authors of the proposed reactions in Equations 1.7-1.9 used computer modeling to show that for protonated triglycine the proton possesses 57% of the charge while the neighboring amide NH and the remaining amide groups contain 15 and 27% of the charge, respectively.[29] These results indicate that electron capture can occur remotely (i.e., a few residues) from the proton but the charged site is still the most favored. Regardless, following capture the electron would be transferred to the site with the highest charge density, which is the protonation site, resulting in the formation of an **H•**. The moiety with the highest hydrogen-atom affinity would then capture the **H•**, for example carbonyl or a disulfide bond, which is consistent with Equations 1.7-1.9.[29]

The ion-radical chemistry in Equations 1.7-1.9 is generally accepted in the ECD literature, however, there is debate over the claim that ECD is a nonergodic process.[25, 26, 30] The term nonergodic means that bond dissociation occurs before the recombination energy associated with a cation capturing an electron can be redistributed into the 3N-6 vibrational modes of the parent ion. The reason nonergodicity is claimed for ECD is that extensive parent ion dissociation is observed despite there only being between 4 and 7 eV of energy released in terms of recombination energy.

For example, redistributing 7 eV of energy into the vibrational modes of a 3 kDa molecule only increases the internal energy by 50—100 K, compared to the 300—600 K typical of vibrational excitation, i.e. CID.[29] Furthermore, it has been suggested that ECD occurs faster than 10^{-12} s[31] which is too fast for energy to be distributed into vibrational modes of the molecule which vibrate on the time scale of 10^{-13} s.

Researchers have found support for the nonergodic claim of ECD by successfully using ECD to dissociate doubly protonated, cyclic peptides.[32] The dissociation of a cyclic peptide via ECD implies that the capture of one electron is responsible for the cleavage of at least two covalent bonds, a ring opening bond cleavage and a peptide backbone cleavage.[32] The authors rationalize their results by claiming electron capture induces a nonergodic cleavage of the ring (which could occur on the 10^{-12} s time scale) to form a radical at the alpha-carbon position, which is consistent with Equation 1.9. It is proposed that the radical at the alpha-carbon position then initiates a free radical reaction cascade along the peptide backbone to cause backbone and side-chain cleavages.

However, other researchers have proposed that the nonergodic argument does not need to be invoked to explain the results from ECD experiments. These researchers used computational results to claim that the amide group can directly capture an electron in a long-lived electronic valence state. The direct electron capture would increase the basicity of the amide carbonyl oxygen so it can exothermically abstract a proton from an amino acid residue. The results suggest that the proton abstraction forms a labile aminoketyl radical that readily dissociates via N-C_α bond scission.[33] Later work by this same group tagged a fixed charge to the N-terminus and protonated a lysine or arginine to form the $\mathbf{[M+2H]^{2+}}$ species for several dipeptides for ECD analysis. Their results supported their position that ECD does not exclusively proceed via a nonergodic mechanism.[34] The results from this group are supported by work where surface induced dissociation (SID) was used to dissociate a peptide radical cation generated by in-source dissociation of $\mathbf{[Cu^{II}(terpy)DRVYIHPF]^{2+}}$.[35] Results from this work show that the dissociation of the odd-electron species was adequately described by RRKM theory and it demonstrated statistical behavior.

While the debate over the ergodicity of ECD is still unresolved, the product ions detected from ECD MS/MS experiments are consistent from laboratory to laboratory. ECD unlike CID or IRMPD, is able to provide extensive peptide and protein backbone cleavage (and thus sequence coverage) while not disrupting labile bonds allowing the sites of post translational modification (e.g., glycosolation[36] or phosphorylation[37]) to be determined. ECD can only be performed on mass spectrometers capable of generating low kinetic energy (~ 1 eV) electrons.[30] Prior to 2004, this limited the application of ECD to FTICR-MS instruments where only static dc and magnetic fields are required for ion trapping.[38] The amplitudes of the rf fields used for QIT and LIT mass spectrometers result in acceleration of free electrons. The acceleration of the electrons results in kinetic energies which are not optimum for capture by a multiply charged cation.[39] The electron capture cross-section for ECD is proportional to the square of the ion charge. As the kinetic energy of the free electrons is varied, two maxima in cross-section values are observed. One maximum occurs using low energy electrons (~ 1 eV) while the other occurs with ~3-13 eV electrons, in the so-called hot or high energy ECD (HECD) range.[40] Typical electron capture cross-sections under low energy ECD conditions are 10^{-11} to 10^{-14} cm^2.[26] HECD has demonstrated the ability to differentiate isomeric leucine and isoleucine due to differences in their secondary, side-chain fragmentation.[41]

Though no work will be presented in this dissertation on the topic of electron transfer dissociation (ETD), it is worth mentioning this MS/MS method due to its similarity to ECD. ETD, introduced in 2004, provides a way to produce ECD-like results in ion trapping mass spectrometers via ion-ion reactions.[42, 43] In ETD a reagent anion (e.g., fluoranthene) is generated from a chemical ionization (CI) source while a multiply charged cation is produced via ESI. Both polarities (anions and cations) are made to interact inside of the same trapping volume, either through co-trapping them or passing one polarity through a trapping volume occupied by the opposite polarity. Under the appropriate conditions, the result of the ion-ion reaction is the transfer of an electron from the anionic reagent to the cationic analyte which causes dissociation of N-C_α bonds just as in ECD.

1.2.2.4 *Electron detachment dissociation (EDD)*

While ECD generates extensive peptide and protein sequence coverage, its use is limited to the positive ion mode. However, acidic analytes are more readily ionized as negative ions. The

anionic complement to ECD was introduced in 2001 and is called electron detachment dissociation (EDD).[44] In EDD, multiply charged anions are irradiated with high kinetic energy (>10 eV) electrons as shown in Equation 1.10:

$$[M - nH]n^- + e^-_{(>10eV)} \rightarrow [M - nH]^{(n-1)-\bullet} + 2e^- \qquad \text{(Equation 1.10).}$$

Under EDD conditions, the charge-reduced species (**[M-nH]$^{(n-1)\bullet}$**) dissociates at the C-C_α bond to form primarily **a•** and **x** product ions (when M is a peptide anion). While decarboxylation is also a major dissociation pathway associated with EDD, density functional theory has predicted that C-C_α bond cleavage is the lowest-energy channel of backbone fragmentation and this is supported by experimental evidence.[45]

Like ECD, EDD has demonstrated the ability to provide extensive peptide sequence coverage while allowing labile PTMs (e.g, phosphorylation) to be retained [45]. EDD does not cleave on the N-terminal side of proline[45] and EDD has been shown to preferentially cleave disulfide bonds.[46] EDD has also been used for the characterization of oligodeoxynucleotides[47, 48], gangliosides[49], oligosaccharides[50], and glycosaminoglycan tetrasaccharides.[51, 52]

1.3 Instrumental descriptions

1.3.1 *Hybrid linear ion trap / time-of-flight (LIT/TOF) mass spectrometer*

The linear ion trap / time of flight mass spectrometer used for the MS/MS work presented in this dissertation is a modified version of the NanoFrontier LIT/TOF manufactured by the Hitachi Corporation (Hitachi High Technologies). This instrument incorporates two LIT devices for parent ion manipulation (i.e., isolation, accumulation, and activation) and a TOF mass analyzer. The NanoFrontier LIT/TOF is also the first commercially available mass spectrometer that allows ECD to be performed in a mass analyzer other than a FTICR-MS instrument.[38, 53] A simplified diagram of the LIT/TOF is shown in Figure 1.3.[53] The theory behind the operation of quadrupole ion trapping devices has been reviewed in the literature.[1, 54] The specific modifications made to the instrument will be provided in the Experimental section of the relevant chapters, but a general description of the instrument operation will be provided here.

For the LIT/TOF instrument in Figure 1.3, ions are formed via nESI from a glass capillary sprayer pulled to a tip opening of 2 – 5 μm using a spray potential typically between 1100 and 2000 V.

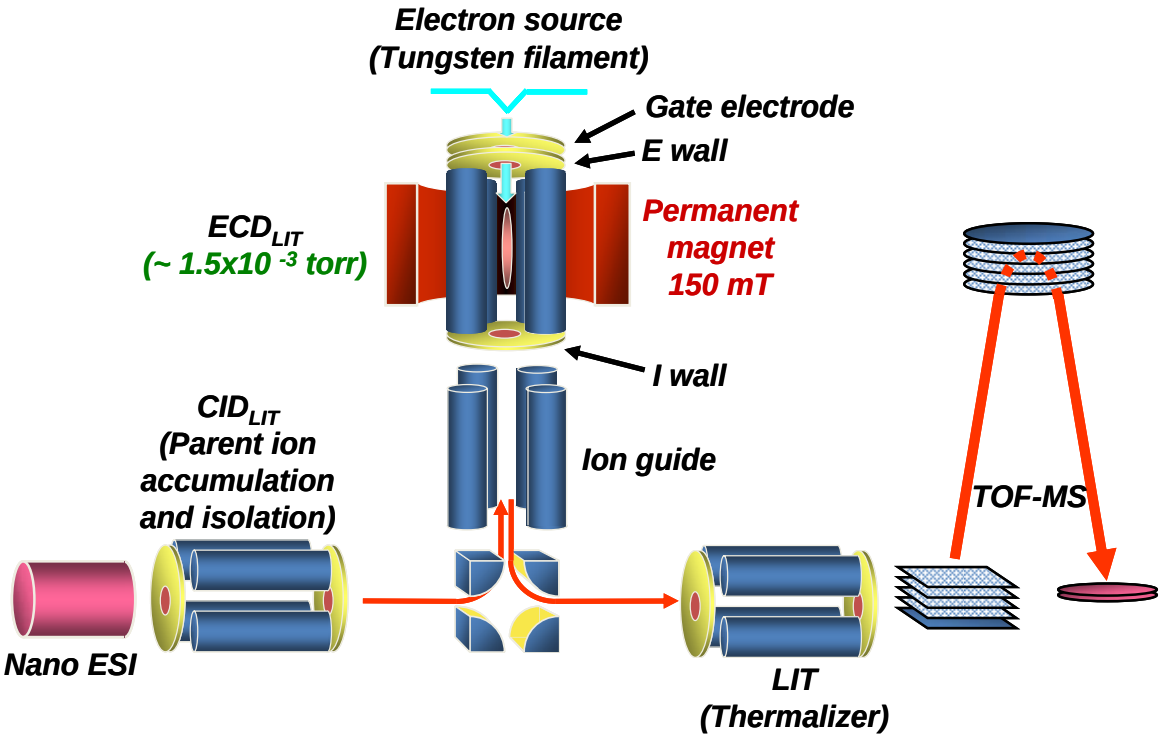

Figure 1.3 Diagram of the nanoFrontier hybrid LIT/TOF mass spectrometer. The diagram is not to scale. Modified from Ref. [57]. Copyright 2007 American Chemical Society.

Ions are trapped and accumulated in the CID_{LIT} for 20 – 100 ms before parent ion isolation is performed. Once the parent ion mass-to-charge has been isolated, it is ejected from the CID_{LIT} and either sent directly through the thermalizer LIT and into the TOF for mass analysis or the ions are directed into the ECD_{LIT} to undergo ECD or EDD MS/MS experiments. Isolated parent ions are ejected axially from the CID_{LIT} so resonance excitation is not used but rather an axial dc gradient is employed. The direction in which the ion beam travels is determined by the voltages applied to the bender electrodes. The thermalizer LIT is used to reduce the width of the kinetic energy distribution of an ensemble of ions prior to TOF analysis.

In the ECD_{LIT} a quadrupolar potential applied to the rod array helps trap the ions in the radial dimension. Axial trapping of the ions is done with dc voltages applied to the I and E wall electrodes and the dc voltage offset applied to the ECD_{LIT} rod array shown in Figure 1.3. The relatively high pressure of helium bath gas in the ECD_{LIT} (i.e, $1.5x10^{-3}$ torr) helps collisionally cool and focus ions to the radial center of the device. In practice, an axial dc potential well of only 1.0 V associated with the I and E wall and the rod offset is sufficient for effective parent ion trapping in the ECD_{LIT}. Once

trapped in the ECD_{LIT} the parent ions can be activated through collisions with the helium bath gas via dipolar excitation (CID), irradiated with IR photons for IRMPD, or exposed to an electron beam generated from a thoriated tungsten filament for ECD or EDD, depending on the ion polarity. The tungsten filament is aligned with the radial center of the ECD_{LIT} rod array, which is the location where the quadrupolar potential is of lowest magnitude. Consequently, injecting electrons into the ECD_{LIT} along the central radial axis is easier than having to inject ions into high amplitudes of the applied rf potential, as is the case for external electron injection in QITMS instruments.[55]

The ECD_{LIT} is housed within a cylindrical, neodymium permanent magnet.[53] A magnetic field strength of 150 mTesla is produced along the radial center of the ECD_{LIT} rod array. The magnetic field helps to radially confine the electron beam generated from the tungsten filament. Radial confinement of the electron beam aids in electron transmission through the ECD_{LIT}. By improving electron transmission through the ECD_{LIT}, the magnetic field also improves the overlap of the electron beam and ion cloud because the ion cloud is radially focused by the aforementioned quadrupolar field. Housing the ECD_{LIT} inside of the permanent magnet has made the ability to perform ECD in a LIT a practicable reality.

1.3.2 *Operation of ECD_{LIT} / EDD_{LIT} cell*

When ECD is being performed the LIT is referred to as the ECD_{LIT}. The LIT is referred to as the EDD_{LIT} during EDD experiments. The same physical instrument components are used for the ECD_{LIT} and EDD_{LIT} modes of operation, but the polarities of the applied voltages are opposite. Slightly different voltage tuning is required in the two modes for optimal ion trapping and ejection. Control of the applied voltages is done using software written in LabVIEW code (National Instruments) by Takashi Baba, PhD. The LabVIEW program provides flexibility in ion manipulation and construction of tailored scan functions. The user has control of the relevant experimental parameters that affect ion trapping and allow ion isolation to be performed in the ECD_{LIT} / EDD_{LIT}. The control software also makes it straight forward to insert a new step in the scan function, for example, to introduce a delay before or after ECD to allow for pre- or post-ECD ion activation by IR radiation, so-called activated ion (AI)-ECD.

The electronics associated with the quadrupole rod set that comprises the ECD_{LIT} / EDD_{LIT} have been modified to allow dipolar resonance excitation to be performed in the device. This modification makes it possible to perform CID in the ECD_{LIT} / EDD_{LIT}, which allows a variety of MS/MS experiments to be conducted when CID is incorporated into the same experiment as ECD. As mentioned previously, free electrons for ECD (and for EDD) experiments are generated using a thoriated tungsten filament (see Figure 1.3) where the potential drop across the filament is between 1.0 and 3.5 V. The kinetic energy of the electrons is determined by the potential difference between the dc potential applied to the filament (this is a different potential than is used for electron generation and is referred to as the filament offset) and the dc offset on the ECD_{LIT} / EDD_{LIT} rod set. The filament and dc offsets are set by the user in the LabVIEW control program. Electron kinetic energies in the range of 0 to 80 eV can be readily obtained.

1.3.3 *Fourier transform ion cyclotron resonance mass spectrometry (FTICR-MS)*

FTICR-MS instruments were first introduced in the early 1970s and still offer the highest mass resolving power and mass measurement accuracy of any mass analyzer.[56-58] The ability of FTICR-MS instruments to provide such high resolving power and mass measurement accuracy comes from the fact that mass analysis is performed based on measuring the frequency of an ion's cyclotron motion within a static, homogenous magnet field.

The FTICR-MS instrument used for MS/MS experiments described in this dissertation is an Q-FTICR mass spectrometer (Bruker Daltonics, Billerica, MA) equipped with a 12-Tesla actively shielded magnet and an Apollo II (Bruker Daltonics, Billerica, MA) electrospray ionization source. A diagram of the Q-FTICR-MS instrument is given in Figure 1.4. The Q portion of the instrument is comprised of the mass selective quadrupole (Extrel, Pittsburgh, PA) followed by an accumulation collision cell/hexapole. This hybrid instrument will be referred to as a Q-FTICR-MS and is capable of performing the external ion accumulation described previously. Similar to other reported Q-FTICR-MS instruments that employ external accumulation[11], the Bruker Q-FTICR-MS is capable of performing CID on mass selected ions in the external Q/hexapole interface. The instrument is also equipped with a hollow, indirectly heated dispenser cathode for the purposes of ECD, see Figure 1.4B. Because the dispenser cathode is hollow a beam of IR photons generated from a 25 W CO_2

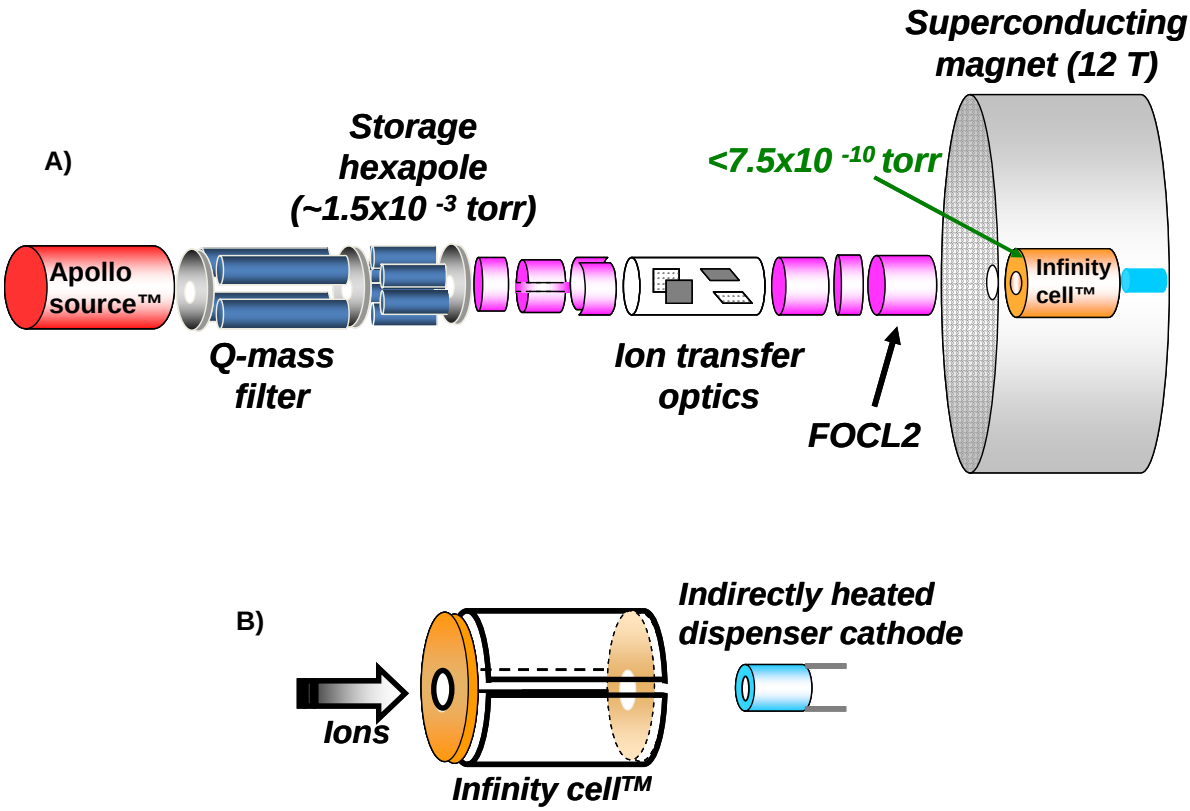

Figure 1.4 A) Diagram of the Bruker Daltonics hybrid Q-FTICR-MS instrument. B) Closer view of the orientation of the ICR cell and dispenser cathode electron source. Diagram is not to scale.

laser can be aligned along the central, radial axis of the ICR cell allowing IRMPD experiments to be performed as well.

Ions are generated via ESI in the Apollo source™ which consists of a two-stage ion funnel and a hexapole ion guide. All ions can be passed through the quadrupole mass filter (Q-mass filter or Q) in rf-only mode and accumulated in the storage hexapole. Typical accumulation times vary between 20 ms and 700 ms. Ions are then extracted out of the storage hexapole by a dc potential gradient and transferred to the ICR cell through a series of ion transfer/focusing optics. The Infinity cell™ aids in trapping incoming ions by using Sidekick trapping, where ions are deflected off of the central axis as they enter the ICR cell. Sidekick trapping increases the residence time ions are in the ICR cell during the accumulation step from less than 1 ms to tens of ms, which increases the number of ions that can be trapped.[9] Sidekick trapping allows the use of the more complex and experimentally unwieldy gated trapping and gas-assisted trapping to be avoided. Once the ions are

trapped in the ICR cell, an excitation pulse is applied to one pair of electrodes that comprise the infinity cell. Ideally the excitation pulse is of constant amplitude across the entire frequency range being excited because each mass-to-charge ratio has a unique cyclotron frequency.[59] The excitation pulse results in an increase in ion cyclotron orbit, bringing the ions closer to the pair of detection plates where an induced image current is acquired and Fourier transformed to obtain a mass spectrum.[58, 60]

1.3.4 *Operation of quadrupole-FTICR-MS*

In addition to passing all ions through the Q mass filter, a single mass-to-charge ratio can be selectively passed and accumulated in the storage hexapole as described when discussing ion isolation in section 1.3.1. By applying a sufficient potential difference between the source hexapole (not shown in Figure 1.4) and the storage hexapole, the ions isolated by the Q mass filter are accelerated into the higher pressure region of the storage hexapole to cause CID. The product ions can then be sent to the ICR cell for mass analysis. Conversely, a parent ion can be isolated and accumulated in the storage hexapole then sent to the ICR cell for ECD or IRMPD MS/MS experiments. The control of the Bruker Q-FTICR-MS is done through pulse-programs which set the appropriate voltages and delay times for ion isolation, accumulation, and dissociation. All of the work presented in this dissertation used the BASIC pulse program.

The greatest difficulty with operating the Q-FTICR-MS is the large number of parameters that can be tuned to optimize ion abundance. The best tuning protocol is to start at the ionization source and tune focusing elements and dc potentials that affect the axial voltage gradient of the ion beam as you move towards the ICR cell. Once the ions reach the ICR cell the trapping potentials and Sidekick voltages should be tuned to provide acceptable sensitivity and mass resolution. Tuning the ICR cell parameters is especially important for ECD experiments because it is critical that the trapped ions are located in the center of the ICR cell for maximum ion-electron overlap. As mentioned, the electrons for ECD experiments are generated from an indirectly heated dispenser cathode. Typically a heater current of 1.5 A is used to activate the electron emissive barium oxide surface. The ECD performance can then be tuned by varying the trapping potentials of the ICR cell and the electron energy and irradiation time.

1.4 Summary

The intent of this chapter was to introduce tandem mass spectrometry (MS/MS) and the different ion activation methods that will be discussed in the subsequent chapters. The overall goal of the work described in this dissertation was to improve the operation of ESI and improve the information content acquired from MS/MS experiments. The topics that will be discussed in each chapter are briefly described here.

Chapter 2 introduces a novel design for a pulsed nESI source. The advantages of nESI over conventional ESI are briefly discussed and the motivations behind pulsing the continuous ESI process are given. Experimental results acquired using a prototype dual nESI source, which is controlled through the application of voltages from a custom-built pulsing circuit, are presented.

Chapter 3 describes a unique method of increasing the amount of information that can be obtained during MS/MS analysis. The iterative accumulation multiplexing (IAM) strategy, originally develop for QITMS instruments[61, 62], was applied to the Q-FTICR-MS instrument for the analysis of peptide mixtures and different protein charge states. The results indicate that the IAM process was successfully implemented using both CID and ECD.

Chapter 4 compares the results between performing ECD in a LIT and an FTICR cell. The spectra presented are the first example of a direct comparison of experimental results obtained for these two instruments. The data shows that very similar ECD results can be obtained from both instruments.

Chapter 5 introduces a technique being referred to as simultaneous ECD, CID (ECD+CID) that was developed for use in the ECD_{LIT} of the hybrid LIT/TOF instrument. The ability to perform ECD+CID is unique to the ECD_{LIT} due to the presence of the helium bath gas used for ion trapping. Results indicate that ECD+CID can improve the extent of peptide sequence coverage compared to performing ECD alone. It has also been demonstrated that under conditions of increased electron flux in the ECD_{LIT}, ECD+CID can aid in reducing the extent of non-dissociative electron capture, which poses challenges for product ion identification.

Chapter 6 provides the first experimental results from EDD being performed in a LIT. The EDD dependence on incident electron energy and irradiation time are presented. Results indicate

that the electron irradiation time needed for EDD in the EDD_{LIT} is significantly shorter than on FTICR-MS instruments. The successful implementation of EDD is demonstrated using acidic and basic peptides.

In Chapter 7, the first results of AI-ECD in a LIT are presented using the protein ubiquitin. The competition between collisional cooling and IR activation at the relatively high pressures of the ECD_{LIT} is discussed.

In Chapter 8 a general summary is provided and ideas for future work related to the projects discussed in the preceeding chapters are given.

1.5 References

1. March, R. E.; Todd, J. F. J. eds. *Quadrupole Ion Trap Mass Spectrometry*. 2nd ed. Chemical Analysis, ed. Winefordner, J. D.; Vol. 165. 2005, John Wiley & Sons, Inc.: Hoboken, NJ. 346.

2. de Hoffmann, E.; Stroobant, V. *Mass Spectrometry: Principles and Applications*. Second ed. 2002, Hoboken, NJ: John Wiley & Sons. 407.

3. Karas, M.; Bachmann, D.; Hillenkamp, F. Influence of the Wavelength in High-Irradiance Ultraviolet Laser Desorption Mass Spectrometry of Organic Molecules. *Analytical Chemistry*. **1985**, 57, p. 2935-2939.

4. Karas, M.; Bahr, U.; Ingendoh, A.; Nordhoff, E.; Stahl, B.; Strupat, K.; Hillenkamp, F. Principles and Applications of Matrix-assisted UV-laser Desorption/Ionization Mass Spectrometry. *Analytica Chimica Acta*. **1990**, 241, p. 175-185.

5. Fenn, J. B.; Mann, M.; Meng, C. K.; Wong, S. F.; Whitehouse, C. M. Electrospray Ionization for Mass Spectrometry of Large Biomolecules. *Science*. **1989**, 246, p. 64-71.

6. Cech, N.; Enke, C. Practical Implications of Some Recent Studies in Electrospray Ionization Fundamentals. *Mass Spectrometry Reviews*. **2001**, 2001, p. 362-387.

7. Van Berkel, G. J.; Kertesz, V. Using the Electrochemistry of the Electrospray Ion Source. *Analytical Chemistry*. **2007**, 79, p. 5510-5520.

8. Chernushevich, I. V.; Loboda, A. V., Thomson, B. A. An Introduction to Quadrupole-Time-of-Flight Mass Spectrometry. *Journal of Mass Spectrometry*. **2001**, 36, p. 849-865.

9. Senko, M. W.; Hendrickson, C. L.; Emmett, M. R.; Shi, S. D. H.; Marshall, A. G. External Accumulation of Ions for Enhanced Electrospray Ionization Fourier Transform Ion Cyclotron Resonance Mass Spectrometry. *Journal of the American Society for Mass Spectrometry*. **1997**, 8, p. 970-976.

10. Belov, M. E.; Nikolaev, E. N.; Anderson, G. A.; Udseth, H. R.; Conrads, T. P.; Veenstra, T. D.; Masselon, C. D.; Gorshkov, M. V.; Smith, R. D. Design and Performance of an ESI Interface for Selective External Ion Accumulation Coupled to a Fourier Transform Ion Cyclotron Mass Spectrometer. *Analytical Chemistry*. **2001**, 73, p. 253-261.

11. Patrie, S. M.; Charlebois, J. P.; Whipple, D.; Kelleher, N. L.; Hendrickson, C. L.; Quinn, J. P.; Marshall, A. G.; Mukhopadhyay, B. Construction of a Hybrid Quadrupole/Fourier Transform Ion Cyclotron Resonance Mass Spectrometer for Versatile MS/MS Above 10 kDa. *Journal of the American Society for Mass Spectrometry*. **2004**, 15, p. 1099–1108.

12. McLafferty, F. W. *Tandem Mass Spectrometry*. 1983, New York: John Wiley and Sons.

13. Busch, K. L.; Glish, G. L.; McLuckey, S. A. *Mass Spectrometry / Mass Spectrometry: Techniques and Applications of Tandem Mass Spectrometry*. 1988, New York: VCH. 333.

14. Glish, G. L.; Vachet. R. W. The Basics of Mass Spectrometry in the Twenty-First Century. *Nature Reviews Drug Discovery*. **2003**, 2, p. 140-150.

15. Marcus, R. A.; Rice. O. K. Session on Free Radicals: The Kinetics of the Recombination of Methyl Radical and Iodine Atoms. *Journal of Physical and Colloid Chemistry*. **1951**, 55, p. 894-908.

16. Sleno, L.; Volmer, D. A. Ion Activation Methods for Tandem Mass Spectrometry. *Journal of Mass Spectrometry*. **2004**, 39, p. 1091-1112.

17. Laskin, J.; Futrell, J. H. Activation of Large Ions in FT-ICR Mass Spectrometry. *Mass Spectrometry Reviews*. **2005**, 24, p. 135-167.

18. McLafferty, F. W.; Bente, I. P. F.; Kronfeld, R.; Tsai, S. C.; Howe, I. Collisional Activation Spectra of Organic Ions. *Journal of the American Chemical Society*. **1973**, 95, p. 2120-2129.

19. Louris, J. N.; Cooks, R. G.; Syka, J. E. P.; Kelley, P.E.; Stafford, G. C.; Todd, J. F. J. Instrumentation, Applications, and Energy Deposition in Quadrupole Ion Trap Mass Spectrometry. *Analytical Chemistry*. **1987**, 59, p. 1677-1685.

20. McLuckey, S. A. Principles of Collisional Activation in Analytical Mass Spectrometry. *Journal of the American Society for Mass Spectrometry*. **1992**, 3, p. 599-614.

21. Bomse, D. S.; Woodin, R. L.; Beauchamp, J. L. Molecular Activation with Low-Intensity CW Infrared Laser Radiation. Multiphoton Dissociation of Ions Derived from Diethyl Ether. *Journal of the American Chemical Society*. **1979**, 101, p. 5503-5512.

22. Dunbar, R.C. Photodissociation of Trapped Ions. *International Journal of Mass Spectrometry*. **2000**, 200, p. 571-589.

23. Boué, S. M.; Stephenson, J. L.; Yost, R. A. Pulsed Helium Introduction into a Quadrupole Ion Trap for Reduced Collisional Quenching During Infrared Multiphoton Dissociation of Electrosprayed Ions. *Rapid Communications in Mass Spectrometry*. **2000**, 14, p. 1391-1397.

24. Payne, A. H.; Glish, G. L. Thermally Assisted Infrared Multiphoton Photodissociation in a Quadrupole Ion Trap. *Analytical Chemistry*. **2001**, 73, p. 3542-3548.

25. Zubarev, R .A.; Kelleher, N. L.; McLafferty, F. W. Electron Capture Dissociation of Multiply Charged Protein Cations. A Nonergodic Process. *Journal of the American Chemical Society*. **1998**, 120, p. 3265-3266.

26. Zubarev, R. A., Horn, D. M.; Fridriksson, E. K.; Kelleher, N. L.; Kruger, N. A.; Lewis, M. A.; Carpenter, B. K.; McLafferty, F. W. Electron Capture Dissociation for Stuctural Characterization of Multiply Charged Protein Cations. *Analytical Chemistry*. **2000**, 72, p. 563-573.

27. O'Connor, P. B.; Lin, C.; Cournoyer, J. J.; Pittman, J. L.; Belyayev, M.; Budnik, B. A. Long-Lived Electron Capture Dissociation Product Ions Experience Radical Migration via Hydrogen Abstraction. *Journal of the American Society for Mass Spectrometry*. **2006**, 17, p. 576 - 585.

28. Savitski, M. M.; Kjeldsen, F.; Nielsen, M. L.; Zubarev, R. A. Hydrogen Rearrangement to and from Radical z Fragments in Electron Capture Dissociation of Peptides. *Journal of the American Society for Mass Spectrometry*. **2007**, 18, p. 113 - 120.

29. Zubarev, R. A.; Haselmann, K. A.; Budnik, B.; Kjeldsen, F.; Jensen, F. Towards an Understanding of the Mechanism of Electron-Capture Dissociation: A Historical Perspective and Modern Ideas. *European Journal of Mass Spectrometry*. **2002**, 8, p. 337-349.

30. Zubarev, R. A. Electron-Capture Dissociation Tandem Mass Spectrometry. *Current Opinion in Biotechnology*. **2004**, 15, p. 12 - 16.

31. Zubarev, R. A. Reactions of Polypeptide Ions with Electrons in the Gas Phase. *Mass Spectrometry Reviews*. **2003**, 22, p. 57 - 77.

32. Leymarie, N.; Costello, C. E.; O'Connor, P. B. Electron Capture Dissociation Initiates a Free Radical Reaction Cascade. *Journal of the American Chemical Society*. **2003**, 125, p. 8949 - 8958.

33. Syrstad, E.A.; Turecek, F. Toward a General Mechanism of Electron Capture Dissociation. *Journal of the American Society for Mass Spectrometry*. **2005**, 16, p. 208-224.

34. Chamot-Rooke, J.; Malosse, C.; Frison, G.; Turecek, F. Electron Capture in Charge-Tagged Peptides. Evidence for the Role of Excited Electronic States. *Journal of the American Society for Mass Spectrometry*. **2007**, 18, p. 2146-2161.

35. Laskin, J.; Futrell, J. H.; Chu, I. K. Is Dissociation of Peptide Radical Cations an Ergodic Process? *Journal of the American Chemical Society*. **2007**, 129, p. 9598-9599.

36. Bakhtiar, R.; Guan, Z. Electron Capture Dissociation Mass Spectrometry in Characterization of Peptides and Proteins. *Biotechnology Letters*. **2006**, 28, p. 1047-1059.

37. Bakhtiar, R.; Guan, Z. Electron Capture Dissociation Mass Spectrometry in Characterization of Post-Translational Modifications. *Biochemical and Biophysical Research Communications*. **2005**, 334, p. 1 - 8.

38. Baba, T.; Hashimoto, Y.; Hasegawa, H.; Hirabayashi, A.; Waki, I. Electron Capture Dissociation in a Radio Frequency Ion Trap. *Analytical Chemistry*. **2004**, 76, p. 4263-4266.

39. Cooper, H.J.; Hakansson, K.; Marshall, A. G. The Role of Electron Capture Dissociation in Biomolecular Analysis. *Mass Spectrometry Reviews*. **2005**, 24, p. 201 - 222.

40. Kjeldsen, F.; Haselmann, K. F.; Budnik, B. A.; Jensen, F.; Zubarev, R. A. Dissociative Capture of Hot (3-13 eV) Electrons by Polypeptide Polycations: an Efficient Process Accompanied by Secondary Fragmentation. *Chemical Physics Letters*. **2002**, 2002, p. 204-206.

41. Savitski, M. M.; Nielsen, M. L.; Zubarev, R. A. Side-Chain Losses in Electron Capture Dissociation to Improve Peptide Identification. *Analyticaly Chemistry*. **2007**, 79, p. 2296-2302.

42. Syka, J.E.P.; Coon, J. J.; Schroeder, M. J.; Shabanowitz, J.; Hunt, D. F. Peptide and Protein Sequence Analysis by Electron Transfer Dissociation Mass Spectrometry. *Proceedings of the National Academy of Sciencies, U.S.A.* **2004**, 101, p. 9528-9533.

43. Xia, Y.; McLuckey, S. A. Evolution of Instrumentation for the Study of Gas-Phase Ion/Ion Chemistry via Mass Spectrometry. *Journal of the American Society for Mass Spectrometry*. **2008**, 19, p. 173-189.

44. Budnik, B.A.; Haselmann, K. F.; Zubarev, R. A. Electron Detachment Dissociation of Peptide Di-Anions: an Electron-Hole Recombination Phenomenon. *Chemical Physics Letters*. **2001**, 342, p. 299-302.

45. Kjeldsen, F.; Silivra, O. A.; Ivonin, I. A.; Haselmann, K. F.; Gorshkov, M.; Zubarev, R. A. C_{α}-C Backbone Fragmentation Dominates in Electron Detachment Dissociation of Gas-Phase Polypeptide Polyanions. *Chemistry European Journal*. **2005**, 11, p. 1803-1812.

46. Kalli, A.; Hakansson, K. Preferential Cleavage of S-S and C-S Bonds in Electron Detachment DIssociation and Infrared Multiphoton Dissociation of Disulfide-Linked Peptide Anions. *International Journal of Mass Spectrometry*. **2007**, 263, p. 71-81.

47. Yang, J.; Mo, J.; Adamson, J. T.; Hakansson, K. Characterization of Oligodeoxynucleotides by Electron Detachment Dissociation Fourier Transform Ion Cyclotron Resonance Mass Spectrometry. *Analytical Chemistry*. **2005**, 77, p. 1876-1882.

48. Mo, J.; Hakansson, K. Characterization of Nucleic Acid Higher Order Structure by High-Resolution Tandem Mass Spectrometry. *Analytical and Bioanalytical Chemistry*. **2006**, 386, p. 675-681.

49. McFarland, M. A.; Marshall, A. G.; Hendrickson, C. L.; Nilsson, C. L.; Fredman, P.; Mansson, J. E. Structural Characterization of the GM1 Ganglioside by Infrared Multiphoton Dissociation, Electron Capture Dissociation, and Electron Detachment Dissociation Electrospray Ionization FT-ICR MS/MS. *Journal of the American Society for Mass Spectrometry*. **2005**, 16, p. 752-762.

50. Adamson, J. T.; Hakansson, K. Electron Detachment Dissociation of Neutral and Sialylated Oligosaccharides. *Journal of the American Society for Mass Spectrometry*. **2007**, 18, p. 2162-2172.

51. Wolff, J.J.; Amster, I. J.; Chi, L.; Linhardt, R. J. Electron Detachment Dissociation of Glycosaminoglycan Tetrasaccharides. *Journal of the American Society for Mass Spectrometry*. **2007**, 18, p. 234-244.

52. Wolff, J.J.; Chi, L.; Linhardt, R. J.; Amster, I. J. Distinguishing Glucuronic from Iduronic Acid in Glycosaminoglycan Tetrasaccharides by Using Electron Detachment Dissociation. *Analytical Chemistry*. **2007**, 79, p. 2015-2022.

53. Satake, H.; Hasegawa, H.; Hirabayashi, A.; Hashimoto, Y.; Baba, T. Fast Multiple Electron Capture Dissociation in a Linear Radio Frequency Quadrupole Ion Trap. *Analytical Chemistry*. **2007**, 79, p. 8755-8761.

54. Douglas, D. J.; Frank, A. J.; Mao, D. M. Linear Ion Traps in Mass Spectrometry. *Mass Spectrometry Reviews*. **2005**, 24, p. 1-29.

55. Silivra, O. A.; Kjeldsen, K.; Ivonin, I. A.; Zubarev, R. A. Electron Capture Dissociation of Polypeptides in a Three-Dimensional Quadrupole Ion Trap: Implementation and First Results. *Journal of the American Society for Mass Spectrometry*. **2005**, 16, p. 22 - 27.

56. Guan, S.; Marshall, A. G. Ion Traps for Fourier Transform Ion Cyclotron Resonance Mass Spectrometry: Principles and Design of Geometric and Electric Configurations. *International Journal of Mass Spectrometry and Ion Processes*. **1995**, 146/147, p. 261 - 296.

57. Comisarow, M.B.; Marshall, A. G. The Early Development of Fourier Transform Ion Cyclotron Resonance (PT-ICR) Spectroscopy. *Journal of Mass Spectrometry*. **1996**, 31, p. 581-585.

58. Marshall, A. G.; Hendrickson, C. L.; Jackson, G. S. Fourier Transform Ion Cyclotron Resonance Mass Spectrometry: A Primer. *Mass Spectrometry Reviews*. **1998**, 17, p. 1-35.

59. Guan, S.; Marshall, A. G. Stored Waveform Inverse Fourier Transform (SWIFT) Ion Excitation in Trapped-Ion Mass Spectrometry: Theory and Applications. *International Journal of Mass Spectrometry and Ion Processes*. **1996**, 157/158, p. 5-37.

60. Amster, I. J. Fourier Transform Mass Spectrometry. *Journal of Mass Spectrometry*. **1996**, 31, p. 1325-1337.

61. Ray, K. L.; Glish, G. L. *A New Multiplexed MS/MS Method for Ion Trapping Instruments*. in *The 48th ASMS Conference on Mass Spectrometry and Allied Topics*. 2000.

62. Cunningham, C. Jr.; Ray, K. L.; Glish, G. L. *Iterative Accumulation Multiplexing TA-CID in a Quadrupole Ion Trap*. in *The 52nd ASMS Conference on Mass Spectrometry and Allied Topics*. 2004.

Chapter 2

Pulsed nano-Electrospray Ionization (nESI)

2.1 Introduction

2.1.1 *Advantages of nESI vs. ESI*

Electrospray ionization mass spectrometry (ESI-MS) has proven to be useful for the analysis of biologically relevant compounds due to its sensitivity, throughput, and ability to analyze large, non-volatile biological molecules from solution.[1] Nano-ESI (nESI) is a low flow rate regime of ESI that has gained widespread use in the study of biopolymers.[2-9] The smaller sprayer tips and lower applied voltages used with nESI reduce sample consumption and result in electrospray droplets of higher surface-to-volume ratios.[10-12] Higher surface-to-volume ratios allow more analyte molecules to be closer to the droplet surface and thus more easily desorbed into the gas phase, thereby improving sensitivity.[11, 13]

2.1.2 *Motivation behind pulsed nESI*

Several researchers have utilized multiple conventional ESI sprayers on a variety of instruments to increase sample throughput. Throughput has been increased by a factor of four while mass measurement accuracies of below 5 ppm were maintained for a variety of metabolites by coupling an ESI source to each of four HPLC effluent streams and using a fifth channel to introduce a lock mass for calibration.[14] In addition to increasing throughput, multiple ESI sources have been used in parallel arrangements to improve mass measurement accuracy[4], reduce adverse affects from multiple solutions interacting prior to analysis[4, 15], and allow ion/ion reactions to be studied.[16-19] Work has also been published on the use of two nESI sprayers operating continuously but at opposite polarities for ion/ion reactions.[20] A dual sprayer setup on the front end of a time-of-flight (TOF) instrument was used to achieve mass accuracies of 3 ppm for ions below

mass-to-charge (*m/z*) 1000 using sub-picomole amounts of sample.[21] Each sprayer was independently and sequentially sampled by alternately switching the high voltage (HV) applied to each sprayer.[21] Controlling the spray voltage of an ESI source allows sample ionization, and thus consumption, to be synchronized with mass analysis. The amount of sample that is consumed yet not analyzed is decreased because the ESI process is effectively made non-continuous on the same time scale as non-beam type instruments (e.g., quadrupole ion trap mass spectrometers, QITMS and Fourier transform ion cyclotron resonance mass spectrometers, FTICR-MS). As a result the ability to switch an ESI source between the on (ionization) and off (no ionization) state is advantageous when limited quantities of sample are available.

The use of HV switching as a means to sample each sprayer has several advantages beyond just reduced sample consumption. No longer is a mechanical barrier (e.g. a baffle) required as the switching mechanism.[21, 22] By avoiding the use of a mechanical barrier the sprayers can be positioned physically closer to the mass spectrometer; which is optimal for nESI. The use of HV switching also allows for shorter transit times between sampling from different sprayers (~1 ms) as opposed to the use of a mechanical switching method (~100 ms).[14] Pulsing a single nESI source has been achieved by holding the sample solution at a high potential and using a cylindrical piezoelectric element to dispense 10 picoliter droplets with a drop-on-demand mechanism.[23] This method demonstrated detection limits comparable to non-pulsed nESI but with lower total sample consumption and greater control of the amount of sample consumed over a given time period.[23]

Overall, nESI improves sensitivity and reduces sample consumption compared to higher flow rate conventional ESI. By pulsing nESI, sample consumption can be reduced even further as the continuous ionization is made periodic to match the duty cycle of mass analysis. Using high voltage to pulse the ESI process on and off makes the implementation of multiple nESI sprayers more straight forward than mechanical means of sprayer control. By using high voltage to control which sprayer is being sampled, multiple sprayers could be positioned for simultaneous sampling. Mechanical switching between sprayers would result in only one sprayer at a time being positioned appropriately to be sampled by the mass spectrometer. Thus, the motivation to pulse nESI using

voltage control involves reduced sample consumption, signal stability, ease of implementation, and the ability to choose between having one or several sprayers operating at a time.

2.1.3 *Previous implementations of pulsed ESI*

Controlled pulsing of the ESI process can lead to more stable mass spectra because the sample flow rate can be matched with the reduced spraying rate. Pulsed ESI can be achieved by externally pulsing the voltage applied to the sprayer and has been successfully demonstrated at a reduced flow rate of 3 μL/min.[24] Recently multiple nESI sprayers have been pulsed in experiments designed to explore ion-ion reactions.[18, 19] By modulating the spray voltage, nESI has been pulsed at a maximum frequency of 350 kHz.[25] However, this frequency was determined by monitoring the current on a lens element immediately following the nESI needle not by detecting ions passed through a mass spectrometer. Work performed in our lab has demonstrated that when the nESI-generated ions are mass analyzed the maximum pulse rate becomes 12 Hz. The 12 Hz rate is a result of mass resolved ion current rise and fall times of 20 ± 3 msec and 61 ± 4 ms, respectively.

It would be beneficial to understand the reasons for the discrepancy in reported pulsing rates. Considering the results from our lab, the 61 ± 4 ms decay-time should include the time it takes to break the Taylor cone, the time to stop the ion flux, and the time the ions require to traverse the mass spectrometer. The portion of the decay-time associated with stopping the ion flux includes the time where ions are still emitted from the liquid protruding from the sprayer tip even after the breaking of the Taylor cone.[26] Results suggest that the ions traverse the mass spectrometer in 250 μsec and the time it takes to break the Taylor cone is less than 50 μsec.[15, 23, 24] These results indicate that the majority of the decay time is in stopping the ion flux. The observed decay time is much longer than some reports found in the literature, which suggest decay times of less than 100 μsec.[24, 25] However, these reports measured the current directly on an electrode that immediately follows the nESI or ESI needle.[15, 23, 24] Additionally, the solutions that were used in determining decay times were pure solvents, high concentration salts, or contained glycol. The ion currents that are reported in the literature are in the 10 to 100 nA region which may be the result of solvent clusters and is much greater than the ion currents expected from desolvated analyte ions. Typical ion currents measured during the experiments that gave a pulsing rate of 12 Hz were on the order of 10-100 pA. This

suggests that the discrepancy between the decay times in other reports versus the 61 msec measured in our experiments is due to the nature of the analyte and the sensitivity of the detector; i.e., the ability of a lens, compared to an electron multiplier, to detect decreasing ion flux.

Despite the large difference in decay times, reports that monitor the ion current in a pulsed electrospray system using a lens show that the trailing edge of the ion signal has a long decay time relative to the rise time.[15, 23-25] In one report, time resolved photos show that ion signal is still present following the termination of the Taylor cone suggesting that charge in the spray solution takes some additional amount of time to dissipate and finally stop ion formation/desolvation.[25] In low flow rate systems, such as the nESI system used for the pulsing work reported in this chapter, the shape of the ion plume can become a mist which is possibly the environment that is created after the Taylor cone has dissipated but while there is still residual charge in the spray.[26] As a result, care must then be taken during nESI pulsing experiments to avoid cross-talk between multiple sprayers.

For the work described here, a dual nESI source has been developed that is controlled using applied voltages either in pulsed or continuous modes of operation. The dual source is used in conjunction with a flared inlet capillary that was built in-house and has been described elsewhere.[27, 28] The source allows mass accuracy, sample throughput, and sprayer-to-sprayer reproducibility to be improved and was designed with the benefits associated with HV switching in mind. Furthermore, the source presented herein utilizes two nESI sprayers yet does not require the instrument to be modified and consequently should be applicable to any mass spectrometer with an atmospheric sampling orifice.

2.2 Experimental

2.2.1 *Samples*

Peptides trialanine (AAA, M_r: 231.25) and leucine enkephalin (YGGFL, M_r: 555.62) and the polymer polyethylene glycol 600 (PEG 600) were purchased from Sigma (St. Louis, MO) and used without further purification. Unless noted otherwise, working solutions of each peptide were made at 100 μM in 75/20/5 by volume acetonitrile/water/formic acid. The PEG 600 solution was made to 100 μM in methanol. HPLC grade acetonitrile, methanol, and water were purchased from Fisher Scientific

(Fair Lawn, NJ). Certified A.C.S. formic and acetic (glacial) acids were also purchased from Fisher Scientific.

2.2.2 *Construction of pulsing circuitry*

The multi-sprayer experiments used two separate EMCO (Sutter Creek, CA; model C25N) negative high voltage power supplies controlled by a timing circuit that was triggered by the scan function of the mass spectrometer. Specifically, at the time in the scan function when ions can be accumulated for mass analysis, the power supplies were triggered to allow ionization to occur. The detailed circuit schematic can be found in Appendix 9.1. In brief, the instrument scan function triggers the monostable multivibrators whose variable output pulse widths dictate the duration for which voltage is applied to each sprayer. The monostable output pulse width is determined by the user through control of an external resistor-capacitor (RC) network associated with each monostable. Specifically, the pulse widths are defined by:

$$t_{w(out)} = C_{ext} R_T \ln 2 = 0.7 C_{ext} R_T \qquad \text{(Equation 2.1)}$$

where C_{ext} and R_T represent the external capacitor and resistor, respectively. Per the data sheet for the monostable (Texas Instruments, Dallas, TX, SN74121), acceptable values for C_{ext} are 10 pF to 10 μF and R_T values must be in the range of 2 to 40 kΩ. Typical ion accumulation times of the instrument used for the pulsed nESI work are on the order of 50 to 100 ms. To operate the monostable in that range of pulse widths ($t_{w(out)}$) a 1.0 μF capacitor and a 100 kΩ variable resistor were used in the external resistor-capacitor network. By changing the resistance over the 2 to 40 kΩ range, the pulse width of the monostable could be varied to agree with the duration of a given accumulation time. The output of the monostable then controls the amount of time the EMCO supply outputs a voltage which controls the electrospray process. The amplitude of the applied high voltage was controlled by a variable resistor that modulates the amplitude of the TTL enable voltage on each EMCO supply. By using one monostable setup for each EMCO supply, each sprayer could be independently operated both in terms of its pulsing as well its spray potential.

2.2.3 *Instrumentation details*

As shown in Figure 2.1A, the nESI multi-sprayer experiments were performed on a Bruker Esquire quadrupole ion trap (Billerica, MA) with a flared inlet capillary developed in-house and

described previously.[27, 28] The flared capillary introduces a wider acceptance area for spray plume sampling which is beneficial for improving sensitivity when a single sprayer is utilized but also allows for the effective use of multiple sprayers. A metal mesh-cap comprised of 88% transmission metal mesh is attached to the flared end of the capillary to create a uniform electric field and allow the expanded acceptance area to be utilized. The incorporation of such a flared capillary requires minimal instrumental modifications and makes the alignment of nESI sprayers with the instrumental sampling orifice much easier.

The multi-sprayer nESI experiments were conducted using a home-built source consisting of two nESI sprayers secured to an X-Y-Z translational stage. The sprayers were each at an angle of 5° with respect to and ~ 1.5 mm off of the axis of the flared inlet capillary. For clarity, the names left sprayer and right sprayer will be used throughout the paper to refer to the side of the transfer capillary that the sprayer is situated on when looking down onto the XZ-plane. A positive x-position will refer to the right side of the transfer capillary. Both sprayers were immobilized on the translational stage such that any movement of the staging mechanism resulted in both sprayers being repositioned concurrently. The sprayers are constructed from Swagelok 1/4" to 1/16" reducing unions which accept 0.060" O.D. x 0.045" I.D. glass capillaries (Drummond Scientific Company, Broomall, PA) that were pulled at one end to ~ 4 μm using a Narishige model PP-830 dual stage glass electrode puller (Narishige International USA, Inc., Easy Meadow, NY). nESI solutions were injected into the pulled sprayer through the non-tapered end. Electrical contact is made with the nESI solution via a platinum wire inserted into the open end of the sprayer which is in contact with the Swagelok body; spray is initiated and maintained through the applied voltage without any pneumatic assistance. Separate, independent EMCO supplies are connected to the Swagelok reducing unions such that the sprayers were electrically isolated from each other. Both sprayers were positioned 1-2 mm from the entrance of the flared inlet capillary and its metal mesh-cap.

2.2.4 *Modes of multiple sprayer operation*

The two sprayers shown in Figure 2.1A could be operated on alternating scans or simultaneously on the same scan by varying the resistance value of the 100 kΩ variable resistor in the external RC network. The timing diagram shown in Figure 2.1B indicates how the source

operates in an alternating (pulsing) mode such that each sprayer operates on every other scan function. For all experiments, the flared inlet capillary of the mass spectrometer is held at -1500 V. To initiate electrospray, the voltage applied to a given sprayer was set to 0 V. With the setup shown in Figure 2.1B, it was found that applying ~ -500 V to a sprayer resulted in loss of ion signal because the potential difference between the sprayer and inlet capillary (i.e., the spray potential) was only 1000 V. Typically a spray potential of 1100 to 1200 V is required under nESI conditions. The ability to stop electrospray without having to pulse the EMCO supply to -1500 V is advantageous for faster temporal response during pulsing operation.

The response time of the pulsing circuit was improved further by adding one 22 kΩ power resistor in parallel to the output of each EMCO HV supply. The use of this load resistor decreased the fall time of the output voltage by 16.4 ms (a 9% improvement). By reducing the fall time of the HV supplies the situation where ionization could still be occurring following the EMCO supply control

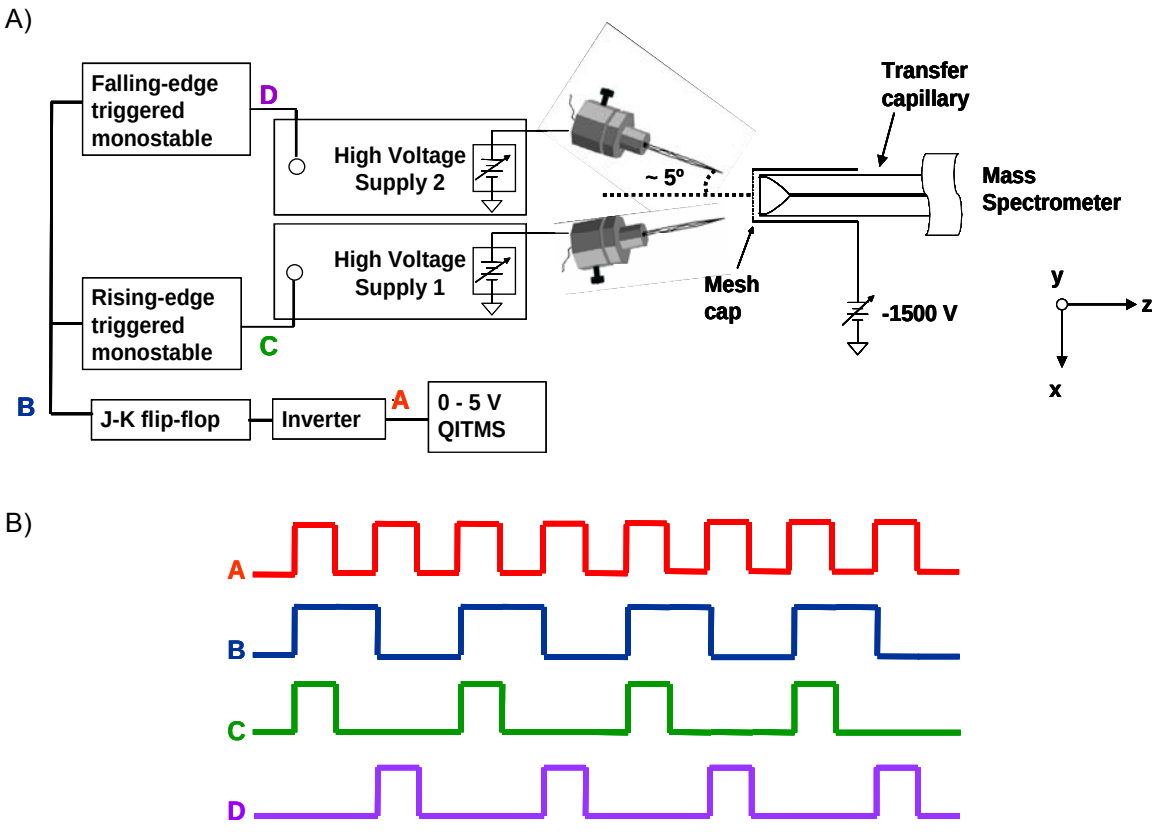

Figure 2.1: A) Schematic of the dual nESI source. B) Timing circuitry displaying the timing diagram for pulsed nESI.

voltage going to the off state is avoided. Consequently, the chance of having carry-over from one accumulation time to the next is removed which reduces the possibility of cross-talk between the two nESI sprayers. It should also be noted that other researchers have shown that the use of such a load resistor aids in source stability.[29]

2.3 Results and Discussion:

2.3.1 *Relaxed acceptance angle requirements with mesh cap cover*

The first concern when introducing multiple sprayers into the source region for a nESI interface is the potential for a reduction in ion abundance from each sprayer. A reduction in abundance could result from the requisite moving of each sprayer off axis to provide room for multiple sprayers and consequently using a less-than-optimal sample introduction scheme. The goal behind using the flared inlet capillary is to increase the acceptance area of the ESI interface and decrease the amount of signal loss that occurs as a sprayer is moved away from the capillary axis. Increasing the acceptance area should allow the ion plume generated from ESI to be sampled by the mass spectrometer over greater distances from the axis of the flared transfer capillary. To test this hypothesis, the signal response for $\mathbf{[M+H]^+_{AAA}}$ was measured as a function of distance in the x-direction across the front of the capillary. Mass spectra were acquired at 0.5 mm intervals. The experiment was performed using the 88% transmission metal mesh at the end of the flared transfer capillary and the standard capillary cover that contains a single, 1 mm diameter acceptance hole. The experiment was repeated in triplicate for both capillary covers. The data in Figure 2.2 show that a higher absolute signal abundance results from using the single hole capillary cover but beyond ±0.5 mm (i.e., the radius of the acceptance hole) no ion signal is detected. When the mesh cover is used, a lower absolute ion abundance is detected, but a distance of greater than 2.0 mm in the x-direction could be used to generate detectable ion signal.

It should be noted that the absolute x-position given for the mesh cap results is not as accurate as the setup where the single hole cover was used. Due to the concentric nature of the single hole capillary cover, its acceptance hole accurately marks the x = 0.0 mm position. When the mesh capillary is used, it is difficult to determine the x = 0.0 mm position with the translational stage setup presently on the instrument. By using the micrometer of the translational stage, the relative x-

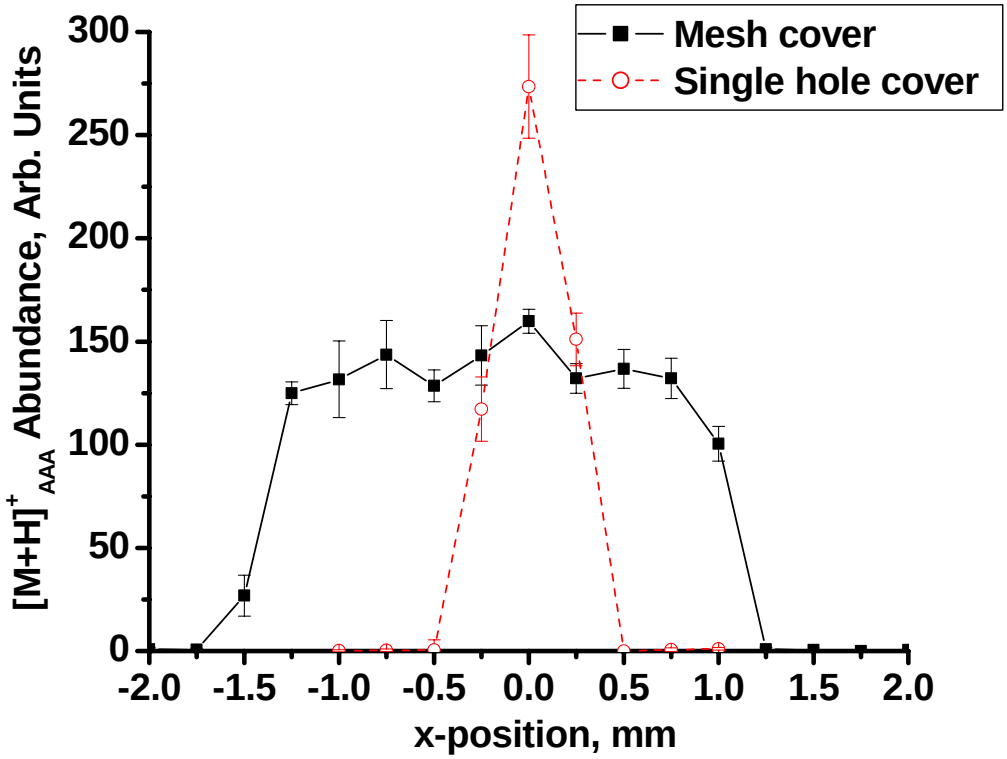

Figure 2.2 Position dependent response of flared transfer capillary for the mesh and single-hole capillary covers. The inner bore of the flared transfer capillary represents an x-position of 0.0 mm.

position (i.e., the 0.5 mm increments) within the mesh cap data can be confidently known, but the absolute x-position could be inaccurate. Regardless, the results in Figure 2.2 clearly show that when the mesh cap is used there is a x-distance of ~ 2.0 mm where movement of the sprayer within that range has no adverse affect on the measured ion signal.

The data displayed in Figure 2.2 was acquired with the sprayer positioned at 0º to the transfer capillary axis. Experiments were performed with the sprayer positioned at three different angles to the axis of the transfer capillary (0º, 30º and 60º) to see if one orientation provided better performance than the others. Using the mesh cover, the signal-to-noise ratio for $\mathbf{[M+H]^+_{AAA}}$ was measured as a function of distance in the x-direction across the front of the capillary by acquiring mass spectra at an interval of every 0.5 mm. The results from these experiments are shown in Figure 2.3 where the average S/N for $\mathbf{[M+H]^+_{AAA}}$ is plotted as a function of x-position. The results in Figure 2.3 suggest that choice of sprayer angle is not critical, assuming an x-position of less than 2.0 mm is used.

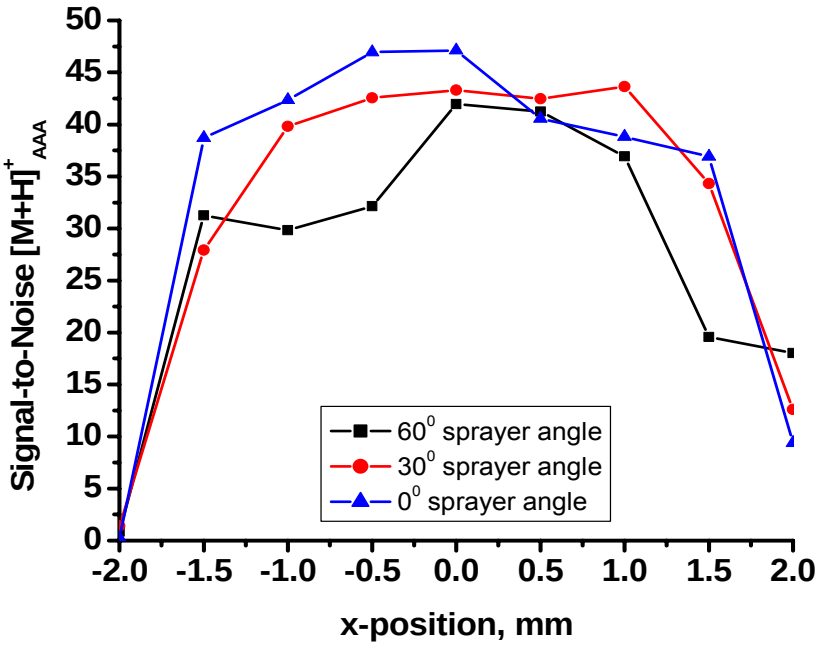

Figure 2.3 ESI response as a function of x-position for three different sprayer orientation angles. The axis of the transfer capillary was taken to be 0º and x = 0.0 mm

2.3.2 *Independent control of multiple sprayers*

nESI sprayers vary with regard to distributions of tip opening sizes and geometries as well as sprayer-counter electrode spacing and alignment. Exact tip-to-tip reproducibility can be problematic especially when trying to perform spectral comparisons for such applications as batch process monitoring or quantification studies. Sprayer tip alignment is often addressed through use of optical microscopes for positioning nESI sprayers in front of an instrument's sampling orifice. The novel design presented here and the use of a flared inlet capillary allow for signal correction of multiple sprayers without the need for extensive sprayer re-alignment. To explore the accuracy of the voltage control, the same solution of YGGFL was put into both sprayers and the potential applied to each sprayer was adjusted until the observed abundances from each sprayer were approximately identical, with only one sprayer operating at a time. For this experiment the voltage applied to the metal mesh capillary cover was -1500 V. When both sprayers were held at 0 V a 75% difference between the signal abundance for the protonated molecule of YGGFL from each sprayer was observed. By adjusting the voltages on the left and right sprayers to -200 V and -240 V, respectively an 8% relative difference between the protonated molecule signal intensities was observed. In other experiments

where the initial difference is not so great a 4% relative difference was readily achievable. It should also be noted that no extra precautions were taken to ensure both sprayers were equal distances from the instrumental sampling orifice, which is indicative of the ability to achieve similar sensitivity without precise sprayer alignment.

2.3.3 *Simultaneous operation for internal calibration*

Improved mass measurement accuracy is beneficial in the spectral interpretation, elemental composition determination, and identification of unknowns. The introduction of an internal calibrant offers one method of improving mass accuracy, especially for trapping mass analyzers, because the analyte and calibrant can be exposed to the same trapping fields and space charge effects. To demonstrate the capability of this setup to address such a situation, both sprayers were operated simultaneously in a continuous fashion. Shown in Figure 2.4 is the resultant spectrum where 100 μM PEG 600 in methanol was sprayed from one sprayer to serve as the calibrant while the analyte, 100 μM YGGFL in 75/20/5 by volume acetonitrile/water/formic acid, was sprayed from the other sprayer. Utilizing this multi-sprayer configuration as shown in Figure 2.4 resulted in an improvement in mass measurement accuracy from 678 ppm to 119 ppm.

The spectrum in Figure 2.4 was obtained by lowering the spray potential of the PEG sprayer (i.e., applying a more negative voltage from its corresponding EMCO supply) from what gives the maximum ion signal, thereby suppressing the ESI process and consequently reducing the amount of ion formation. The suppression of the PEG signal in Figure 2.4 was necessary to avoid adversely affecting the MS signal for YGGFL due to the space charge capacity imposed by the ion trapping volume. This deliberate signal suppression further illustrates the ability of the setup to allow for independent control of the ionization processes by adjusting ESI potentials applied to each sprayer separately. Without the ability to spray different sample solutions from their own, independent sprayers a mixture of the samples would have to be used. It is common that when multiple samples are in the same solution that one of the analytes will experience signal suppression. Results obtained in our lab by spraying Gramicidin S and PPG from separate sprayers demonstrated that both analytes are effectively detected. Separate sprayers allow each sample to be prepared independently in-terms

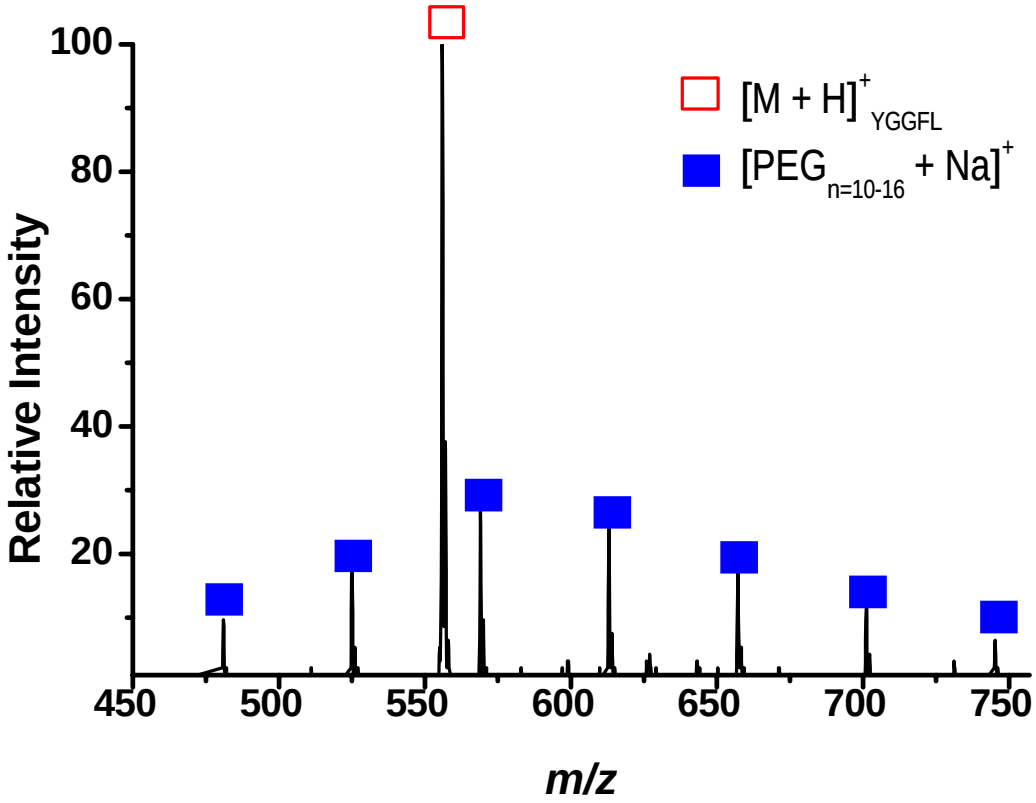

Figure 2.4 PEG 600 solution (closed squares) and YGGFL solutions (open square) spraying simultaneously from their respective sprayers.

of solvent and other additives (i.e. the addition of sodium to the PPG solution). If these two analytes are sprayed from the same solution the PPG signal is significantly suppressed (data not shown).[28]

2.3.4 *Source stability during pulsed operation*

Another advantage of the proposed multiplexed source is the ability to introduce multiple analytes from separate solutions in an alternating fashion. The source can be pulsed by controlling the voltage applied to the desired nESI sprayer. This pulsing can be synchronized with the ion accumulation and injection sequence, and ultimately the mass analysis step of the analyzer. Such capabilities avoid the situation where a nESI sprayer may be operating without being sampled by the mass spectrometer. Synchronizing ionization with mass analysis allows lower sample flow rates to be used and reduces sample consumption. The results in Figure 2.5 show the ability of the pulsed nESI system to introduce a different sample on consecutive instrumental scans. Solutions of AAA and YGGFL were directly infused into their respective sprayers and alternately pulsed for 30 minutes.

In Figure 2.5, the two spectra (scans 3939 and 3940) show that on consecutive scans only one sprayer is being sampled at a time and alternating pulsing has been achieved. The bottom pane of the figure is a histogram representing the signal intensity for the protonated molecules of AAA and YGGFL over a series of instrumental scans where a scan was executed every 450 msec. As is evident from the histogram, alternating pulsing was achieved for the duration of the experiment, where scan number 3960 represents an elapsed experimental time of 29.7 minutes. The

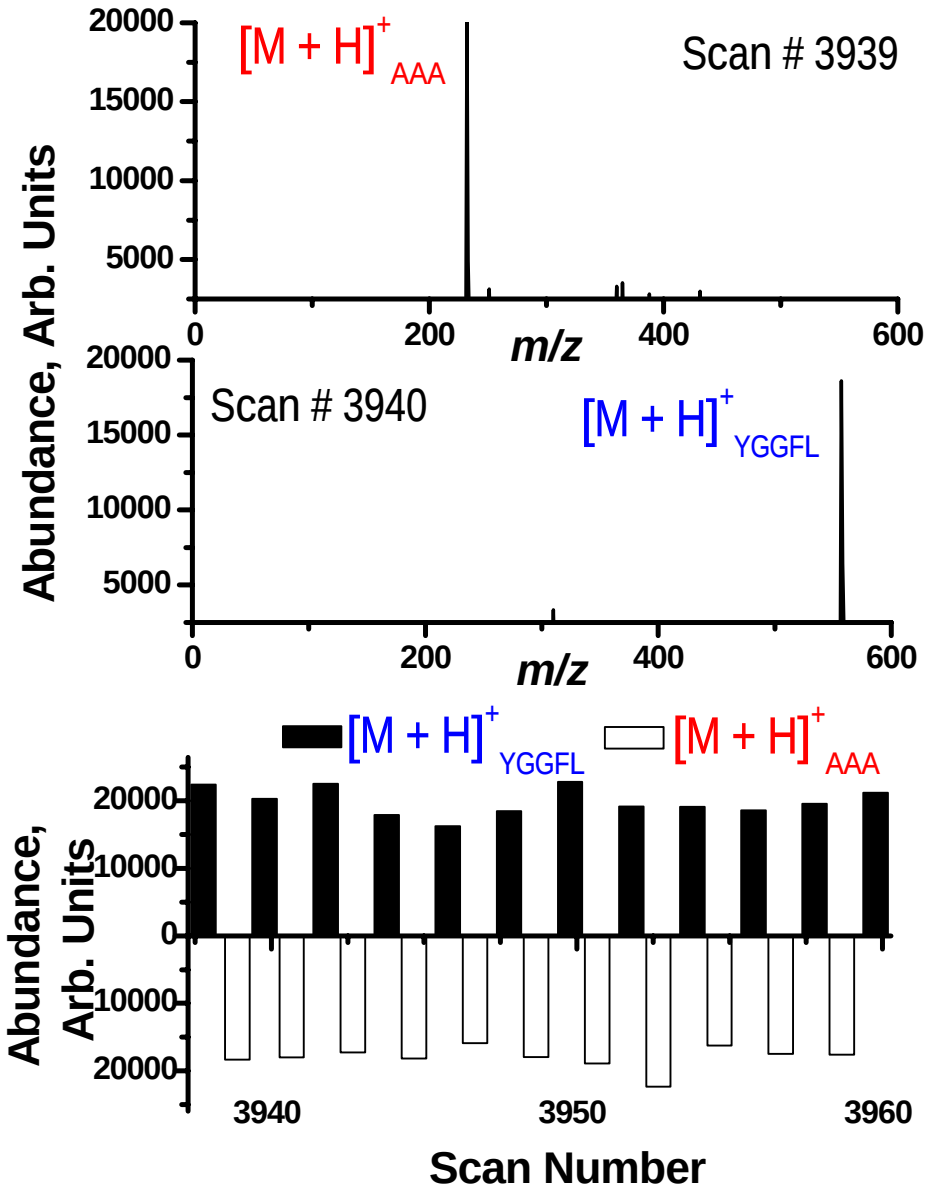

Figure 2.5 Consecutive mass spectra and histogram illustrating the dual pulsing mode of operation for AAA and YGGFL solutions.

demonstrated stability of the pulsing mode of operation is promising for coupling this source to relevant separation techniques (e.g. HPLC).

2.4 Conclusions

A dual nESI source has been developed where the desired mode of operation (i.e. both sprayers operating continuously or both sprayers being pulsed in an alternating manner) can be realized by controlling the voltage applied to each sprayer rather than mechanically switching the sprayers. The novel, multi-sprayer source design presented here should be compatible with most mass analyzers while requiring minimal instrumental modifications. The dual source provides a method to introduce analyte and internal calibrant to the mass spectrometer from independent nESI sprayers for the purpose of improving mass measurement accuracy. By synchronizing the voltages applied to the sprayers with the ion accumulation event sample loss and consumption can be minimized. Both simultaneous and pulsing modes of operation can be achieved without having to re-position the nESI sprayers and can be precisely controlled by means of regulating the voltages applied to the sprayers. Finally, the symmetry about the axis of the instrument sampling orifice should permit the installation of more sprayers on the same circumference as the existing two sprayers but on different planes with respect to the sampling orifice to increase the throughput realized with this system.

2.5 References:

1. Fenn, J. B.; Mann, M.; Meng, C. K.; Wong, S. F.; Whitehouse, C. M. Electrospray Ionization for Mass Spectrometry of Large Biomolecules. *Science*. **1989**, 246, p. 64-71.

2. Körner, R.; Wilm, M.; Morand, K.; Schubert, M.; Mann, M. Nano Electrospray Combined with a Quadrupole Ion Trap for the Analysis of Peptides and Protein Digests. *Journal of the American Society for Mass Spectrometry*. **1996**, 7, p. 150-156.

3. Marina, A.; Carcia, M. A.; Albar, J. P.; Yague, J.; Castro, J. A. L.; Vazquez, J. High-sensitivity Analysis and Sequencing of Peptides and Proteins by Quadrupole Ion Trap Mass Spectrometry. *Journal of Mass Spectrometry*. **1999**, 34, p. 17-27.

4. Hannis, J. C.; Muddiman, D. C. A Dual Electrospray Ionization Source Combined With Hexapole Accumulation to Achieve High Mass Accuracy of Biopolymers in Fourier Transform Ion Cyclotron Resonance Mass Spectrometry. *Journal of the American Society for Mass Spectrometry*. **2000**, 11, p. 876-883.

5. Emmett, M. R.; Caprioli, R. Micro-Electrospray Mass Spectrometry: Ultra-High-Sensitivity Analysis of Peptides and Proteins. *J. Am. Soc. Mass Spectrom.* **1994**, 5, p. 605-613.

6. Niessen, W. M. A.; Tinke, A. P. Liquid Chromatography-mass spectrometry General Principles and Instrumentation. *Journal of Chromatography A*. **1995**, 703, p. 37-57.

7. Zeng, L.; Kassel, D. B. Developments of a Fully Automated Parallel HPLC/Mass Spectrometry System for the Analytical Characterization and Preparative Purification of Combinatorial Libraries. *Analytical Chemistry*. **1998**, 70, p. 4380-4388.

8. Bednar, P.; Papouskova, B.; Muller, L.; Bartak, P.; Stavek, J.; Pavlousek, P.; Lemr, K. Utilization of Capillary Electrophoresis/mass Spectrometry (CE/MSn) for the Study of Anthocyanin Dyes. *Journal of Separation Science*. **2005**, 28, p. 1291-1299.

9. Soler, C.; Manes, J.; Pico, Y. Comparison of Liquid Chromatography using Triple Quadrupole and Quadrupole Ion Trap Mass Analyzers to Determine Pesticide Residues in Oranges. *Journal of Chromatography A*. **2005**, 1067, p. 115-125.

10. Fong, K. W. Y.; Chan, T. W. D. A Novel Nonmetallized Tip for Electrospray Mass Spectrometry at Nanoliter Flow Rate. *Journal of the American Society for Mass Spectrometry*. **1999**, 10, p. 72-75.

11. Wilm, M.; Mann, M. Analytical Properties of the Nanoelectrospray Ion Source. *Analytical Chemistry*. **1996**, 68, p. 1-8.

12. Glish, G. L.; Vachet, R. W. The Basics of Mass Spectrometry in the Twenty-First Century. *Nature Reviews*. **2003**, 2, p. 140-150.

13. Mann, M. Electrospray: Its Potential and Limitations as an Ionization Method for Biomolecules. *Journal of Mass Spectrometry*. **1990**, 25, p. 575-587.

14. Leclercq, L.; Delatour, C.; Hoes, I.; Brunelle, F.; Labrique, X.; Castro-Perez, J. Use of a Five-Channel Multiplexed Electrospray Quadrupole Time-of-Flight Hybrid Mass Spectrometer for Metabolite Identification. *Rapid Communications in Mass Spectrometry*. **2005**, 19, p. 1611-1618.

15. Zhou, F.; Shui, W.; Lu, Y.; Yang, P.; Guo, Y. High Accuracy Mass Measurement of Peptides with Internal Calibration using a Dual Electrospray Ionization Sprayer System for Protein Identification. *Rapid Communications in Mass Spectrometry*. **2002**, 16, p. 505-511.

16. Ogorzalek-Loo, R. R.; Udseth, H. R.; Smith, R. D. Evidence of Charge Inversion in the Reaction of Singly Charged Anions with Multiply Charged Macroions. *Journal of Physical Chemistry*. **1991**, 95, p. 6412-6415.

17. Ogorzalek-Loo, R. R.; Udseth, H. R.; Smith, R. D. A New Approach for the Study of Gas-Phase Ion-Ion Reactions Using Electrospray Ionization. *Journal of the American Society for Mass Spectrometry*. **1992**, 3, p. 695-705.

18. Xia, Y.; Liang, X.; McLuckey, S. A. Pulsed Dual Electrospray Ionization for Ion/Ion Reactions. *Journal of the American Society for Mass Spectrometry*. **2005**, 16, p. 1750 - 1756.

19. Liang, X.; Han, H.; Xia, Y.; McLuckey, S. A. A Pulsed Triple Ionization Source for Sequential Ion/Ion Reactions in an Electrodynamic Ion Trap. *Journal of the American Society for Mass Spectrometry*. **2007**, 18, p. 369-376.

20. Danell, R. M.; Myer, M. J.; Danell, A. S. *Development and Testing of a Computer-Controlled Dual Polarity Dual nanoESI Source on a Quadrupole Ion Trap for Ion/Ion Reactions*. in *55th ASMS Conference on Mass Spectrometry and Allied Topics*. 2007. Indianapolis, Indiana.

21. Satomi, Y.; Kudo, Y.; Sasaki, K.; Hase, T.; Takao;, T. Accurate Mass Measurement in nano-Electrospray Ionization Mass Spectrometry by Alternate Switching of High Voltage Between Sample and Reference Sprayers. *Rapid Communications in Mass Spectrometry*. **2005**, 19, p. 540-546.

22. Wolff, J.; Eckers, C.; Sage, A. B.; Giles, K.; Bateman, R. Accurate Mass Liquid Chromatography/Mass Spectrometry on Quadrupole Orthogonal Acceleration Time-of-Flight Mass Analyzers using Switching Between Seperate Sample and Reference Sprays. 2. Applications using Dual-Electrospray Ion Source. *Analytical Chemistry*. **2001**, 73, p. 2605-2612.

23. Berggren, W. T.; Westphall, M. S.; Smith, L. M. Single-Pulse Nanoelectrospray Ionization. *Analytical Chemistry*. **2002**, 74, p. 3443-3448.

24. Wei, J.; Shui, W.; Zhou, F.; Lu, Y.; Chen, K.; Xu, G.; Yang, P. Naturally and Externally Pulsed Electrospray. *Mass Spectrometry Reviews*. **2002**, 21, p. 148-162.

25. Alexander, M. S.; Paine, M. D.; Stark, J. P. W. Pulsation Modes and the Effect of Applied Voltage on Current and Flow Rate in Nanoelectrospray. *Analytical Chemistry*. **2006**, 78, p. 2658-2664.

26. Koerner, T.; Turck, K.; Brown, L.; Oleschuk, R. D. Porous Polymer Monolith Assisted Electrospray. *Analytical Chemistry*. **2004**, 76, p. 6456-6460.

27. Glish, G. L.; Danell, R. M. *Electrospray Ionization Device*. **2004**.

28. Danell, R. M.; Glish, G. L. *Advances in Ion Source and Quadrupole Ion Trap Performance and Design*. **2001**, The University of North Carolina: Chapel Hill.

29. Cech, N.; Enke, C. Practical Implications of Some Recent Studies in Electrospray Ionization Fundamentals. *Mass Spectrometry Reviews*. **2001**, 2001, p. 362-387.

Chapter 3

Iterative Accumulation Multiplexing (IAM) on a Quadrupole Fourier Transform Ion Cyclotron Resonance Mass Spectrometer (Q-FTICR-MS)

3.1 Introduction

3.1.1 *Examples of multiplexed tandem mass spectrometry (MS/MS)*

The use of mass spectrometry as a technique for analyte identification is significantly aided by the ability to perform tandem mass spectrometry (MS/MS) on each analyte of interest. Conventionally, MS/MS is done on one analyte at a time. Multiplexed tandem mass spectrometry increases the number of species that undergo MS/MS in a set amount of time. The information generated by carrying out multiplexed MS/MS allows several species to be identified in parallel and signal-to-noise ratios to be improved due to the multiplex advantage. Analyzing multiple parent ions simultaneously is possible by maintaining parent-product ion correlations through an encoding process.[1-11]

Different encoding schemes have been utilized in multiplexed MS/MS. Several researchers have used Fourier transform ion cyclotron resonance (FTICR) mass analyzers to manipulate parent ions. A variable delay has been used between excitation pulse events to encode a parent ion participating in an ion-molecule reaction to determine a pathway for mass transfer.[2] Hadamard transform techniques have been used to perform multiplexed MS/MS on an eleven component mixture as well as to determine all potential dissociation pathways of three different parent ions concurrently.[3] Five ion-molecule proton-transfer reactions have been analyzed simultaneously through the use of stored waveform ion modulation (SWIM).[4] In each of these examples, the parent ion manipulation results in an encoded signal response that is imparted onto the generated product ions. The product ions can then be correlated (i.e. decoded) to their respective parent ions because

related ions have undergone the same signal modulation (i.e. encoding process). Other multiplexed approaches have utilized known ion-related properties (e.g. dissociation rate constants or accurate product ion masses) to help decode the convoluted parent-product ion relationships observed when multiple parent ions are encoded and analyzed simultaneously.[5, 6] It has also been demonstrated that parent-product ion correlations can be maintained by encoding the relative amount of each parent ion of interest on quadrupole ion trap mass spectrometers (QITMS).[7-9]

3.1.2 *Initial IAM experiments performed on a QITMS*

Iterative accumulation multiplexing (IAM) is a multiplexing approach that was developed in our laboratory and encodes the relative amount of ions by controlling individual ion accumulation times.[7, 8] The encoding process used for performing IAM on the QITMS involves sequentially filling the ion trap and iteratively removing all ions but those of interest. The ion to be accumulated for the longest amount of time is the only ion not ejected from the trap following the first fill. This ion remains stored in the QITMS while the trap is refilled with ions. Following the second fill, all ions are ejected from the trap except the ion that remained from the last fill and the next ion of interest. By repeating this iterative process multiple parent ions can be encoded with different relative accumulation times and consequently different abundances. Once the ions are encoded they can be dissociated by some method of MS/MS to form product ions which are then mass analyzed. Typically MS/MS provides structural information about the starting, intact parent ion but because multiple parent ions have been dissociated it is difficult to determine which product ions are associated with which parent ion. Repeating the iterative accumulation process a second time, but changing the order in which the parent ions of interest are encoded, results in the formation of product ions with abundances that differ from the first set of MS/MS results. By dividing the abundances from the first and second sets of MS/MS results, the ratio of the product ion abundances should be the same as the ratio of parent ion accumulation times used to acquire each MS/MS spectrum. As a result, an IAM experiment makes it possible to obtain MS/MS information on multiple analytes in the time it takes to acquire only two MS/MS spectra.

The successful implementation of the IAM experiment requires a mass spectrometer where there is a known relationship between signal response and ion accumulation time. Hybrid quadrupole

Fourier transform ion cyclotron resonance mass spectrometers (Q-FTICR-MS) allow ions to be accumulated externally to the ICR cell in a user-defined manner.[12] By accumulating different ions for unique amounts of time the observed abundances of each ion can be encoded. Unlike the QITMS instrument, parent ion accumulation is performed in a hexapole collision cell which is not capable of being operated mass selectively. To successfully implement the IAM process the parent ions must be accumulated mass selectively. The Q-FTICR-MS available to our lab contains a quadrupole mass filter located right before the collision hexapole. Thus, ion encoding for the purpose of multiplexed MS/MS can be performed external to the ICR cell.

3.1.3 *Utility of encoding multiple parent ions external to the FTICR cell*

The multi-channel detection inherent in FTICR-MS allows one transient acquisition to simultaneously provide information on all mass-to-charge ratios independently due to the superposition principle. In an IAM experiment a reduction in the amount of time required for an analysis is realized that is proportional to half the number of parent ions being considered, as long as the total encoding time is shorter than the time needed for mass analysis in the ICR cell. The ability to reduce the amount of time needed for FTICR-MS acquisitions of several analytes is advantageous due to the inherently long acquisition times encountered.[13]

Performing the ion encoding in the external collision hexapole avoids having to encode the ions within the ICR cell. With ion encoding done externally, the ICR cell can be used solely for mass analysis. Therefore ICR cell conditions can be optimized for detection and not compromised for ion manipulation. By injecting encoded ions into the ICR cell the ions begin on the cell axis which is ideal for accurate mass measurement.[14] If ion encoding is done in the ICR cell, for example by the two-dimensional FTICR-MS technique,[2, 4] care must be taken to bring the ions back to the cell axis before the excitation pulse is applied for detection. Another advantage of encoding the ions and performing multiplexed MS/MS (i.e., IAM) in the external collision hexapole is that it is straight forward to perform collision induced dissociation (CID). On the contrary, for CID to be performed in the ICR cell a collision gas must be introduced into the ultra high vacuum. The gas must then be pumped away following parent ion dissociation but prior to product ion excitation and detection to maintain detection sensitivity and mass resolving power.[15] Finally, external encoding of the ions makes it

possible to mass analyze an ion packet in the ICR cell while externally accumulating the next ion packet. The use of external ion accumulation has allowed hybrid FTICR-MS instruments to reach duty cycles close to 100%.[12, 16]

The work presented here describes a multiplexed MS/MS experiment (i.e., IAM) designed to reduce the amount of time needed to obtain MS/MS spectra of multiple parent ions. IAM has been performed on a Q-FTICR-MS instrument where the ions are encoded externally to the ICR cell and MS/MS data are acquired on multiple analytes in only two MS/MS spectra. Experiments were done using CID and a six-component peptide mixture resulting in a 3-fold reduction in analysis time. Electron capture dissociation (ECD) was also incorporated into the IAM experiment using the same six-component peptide mixture and three different charge states of one protein.

3.2 Experimental

3.2.1 *Samples*

The peptides bradykinin (RPPGFSPFR, M_r: 1060.21), granuliberin R (FGFLPIYRRPAS, M_r: 1422.68), neurotensin (pELYENKPRRPYIL, M_r: 1672.92), and angiotensin I (DRVYIHPFHL, M_r: 1296.48), the protein cytochrome c (from equine heart, M_r: 12,384), and HPLC-grade methanol were purchased from Sigma-Aldrich, Inc. (St. Louis, MO). The peptides substance P (RPKPQQFFGLM; free acid, M_r: 1348.70), alpha-mating factor (WHWLQLKPGQPMY, M_r: 1683.97), and cardiodilatin (NPMYNAVSNADLMDFK; 1-16, human, M_r: 1830.10) were purchased from the American Peptide Company (Sunnyvale, CA). Water (HPLC grade) and acetic acid (A.C.S. certified) were purchased from Fisher Scientific (Fair Lawn, NJ). All peptides were used without further purification and diluted in 50:50 v% methanol/water resulting in each mixture component being present at a concentration of ~ 5 μM. Acetic acid (1% by volume) was added to the final sample mixture to aid in the electrospray process.

3.2.2 *Hardware and software setup for controlling the Q-FTICR-MS instrumentation*

The experiments were performed on an apex-Qe (Qh-FTICR) mass spectrometer (Bruker Daltonics, Billerica, MA) equipped with a 12-Tesla actively shielded magnet and an Apollo II (Bruker Daltonics, Billerica, MA) electrospray ionization source. The Qh interface is comprised of the mass selective quadrupole (Extrel, Pittsburgh, PA), the accumulation collision cell/hexapole, and their

corresponding electronics. The standard apex-Qe electronics require an ICR cell detection event to occur before a different mass-to-charge ratio can be mass selectively passed through the quadrupole. To circumvent this limitation and allow several ions of different mass-to-charge to pass through the quadrupole before they are injected into the ICR cell and detected, modified electronics and software (LabVIEW 7.1, National Instruments, TX) have been added as shown in Figure 3.1. The modified electronics are used to control the mode of quadrupole operation (mass selective or rf only mode), the rf and dc voltage applied to the quadrupole rods to select which analyte to isolate, the collision voltage (relative voltage difference between the dc pole biases applied to the source and collision hexapoles), and the collision hexapole extract bias voltage (dc pole bias applied to the collision hexapole rods when ions are transferred from the collision hexapole to the ICR cell).

A modular design was used for the instrument modifications where the standard Qh interface

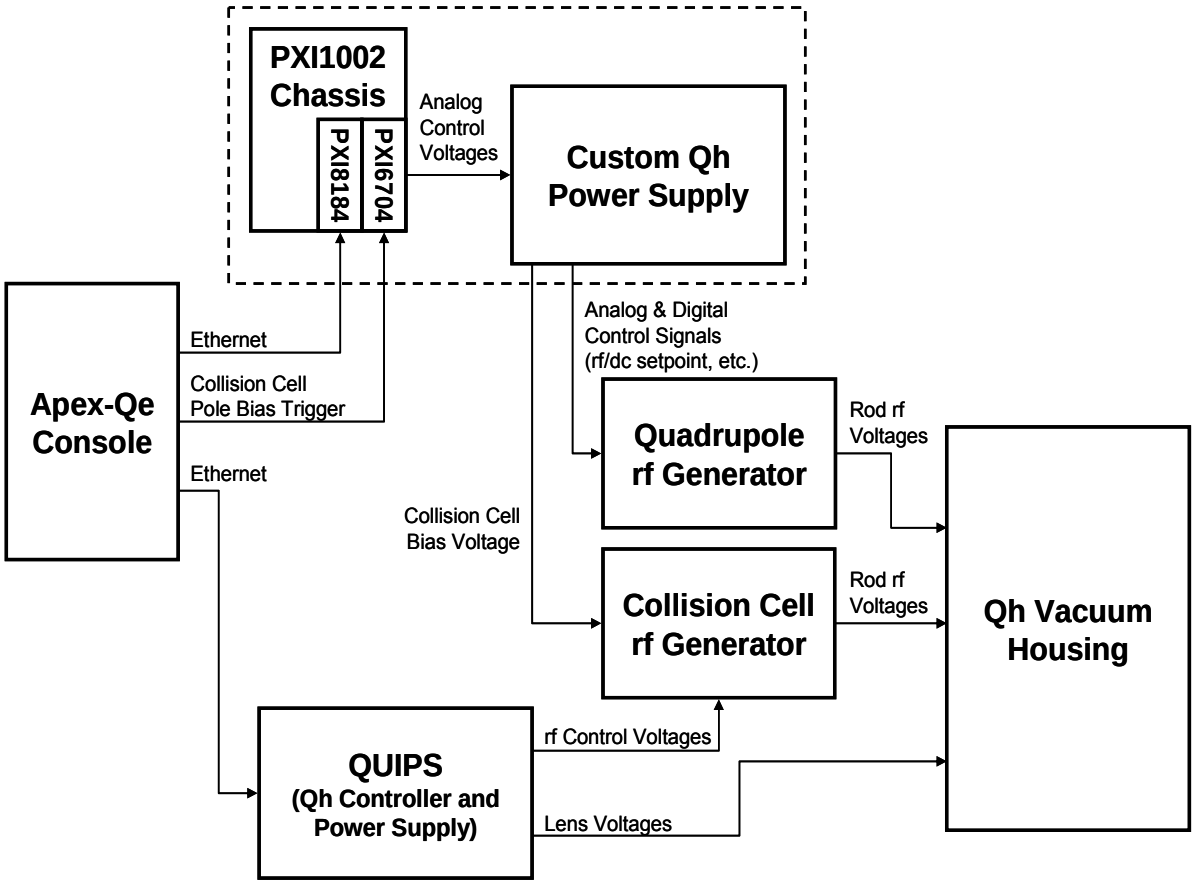

Figure 3.1 Simplified block diagram of the Qh Interface Electronics. The components enclosed by the dashed line indicate the modified hardware required for the IAM experiments. The LabVIEW program that is run on the PXI1002 Chassis controls the relative ion accumulation times and specifies the collision voltage to be applied to a given parent ion of interest for performing CID.

electronics are disconnected and replaced with the modified electronics identified by the dashed line in Figure 3.1. By using the modular design, normal instrument operation was maintained for all other users of this shared mass spectrometer simply by removing the modified electronics and reconnecting the standard power supplies. Also, the modular design limits the risk of damage to the modified electronics module ensuring that the implementation of the IAM experiment would not harm any components essential for routine instrument operation.

Communication between the main instrument electronics and the modified Qh control electronics and software is accomplished through the use of a trigger output (Collision Cell (h2) Pole Bias) from the apex-Qe console. As shown in Figure 3.2, the transition of this trigger to a LO state signals the start of the accumulation event in the collision cell. At this point the custom software is activated and initiates the voltage sequence necessary to execute the IAM experiment. The control program runs on a PXI, Windows XP based computer (PXI8184, National Instruments) housed in a

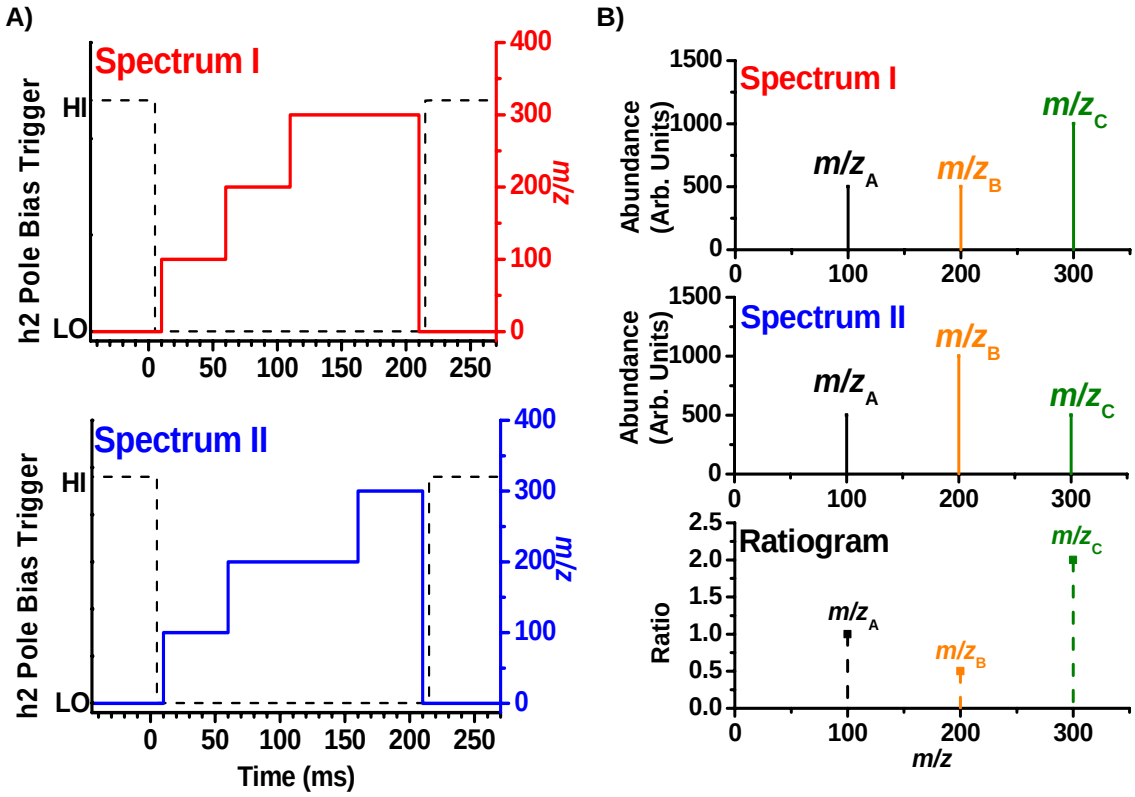

Figure 3.2 IAM procedure used on the Q-FTICR-MS. A) The total amount of time ions can be accumulated in the collisional hexapole is determined by the user-defined duration of the h2 Pole Bias Trigger LO state. B) From the relative accumulation times in A), the relative abundances in the mass spectra can be decoded into ions corresponding to one unique, encoded ratio.

PXI chassis (PXI1002, National Instruments). The PXI chassis also houses an analog output card (PXI6704, National Instruments) that provides the low voltage control signals to the standard Qh electronics and custom power supplies for the collision cell bias voltage. Once the IAM control program is initiated a stepwise procedure commences. Illustrated in Figure 3.2A, at each step the mass selective quadrupole rf and dc voltages are set to pass a given mass-to-charge value ("*m/z*-equivalent rf/dc control voltage"). Additionally the collision voltage for that mass-to-charge is set ("Collision Cell Bias Voltage") so that the desired dissociation (i.e., CID) is achieved. A unique collision cell bias voltage can be set for each ion (over the range of 0 to -150 V, for positive ions) so optimal CID conditions can be realized for every analyte independently. These voltages are set for the desired IAM accumulation time and the process is repeated for every ion of interest. The user enters the IAM *m/z* value of interest, its collision energy, and accumulation time into the custom LabVIEW control software prior to starting the instrumental scan. It should also be possible to modify the LabVIEW control program to allow a range of collision cell bias voltages to be used during the isolation and accumulation of each mass-to-charge ratio. The ability to vary the collision cell bias voltage for a given parent ion mass-to-charge ratio could be useful in the analysis of unknowns.

3.2.3 *IAM procedure: the encoding and decoding methods*

The key aspect to IAM is that two spectra are collected, each at different relative accumulation times for the parent ions of interest. A "ratiogram" is then generated by dividing the ion abundances of the two acquired spectra. The procedure for performing IAM to generate a ratiogram on the Q-FTICR-MS is depicted in Figure 3.2B. Consider an IAM experiment for a three-component mixture comprised of ions A, B, and C. By varying the relative accumulation times (see Figure 3.2A), each ion is uniquely encoded. The first of two spectra (Spectrum I) is acquired with the relative A : B : C accumulation times of 1 : 1 : 2. The second spectrum (Spectrum II) is acquired with the relative A : B : C accumulation times of 1 : 2 : 1. Assuming a constant flow of ions from the electrospray source and by keeping all instrumental parameters the same except the relative accumulation times while acquiring the two spectra, changes in signal response should be due only to changes in accumulation time, as shown in Figure 3.2B. Thus by dividing the spectral abundances of Spectrum I by those of

Spectrum II, a ratiogram is generated where each species is seen to have a unique ratio (A : B : C = 1 : 0.5 : 2).

3.2.4 *Multiplexed MS/MS experiments (CID and ECD)*

Protonated molecules are generated by ESI and sequentially selected by the quadrupole and accumulated in the collision hexapole as dictated by the LabVIEW control software mentioned above. CID is achieved by transferring ions into the collision hexapole through the user-specified potential difference established between the source and collision hexapoles. Control experiments were performed where CID was performed on each parent ion individually and the CID voltage that resulted in the largest fragmentation efficiency was chosen for use in the IAM experiments. Unless otherwise noted, the CID voltages used for bradykinin, substance P, granuliberin R, neurotensin, alpha-mating factor, and cardiodilatin were 18 V, 22 V, 28 V, 33 V, 26 V, and 24 V, respectively. All product and remaining parent ions are then sent to the ICR cell for detection.

Ions are extracted from the collision hexapole and transferred to the ICR using a dc potential gradient. As the ions enter the ICR cell their axial translation is stopped by a dc potential applied to the back trapping electrode of the ICR cell (~1.5 V). Because the magnetic field has no effect on the motion of ions in the axial direction, the ions are repelled by the dc potential on the back trapping plate. To prevent ion loss out of the front of the ICR cell, a trapping dc potential is applied to the front (entrance) trapping electrode (~1.3V). The trapping voltage on the ICR cell entrance electrode is applied at a user-defined time after the establishment of the dc potential gradient for ion extraction from the collision hexapole. The user-defined time is referred to as the time-of-flight (TOF) parameter. The time needed to transfer an ion from the collision hexapole to the ICR cell will depend on the ion's mass-to-charge ratio because all ions should have similar kinetic energies leaving the hexapole. Thus the TOF parameter acts as a mass-to-charge filter because different mass-to-charge ratios will take different amounts of time to be transferred from the collision hexapole to the ICR cell. The TOF parameter used for the work described in this chapter was 1.5 ms. For the IAM-CID results presented in this chapter, ion detection was performed in broadband mode using 512 K data points resulting in a transient duration of 262.1 ms. Each acquired spectrum is the result of summing 50 individual spectra.

ECD can also be incorporated into the IAM experiment by following the procedure previously described for CID but with two variations. First, parent ions are accumulated without undergoing CID; second, the encoded parent ions are sent to the ICR cell where they undergo ECD. For ECD experiments involving the doubly charged peptide parent ions the cathode bias was set to -1.1 V, the ECD lens was set to +15 V, 1.5 A was supplied to the cathode heater, and the electron irradiation time was 10.0 ms. For the peptide IAM-ECD experiments, ion detection within the ICR cell was performed in broadband mode using 512 K data points. Because the mass-to-charge range acquired for the peptide ECD experiments was the same as for the CID experiments, the transient duration for the IAM-ECD experiments was also 262.1 ms. But due to the use of a 10.0 ms electron irradiation time, the duty cycle is reduced by 3.8 % for the IAM-ECD experiments compared to the IAM-CID experiments. Each peptide IAM-ECD spectrum is the result of summing 50 individual spectra.

Slightly different ECD parameters were used for cytochrome c experiments, where the cathode bias was 1.7 V, the ECD lens was set to +15 V, 1.7 A was supplied to the cathode heater, and the electron irradiation time was 2.0 ms. Ion detection was performed in broadband mode using 512 K data points resulting in a transient duration of 327.7 ms because a larger mass-to-charge range was detected than for the peptide experiments. For cytochrome c, the incorporation of a 2.0 ms electron irradiation time results in a 0.6 % reduction in duty cycle compared to if ECD had not been used. The acquired spectrum is the summation of 50 individual spectra.

3.3 Results and Discussion

3.3.1 *Calibration curve for external ion accumulation*

The successful implementation of an IAM experiment is predicated on there being a known relationship between ion accumulation time in the collision hexapole and signal response. Control experiments were performed to determine the linearity between ion accumulation time and ion abundance. Shown in Figure 3.3A is the result of using a three peptide mixture where the protonated molecules are passed sequentially through the mass-selective quadrupole for equal amounts of time. The total accumulation time along the x-axis represents the sum of the individual accumulation times. For example, when a total accumulation time of 120 ms was used each ion was accumulated for 40 ms. The results in Figure 3.3A show that there is a linear signal response for total accumulation

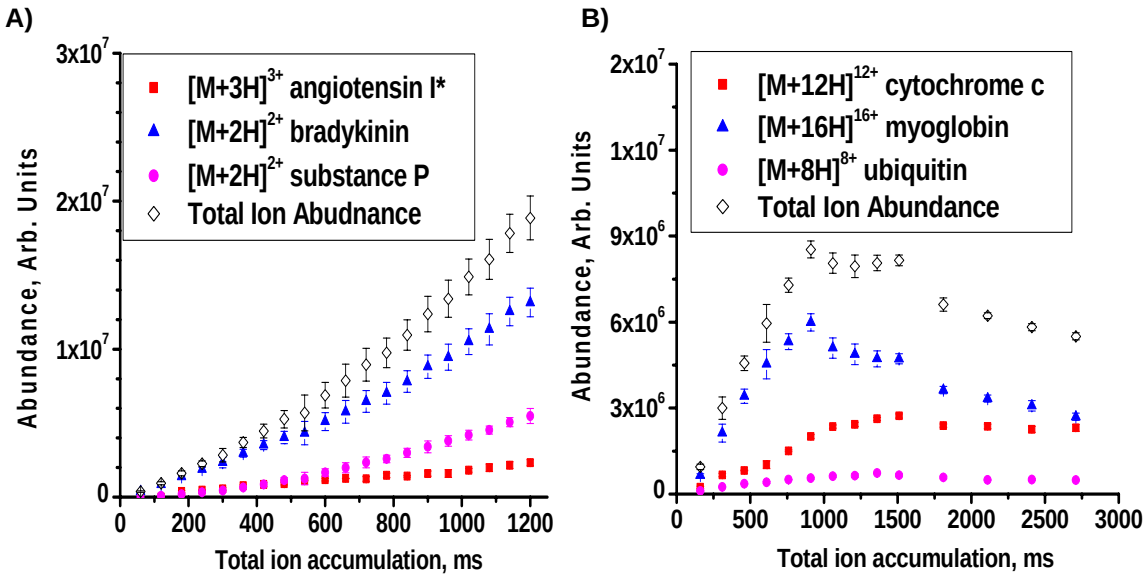

Figure 3.3 A) Peptide ion abundance as a function of accumulation time in the collisional hexapole under IAM conditions. *The abundances of **[M+3H]**$^{3+}$ angiotensin I were multiplied by 10 for clarity. B) Protein ion abundance as a function of accumulation time in the collision hexapole. Error bars represent ± one standard deviation calculated from three repeat measurements.

times less than ~600 ms. At times longer than 600 ms the abundance departs from linearity but the trend in total ion abundance still accurately represents the sum of the individual ion abundances. The data in Figure 3.3A also suggests that the space charge limit for the collision hexapole had not been reached even at the longest accumulation times. The space charge limit represents the largest amount of charge that can be stored within a given trapping volume and should result in the ion abundance reaching a maximum value. However, because two spectral acquisitions are required to generate the ratiogram for an IAM experiment, it is necessary to use total accumulation times that are within the range of a constant slope for the curve in Figure 3.3A. Thus, the total ion accumulation time for peptide IAM experiments was kept ≤ 600 ms to work on the linear portion of the calibration curve.

A calibration curve relating ion accumulation time and signal abundance was also constructed for protein parent ions, the result is shown in Figure 3.3B. Again, the parent ions were mass-selectively accumulated in the collision hexapole for equal amounts of time where the sum of the individual times is given along the x-axis of the calibration curve. The space charge limit of the collision hexapole is reached at ~900 ms using the protein parent ions, as demonstrated by the

maximum ion abundance in Figure 3.3B. Due to their higher charge states (e.g., +8, +12, +16) it was expected that the protein ions should reach the space charge limit at shorter accumulation times than the peptide ions. Based on the results in Figure 3.3B, the total ion accumulation time for the IAM-ECD protein experiment was kept ≤ 900 ms.

3.3.2 *Parent ion encoding*

IAM experiments were performed on the Q-FTICR-MS instrument using a six-peptide mixture. The encoding parameters and resulting peak abundances for the six analytes are listed in Table 3.1. The amount of time each parent ion was accumulated in the collision hexapole before being detected to generate Spectrum I is listed in the second row of Table 3.1. Also in the second row, the monoisotopic peak abundances are listed for each parent ion as determined by Bruker

Table 3.1 Encoding scheme used for peptide IAM experiments. The theoretical ratios are found by dividing the Spectrum I accumulation times by the Spectrum II accumulation times. The observed ratios are determined by dividing the Spectrum I abundances by the Spectrum II abundances.

Peptide	$[M+2H]^{2+}$ bradykinin	$[M+2H]^{2+}$ subs. P	$[M+2H]^{2+}$ gran. R	$[M+2H]^{2+}$ Neurotensin	$[M+2H]^{2+}$ α-mating factor	$[M+2H]^{2+}$ Cardiodilatin
m/z	530.7880	674.8634	711.9039	836.9621	842.4268	915.4135
Spectrum I time, ms	100	150	50	100	50	150
Parent ion abundance (Arb. Units)	6.2×10^7	5.1×10^8	1.0×10^8	2.2×10^8	7.4×10^7	3.0×10^8
Spectrum II time, ms	50	100	150	150	100	50
Parent Ion abundance (Arb. Units)	2.7×10^7	3.0×10^8	2.5×10^8	2.9×10^8	1.2×10^8	8.9×10^7
Requested ratio	2.0	1.5	0.33	0.67	0.50	3.0
Observed ratio	2.3	1.7	0.40	0.76	0.62	3.4

Daltonic's SNAP2 algorithm within the Bruker Data Analysis software suite. Row three contains the accumulation time and resulting monoisotopic peak abundances for Spectrum II. The theoretical ratios expected from this encoding scheme are listed in row four for each peptide, calculated by dividing the Spectrum I accumulation times by the Spectrum II accumulation times. The observed ratios in row five were calculated by dividing the abundances of the respective species in Spectrum I

by their corresponding abundances in Spectrum II. For the peptides studied, it was empirically determined that having a constant total accumulation time allowed for better agreement between theoretical and observed ratios in most instances. The reason for this better performance is still under investigation. However, preliminary results suggest that the behavior may be related to the ability to duplicate possible space charge or ion loss conditions, or both, in Spectrum I and II by keeping the total accumulation time constant.

In a separate set of experiments to quantify the instrumental scan-to-scan reproducibility, five consecutive scans of an equal-molar mixture of bradykinin, substance P, and granuliberin R were acquired. The results showed that the largest relative standard deviation for scan-to-scan peak abundance and observed parent ion monoisotopic peak centroid value were 4.56% and 4.64×10^{-6}%, respectively. This reproducibility adds confidence to the encoding procedure because two consecutive scans are required to generate a ratiogram.

Encoding the ions using the accumulation times listed in Table 3.1 and performing CID (IAM-CID) resulted in the theoretical ratios for the parent ions of interest being imparted to their respective product ions. As shown in Figure 3.4A conducting CID on six parent ions simultaneously produces complex spectra. The benefit of the IAM procedure is illustrated in Figure 3.4B where the monoisotopic and ^{13}C peaks for selected product ions from granuliberin R, cardiodilatin, and substance P are overlaid along with their respective observed ratios. For granuliberin R, the requested ratio for the $\mathbf{[M+2H]^{2+}}$ parent ion encoding is 0.33 where the observed ratio for the parent ion is 0.40 (see Table 3.1) and the observed ratio for the $\mathbf{y_6\text{-}NH_3}$ product ion is 0.38 (see Figure 3.4B). Thus there is a 13% difference between the observed product ion ratio and the requested parent ion ratio but only a 5% difference between the experimentally observed parent and product ion ratios. For cardiodilatin, there is a 14% difference between the observed $\mathbf{y_9}$ product ion ratio and the requested parent ion but only a 3% difference between the experimentally observed parent and product ion ratios. The substance P $\mathbf{a_9\text{-}NH_3}$ product ion showed a 12% difference between the observed ratio and the requested parent ion ratio and no difference between the experimentally observed parent and product ion ratios. The results show that there is an average difference of 13% between the requested and observed ratios but the average difference between the observed parent

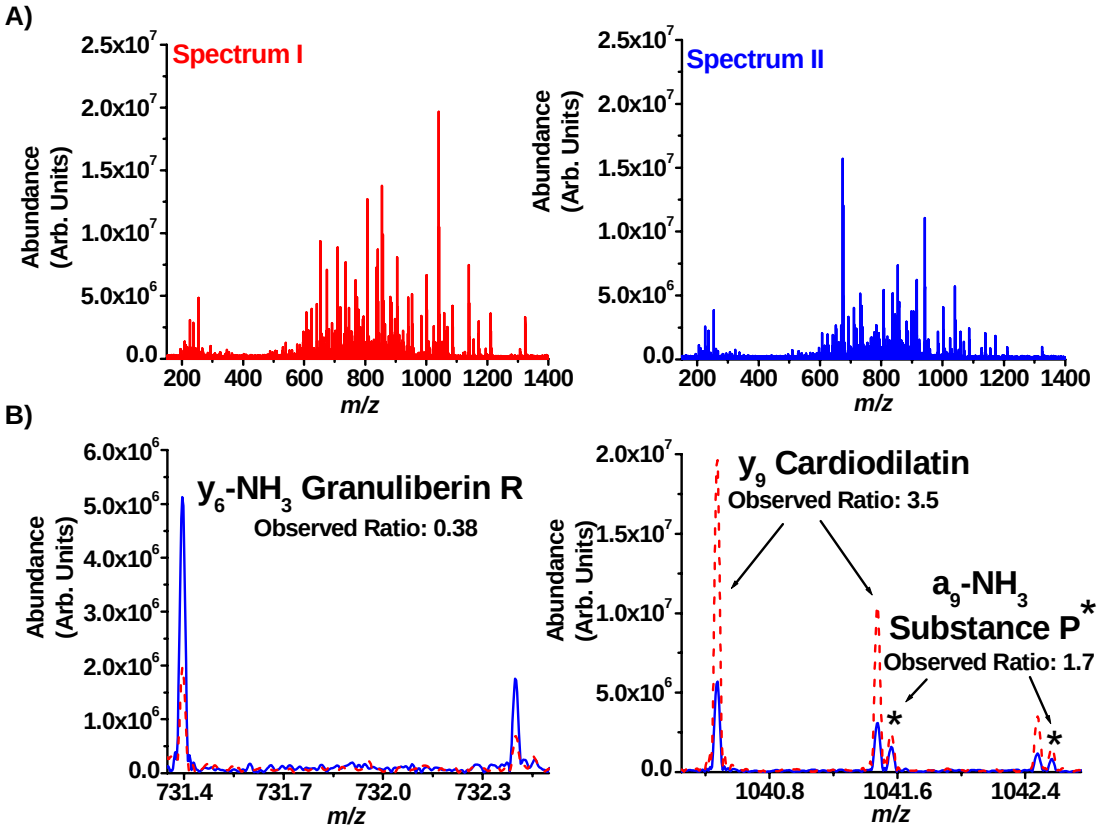

Figure 3.4 (A) CID spectra that resulted from the encoding scheme in Table 3.1; (B) Monoisotopic and ^{13}C peaks for selected product ions overlaid from Spectrum I (red, dashed) and Spectrum II (blue, solid) around cardiodilatin, granuliberin R, and substance P. The asterisks in the cardiodilatin spectrum denote the $\mathbf{a_9\text{-}NH_3}$ peak of substance P (see text).

ion ratios and their respective product ion ratios is only 3%. The 3% difference is evidence that the encoding scheme is effective in transferring the encoding of the parent ions on to their respective product ions.

The product ions in Figure 3.4B are instructive to note for two reasons. First, the substance P $\mathbf{a_9\text{-}NH_3}$ and the cardiodilatin $\mathbf{y_9}$ product ions could be identified as coming from different parent ions based solely on their observed ratios. Second, the $\mathbf{a_9\text{-}NH_3}$ substance P peak was acquired with a mass resolving power of 26,947 which is sufficient to allow it to be resolved from the ^{13}C peak of $\mathbf{y_9}$ cardiodilatin. No effort was made at maximizing the resolving power of this instrument while performing the experiment shown in Figure 3.4. The high resolving power offered by FTICR-MS allows product ion information to be retained during the IAM-FTICR-MS process that would have been lost when using most any other mass spectrometer, including the QITMS[7, 8].

3.3.3 *Ratiogram for the simplification of complex MS/MS results*

To aid in simplifying data interpretation, the product ions generated from the two CID spectra (Spectrum I and II) can be represented in a ratiogram, as shown in Figure 3.5. Monoisotopic peak lists were generated using Bruker Daltonic's SNAP2 algorithm. The monoisotopic peak lists for Spectra I and II were divided to create the ratiograms. A mass-to-charge tolerance of ≤ 5 ppm was used to ensure that the same product ion was used in Spectra I and II to calculate a given ratio. The product ions associated with each ratio were annotated by comparing observed mass-to-charge values to those generated *in silica* by the MS-Product functionality within Protein Prospector (Protein Prospector 4.0.8, University of California). The average mass measurement accuracy for the product ions in Figure 3.5 was 0.47 ppm, indicating that the high mass measurement accuracy typical of this instrument was maintained during the IAM experiment. The ratios are grouped around their respective theoretical ratios allowing the product ions to be discerned from one another. Some of the

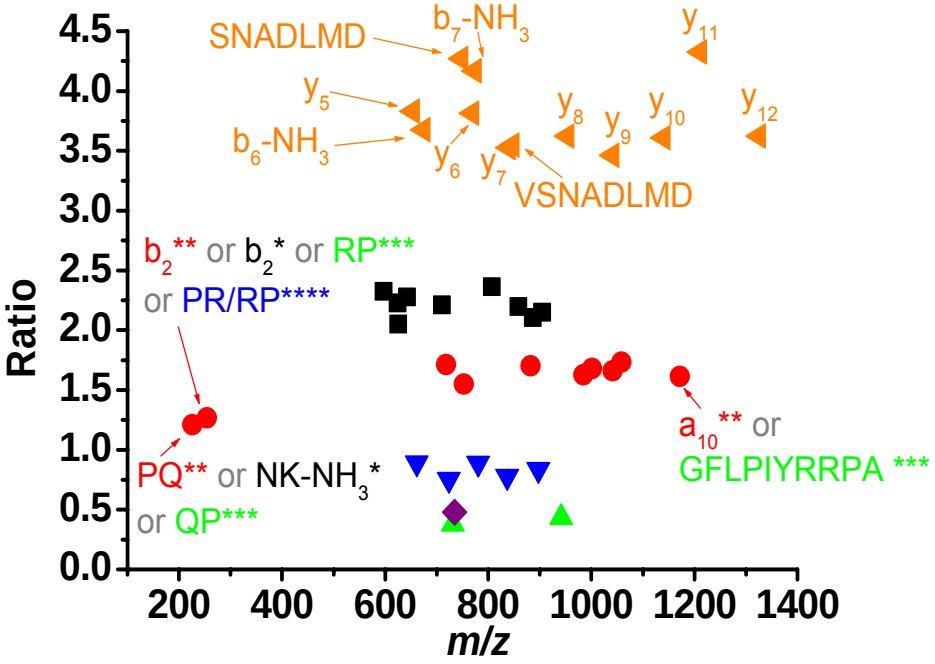

Figure 3.5 Ratiogram from the IAM-CID experiment using parent ions and encoding scheme outlined in Table 3.1. The product ions labeled with asterisks are isomers of the labeled mass-to-charge value. The correct annotation for an isomeric product ion in the ratiogram is the first one listed for a given mass-to-charge value (see text). Each asterisk (or multiple asterisk) corresponds to a specific parent ion: bradykinin (■)*; substance P (●)**; granuliberin R (▲)***; neurotensin (▼)****; α-mating factor (♦); cardiodilatin (◀).

observed ratios in Figure 3.5 are slightly higher than their theoretical values. Experiments are currently being conducted to gain a better understanding of ion accumulation in the collision hexapole and ion transfer to and ion storage in the ICR cell. Preliminary results have shown a mass-to-charge dependence on the efficiency of ion extraction from the collision hexapole and ion flight times to the ICR cell. Similar results have been described by other research groups.[17] It is proposed that at a given charge density within the collision hexapole ion-ion Coulombic repulsion can work with or against the dc potential gradient for ion extraction, depending on how the Coulombic repulsive force is directed. The flight times of ions from the collision hexapole to the ICR cell will decrease when the Coulombic repulsion aids in ion extraction. Conversely, ion flight times will increase when Coulombic repulsion works against the dc potential gradient for ion extraction. Smaller mass-to-charge ions exert a greater space charge effect on larger mass-to-charge ions, therefore differences in the relative abundances of each mass-to-charge ratio will change ion flight times of different mass-to-charge ratios to different extents. Because the IAM technique changes the relative abundance of each mass-to-charge ratio in the collision hexapole ion flight times may also be changed. Any changes in ion flight times will effect the amount of each species trapped in the ICR which would result in an incorrect measurement of ion abundance. An error in determining ion abundance would produce error in the calculation of ratios for an IAM experiment.

Also in Figure 3.5, there are instances where a product ion was observed at a mass-to-charge ratio that could represent a product ion from more than one of the potential parent ions. For example, the product ion at *m/z* 226.1186 could represent the isomers **PQ** or **QP** or the isobaric **NK-NH_3** from substance P, α-neurokinin, and neurotensin, respectively. Because the product ions in question are isomers or isobars mass measurement accuracy and resolving power alone cannot determine which parent ion (e.g., substance P, alpha-mating factor, or neurotensin) produced *m/z* 226.1186. However, due to the encoding scheme used in the IAM experiment the parent-product ion relationship for *m/z* 226.1186 is known. The encoding scheme for the parent ions used to generate the ratiogram in Figure 3.5 is set by the user the product ions can be unambiguously assigned to their respective parent ion assuming only one parent ion fragments to that particular product ion. If more than one parent ion fragments to the same isomeric product ions

then the ratio should be a linear combination of the ratios of the parent ion encoding scheme, which may or may not give ambiguous results. In the present example, the product ion at *m/z* 226.1186 can be confidently annotated as the **PQ** internal fragment from substance P (the other possible isomeric product ions are labeled with asterisks in Figure 3.5 which correspond to their respective parent ions). A similar situation was observed for four isomeric/isobaric product ions at *m/z* 254.1611 and also for two isomeric product ions at *m/z* 1171.6735. Control experiments were performed where each parent ion was individually isolated and dissociated by CID at the same conditions used for the IAM experiment. The product ions generated from the control experiments corroborate the identifications made via the IAM experiment. The correct annotation of these isomeric product ions verifies the utility of the encoding process to accurately assign product-parent ion correlations for isomeric product ions that are only formed from one parent ion.

3.3.4 *IAM-CID results*

In Figure 3.5, at least one product ion for each parent peptide was observed, however there are a limited number of product ions for certain parent ions (e.g. granuliberin R and alpha-mating factor). To determine if the IAM process is affecting the parent ion dissociation, control experiments were performed where each peptide was dissociated individually and the extent of their dissociation was compared to the extent each peptide was dissociated during IAM. The extent of dissociation can be represented by MS/MS efficiency, defined here as (Σ(product ion abundances) / initial parent ion abundance). The results of this comparison are given in Table 3.2. For the control experiments, each peptide was individually isolated from the six-peptide mixture, accumulated for 100 ms (chosen because it is the average of Spectrum I or Spectrum II accumulation times), and dissociated using the same CID voltage utilized during the IAM experiment (as listed in the Experimental section). The MS/MS efficiencies listed in Table 3.2 for the control experiments are the average (± one standard deviation) of three trials. For the IAM efficiencies, the IAM experiment described by Table 3.1 was performed with and without CID in duplicate. For each IAM experiment, Spectrum I was acquired without CID and with CID as was Spectrum II so MS/MS efficiencies could be calculated for each parent ion under both Spectrum I and II conditions. Therefore the efficiencies listed in Table 3.2 for each parent ion are the average of four MS/MS efficiency values.

Table 3.2 MS/MS efficiency comparison between the control and IAM conditions. The control experiment (see text) was performed on each peptide in triplicate.[†] Four MS/MS efficiency values (see text) for each parent ion were averaged to determine the IAM MS/MS efficiency.[‡]

	Control Experiments	IAM Experiments			
Peptide	MS/MS Efficiencies n = 3[†], (%)	Spectrum I time, ms	Spectrum II time, ms	Requested ratio	MS/MS Efficiencies n = 4[‡], (%)
bradykinin	46.79 ± 1.70	100	50	2	30.99 ± 2.87
subs. P	18.80 ± 1.10	150	100	1.5	11.64 ± 0.67
gran. R	11.97 ± 0.36	50	150	0.33	4.14 ± 0.70
neurotensin	10.34 ± 0.91	100	150	0.67	9.29 ± 2.53
α-mating factor	18.85 ± 2.61	50	100	0.50	13.07 ± 1.80
cardiodilatin	67.93 ± 4.05	150	50	3.0	21.25 ± 2.61

For a given set of IAM experiments only product ions in the CID ratiogram attributable to a given parent ion were considered in calculating the MS/MS efficiencies. The reason for only using product ions found in the CID ratiogram is shown in Figure 3.6. The CID spectrum of **$[M+2H]^{2+}$** cardiodilatin acquired conventionally is shown in Figure 3.6A. Figures 3.6B and 3.6C are the reconstructed CID spectra of **$[M+2H]^{2+}$** cardiodilatin under Spectrum I and II conditions from Table 3.1, respectively. The annotated peaks in Figure 3.6C correspond to those for cardiodilatin in Figure 3.5. Despite there being more product ions present in Figure 3.6B, for the decoding step of the IAM process (i.e., Spectrum I / Spectrum II) to provide meaningful results, only the abundances of those ions present in both Spectrum I and II can be considered. Therefore, even though the reconstructed CID results for Spectrum I contains more product ions than Spectrum II, the number of product ions that can be included in the ratiogram is limited to those present in the spectrum with the fewest number of product ions, i.e. Spectrum II. The result of this limitation is that IAM efficiencies would be expected to be lower than the control experiments, because fewer product ion abundances would be considered in the MS/MS efficiency calculation (e.g., compare 13 product ions in Figure 3.6C to 33 product ions in Figure 3.6A). While the results from Table 3.2 support this idea, it should be emphasized that the IAM process itself is not the cause for the reduced MS/MS efficiencies. Rather, the limitation is the relatively short parent ion accumulation times (e.g., 50 ms) used for the peptide

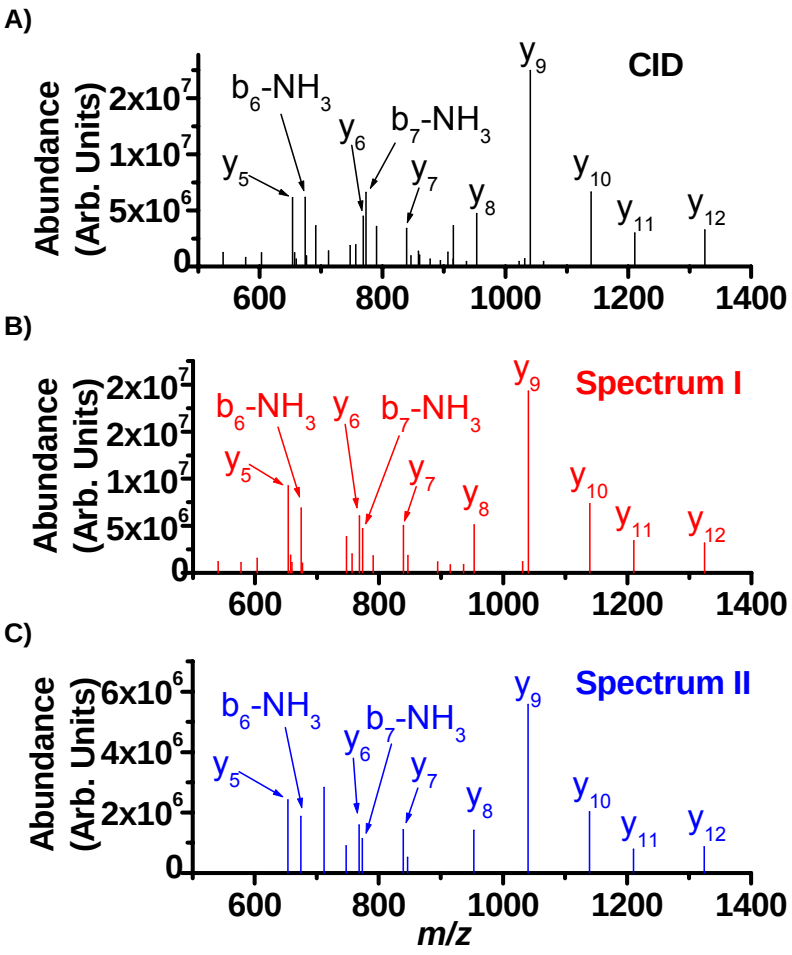

Figure 3.6 CID spectra of **[M+2H]$^{2+}$** cardiodilatin: (A) CID spectrum after individually isolating and accumulating the parent ion; (B) Product ion spectrum reconstructed from an IAM experiment performed under the Spectrum I conditions given in Table 3.1 for cardiodilatin; (C) Product ion spectrum reconstructed from an IAM experiment performed under the Spectrum II conditions given in Table 3.1 for cardiodilatin.

IAM experiments presented in Figures 3.4 and 3.5 and Table 3.2. By reducing the accumulation time a smaller absolute number of product ions are formed and stored in the collision hexapole. Thus, when the ions are sent to the ICR cell for detection there are fewer of them resulting in a smaller induced current. The resulting ICR signal may not produce a signal-to-noise ratio sufficient enough for those ions to be detected. To avoid such a situation, the IAM encoding scheme could be changed to incorporate longer accumulation times. Note that as long as the total encoding time is shorter than the time to acquire the transient image current, there is no loss of duty cycle because while one set of ions is being detected, the next set is being prepared for injection into the ICR cell.

A second IAM experiment was performed using the same analytes listed in Table 3.I, but with different relative accumulation times. The altered encoding scheme resulted in the doubly protonated parent ions of bradykinin, substance P, granuliberin R, neurotensin, alpha-mating factor, and cardiodilatin having requested ratios of 3.5, 2.0, 1.2, 0.8, 0.5, and 0.3, respectively. The ratiogram for this experiment is shown in Figure 3.7. These ratios are approximately the inverse of those listed in Table 3.1. For this second IAM experiment the requested ratio for alpha-mating factor was kept the same as the previous experiment (i.e., 0.5) but the Spectrum I accumulation time was increased to 75 ms. By increasing the accumulation time three alpha-mating factor product ions were observed in the ratiogram, compared to only one when a Spectrum I accumulation time of 50 ms was used in the first IAM experiment. Also demonstrated in the ratiogram of Figure 3.7 is the independence of requested

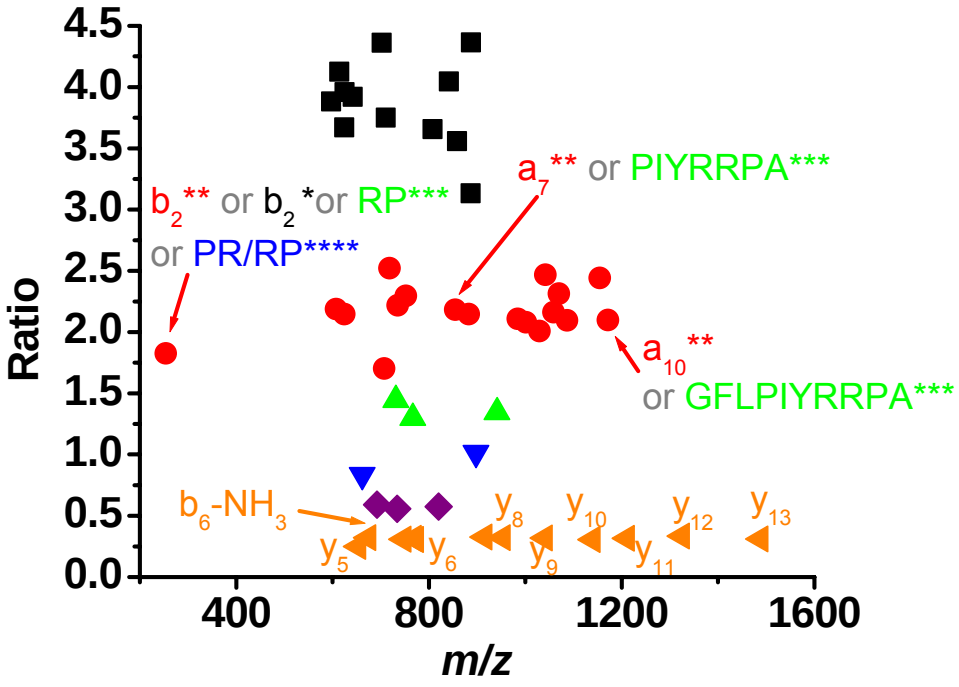

Figure 3.7 Ratiogram from the second IAM-CID experiment. The accumulation times (in ms) for each analyte for Spectra I/II were: bradykinin (175 ms / 50 ms); substance P (150 ms / 75 ms); granuliberin R (125 ms / 100 ms); neurotensin (100 ms / 125 ms); α-neuorkinin (75 ms / 150 ms); cardiodilatin (50 ms / 175 ms). Each asterisk (or multiple asterisk) corresponds to a specific parent ion: bradykinin (■)*; substance P (●)**; granuliberin R (▲)***; neurotensin (▼)****; α-mating factor (♦); cardiodilatin (◄). The product ions labeled with asterisks are isomers of the labeled mass-to-charge value. The correct annotation for an isomeric product ion in the ratiogram is the first one listed for a given mass-to-charge value (see text).

ratio on mass-to-charge value of the encoded parent ions. For example, the encoding of cardiodilatin in the first and second IAM experiments was 3.0 and 0.3, respectively. As the ratiograms in Figure 3.5 and Figure 3.7 indicate, the product ions for cardiodilatin are accurately encoded for both conditions.

3.3.5 *IAM-ECD results*

ECD can also be incorporated into the IAM experiment, allowing its benefits to be realized (e.g. improved sequence coverage and retention of post translational modifications).[18] Conducting IAM-ECD on the same six-peptide mixture and encoding scheme presented in Table 3.1 resulted in the ratiogram shown in Figure 3.8. In addition to the expected ECD-related **c**- and **z**-product ions, **y**-ions are also observed. It has been proposed in the literature that the presence of product ions characteristic of a slow-heating process (e.g. **b**- or **y**-ions) can be attributed to vibrational excitation due to blackbody infrared irradiation from the ECD cathode.[19] While at least one ECD-related ion associated with each parent ion was formed due to the electron capture process, the sequence

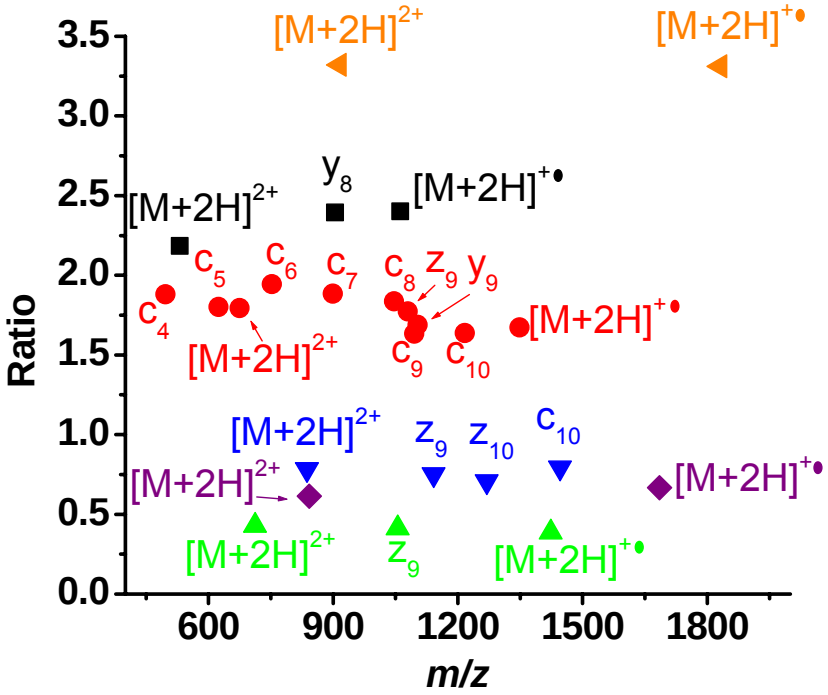

Figure 3.8 IAM-ECD ratiogram using encoding scheme outlined in Table 3.1. Product ion annotation follows: bradykinin (■); substance P (●); granuliberin R (▲); neurotensin (▼); α-mating factor (♦); cardiodilatin (◄).

coverage for all of the species except substance P is poor. There are two reasons for the poor sequence coverage. First, the peptide parent ions were doubly charged and it is well established that the electron capture cross section increases linearly with the square of the parent ion charge state.[18] Without the capture of an electron no parent ion dissociation and thus no peptide sequence information would produced. The poor dissociation observed in Figure 3.8 is thus consistent with the trend towards non-dissociative electron capture with decreasing charge state.[20] The second reason for the poor peptide ECD sequence coverage is due to a limitation of the current instrument capabilities, namely that only one set of ECD parameters can be used during a given IAM experiment. It is widely accepted that different species require different optimal ECD parameter settings.[19] However, being limited to one set of ECD conditions is a limitation of the instrumental software and not one inherent to the IAM process.

3.3.6 *Existing software limitations for IAM-ECD*

To explore the utility of IAM-ECD while not having to consider the constraint of only being able to use one set of ECD parameters, IAM-ECD was performed on three different charge states (+14, +12, and +10) of cytochrome c. The +10, +12, and +14 charge states were accumulated for 300 ms each for Spectrum I and for 150, 200, and 300 ms for Spectrum II,

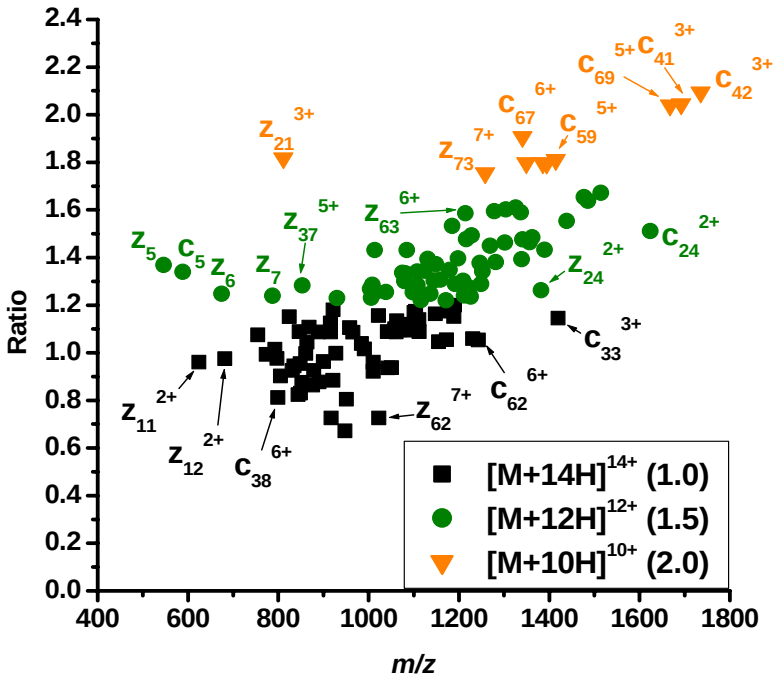

Figure 3.9 IAM-ECD ratiogram for three charge states of cytochrome c. Charge states **[M+Fe(III)+9H]$^{+10}$**, **[M+Fe(III)+11H]$^{+12}$**, and **[M+Fe(III)+13H]$^{+14}$** are represented by (**M^{+10}**), (**M^{+12}**), and (**M^{+14}**), and were encoded to achieve ratios of 2.0, 1.5, and 1.0 respectively. A total of 131 product ions were observed.

respectively. The ECD parameters were as listed in the Experimental section and the resulting ratiogram from this experiment is displayed in Figure 3.9. Several product ions (i.e., **c**-, **z**-, **b**-, or **y**-product ions) were observed and display a general trend of lower parent ion charge states producing higher mass-to-charge product ions. Furthermore, the ratiogram demonstrates the ability for one set of ECD conditions to be used during an IAM experiment to produce product ions from different parent ions.

It would be of interest to determine if charge state-dependent dissociation information can be retained during the IAM experiment. Using the **c** and **z** product ions from the ratiogram in Figure 3.9 the location of cytochrome c backbone cleavage was plotted for each parent ion charge state to produce Figure 3.10. From Figure 3.10, it appears that the charge state of the parent ion has little

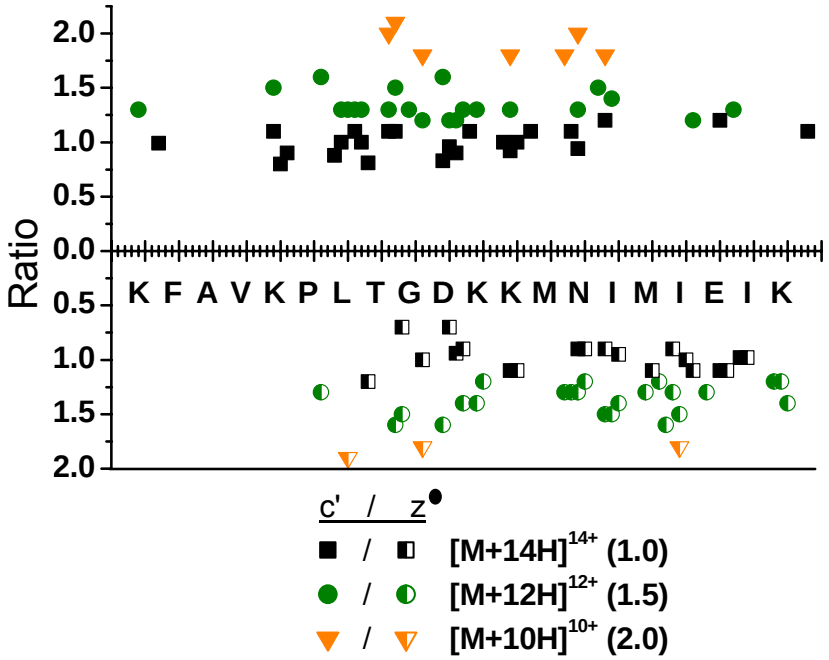

Figure 3.10 Locations of cytochrome c backbone cleavage for each parent ion charge state (+10, +12, and +14) considering only the c and z ions represented in Figure 3.9.

effect on where the protein backbone is cleaved under these experimental conditions. Overall, **c**-ion formation is favored most likely due to the heme group covalently bound to Cys 14 and Cys 17.

3.4 Conclusions

Iterative accumulation multiplexing (IAM) has been successfully implemented external to the ICR cell on a hybrid Q-FTICR-MS instrument. The IAM experiment allowed MS/MS of six analytes to be performed in two MS/MS experiments without sacrificing ICR performance (i.e. mass measurement accuracy or mass resolving power). Product ion information generated by IAM is provided by ratiograms that are comprised of species recorded with high mass measurement accuracy.

3.5 References:

1. McLafferty, F. W.; Stauffer, D. B.; Loh, S. Y.; Williams, E. R. Hadamard Transform and "No-Peak" Enhancement in Measurement of Tandem Fourier Transform Mass Spectra. *Analytical Chemistry*. **1987**, 59, p. 2212-2213.

2. Pfändler, P.; Bodenhausen, G.; Rapin, J.; Houriet, R.; Gäumann, T. Two-Dimensional Fourier Transform Ion Cyclotron Resonance Mass Spectrometry. *Chemical Physics Letters*. **1987**, 138, p. 195-200.

3. Williams, E. R.; Loh, S. Y.; McLafferty, F. W.; Cody, R. B. Hadamard Transform Measurement of Tandem Fourier-Transform Mass Spectra. *Analytical Chemistry*. **1990**, 62, p. 698-703.

4. Ross, C. W. I.; Guan, S.; Grosshans, P. B.; Ricca, T. L.; Marshall, A. G. Two-Dimensional Fourier Transform Ion Cyclotron Resonance Mass Spectrometry/Mass Spectrometry with Stored-Waveform Ion Radius Modulation. *Journal of the American Chemical Society*. **1993**, 15, p. 7854-7861.

5. Schnier, P. D.; Williams, E. R. Analysis of Isomeric Mixtures Using Blackbody Infrared Radiative Dissociation: Determining Isomeric Purity and Obtaining Individual Tandem Mass Spectra Simultaneously. *Analytical Chemistry*. **1998**, 70, p. 3033-3041.

6. Masselon, C.; Anderson, G. A.; Harkewicz, R.; Bruce, J. E.; Pasa-Tolic, L.; Smith, R. D. Accurate Mass Multiplexed Tandem Mass Spectrometry for High-Throughput Polypeptide Identification from Mixtures. *Analytical Chemistry*. **2000**, 72, p. 1918-1924.

7. Ray, K. L.; Glish, G. L. *A New Multiplexed MS/MS Method for Ion Trapping Instruments*. in *The 48th ASMS Conference on Mass Spectrometry and Allied Topics*. 2000.

8. Cunningham, C. Jr.; Ray, K. L.; Glish, G. L. *Iterative Accumulation Multiplexing TA-CID in a Quadrupole Ion Trap*. in *The 52nd ASMS Conference on Mass Spectrometry and Allied Topics*. 2004.

9. Wilson, J.; Vachet, R. W. Multiplexed MS/MS in a Quadrupole Ion Trap Mass Spectrometer. *Analytical Chemistry*. **2004**, 76, p. 7346 - 7353.

10. Belov, M. E.; Buschbach, M. E.; Prior, D. C.; Tang, K.; Smith, R. D. Multiplexed Ion Mobility Spectrometry-Orthognal Time-of-Flight Mass Spectrometry. *Analytical Chemistry*. **2007**, 79, p. 2451 - 2462.

11. Belov, M. E.; Clowers, B. H.; Prior, D. C.; Danielson, W. F. I.; Liyu, A. V.; Petritis, B. O.; Smith, R. D. Dynamically Multiplexed Ion Mobility Time-of-Flight Mass Spectrometry. *Analytical Chemistry*. **2008**, 80, p. 5873 - 5883.

12. Belov, M. E.; Nikolaev, E. N.; Anderson, G. A.; Udseth, H. R.; Conrads, T. P.; Veenstra, T. D.; Masselon, C. D.; Gorshkov, M. V.; Smith, R. D. Design and Performance of an ESI Interface for Selective External Ion Accumulation Coupled to a Fourier Transform Ion Cyclotron Mass Spectrometer. *Analytical Chemistry*. **2001**, 73, p. 253-261.

13. Amster, I. J. Fourier Transform Mass Spectrometry. *Journal of Mass Spectrometry*. **1996**, 31, p. 1325-1337.

14. Marshall, A. G.; Hendrickson, C. L.; Jackson, G. S. Fourier Transform Ion Cyclotron Resonance Mass Spectrometry: A Primer. *Mass Spectrometry Reviews*. **1998**, 17, p. 1-35.

15. Laskin, J.; Futrell, J. H. Activation of Large Ions in FT-ICR Mass Spectrometry. *Mass Spectrometry Reviews*. **2005**, 24, p. 135-167.

16. Patrie, S. M.; Charlebois, J. P.; Whipple, D.; Kelleher, N. L.; Hendrickson, C. L.; Quinn, J. P.; Marshall, A. G.; Mukhopadhyay, B. Construction of a Hybrid Quadrupole/Fourier Transform Ion Cyclotron Resonance Mass Spectrometer for Versatile MS/MS Above 10 kDa. *Journal of the American Society for Mass Spectrometry*. **2004**, 15, p. 1099–1108.

17. van Agthoven, M.A.; Hendrickson, C. L.; Beu, S. C.; Blakney, G. T.; Quinn, J. P.; Marshall, A. G. *Optimal Event Sequences for Octopole-Quadrupole-Octopole External Ion Introduction for Fourier Transform Ion Cyclotron Resonance Mass Spectrometry*. in *The 55th ASMS Conference on Mass Spectrometry and Allied Topics*. 2007.

18. Cooper, H. J.; Hakansson, K.; Marshall, A. G. The Role of Electron Capture Dissociation in Biomolecular Analysis. *Mass Spectrometry Reviews*. **2005**, 24, p. 201 - 222.

19. Polfer, N. C.; Haselmann, K.; Zubarev, R. A.; Langridge-Smith, P. R. R. Electron Capture dissociation of polypeptides using a 3 Tesla FTICRMS. *Rapid Communications in Mass Spectrometry*. **2002**, 16, p. 936-943.

20. Swaney, D. L.; McAlister, G. C.; Wirtala, M.; Schwartz, J. C.; Syka, J. E. P.; Coon, J. J. Supplemental Activation Method for High-Efficiency Electron-Transfer Dissociation of Doubly Protonated Peptide Precursors. *Analytical Chemistry*. **2007**, 79, p. 477 - 485.

Chapter 4

Electron Capture Dissociation (ECD) in a Linear Ion Trap (LIT) versus a Quadrupole Fourier Transform Ion Cyclotron Resonance Mass Spectrometer (Q-FTICR-MS)

4.1 Introduction

4.1.1 *Brief history of ECD (FTICR-MS → LIT)*

Electron capture dissociation (ECD) has become an important tool for tandem mass spectrometry (MS/MS) analyses.[1-3] Despite there still being significant debate about the mechanism of ECD,[4-10] its ability to provide extensive sequence coverage (the percentage of possible peptide backbone sites that are cleaved) while retaining labile groups (e.g., post translational modifications, PTMs) is unanimously accepted. Consequently, ECD has been used for the determination of binding sites for various PTMs[11-15] and the sequencing of peptides, proteins,[1-3, 5, 16-18] and other biologically relevant molecules.[19, 20] Furthermore, the information provided by ECD is often complementary to that garnered from "slow heating" activation methods (i.e., collision induced dissociation, CID and infrared multiphoton dissociation, IRMPD).[21, 22] The increased popularity of ECD is evidenced by several review articles that have been published on this topic.[23-26]

All initial ECD experiments were performed in Fourier transform ion cyclotron resonance mass spectrometers (FTICR-MS) due to this instrument's ability to allow low energy electrons to react with trapped ions for long times (e.g., milliseconds).[26] The residence times of ions in time-of-flight (TOF) and quadrupole instruments are too short to achieve effective ECD.[22] Preliminary work directed at achieving ECD in radio frequency (rf) ion trap instruments was also unsuccessful due to the difficulty in producing low energy electrons in the presence of the inherent radio frequency potential.[27] As a result, ECD remained a technique that was practicable only to those who had

access to a FTICR instrument.

In 2004, ECD was demonstrated in a linear ion trap (LIT).[28] Within months, the implementation of ECD on a three-dimensional ion trap was reported.[29] In 2006, ECD was demonstrated in a digital ion trap.[30] As a result of such work, the advantages of ECD became available to a greater number of mass spectrometrists. In 2007 a practicable version of the ECD LIT (referred to here as the ECD_{LIT}) was developed and incorporated into a hybrid instrument where the ECD_{LIT} was located between a conventional LIT and a reflectron TOF mass analyzer.[31] Having access to both the ECD_{LIT} and a 12-Tesla hybrid quadrupole-FTICR (Q-FTICR-MS) presented the opportunity to directly compare the ECD operation for both instruments.

4.1.2 *Important instrumental differences*

There are several important differences between the experimental conditions used in the FTICR-MS and in the ECD_{LIT} during ECD experiments. A helium bath gas is used in the ECD_{LIT} resulting in a pressure that is six orders of magnitude higher than in the FTICR-MS, where no bath gas is used. As the parent ions undergo collisions with the bath gas, some of the ion's kinetic and internal energy is transferred to kinetic energy of the bath gas. As described in the Chapter 1, increasing the pressure of the bath gas increases the number of ions undergoing collisions, but more importantly the probability of an individual ion to undergo multiple collisions also increases. As a result, the internal energy of ions in the ECD_{LIT} is expected to be lower than in the FTICR due to the parent ion undergoing more collisions in the higher pressure conditions of the ECD_{LIT}. The effect this difference in internal energy has on the ECD results from the ECD_{LIT} and FTICR-MS instrument has not been studied.

Performing ECD in a FTICR-MS requires the product ions to be detected by measuring a current they induce on the ICR cell electrodes. The time necessary to measure the induced current in FTICR-MS can be as long as 1.0 s per spectrum (compared to 0.1 seconds for other mass analyzers).[32] In the ECD_{LIT} the product ions are detected with a reflectron TOF that significantly increases the speed of data acquisition.

The electron sources for each instrument are based on different designs. For the ECD_{LIT} a bent, edge thoriated tungsten filament is used to generate an electron beam with a diameter < 1 mm

and a typical current density of 1 μA/mm^2.[31] Because electrons are only emitted from the tip of the bend in the bent filament, a beam of electrons with well-defined axial kinetic energy is produced. While FTICR-MS instruments began using filament-style electron sources, modern instruments typically employ dispenser cathodes with surface areas of 100 mm^2 in an effort to improve ion-electron overlap.[33] Under normal operating conditions similar currents are used for both the bent filament and the dispenser cathodes, therefore an electron beam density of 0.005 μA/mm^2 is created in FTICR-MS instruments. As a result, the electron density in the ECD_{LIT} is 200 times greater than in the FTICR-MS.[31]

The alignment of the ion and electron beams for maximum overlap is difficult to achieve on FTICR-MS instruments. The ideal condition for FTICR-MS ECD is that the ions and electrons are injected on the central axis of the ICR cell, which itself is located in the cylindrical center of a homogeneous magnetic field (see Chapter 1, Figure 1.4). Ions are trapped axially by dc voltages applied to the front and back axial trapping electrodes. However, the positive (for cations) axial dc trapping potentials radially displace the ions so that the circumference of the path followed by the center of an ions' cyclotron orbit is displaced from the ICR cell central axis. The path followed by the center of an ion's cyclotron orbit is referred to as magnetron motion.[34] As the trapping voltages increase in magnitude the displacement of the ions from the ICR cell central axis, and thus the magnitude of magnetron motion, increases. The best situation for trapping ions in the ICR cell would be to use the smallest axial dc trapping potentials possible. Unfortunately, the dc voltages on the front and back trapping electrodes must be large enough to effectively trap the ions, therefore the introduction of magnetron motion is inevitable. [35] To compensate for ion displacement from the ICR central axis, electron beams with a diameter sufficiently large enough to encompass all of the ions trapped within the ICR cell are used to maximize ion-electron overlap. As mentioned previously, hollow dispenser cathodes have become the standard electron source for FTICR-MS ECD experiments, replacing filament type sources due to the increased electron beam diameter of the cathode sources.[25] However, it has been shown that with FTICR-MS instruments only those ions interacting with electrons at the moment of electron injection into the ICR cell result in ECD and ions do not rotate into the electron beam over the course of an ECD experiment.[35] To address this

issue, improved ion-electron overlap in FTICR-MS instruments has been demonstrated by introducing a delay between ion and electron injections where the appropriate delay is determined by the number of ions present and the specific axial trapping voltages used.[35] The delay ensures electrons are only injected into the ICR cell when the periodicity of magnetron motion results in the ions being located within the area overlapped by the electron beam. Unfortunately, this delay is difficult to implement in real time due to fluctuations in the number of ions that are introduced into the ICR cell; for example, during a liquid chromatography (LC)-MS analysis where the sample concentration varies with time. As an alternative, the need to know the exact delay between ion and electron introduction can be avoided by using sufficiently long electron irradiation times such that electrons will be injected into the ICR cell for a duration equal to or longer than the period of magnetron motion.[35] The experiment becomes even more difficult when high energy ECD (HECD) is attempted. The difficulty arises due to the aforementioned alignment challenges and the two-to-three order of magnitude lower electron capture cross section experienced at the higher electron kinetic energies required for HECD.[4]

4.1.3 *Benefits of performing ECD in the ECD_{LIT}*

Sufficient ion-electron overlap is more easily achieved in the ECD_{LIT} making the implementation of ECD more straightforward than on the FTICR-MS. The improved overlap is due to the unique combination of the radial ion-focusing effect of the applied rf potential, the dampening collisions the ions undergo with the helium bath gas present within the ECD_{LIT}, and the magnetic field that surrounds the ECD_{LIT}.[31] The ECD_{LIT} is a device which uses an electrodynamic potential to establish a quadrupolar field in the radial dimension. This quadrupolar field imparts a restoring force upon ions to bring them back to the central axis of the rod set.[32] In addition, helium bath gas is used to aid in the trapping and focusing ions to the LIT central axis through the process of collisional cooling.[32] With the ions focused to the axis within the LIT, alignment of the electron beam along this same axis ensures good ion-electron overlap. Such electron alignment is achieved through two means. First, the thoriated tungsten filament is shaped and center mounted on the back flange of the ECD cell, thereby ensuring the filament is aligned with the ECD_{LIT} central axis. Second, the homogenous magnetic field (~150 mTesla) established parallel to the ECD_{LIT} axis by a cylindrical,

neodymium permanent magnet aids in radially confining the electron beam generated from the tungsten filament.[31] Thus, unlike within the ICR cell, the electric and magnetic fields in the ECD_{LIT} work together to create significant ion-electron overlap without the need for extensive tuning by the user.

Despite the prominence of ECD in the literature, there has been no detailed comparison of ECD operation between the ECD_{LIT} and FTICR-MS because no other lab has had access to both instruments. The operation of ECD on both the ECD_{LIT} and FTICR-MS will be presented in this chapter. The electron energy and irradiation time dependence of ECD will be characterized for both instruments, including considerations associated with performing HECD. Spectra acquired at optimal conditions will be compared and the parent ion internal energy on each instrument will be examined using the peptide substance P.

4.2 Experimental

4.2.1 *Samples*

Substance P (RPKPQQFFGLM; free acid, M_r: 1348.70), melittin (GIGAVLKVLTTGLPALISWIKRKRQQ-NH_2, M_r: 2846.46) and bovine ubiquitin (M_r: 8.6 kDa) were obtained from Sigma-Aldrich (St. Louis, MO) and used without further purification. Beta-endorphin (M_r: 3465.00) was purchased from Peptide International (Louisville, KY) and also used without further purification. All analytes were dissolved in water and then diluted to 5 μM in the appropriate solvent. The solvent systems used for the FTICR and LIT/TOF instruments were 49.5/49.5/1 and 79.5/19.5/1 (%v) water/acetonitrile/formic acid, respectively. Ions for the FTICR experiments were generated from conventional electrospray ionization (ESI) where the sample solutions were introduced at flow rates of 1.5 μL/min with the capillary voltage set at 4390 V. Ionization on the LIT/TOF instrument was achieved with direct infusion nano-ESI (nESI) and a spray potential of 1100-1300 V.

4.2.2 *Experimental parameters for each instrument*

FTICR-MS Instrumentation

FTICR-MS experiments were performed on an apex-Qe mass spectrometer equipped with a 12-Tesla actively shielded magnet and an Apollo II source (Bruker Daltonics, Billerica, MA). The specific charge state of each parent ion was isolated externally to the ICR cell by a mass-selective

quadrupole (Extrel, Pittsburgh, PA) and accumulated in the external accumulation/collision hexapole. Typical parent ion accumulation times were between 200 and 700 ms. The isolated parent ions were then sent to the ICR cell and trapped using Sidekick^{TM} conditions. For substance P, the Sidekick parameter was 3.0 V with a Sidekick offset of -1.7 V, excitation amplitude of -0.50 dB, analyzer entrance of -3.0 V, and front/back cell trap plate voltages of 1.3/1.5 V. The conditions were the same for beta-endorphin except a Sidekick of 4.0 V and an analyzer entrance of -1.0 V were used. For ion transfer from the collision hexapole and storage in the ICR cell, a time-of-flight ("TOF" parameter in Apex) of 1.5 ms and 1.2 ms were used for substance P and beta-endorphin, respectively. The TOF parameter determines how long the voltages are set to extract the ions from the collision hexapole and trap them in the ICR cell. If the trapping and extraction voltages are kept constant, as the mass-to-charge ratio of the ions accumulated in the collision hexapole changes, the "TOF" parameter has to be adjusted to account for the difference in flight times associated with different mass-to-charge ratios.

Electrons used for ECD on the FTICR-MS were generated from a hollow dispenser cathode and the axial kinetic energy of the electrons was determined by the ECD bias. The ECD bias is requested by the user in the Bruker software and defines the potential difference between the cathode and the effective potential in the center of the ICR cell. To simplify ECD operation and simulate typical operating conditions, no delay between ion and electron injection was used. For the electron energy dependent experiments, the electron irradiation time (referred to as "ECD Pulse Length" in the Apex software, but ECD duration in this manuscript) was kept constant at 40 ms and 20 ms for substance P and beta-endorphin, respectively. Electrons with axial kinetic energies of 0.7 eV were used for both peptides during the ECD duration experiments. The optimal substance P and beta-endorphin ECD spectra were acquired with electron energies and irradiation times of 0.7 eV, 40 ms and 1.2 eV, 16 ms, respectively. The HECD electron energy dependent experiments used electron irradiation times of 10 ms and 3 ms, for substance P and beta-endorphin, respectively. For all ECD experiments the ECD Lens was set to +15.0 V and a current of 1.5 A was supplied to the cathode heater. Ion detection in the Q-FTICR-MS was performed in broadband mode over the 92 to 2000 mass-to-charge range. Using 512 K data points resulted in a transient duration of 131.1 ms.

For the substance P electron kinetic energy and irradiation time dependence results, 10 spectra were summed at each parameter to give the final spectrum acquired at a given electron kinetic energy or irradiation time. Five beta-endorphin spectra were summed at each parameter during the electron kinetic energy and irradiation time dependence experiments. The optimized ECD spectra for substance P and beta-endorphin each represent the summation of 20 individual spectra.

ECD_{LIT} Instrumentation

Ions were accumulated in the first linear ion trap (referred to as the CID_{LIT}) for 100 ms before parent ions for ECD were isolated, then transferred to the ECD_{LIT}. For the results in this chapter the ECD_{LIT} trapping conditions used dc voltages of 29.0 V, 19.5 V, 28.0 V, and 30.0 V applied to the back trap plate (E wall), ECD offset (dc potential on the ECD_{LIT} rod set), front trap plate (I wall), and ion guide (Ion guide offset), respectively. Following ECD, the product ions are sent to the TOF for mass analysis.

The axial kinetic energy of the electrons can be determined by the potential difference between the ECD trap rods (ECD offset) and the tungsten filament (filament offset). The filament offset is the dc bias, relative to ground, applied to the tungsten filament. For the electron energy dependent experiments, the electron irradiation time (ECD duration) was kept constant at 50 ms and 13 ms for substance P and beta-endorphin, respectively. An electron energy of 1.2 eV was used for both peptides during the electron irradiation time dependent experiments. The optimal substance P and beta-endorphin ECD_{LIT} spectra were acquired with electron energies and irradiation times of 1.2 eV, 50 ms and 1.1 eV, 13 ms, respectively.

For the electron kinetic energy and irradiation time dependence experiments performed on the ECD_{LIT} instrument, 21 ECD_{LIT} fills were summed to generate the mass spectrum at each electron kinetic energy or irradiation time for both substance P and beta-endorphin. The optimal substance P and beta-endorphin ECD_{LIT} spectra were the summation of 420 ECD_{LIT} fills each.

4.3 Results and Discussion

4.3.1 *Measurement of electron kinetic energy on the Q-FTICR-MS and ECD_{LIT} instruments*

Before a direct comparison of ECD on the FTICR-MS and ECD_{LIT} instruments could be made, it was necessary to determine the actual axial electron kinetic energies used for each system. The

tungsten filament used in the ECD_{LIT} results in a narrow kinetic energy distribution due to the well-defined dc potential at its edge.[31] Consequently, the axial electron kinetic energy for the ECD_{LIT} system can be determined from the potential difference between the tungsten filament and the ECD_{LIT}. But first, this applied potential difference must be corrected for by the difference in work functions between the tungsten filament and stainless steel ECD_{LIT} rods, where the work function refers to the amount of energy needed to transfer an electron from the Fermi level into vacuum. It is necessary to consider the work functions for the filament and the ECD_{LIT} rods because the difference in surface potential between both components defines the electron kinetic energy. The difference in surface potential is determined by the difference in the Fermi levels of each solid, where the Fermi level refers to the highest occupied molecular orbital in the valence band. The work function for stainless steel is 4.4 eV[36], for thoriated tungsten it is 2.65 eV.[37] Thus, to negate the inherent potential difference between the stainless steel rods and the thoriated tungsten filament (i.e., electron kinetic energies begin at 0.0 eV), the difference in their work functions must be overcome by a potential difference applied between them. Therefore, the reported electron energy was found by adding 1.75 V (the difference in work functions) to the difference between the “ECD offset” and “filament offset.” By making this correction, absolute rather than relative, electron kinetic energies can be determined for the ECD_{LIT} instrument.

The FTICR-MS uses a hollow, indirectly heated dispenser cathode to generate electrons for ECD. This type of electron source is widely known to produce a broad distribution of electron kinetic energies.[33] In addition, under normal operating conditions it is possible for the electrons to be reflected by the ion transfer optics located on the source side of the ICR cell; this process has been called multiple-pass ECD.[25] Multiple-pass ECD introduces uncertainty to the measurement of actual electron axial kinetic energies on FTICR-MS instruments. It is proposed that when the reflected electrons re-enter the ICR cell, a portion of their axial kinetic energy is transferred to radial energy resulting in an increased number of low axial-kinetic energy electrons.[25] To obtain a reliable electron kinetic energy measurement associated with the ICR system it would be advantageous to avoid the multiple-pass ECD condition. Electron reflection brought about by the ion optics on the source side of the ICR cell can be prevented by connecting an external dc power supply to the last

element of the Einzel lens located before the magnet (FOCL2 shown in Figure 4.1A). In addition, applying a dc potential to FOCL2 through a current-measuring device allows the electron current extracted from the ECD cathode and passed through the ICR cell to be detected. By monitoring the current on FOCL2 and creating electron stopping curves at a requested ECD bias, the actual electron kinetic energy can be determined.[38, 39] A circuit was designed and constructed in-house to perform the electron energy measurements and is described in Appendix 9.2. In brief, two voltage

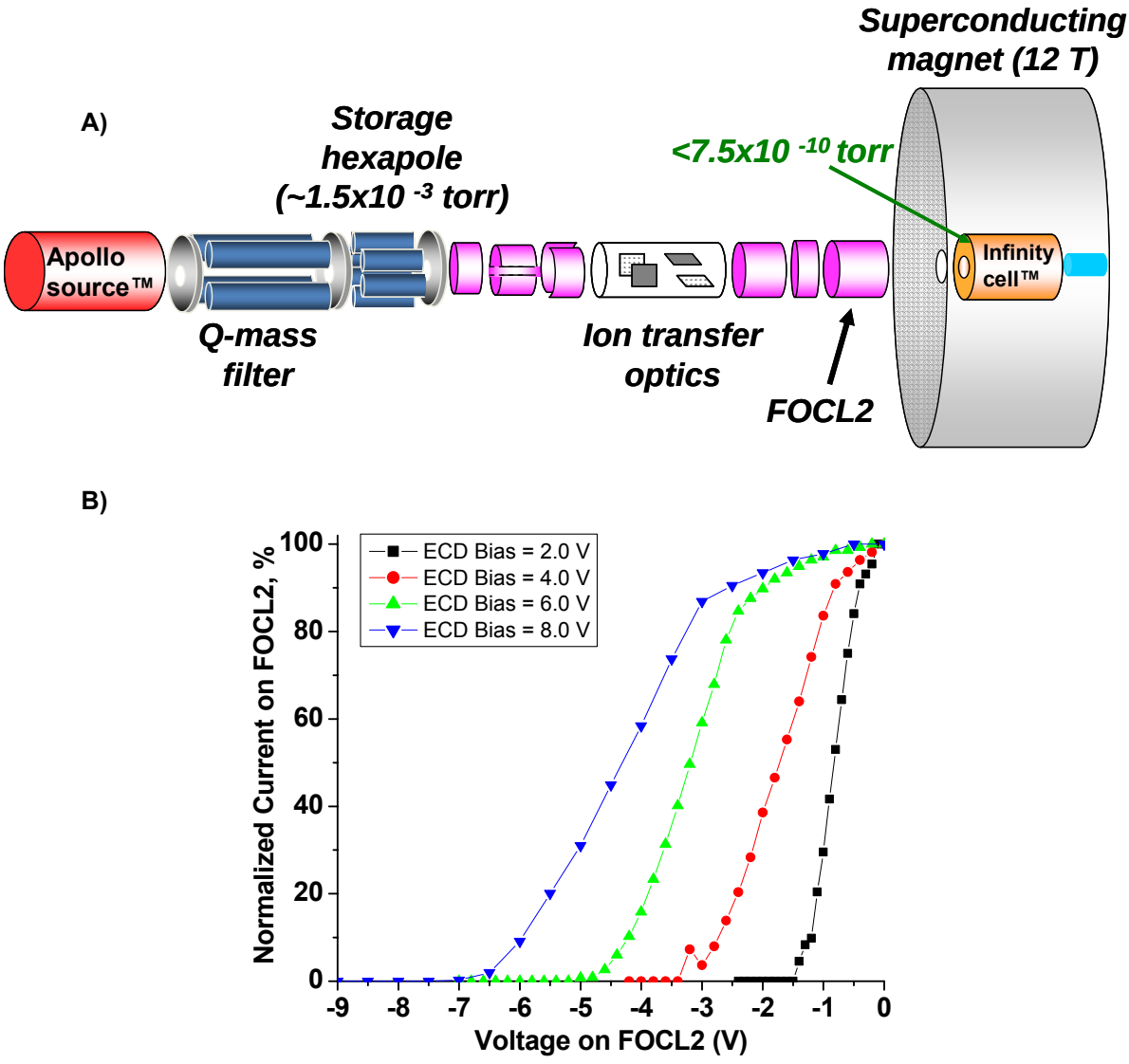

Figure 4.1. A) Q-FTICR-MS instrument diagram showing orientation of FOCL2 and the hollow dispenser cathode electron source. B) Electron stopping curves measured on lens element FOCL2 at different ECD biases. The ECD biases examined were 2.0 V (squares), 4.0 V (circles), 6.0 V (upward triangles), 8.0 V (downward triangles).

followers and a differentiator circuit are used to measure the voltage drop across a load resistor which converts the measured electron current on FOCL2 to a voltage equivalent that can be measured on a digital oscilloscope. At a requested ECD bias, dc voltages (starting at 0.0 V and proceeding to more negative values) were applied to FOCL2 and the voltage-equivalent currents were measured on the oscilloscope. For the electron energy measurements, relevant experimental parameters were held constant at values typically used for ECD: Sidekick = 4.0 V, Sidekick offset = -1.7 V, Excitation amplitude = -0.5 dB, Front/Back trap plates = 1.3/1.5 V, Analyzer entrance = -1.0 V, ECD lens = 15.0 V, cathode heater current = 1.5 A, and ECD duration = 50 ms.

Plotted in Figure 4.1B are the electron stopping curves measured on FOCL2 for four requested ECD biases using the circuit described in Appendix 9.2. For each ECD bias, the recorded currents are normalized to the current measured for that requested ECD bias when 0.0 V was applied to FOLC2. The distribution of kinetic energies at a given ECD bias for the data in Figure 4.1B can be found by taking the first derivative for each curve. The full width at half maximum (FWHM) values for the first derivatives (i.e., distribution of kinetic energies) were 0.8, 2.0, 1.8, and 3.0 V for ECD biases 2.0, 4.0, 6.0, and 8.0 V, respectively. The FWHM values show that as the requested electron energy increases, the width for the distributions of kinetic energies also increases. Evidence of this wider energy distribution can be seen in Figure 4.1B where more pronounced low-energy tails are seen for the larger ECD biases (e.g., 6.0 and 8.0 V). It can also be seen in Figure 4.1B that as the requested electron energy increases, fewer electrons have the proper energy for optimal electron capture (i.e., near thermal electrons). This observation is consistent with experimental results that demonstrate reduced ECD efficiency as the ECD bias is increased at a constant ECD duration.[39] Such a trend illustrates that the optimal bias for ECD on this instrument under the present conditions is ≤ 2.0 V. If larger ECD biases are used, only the electrons that comprise the low energy-tail would participate in the ECD reaction.[26]

The data in Figure 4.1B was used to establish a calibration curve for electron energy as a function of requested ECD bias on the FTICR-MS. For a given ECD bias, the electron kinetic energy is given by the mean of the first derivative of the curves in Figure 4.1B. The electron kinetic energy for ECD biases of 2.0, 4.0, 6.0, and 8.0 V were found to be 0.9, 1.8, 3.0, and 4.5 eV, respectively.

Determining the absolute (i.e., referenced to ground) electron kinetic energy on the FTICR-MS allowed a direct comparison to the absolute electron energies from the LIT/TOF instrument.

4.3.2 *Electron energy dependence*

Once the absolute electron kinetic energies on the ECD_{LIT} and FTICR-MS instruments could be directly compared, the effect of electron energy using a constant ECD duration was studied. The first analyte used for this work was the peptide substance P due to its common usage in the ECD community for instrument tuning and characterization as well as the simple dissociation pattern it produces (i.e., a c-series of product ions). The results of substance P ECD on both instruments as a function of electron energy are shown in Figure 4.2. Plotted in Figures 4.2A and 4.2C are the

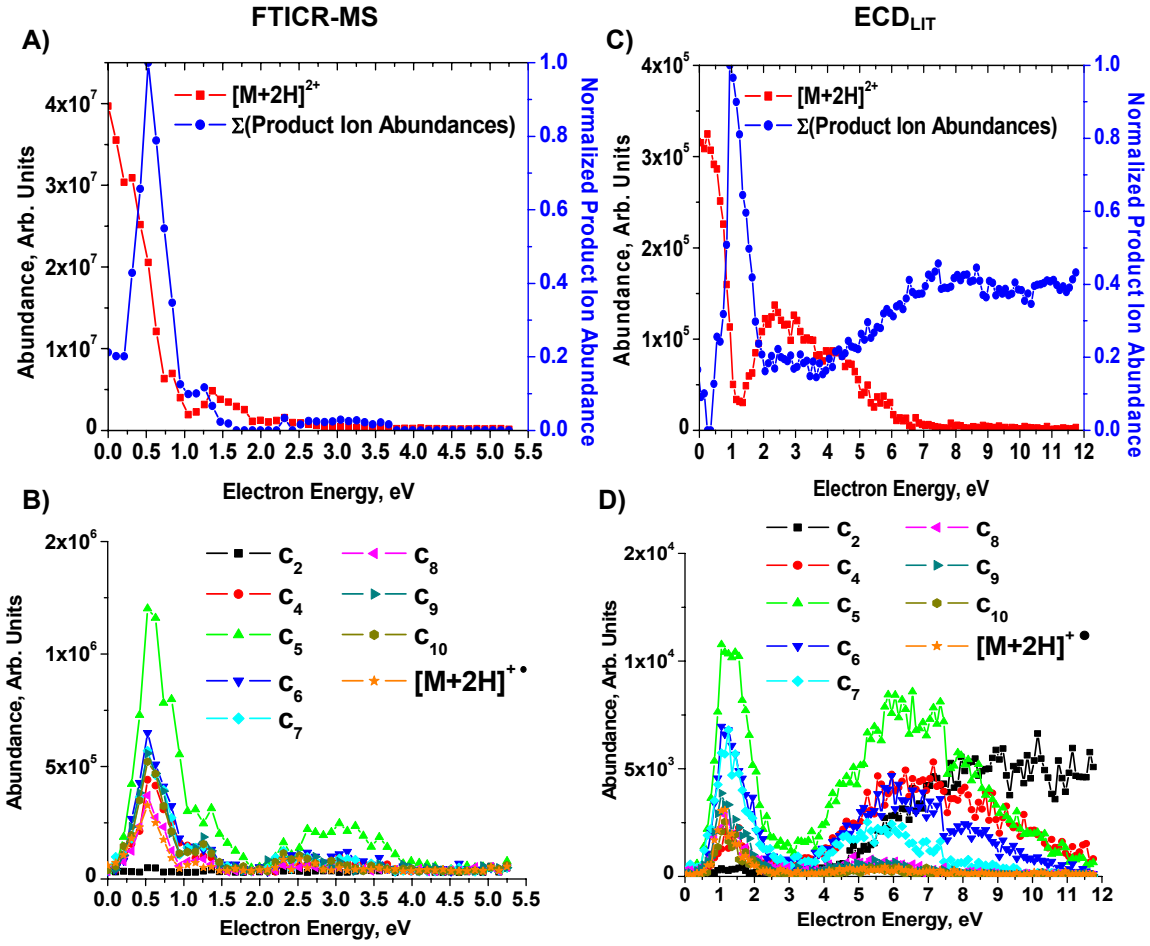

Figure 4.2. Electron energy dependence of ECD for **[M+2H]$^{2+}$** substance P. A) and B) Extracted ion currents for selected ions following ECD on the Q-FTICR-MS; ECD duration = 40 ms. C) and D) Extracted ion currents for selected ions following ECD on the ECD_{LIT}; ECD duration = 50 ms. Abscissa values refer to the kinetic energy of the electrons in the axial direction.

abundance of the **[M+2H]$^{2+}$** parent ion remaining after electron irradiation and the normalized total product ion abundance for all c-ions generated from ECD on the FTICR-MS and ECD$_{LIT}$ instruments, respectively. The observed maximum product ion abundance occurs at very similar axial electron kinetic energies on both instruments. However, at electron energies greater than 2.0 eV the product ion abundances for the ECD$_{LIT}$ increase and eventually plateau. This second region of increased product ion abundance observed on the ECD$_{LIT}$ is attributable to HECD and highlights a practical difference between the two instruments. Specifically, to achieve both the normal and HECD bands with the ECD$_{LIT}$ at a constant electron irradiation time only the electron energies must be varied. In contrast, to achieve HECD on the FTICR-MS instrument the electron irradiation time must be reduced. The trend of requiring shorter irradiation times to allow the use of greater electron energies when Sidekick^{TM} trapping is used is consistent with the literature.[39] However, it has been observed that gated trapping on FTICR-MS instruments increases the number of parent ions in the ICR cell and allows HECD to be achieved simply by changing the electron energy at a constant electron irradiation time.[39] But the use of gated trapping on FTICR-MS instruments is not a viable option when sample is limited or the time required for the requisite multiple ICR cell fills is unavailable.

The extracted ion currents for the c-product ions and the charge-reduced ion resulting from ECD are plotted as a function of electron energy for both instruments in Figures 4.2B and 4.2D. On the FTICR-MS instrument the product ions clearly show a local maximum with ~0.7 eV electrons as well as a small HECD band between 2.5 and 4.0 eV (Figure 4.2B). The electron energy needed to begin HECD in Figure 4.2 is in agreement with the literature but the range of electron kinetic energies over which it is observed is (i.e., 2.5 – 4.0 eV) is small, (see Figure 4 of Reference [4]). The ECD$_{LIT}$ instrument also shows a local product ion maximum with electron energies of 1.0 eV but there is a more prominent HECD band with electron energies between 3.0 – 12.0 eV (Figure 4.2D); this trend is consistent with previous results for this ECD$_{LIT}$ instrument.[31] Furthermore, the HECD band on the LIT is observed for the $\mathbf{c_2}$ and $\mathbf{c_4}$ – $\mathbf{c_7}$ ions while for the FTICR-MS only the $\mathbf{c_5}$ ion is observed. The observation of the $\mathbf{c_2}$ and $\mathbf{c_4}$ – $\mathbf{c_7}$ ions on the ECD$_{LIT}$ is indicative of more efficient ECD, as evidenced by the relative abundance of the product ions in the HECD band versus the low electron energy region, compared to the FTICR-MS at these higher electron energies.

A unique feature of the results in Figure 4.2D is the observation of the $\mathbf{c_2}$ ion on the ECD_{LIT}. Previous ECD experiments performed on this instrument have not revealed this product ion. The mass-to-charge ratio of $\mathbf{c_2}$ is 271.188, which is in the region where noise from electron ionization (EI) of background gases is observed; thus, control experiments were performed to verify the identity of the $\mathbf{c_2}$ ion. Specifically, with a spray potential of 0.0 V (i.e., no ions were being generated from nESI) the same ECD conditions used for Figure 4.2D were applied and no peak at *m/z* 271.188 was observed. Also, ions were generated with a spray potential of 1200 V but were directed away from the ECD_{LIT} by the quadrupole bender and again, no peak was observed at *m/z* 271.188. Therefore, the presence of $\mathbf{c_2}$ in Figure 4.2D is not an instrument artifact or background ion. The formation of a $\mathbf{c_2}$ ion from substance P signifies that every N-C_α carbon bond that could be broken by ECD has been dissociated; because cleavage N-terminal to proline is not possible with ECD due to the cyclic structure of its side chain.

Beta-endorphin was used to study the dependence of electron energy response on parent ion charge state. Under the ESI conditions described previously, beta-endorphin readily forms the $\mathbf{[M+5H]^{5+}}$ charge state (*m/z* 693.572), which was used as the parent ion for the axial electron kinetic energy study shown in Figure 4.3. The $\mathbf{[M+5H]^{5+}}$ ion produced results similar to those observed for the $\mathbf{[M+2H]^{2+}}$ ion of substance P (Figure 4.2). In Figure 4.3A, the FTICR-MS results show a low energy ECD region but no defined HECD band. Conversely, in Figure 4.3C the ECD_{LIT} data indicates the presence of the low energy and HECD bands with the total product ion abundance reaching a plateau at electron energies greater than 7.0 eV. The dissociation of beta-endorphin resulted in product ion maxima on both instruments at electron energies of ~ 0.7 – 1.2 eV, in agreement with the substance P results. Plotting the extracted ion currents for five selected product ions on the FTICR-MS in Figure 4.3B reveals an even less pronounced HECD band than was seen with substance P. Examining the same product ions for the LIT (Figure 4.3D), a clear HECD region is seen and the relative abundance of the $\mathbf{z_3}$ and $\mathbf{c_4}$ product ions remains large at axial electron energies greater than 8.0 eV. The $\mathbf{z_3}$ and $\mathbf{c_4}$ ion abundances are greater than the other product ions in Figure 4.3D over the entire range of electron energies examined. This trend is attributable to singly charged product ions having a smaller electron capture cross-section (σ) than multiply charged

product ions because the cross-section increases linearly with the square of the ion charge (z^2).[16] The difference between the ECD_{LIT} and FTICR-MS in abundance for different product ion charge states is more noticeable in the ECD_{LIT} due to the better ion-electron overlap than in the FTICR-MS. The same ECD dependence on electron kinetic energy seen in Figures 4.2 and 4.3 was also observed in both instruments using other multiply charged analytes (melittin (**[M+4H]**$^{4+}$, *m/z* 712.196) and ubiquitin (**[M+11H]**$^{11+}$, *m/z* 779.155)). Both melittin and ubiquitin showed the same effect of electron kinetic energy as beta-endorphin and displayed local maxima for ECD product ion abundance at electron kinetic energies of 1.0 – 1.5 eV. Thus, the effect of electron energy on ECD for both instruments (i.e., the electron energy that results in maximum product ion abundance and the

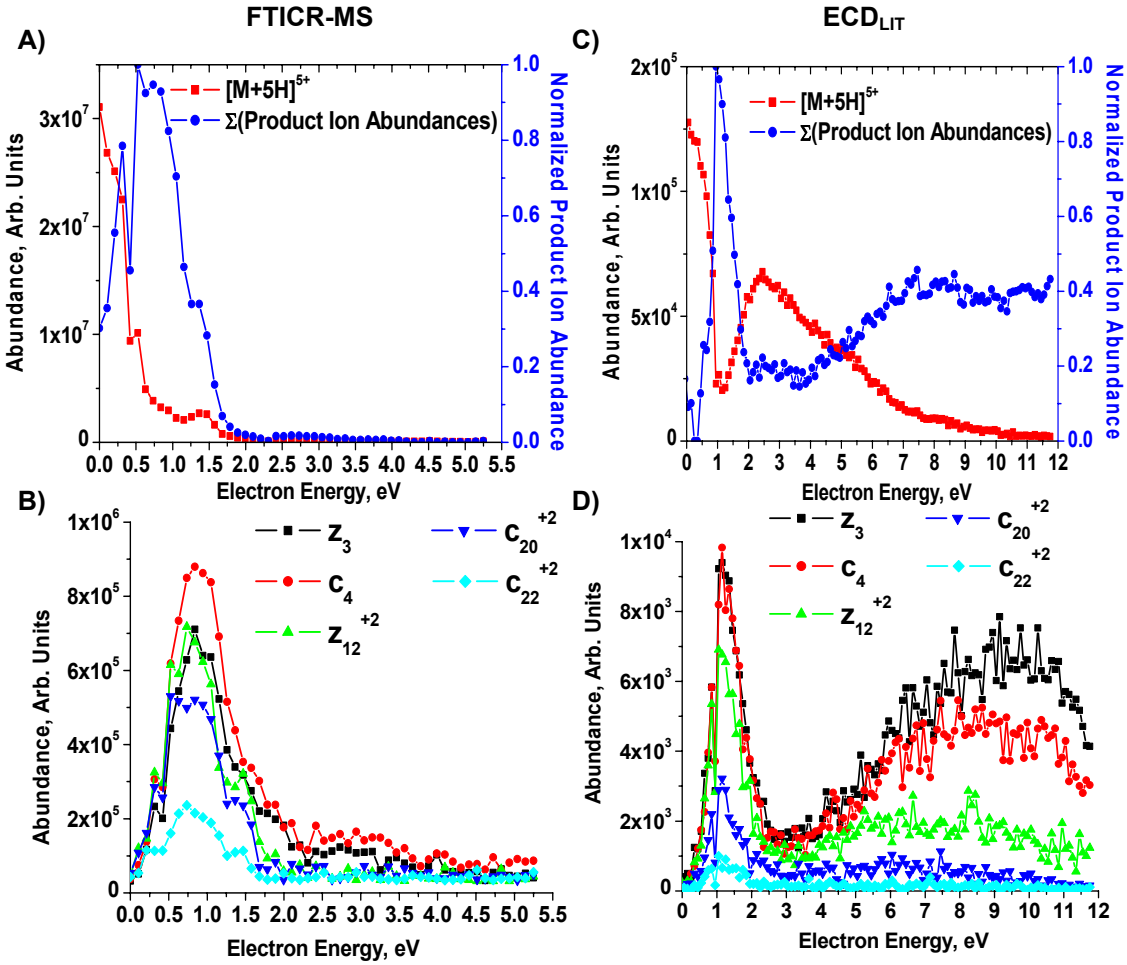

Figure 4.3 Electron energy dependence of ECD for **[M+5H]**$^{5+}$ beta-endorphin. A) and B) Extracted ion currents for selected ions following ECD on the Q-FTICR-MS; ECD duration = 20 ms. C) and D) Extracted ion currents for selected ions following ECD on the ECD_{LIT}; ECD duration = 13 ms. Abscissa values refer to the kinetic energy of the electrons in the axial direction.

presence or absence of a HECD band) is independent of parent ion charge state and amino acid sequence.

4.3.3 *Electron irradiation time dependence*

With the axial electron kinetic energy required for maximum ECD product ion abundance determined for both instruments, the next parameter to be optimized was the electron irradiation time (ECD duration). To do this, 0.7 eV and 1.2 eV electron kinetic energies were used for the FTICR-MS and ECD_{LIT} instruments, respectively as the ECD duration was varied from 2 to 100 ms. Substance P and beta-endorphin were again used as model analytes, and the results for substance P are shown in Figure 4.4. The FTICR-MS results in Figures 4.4A and 4.4B reveal that after ~ 30 ms of ECD

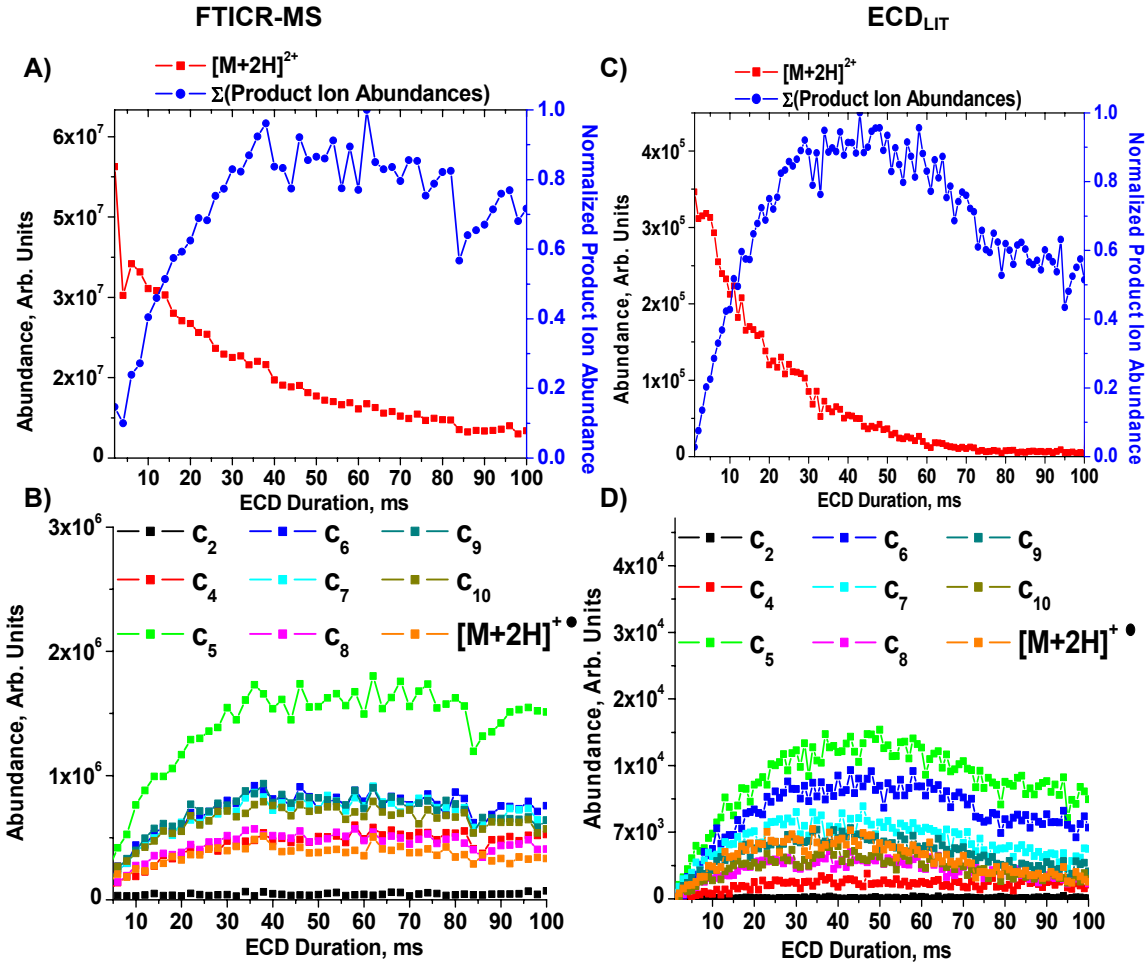

Figure 4.4. Electron irradiation (ECD duration) dependence of ECD for **[M+2H]$^{2+}$** substance P. A) and B) Extracted ion currents for selected ions following ECD on the Q-FTICR-MS. Electron kinetic energy = 0.7 eV C) and D) Extracted ion currents for selected ions following ECD on the ECD_{LIT}; Electron kinetic energy = 1.2 eV.

duration no further increase in product ion abundance is achieved despite a continued reduction in the parent ion abundance at longer irradiation times. This observation is attributable to the neutralization of primary product ions. The singly charged **c**-ions can capture another electron and become neutralized; but because of their reduced electron-capture cross section (recall σ is proportional to $(z)^2$) the c-ions have a slower rate of electron capture than the doubly charged parent ion. Consequently, the product ion abundance does not decrease as rapidly as the **$[M+2H]^{2+}$** parent ion resulting in an almost constant product ion abundance.

The ECD_{LIT} data in Figures 4.4C and 4.4D show that while the product ion abundance is also maximized by an ECD duration of ~ 30 ms, it is reduced (rather than reaching a plateau) at longer irradiation times (i.e., up to an ECD duration of 80 ms). The decrease in product ion abundance corresponds to irradiation times (i.e., 65 – 70 ms) where the parent ion (i.e., **$[M+2H]^{2+}$**) is no longer present. Similar to the FTICR-MS case, this trend can be explained by the neutralization of the singly-charged c-ion products. Because the electron current density in the LIT device is ~200 times greater than the FTICR-MS, the product ion neutralization is more pronounced in the ECD_{LIT}, as shown in Figures 4.4C and 4.4D.

Charge neutralization of product ions is considered a major limitation to ECD efficiency.[35] As the results from Figure 4.4 illustrate, choosing the appropriate electron irradiation time is important for achieving optimal ECD operation; especially for the ECD_{LIT}. Due to the aforementioned charge-state dependence of electron capture, the choice of irradiation time is even more critical for highly charged parent ions. This is demonstrated in Figure 4.5, where the effect of ECD duration for beta-endorphin (**$[M+5H]^{5+}$**) is studied for both instruments. For the FTICR-MS the extracted ion current of the residual parent ion in Figure 4.5A reaches baseline levels at ~ 50 ms (compared to ~ 90 ms for doubly charge substance P, Figure 4.4A). The product ion abundance reaches a maximum with an irradiation time of 10 ms and decreases, rather than reaching a plateau, at longer irradiation times. Examining the extracted ion currents for selected product ions in Figure 4.5B shows that the abundance of multiply-charged product ions decreases more rapidly than singly-charged ions as the ECD duration is increased. Because the electron capture cross section is smaller for the singly charged ions (i.e, $\mathbf{z_3}$ and $\mathbf{c_4}$) their abundance decreases less rapidly than the multiply charged product

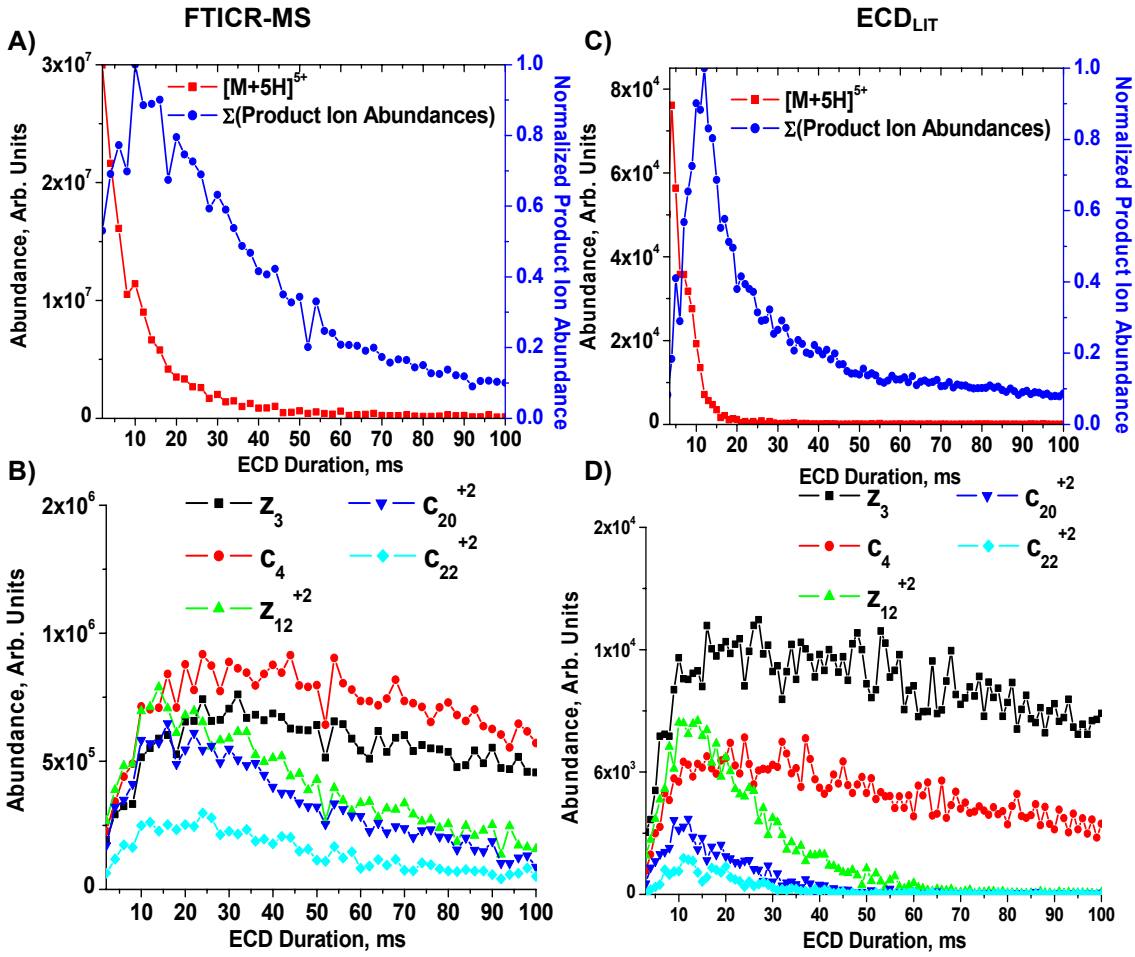

Figure 4.5. Electron irradiation (ECD duration) dependence of ECD for **[M+5H]$^{5+}$** beta-endorphin. A) and B) Extracted ion currents for selected ions following ECD on the Q-FTICR-MS. Electron kinetic energy = 0.7 eV C) and D) Extracted ion currents for selected ions following ECD on the ECD$_{LIT}$; Electron kinetic energy = 1.2 eV.

ions at longer irradiation times.

The ECD$_{LIT}$ data in Figures 4.5C and 4.5D illustrate the same general trend as the FTICR-MS, namely that as the parent ion charge state increases a shorter ECD duration is required to achieve maximum product ion abundance. However, the ECD$_{LIT}$ results show a more dramatic charge-state effect than the FTICR-MS. In Figure 4.5C, the residual parent ion abundance approaches zero at an irradiation time of 20 ms and the maximum product ion abundance occurs at ~ 12 ms; compared to 80 ms and 30 ms, respectively for doubly charge substance P on the ECD$_{LIT}$. This shift towards shorter ECD durations with higher charge state is related to the charge dependent electron capture relationship and is clearly shown in Figure 4.5D. Plotting the extracted ion currents for product ions of interest reveals that in the ECD$_{LIT}$ the abundance of multiply charged product ions approaches zero at

irradiation times much shorter than in the FTICR-MS. For the doubly charged ions shown in Figure 4.5D, their maximum abundances correspond with the total product ion abundance maximum (Figure 4.5C) at ~12 ms. The more pronounced effect of ion charge state for the ECD_{LIT} compared to the FTICR-MS is due to a higher flux of electrons in the ECD_{LIT}. Because the electron beam density is 200 times higher in the ECD_{LIT} than the FTICR-MS, over the same amount of time more electrons are produced to interact with ions in the ECD_{LIT}. As more ion-electron interactions occur, the trend for charge state-dependent electron capture cross section becomes more noticeable. While similar ECD results are observed on both the FTICR-MS and ECD_{LIT} instruments for shorter ECD durations, at longer times (i.e., greater than 50 ms for substance P and greater than 15 ms for beta-endorphin) the effect of the higher electron density of the ECD_{LIT} becomes noticeable.

Overall, the data in Figures 4.4 and 4.5 show that the ion-electron overlap in the ECD_{LIT} is greater than in the FTICR-MS as evidenced by the shorter ECD durations needed to neutralize the product ions. Also, the range of electron irradiation times suitable for performing ECD is narrower for the ECD_{LIT}; this is especially seen for more highly charged parent ions (e.g., **$[M+5H]^{5+}$** beta-endorphin, Figure 4.5A vs. 4.5C). Similar trends were observed using **$[M+4H]^{4+}$** melittin and were very pronounced with **$[M+11H]^{11+}$** ubiquitin where the parent ion abundance was reduced to baseline levels in ~ 7 ms of electron irradiation for the ECD_{LIT} while for the FTICR ~ 20 ms were required.

4.3.4 *ECD spectral comparisons*

The previous characterization allowed the electron energy and irradiation time that provided the highest ECD efficiencies for both the ECD_{LIT} and FTICR-MS to be determined. Using those parameters, the ECD spectra acquired under low-electron energy conditions for substance P and beta-endorphin were acquired for both instruments. The spectra were surprisingly similar despite the six orders of magnitude difference in background pressure between the high and ultra-high vacuum of the ECD_{LIT} and FTICR-MS instruments, respectively. The substance P ECD spectra for each instrument are shown in Figure 4.6; with the FTICR-MS data shown on top (Figure 4.6A) and the ECD_{LIT} results on the bottom (Figure 4.6B). It is immediately clear that the same c-series of product ions are seen on both instruments as well as the odd-electron, charge-reduced ion. The differences between the spectra are the presence of the **z_9** ion in the FTICR-MS and the relative abundances of

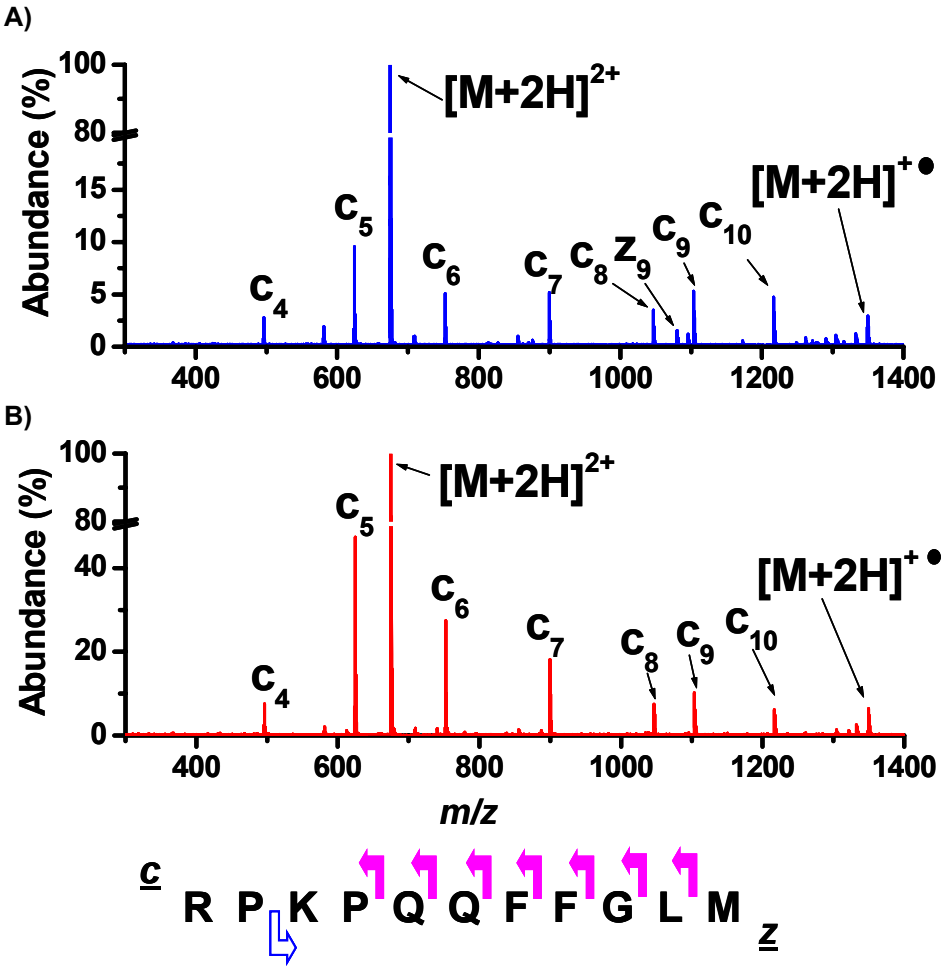

Figure 4.6. ECD spectral comparison of **$[M+2H]^{2+}$** substance P. A) Q-FTICR-MS spectrum; axial electron kinetic energy = 0.7 eV, ECD duration = 40 ms. B) ECD_{LIT} spectrum; axial electron kinetic energy = 1.2 eV, ECD duration = 50 ms.

the observed product ions on each instrument. The parent ion dissociation is summarized in the substance P sequence shown at the bottom of Figure 4.6. A solid arrow indicates a site of backbone cleavage observed on both instruments and the open arrow represents cleavage unique to only one instrument (where the FTICR-MS and ECD_{LIT} instruments are represented by blue and red arrows, respectively). For both instruments no cleavage from ECD is observed for the N-C_α bond N-terminal to proline. While the spectra shown in Figure 4.6 suggest that the MS/MS efficiency for the ECD_{LIT} is greater than that of the FTICR-MS, the relative abundances of the product ions are misleading. Fragmentation efficiencies for the ECD_{LIT} are typically higher than for the FTICR-MS; however, collection efficiencies can be worse, resulting in similar MS/MS efficiencies between the two

instruments. For example, the fragmentation, collection, MS/MS, and electron capture efficiencies (%) for the ECD_{LIT}/FTICR instruments for the data in Figure 4.6 are 53/25, 17/32, 9/8, and 92/76, respectively.

Conducting ECD on beta-endorphin with both instruments at their previously determined optimal electron energy and irradiation times resulted in the spectra displayed in Figure 4.7. Again, the FTICR-MS data is shown on top (Figure 4.7A) and the ECD_{LIT} results are on the bottom (Figure 4.7B). The spectra are remarkably similar, varying only in their relative product ion abundances. By plotting a region of the mass-to-charge axis that does not include the parent ion, the spectral similarities become very evident, as shown in both insets of Figure 4.7. The backbone cleavage is summarized on the beta-endorphin amino acid sequence shown in the bottom of the figure. Different charge states resulting from the same backbone cleavage were considered together (i.e., if $\mathbf{c_4^{+2}}$ and $\mathbf{c_4^{+3}}$ were both observed, only one arrow is used to represent cleavage after phenylalanine). Cleavage at every N-C_α bond was achieved on both instruments except for N-terminal to proline. The fragmentation, collection, MS/MS, and electron capture efficiencies (%) for the ECD_{LIT}/FTICR instruments for the data in Figure 4.7 are 93/61, 75/65, 70/40, and 95/75, respectively. Here the collection efficiency was greater for the ECD_{LIT} than the FTICR-MS which allows the MS/MS efficiency on the ECD_{LIT} to approach 70% compared to only 40% on the FTICR-MS. The collection efficiency is greater for the beta-endorphin ECD than for substance P due to the greater sensitivity of the MCP towards higher charge state ions. The comparison between the substance P and beta-endorphin MS/MS efficiencies highlights the advantage of performing ECD on parent ions of higher charge state. Because of the inherent charge neutralization, ECD is typically a less sensitive dissociation method than CID or IRMPD, especially for doubly charged parent ions.[22] Because mass spectrometry requires the analyte to have a charge to be detected, the loss of charge associated with ECD, but absent in CID or IRMPD, makes ECD a less sensitive technique. The parent ion of beta-endorphin for the ECD experiments was the $\mathbf{[M+5H]^{5+}}$ charge state. ECD conditions (i.e., electron energy and irradiation time) were chosen to favor the formation of first generation product ions and prevent excessive charge neutralization, therefore a significant amount of product ions in charge states greater than +2 should be present. Consequently, the reduction in

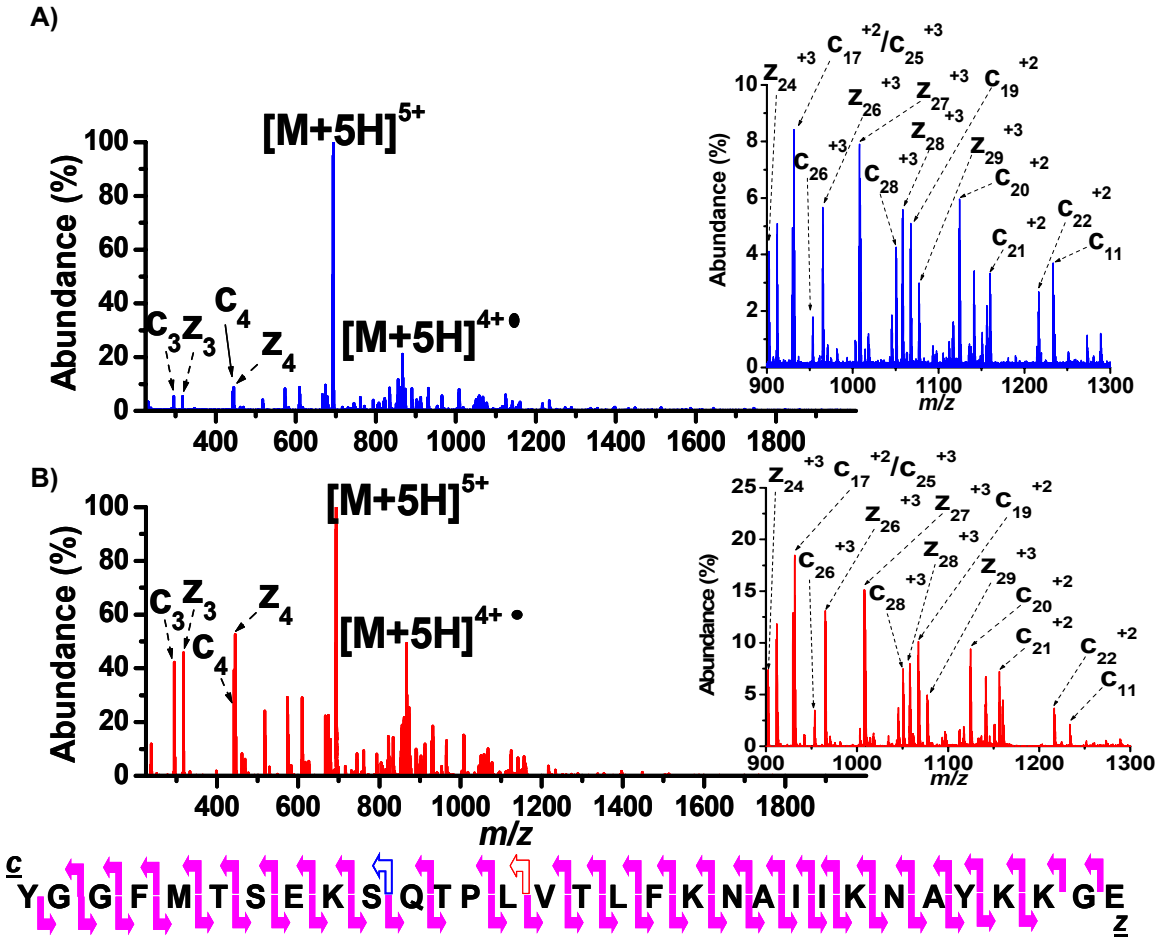

Figure 4.7. ECD spectral comparison of **[M+5H]$^{5+}$** beta-endorphin. A) Q-FTICR-MS spectrum; axial electron kinetic energy = 0.7 eV, ECD duration = 16 ms. Inset: *m/z* 900-1300 region. B) ECD_{LIT} spectrum; axial electron kinetic energy = 1.1 eV, ECD duration = 13 ms. Inset: *m/z* 900-1300 region.

signal due to loss of charge should be decreased for more highly charged parent ions. This results in better collection efficiencies and a concurrent increase in MS/MS efficiency, both of which were observed by changing analytes from the **[M+2H]$^{2+}$** ion of substance P to the **[M+5H]$^{5+}$** ion of beta-endorphin.

In general, the data in Figures 4.6 and 4.7 show that very similar ECD spectra can be acquired on both the ECD_{LIT} and FTICR-MS instruments when the optimal conditions are used for each. Very similar ECD spectra between the two instruments were also observed for **[M+4H]$^{4+}$** melittin and **[M+11H]$^{11+}$** ubiquitin. The results of performing ECD on all four analytes, which represent a range of molecular weights (M_r), number of amino acid residues, and charge state, are summarized in Table 4.1. Similar sequence coverage for each analyte was observed on both

instruments. Also, the electron capture cross-section increased linearly with the square of the analyte charge on both the ECD_{LIT} and the FTICR-MS, in agreement with reported cross-sections from FTICR ECD.[16] The electron capture cross sections reported in Table 4.1 were found by plotting the ln(**$[M+nH]^{n+}_{residual}$ / $[M+nH]^{n+}_{initial}$**) as a function of ECD duration. The slope of this plot is equal to [(σ * electron current)/(electron charge * electron beam area)], from which the electron capture cross-section can be determined from experimental data. For the FTICR-MS instrument, the area of the electron beam as it enters the ICR cell could not be measured directly but was taken to be 19 mm^2 based on a published value from the same Bruker instrument.[39] The electron capture cross-sections are similar for the ECD_{LIT} and FTICR-MS instruments. Therefore, whichever instrument reduces the parent ion abundance with shorter ECD durations would demonstrate better ion-electron overlap; results thus far suggest that this is the case for the ECD_{LIT} instrument.

Table 4.1. Comparison of ECD on the FTICR-MS and ECD_{LIT} instruments for different analytes representing a range of M_r, and number of amino acid residues (parent ion charge state is given in parantheses).
[a]Sequence Coverage = (# of N-C_α bonds cleaved / total # of N-C_α bonds)
[b]Slope of {$\ln(I/I_0)$ as f(ECD Duration)} = [σ * (e^- current)] / [e * (area of e^- beam)]

Analyte	M_r	# of Amino Acids	ECD_{LIT} Sequence Coverage[a]	FTICR-MS Sequence Coverage[a]	ECD_{LIT} Cross Section (σ, cm^2)[b]	FTICR-MS Cross Section (σ, cm^2)[b]
substance P	1347.7	11 (+2)	70	80	$1.70x10^{-13}$	$6.88x10^{-13}$
melittin	2844.8	26 (+4)	88	92	$7.10x10^{-13}$	$1.48x10^{-12}$
beta-endorphin	3462.8	31 (+5)	97	97	$9.97x10^{-13}$	$1.56X10^{-12}$
ubiquitin	8559.6	76 (+11)	79	81	$2.41x10^{-12}$	$4.00x10^{-12}$

4.3.5 *High energy ECD (HECD)*

It is worth reiterating that, despite the large (six orders of magnitude) difference in background pressure associated with the ECD_{LIT} and FTICR-MS instruments, the electron energies and irradiation times required for optimal ECD are very similar. However, as has been noted in Figures 4.2 and 4.3, the ability to perform HECD varies significantly between the instruments. HECD is realized on the ECD_{LIT} simply by changing the electron axial kinetic energy whereas on the FTICR-MS only a minimal HECD band is observed. This seems to be in contrast to the literature where FTICR HECD has been reported.[4, 23] As referenced when discussing Figure 4.2,

researchers have demonstrated the ability to realize ECD on FTICR instruments over an electron energy range of 0 – 50 eV.[39] In such a case, the number of parent ions had to be increased by using multiple ICR cell fills such that even under conditions of reduced electron capture enough product ions were formed to be detected. Conversely, these researchers found that under typical conditions (i.e., the same ones used for the data presented thus far in this chapter) where a single ICR cell fill is used, ECD was only observed with electron energies of 0 – 3 eV. This observation is in agreement with the experimental results presented in Figures 4.2 and 4.3 above. However, to ensure a fair comparison between the two instruments, it was necessary to attempt HECD under optimal conditions on the FTICR. Attempts at using multiple cell fills to achieve HECD proved unsuccessful. Another method has been reported in the literature that allows higher electron kinetic energies to be used and it involves shortening the electron irradiation times.[39] At a given ECD duration, the maximum fragmentation efficiency is obtained by balancing the electron capture cross-section with the electron flux. With low kinetic energy electrons, the electron capture cross-section is higher than under HECD conditions, but the electron flux is lower. At a given electron source (i.e., indirectly heated dispenser cathode) temperature, the flux is mainly set by the potential difference between the electron source and the ICR cell. As the kinetic energy of the electrons increases, a shorter ECD duration is needed to maintain a flux of electrons suitable for electron capture under the conditions of reduced electron capture cross-section characteristic of HECD.[39]

The FTICR-MS ECD results of varying the electron energies at a reduced ECD duration of 10 ms for **$[M+2H]^{2+}$** substance P (reduced from the previous 40 ms used for Figure 4.2A, B) are shown in Figure 4.8. The normalized total product ion abundance in Figure 4.8A shows a distinct HECD band between 3.5 and 5.0 eV. Plotting the extracted ion abundances in Figure 4.8B shows that all product ion abundances reach a local maximum that corresponds to the HECD region. This result agrees with the established trend that for a given ECD duration the maximum ECD efficiency is reached when the compromise between the electron capture cross section and electron flux is optimized.[39] As mentioned previously, for a given cathode temperature the electron flux is primarily established by the potential difference between the cathode and the potential at the center of the ICR cell.[39] The maximum product ion abundance for low energy ECD still occurred with 0.7 – 1.2 eV

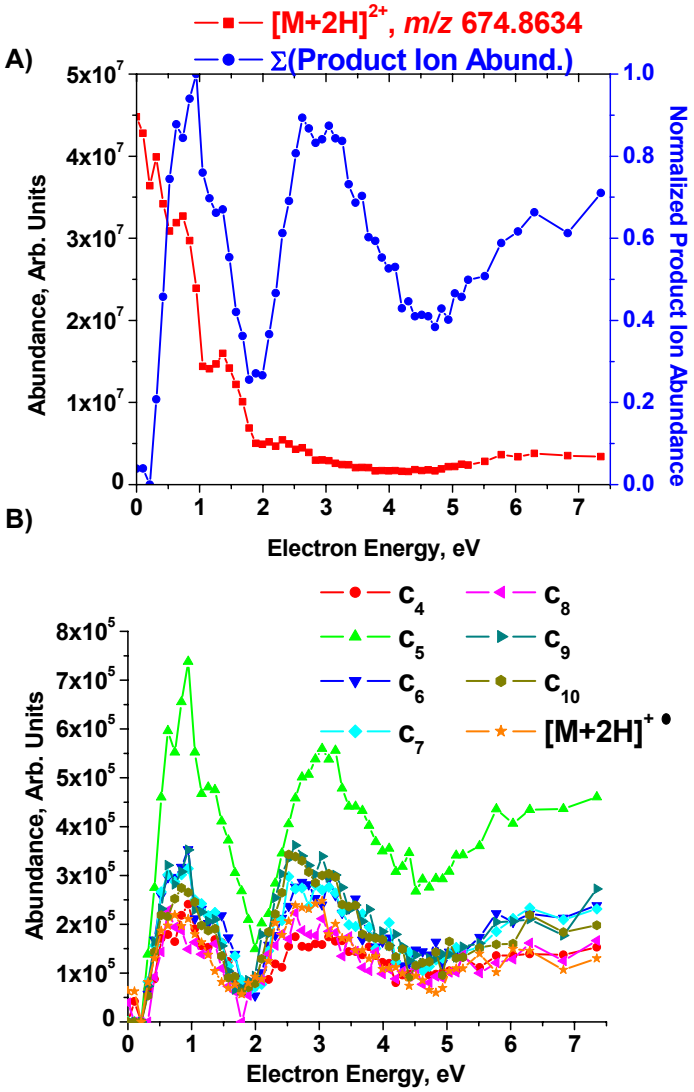

Figure 4.8. Electron energy dependence of HECD for **[M+2H]$^{2+}$** substance P on the Q-FTICR-MS. A) Extracted parent ion current and normalized total product ion abundance following HECD. B) Extracted ion currents for selected ions following HECD. ECD duration = 10 ms; abscissa values refer to the kinetic energy of the electrons in the axial direction.

electrons as shown in Figure 4.8B; this demonstrates that both ECD and HECD can be achieved on the FTICR-MS by varying only the electron energy if the appropriate electron flux is chosen. Under the conditions used to acquire the data in Figure 4.8, the fragmentation, collection, and MS/MS efficiencies for an electron kinetic energy of 0.7 eV were 6.2%, 65.6%, and 4.0%, respectively. Recall that the fragmentation, collection, and MS/MS efficiencies when ECD was performed at the longer ECD duration of 40 ms (i.e., Figure 4.6) were 25%, 32%, and 8%, respectively. The results indicate that while using shorter ECD durations allows both low energy ECD and HECD to be performed on the FTICR-MS, the ECD efficiency is better under the typical low energy ECD conditions (i.e., those used for Figure 4.6).

However, the substance P results of Figure 4.8 were the exception; for **[M+4H]$^{4+}$** melittin, **[M+5H]$^{5+}$** beta-endorphin, and **[M+11H]$^{11+}$** ubiquitin the results were quite different. For example, ECD as a function of electron energy for beta-endorphin at a reduced ECD duration of 3 ms (reduced from 20 ms in Figure 4.3) is shown in Figure 4.9. By reducing the ECD duration the parent ion was

able to be detected to higher electron energies while the normalized total product ion abundance showed only one maximum centered around 2.0 eV electrons. The extracted ion currents in Figure 4.9B clearly demonstrate that rather than discrete low and high energy ECD regions there is only one ECD band over the electron kinetic energy range shown. This distribution appears to represent a broadening of the low energy ECD region rather than the formation of a HECD band that merges with its low energy counterpart due to the absence of an abundance maximum at low (e.g., 0.7 eV) electron energies. The same trend was also observed for melittin and ubiquitin and became more apparent as the charge state of the parent ion increased. The broadening effect observed here has been observed by others as a result of increasing the number of parent ions able to participate in ECD.[39] However, the data in Figure 4.9 was acquired using the same number of ions as were used for the results in Figure 4.3. The electron kinetic energy that gave the most abundant product ions under the conditions used to acquire the data in Figure 4.9 was 2.0 eV, resulting in fragmentation, collection, and MS/MS efficiencies of 58%, 49%, and 29%, respectively. In Figure 4.3, an electron kinetic energy of 0.7 eV produced the highest product ion abundances, resulting in fragmentation, collection, and MS/MS efficiencies of 61%, 65%, and 40%,

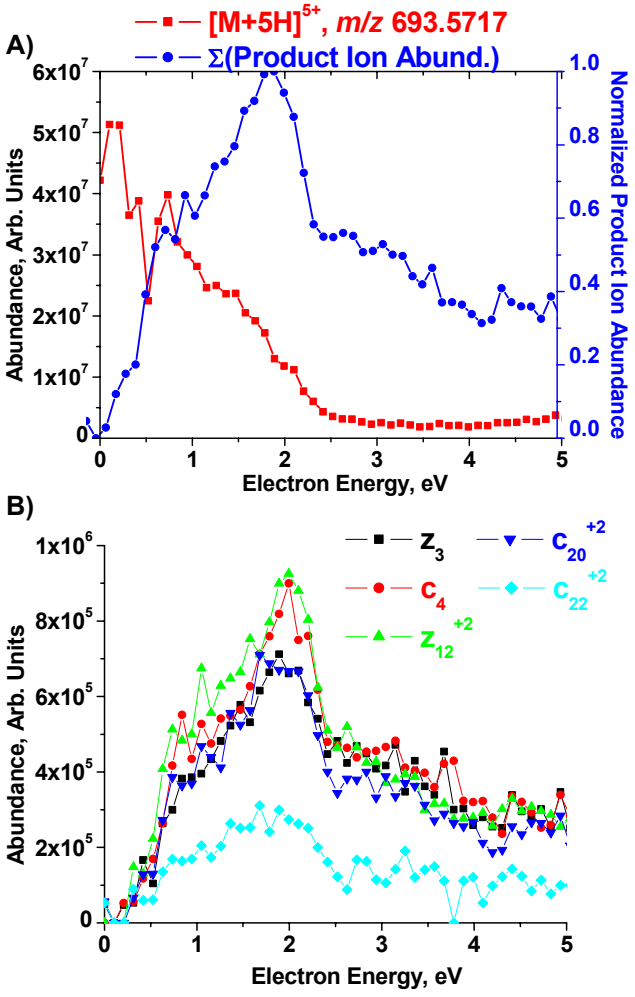

Figure 4.9. Electron energy dependence of HECD for **[M+5H]$^{5+}$** beta-endorphin on the Q-FTICR-MS. A) Extracted parent ion current and normalized total product ion abundance following HECD. B) Extracted ion currents for selected ions following HECD. ECD duration = 3 ms; abscissa values refer to the kinetic energy of the electrons in the axial direction.

respectively. Based on the efficiency values, the results from Figure 4.9 and 4.3 suggest that more efficient ECD is performed with lower energy electrons and longer ECD duration times, when the same number of parent ions are in the ICR cell.

The results from Figure 4.8 show that HECD can be achieved on the FTICR instrument under the appropriate set of conditions. Overall, it appears that on the FTICR-MS the ability to perform HECD comes at the cost of being able to do low-energy ECD, especially for higher charge state parent ions. More importantly, the results from Figures 4.8 and 4.9, when compared to the data in Figures 4.2 and 4.3, show that both low and high energy ECD can be achieved more readily with the ECD_{LIT} instrument without having to re-optimize the electron irradiation time.

4.3.6 *Multiple-pass ECD on the Q-FTICR-MS*

Typically the discrepancies between ECD_{LIT} and FTICR-MS ECD results have been attributed to the difference in parent ion internal energy in each system.[31] Specifically, it has been proposed that the higher pressures found in radio frequency ion trap instruments allow ion internal energy to be transferred to the helium bath gas through collisions; whereas such cooling does not occur at the lower pressures found in FTICR-MS. The effect of this cooling manifests itself in more extensive parent ion dissociation upon electron capture in FTICR-MS versus ECD_{LIT} instruments. However, the ECD spectra presented in this chapter are strikingly similar between the ECD_{LIT} and FTICR-MS instruments. This suggests that the parent ion internal energy in the ECD_{LIT} is comparable to that in the FTICR-MS. To test this hypothesis, the abundance of **c•** ions associated with $\mathbf{c_4'}$ – $\mathbf{c_6'}$ ions following ECD of substance P (free acid form) can be used to probe the internal energy of the parent ion.[25] It has been proposed that the formation of **c•** ions corresponds to ions with low internal energy that keeps the intermediate **[c'+z•]** complex intact. The formation of this intermediate structure allows H-atom transfer from a N-terminal fragment (**c'** ion) to a C-terminal ion (z• ion) resulting in the formation and detection of a **c•** ion. The **[c'+z•]** complex hypothesis has found support from published results which have shown that when the internal energy of the $\mathbf{[M+2H]^{2+}}$ substance P parent ion is increased by absorbing IR radiation, the **c•/c'** ratio decreases.[40] Shown in Figure 4.10 are the mass-to-charge regions around $\mathbf{c_4}$, $\mathbf{c_5}$, $\mathbf{c_6}$, and $\mathbf{c_7}$, respectively from the substance P ECD spectra from Figure 4.6. For both instruments **c•** ions are seen for $\mathbf{c_4}$ through $\mathbf{c_6}$,

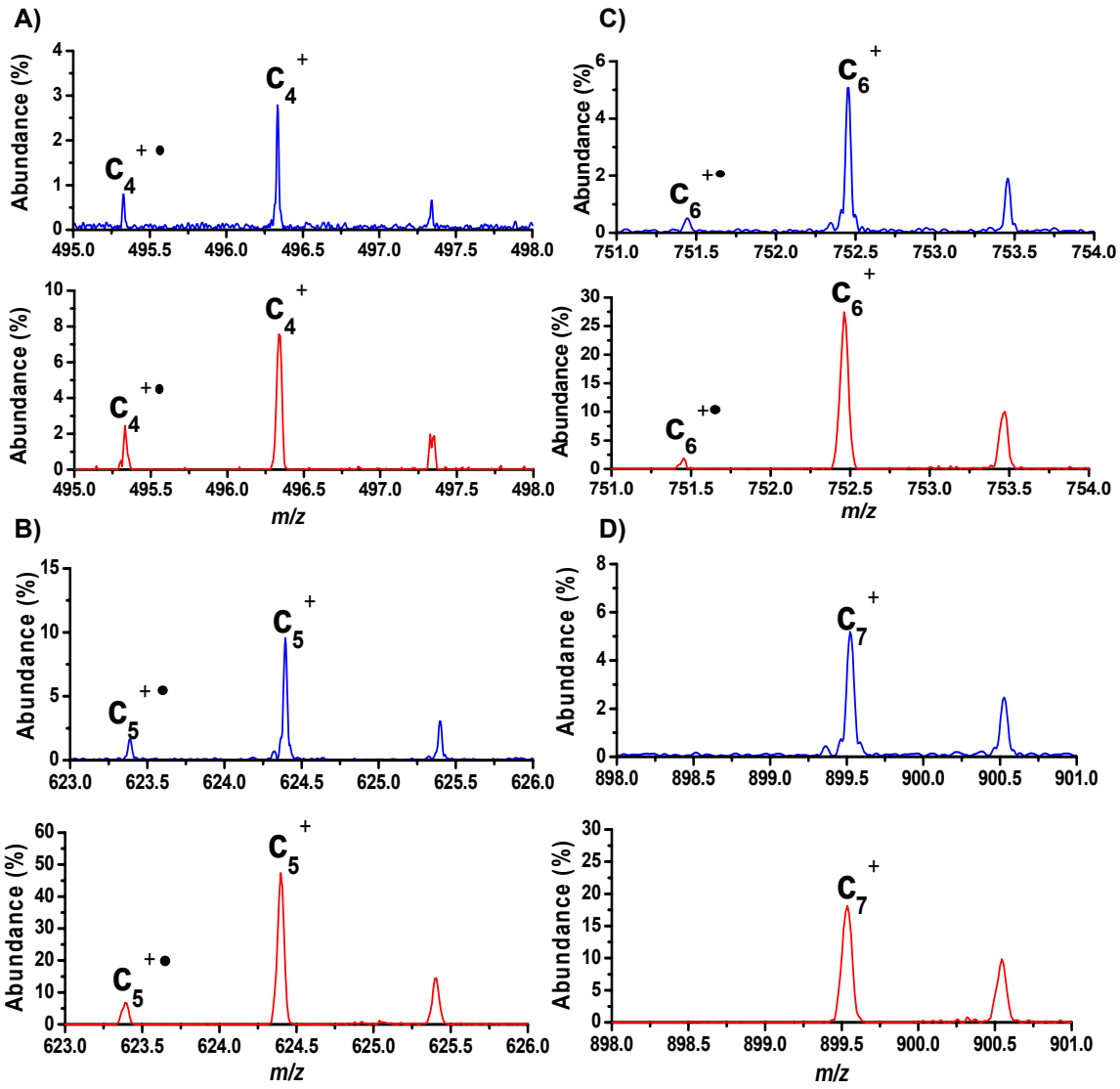

Figure 4.10. c'/c• comparison of substance P **[M+2H]**$^{2+}$ ECD A) $\mathbf{c_4}$ ion from Q-FTICR-MS (top) and ECD_{LIT} (bottom) spectra. B) $\mathbf{c_5}$ ion from FTICR-MS (top) and ECD_{LIT} (bottom) spectra. C) $\mathbf{c_6}$ ion from FTICR-MS (top) and ECD_{LIT} (bottom) spectra. D) $\mathbf{c_7}$ ion from FTICR-MS (top) and ECD_{LIT} (bottom) spectra. The spectra were generated from the data in Figure 4.6 (i.e., the FTICR-MS axial electron kinetic energy = 1.2 eV and ECD duration = 40 ms; for the ECD_{LIT} the axial electron kinetic energy = 1.2 eV and ECD duration = 50 ms).

while $\mathbf{c_7}$ shows no radical ion.

The similarities between the ECD spectra and the observation of **c•** ions for both instruments suggest that the ECD parent ions presumably have very similar internal energies in both the ECD_{LIT} and FTICR-MS. An explanation for the similar internal energy, despite the large difference in pressure and thus collisional cooling, involves the use of multipole ion accumulation in both

instruments. In the LIT/TOF instrument parent ions are accumulated and isolated in the CID_{LIT} before they are sent to the ECD_{LIT}. The CID_{LIT} is heated to ~120ºC, thus the parent ion internal energy may be increased through collisions with the heated bath gas. The parent ions, now with more internal energy, are sent to the ECD_{LIT} and irradiated with electrons. In the FTICR-MS system parent ions are accumulated in a collision hexapole (~$1.5x10^{-3}$ torr) which is at ambient temperature, uses argon as a bath gas, and is located external to the ICR cell. Though the external hexapole on the FTICR-MS instrument is not heated, any internal energy gained by the parent ions through collisions with the argon bath gas would not be removed in the ICR cell due to the ultrahigh vacuum conditions. The parent ion internal energies thus may be comparable in both systems, thereby explaining the similar ECD spectra acquired on both the FTICR-MS and ECD_{LIT} instruments. It has also been suggested that the temperature increase of the ECD_{LIT} itself, resulting from the tungsten filament operating at ~ 2000 ºC, could impart energy into the parent ion. However, increasing ion internal energy due to the filament seems unlikely because no difference in ECD spectra is observed as a function of time after turning the filament on.

Reports in the literature have also shown that at a given parent ion internal energy, maximal **c•** ion formation for substance P is observed at lower (e.g., 0.0 eV) electron kinetic energies.[25, 40] Published results have demonstrated that **c•** ions form from doing ECD on $\mathbf{[M+2H]^{2+}}$ substance P under multiple-pass ECD but not single pass ECD conditions on FTICR-MS instruments.[25] It is reasoned that as an electron makes multiple-passes through the magnetic fringe field, some of the electron's axial kinetic energy is transferred into a perpendicular component. It was acknowledged that the electron beam diameter may increase from the added perpendicular components, but that the increase would be insignificant compared to the beam dimensions overall.[25] The electrons relax to the axial center of the ICR cell as they lose some of their axial kinetic energy. As the number of electrons that relax to the axial center of the ICR cell increases, the local potential they generate aids in slowing down incoming electrons. The result is the creation of a significant portion of low energy electrons which are responsible for the formation of the **c•** ions.[25] All of the ECD data in this chapter taken on the FTICR-MS was acquired under multiple-pass ECD conditions. This was verified by observing the predicted **c•** ions for substance P and due to the fact that the dc potential applied to

FOCL2 was kept constant at -2.0 V during electron injection into the ICR cell. In the ECD_{LIT} system multiple-pass ECD is not possible due to the dc potentials placed on the axial trapping electrodes. Therefore, for the explanation that low energy electrons are required for **c•** ion formation to be accurate, a maximum in **c•** ion formation should be realized with low energy electrons. This trend is observed in Figure 4.11 where for the FTICR-MS (Figure 4.11A) and ECD_{LIT} (Figure 4.11B) the abundance of the $\mathbf{c_5'}$ and $\mathbf{c_5•}$ for each instrument is normalized to itself and plotted as a function of axial electron kinetic energy. The data shows that $\mathbf{c_5•}$ is only formed under low energy conditions in both instruments. Therefore, the results shown in Figure 4.11 support the idea that only those electrons with kinetic energies low enough to be reflected back into the ICR cell (i.e., less than ~1.5 eV) are suitable for c• formation in the FTICR-MS instrument. Also shown in Figure 4.11 is the ability of the ECD_{LIT} to generate enough low kinetic energy electrons under single-pass conditions to observe **c•** ions. The ability to observe **c•** ions under typical (i.e., single pass) settings with the ECD_{LIT}, is due to the 200-fold higher electron beam density it employs relative to the FTICR-MS instrument. The reason that only low kinetic energy electrons are required for **c•** formation is most likely due to these electrons imparting less energy into internal vibrational modes of the

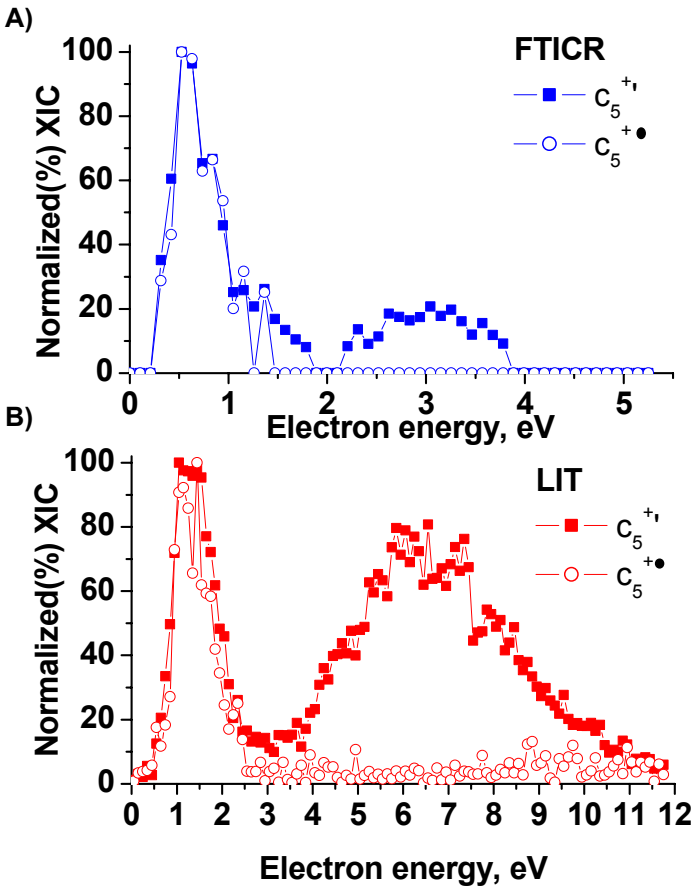

Figure 4.11. Axial electron kinetic energy dependence for the formation of the $\mathbf{c_5'}$ and $\mathbf{c_5•}$ ions from ECD of substance P $\mathbf{[M+2H]^{2+}}$. Plots are from the data in Figure 4.2. A) Q-FTICR-MS results; ECD duration = 40 ms. B) ECD_{LIT} results; ECD duration = 50 ms. Abscissa values refer to the kinetic energy of the electrons in the axial direction.

parent ion, compared to high kinetic energy electrons. Thus, a consistent explanation for the data in Figures 4.10 and 4.11 exists, namely that the amount of internal energy present in the parent ion dictates the **[c'+z•]** complex lifetime and extent of **c•** formation and that the parent ion internal energies in the ECD_{LIT} and FTICR-MS instruments are comparable.

4.4 Conclusions

The results presented in this chapter show that ECD results are consistent between the ECD_{LIT} and FTICR-MS instruments despite a six-order of magnitude difference in background pressure. Results suggest that the parent ion internal energy is comparable between the two instruments because the ECD spectra from both systems are similar. The comparable parent ion internal energies are presumably due to the use of multipole devices of similar pressure (~7.5×10^{-3} torr) for parent ion accumulation before ECD in both mass spectrometers. One noticeable difference between the ECD_{LIT} and FTICR-MS is the ease with which HECD can be performed. While HECD can be achieved on both instruments, the routine application of HECD is more straightforward using the ECD_{LIT}.

The generation of **c•** ions during the FTICR-MS ECD experiments indicate that the instrument is typically operated under conditions suitable for multiple-pass ECD. However, due to the 200-fold higher electron beam density in the ECD_{LIT} compared to the FTICR-MS, it is possible for the ECD_{LIT} to generate enough low axial kinetic energy electrons for efficient ECD under single-pass conditions. This conclusion is supported by the presence of **c•** ions for certain substance P product ions as well as very similar electron energy dependence results between multiple-pass ECD on the FTICR-MS and single pass ECD on the ECD_{LIT}.

4.5 References

1. Zubarev, R. A.; Kelleher, N. L.; McLafferty, F. W. Electron Capture Dissociation of Multiply Charged Protein Cations. A Nonergodic Process. *Journal of the American Chemical Society*. **1998**, 120, p. 3265-3266.

2. Kruger, N. A.; Zubarev, R. A.; Horn, D. M.; McLafferty, F. W. Electron Capture Dissociation of Multiply Charged Peptide Cations. *International Journal of Mass Spectrometry*. **1999**, 185/186/187, p. 787-793.

3. Kruger, N. A.; Zubarev, R. A.; Carpenter, B. K.; Kelleher, N. L.; Horn, D. M.; McLafferty, F. W. Electron Capture Versus Energetic Dissociation of Protein Ions. *International Journal of Mass Spectrometry*. **1999**, 1999, p. 1-5.

4. Zubarev, R. A.; Haselmann, K. F.; Budnik, B.; Kjeldsen, F.; Jensen, F. Towards an Understanding of the Mechanism of Electron-Capture Dissociation: A Historical Perspective and Modern Ideas. *European Journal of Mass Spectrometry*. **2002**, 8, p. 337-349.

5. Leymarie, N.; Costello, C. E.; O'Connor, P. B. Electron Capture Dissociation Initiates a Free Radical Reaction Cascade. *Journal of the American Chemical Society*. **2003**, 125, p. 8949 - 8958.

6. Syrstad, E. A.; Turecek, F. Toward a General Mechanism of Electron Capture Dissociation. *Journal of the American Society for Mass Spectrometry*. **2005**, 16, p. 208-224.

7. Holm, A. I. S.; Hvelplund, P.; Kadhane, U.; Larsen, M. K.; Liu, B.; Nielsen, S. B.; Panja, S.; Pedersen, J. M.; Skrydstrup, T.; Stochkel, K.; Williams, E. R.; Worm, E. S. On the Mechanism of Electron-Capture-Induced Dissocaition of Peptide Dications from 15N-Labeling and Crown-Ether Complexation. *The Journal of Physical Chemistry A*. **2007**, 111, p. 9641-9643.

8. Jones, J. W.; Sasaki, T.; Goodlett, D. R.; Turecek, F. Electron Capture in Spin-Trap Capped Peptides. An Experimental Example of Ergodic Dissociation in Peptide Cation-Radicals. *Journal of the American Society for Mass Spectrometry*. **2007**, 18, p. 432-444.

9. Laskin, J.; Futrell, J. H.; Chu, I. K. Is Dissociation of Peptide Radical Cations an Ergodic Process? *Journal of the American Chemical Society*. **2007**, 129, p. 9598-9599.

10. Chamot-Rooke, J.; Malosse, C.; Frison, G.; Turecek, F. Electron Capture in Charge-Tagged Peptides. Evidence for the Role of Excited Electronic States. *Journal of the American Society for Mass Spectrometry*. **2007**, 18, p. 2146-2161.

11. Bakhtiar, R.; Guan, Z. Electron Capture Dissociation Mass Spectrometry in Characterization of Post-Translational Modifications. *Biochemical and Biophysical Research Communications*. **2005**, 334, p. 1 - 8.

12. Shi, S. D. H.; Hemling, M. E.; Carr, S. A.; Horn, D. M.; Lindh, I.; McLafferty, F. W. Phosphopeptide/Phosphoprotein Mapping by Electron Capture Dissociation Mass Spectrometry. *Analytical Chemistry*. **2001**, 73, p. 19 - 22.

13. Håkansson, K.; Cooper, H. J.; Emmett, M. R.; Costello, C. E.; Marshall, A. G.; Nilsson, C. L. Electron Capture Dissociation and Infrared Multiphoton Dissociation MS/MS of an N-Glycosylated Tryptic Peptide to Yield Complementary Sequence Information. *Analytical Chemistry*. **2001**, 73, p. 4530 - 4536.

14. Adamson, J. T.; Håkansson, K. Infrared Multiphoton Dissociation and Electron Capture Dissociation of High-Mannose Type Glycopeptides. *Journal of Proteome Research*. **2006**, 5, p. 493 - 501.

15. Chamot-Rooke, J.; van der Rest, G.; Dalleu, A.; Bay, S.; Lemoine, J. The Combination of Electron Capture Dissociation and Fixed Charge Derivatization Increases Sequence Coverage for O-Glycosylated and O-Phosphorylated Peptides. *Journal of the American Society for Mass Spectrometry*. **2007**, 18, p. 1405-1413.

16. Zubarev, R. A.; Horn, D. M.; Fridriksson, E. K.; Kelleher, N. L.; Kruger, N. A.; Lewis, M. A.; Carpenter, B. K.; McLafferty, F. W. Electron Capture Dissociation for Stuctural Characterization of Multiply Charged Protein Cations. *Analytical Chemistry*. **2000**, 72, p. 563-573.

17. Fung, Y. M. E.; Liu, H.; Chan, T. W. D. Electron Capture Dissociation of Peptides Metalated with Alkaline-Earth Metal Ions. *Journal of the American Society for Mass Spectrometry*. **2006**, 17, p. 757 - 771.

18. Savitski, M. M.; Nielsen, M. L.; Zubarev, R. A. Side-Chain Losses in Electron Capture Dissociation to Improve Peptide Identification. *Analytical Chemistry*. **2007**, 79, p. 2296-2302.

19. Håkansson, K.; Hudgins, R. R.; Marshall, A. G. Electron Capture Dissociation and Infrared Multiphoton Dissociation of Oligodeoxynucleotide Dications. *Journal of the American Society for Mass Spectrometry*. **2003**, 14, p. 23-41.

20. Adamson, J.T.;K. Håkansson; Electron Capture Dissociation of Oligosaccharides Ionized with Alkali, Alkaline Earth, and Transition Metals. *Analytical Chemistry*. **2007**, 79, p. 2901 - 2910.

21. Zubarev, R. A.; Zubarev, R. A.; Savitski, M. M. Electron Capture/Transfer versus Collisionally Activated/Induced Dissociation: Solo or Duet? *Journal of the American Society for Mass Spectrometry*. **2008**, 19, p. 753 - 761.

22. Zubarev, R. A. Electron-Capture Dissociation Tandem Mass Spectrometry. *Current Opinion in Biotechnology*. **2004**, 15, p. 12 - 16.

23. Cooper, H. J.; Håkansson, K.; Marshall, A. G. The Role of Electron Capture Dissociation in Biomolecular Analysis. *Mass Spectrometry Reviews*. **2005**, 24, p. 201 - 222.

24. Bakhtiar, R.; Guan, Z. Electron Capture Dissociation Mass Spectrometry in Characterization of Peptides and Proteins. *Biotechnology Letters*. **2006**, 28, p. 1047-1059.

25. Tsybin, Y. O.; Quinn, J. P.; Tsybin, O. Y.; Hendrickson, C. L.; Marshall, A. G. Electron Capture Dissociation Implementation Progress in Fourier Transform Ion Cyclotron Resonance Mass Spectrometry. *Journal of the American Society for Mass Spectrometry*. **2008**, 19, p. 762 - 771.

26. Zubarev, R. A., Reactions of Polypeptide Ions with Electrons in the Gas Phase. *Mass Spectrometry Reviews*. **2003**, 22, p. 57 - 77.

27. Vachet, R. W.; Clark, S. D.; Glish, G. L. in *Proceedings of the 43rd ASMS Conference on Mass Spectrometry and Allied Topics*. 1995.

28. Baba, T.; Hashimoto, Y.; Hasegawa, H.; Hirabayashi, A.; Waki, I. Electron Capture Dissociation in a Radio Frequency Ion Trap. *Analytical Chemistry*. **2004**, 76, p. 4263-4266.

29. Silivra, O. A.; Kjeldsen, F.; Ivonin, I. A.; Zubarev, R. A. Electron Capture Dissociation of Polypeptides in a Three-Dimensional Quadrupole Ion Trap: Implementation and First Results. *Journal of the American Society for Mass Spectrometry*. **2005**, 16, p. 22 - 27.

30. Ding, L.; Brancia, F. L. Electron Capture Dissociation in a Digital Ion Trap Mass Spectrometer. *Analytical Chemistry*. **2006**, 78, p. 1995-2000.

31. Satake, H.; Hasegawa, H.; Hirabayashi, A.; Hashimoto, Y.; Baba, T. Fast Multiple Electron Capture Dissociation in a Linear Radio Frequency Quadrupole Ion Trap. *Analytical Chemistry*. **2007**, 79, p. 8755-8761.

32. March, R. E.; Todd, J. F. J. *Quadrupole Ion Trap Mass Spectrometry*. Second ed. Chemical Analysis (A series of monographs on analytical chemistry and its applications), ed. J.D. Winefordner. Vol. 165. 2005, Hoboken, N. J.: John Wiley & Sons, Inc. 35.

33. Tsybin, Y. O.; Hakansson, P.; Budnik, B.; Haselmann, K.; Kjeldsen, F.; Gorshkov, M.; Zubarev, R. A. Improved Low-Energy Electron Injection Systems for High Rate Electron Capture Dissociation in Fourier Transform Ion Cyclotron Resonance Mass Spectrometry. *Rapid Communications in Mass Spectrometry*. **2001**, 15, p. 1849-1854.

34. Amster, I.J. Fourier Transform Mass Spectrometry. *Journal of Mass Spectrometry*. **1996**, 31, p. 1325-1337.

35. Tsybin, Y. O.; Hendrickson, C. L.; Beu, S. C.; Marshall, A. G. Impact of Ion Magnetron Motion on Elecron Capture Dissociation Fourier Transform Ion Cyclotron Resonance Mass Spectrometry. *International Journal of Mass Spectrometry*. **2006**, 255-256, p. 144-149.

36. http://www.pulsedpower.net/WorkFunctions.htm.

37. http://other.nrl.navy.mil/CREBWorkShop/Shih.pdf.

38. Polfer, N. C.; Haselmann, K.; Zubarev, R. A.; Langridge-Smith, P. R. R. Electron Capture Dissociation of Polypeptides using a 3 Tesla FTICRMS. *Rapid Communications in Mass Spectrometry*. **2002**, 16, p. 936-943.

39. Tsybin, Y. O.; Witt, M.; Baykut, G.; Hakansson, K. Electron Capture Dissociation Fourier Transform Ion Cyclotron Resonance Mass Spectrometry in the Electron Energy Range 0-50 eV. *Rapid Communications in Mass Spectrometry*. **2004**, 18, p. 1607-1613.

40. Tsybin, Y. O.; He, H.; Emmett, M. R.; Hendrickson, C. L.; Marshall, A. G. Ion Activation in Electron Capture Dissociation to Distinguish between N-Terminal and C-Terminal Product Ions. *Analytical Chemistry*. **2007**, 79, p. 7596-7602.

Chapter 5

Simultaneous Electron Capture Dissociation and Collision Induced Dissociation (ECD+CID)

5.1 Introduction

5.1.1 *Utility of activated ion(AI)-ECD for improved sequence coverage*

Electron capture dissociation (ECD) has become an important tool for tandem mass spectrometry (MS/MS) analyses.[1-3] Since 2004, it has become possible to interact electrons with multiply charged cations in mass spectrometers other than Fourier transform ion cyclotron resonance (FTICR-MS) instruments.[4-11]. Recently a practicable hybrid linear ion trap (LIT) time-of-flight (TOF) mass spectrometer where ECD is performed in a LIT (ECD_{LIT}) has been developed.[12] However, the MS/MS efficiency (i.e, the percentage of isolated parent ion converted to and detected as product ions) for doubly charged substance P on the ECD_{LIT} is still only 9%[13]. This efficiency measurement is in agreement with literature reports of ECD performed on FTICR-MS instruments where the conversion efficiency of parent ions to product ions is between 5 and 30%.[14] Activated ion ECD (AI-ECD) has been used to improve the extent of dissociation observed with respect to performing ECD alone.[15-22] Often supplemental activation is required in ECD to help disrupt non-covalent, intramolecular interactions[15] by increasing the amount of parent ion internal energy.[23] Because most ECD experiments to-date have been performed under the ultra-high vacuum conditions of FTICR-MS, infrared (IR) radiation has been the ion activation method of choice because it does not require the addition of a neutral collision gas or a surface to increase the ion internal energy.[24] IR radiation is more convenient to use in FTICR-MS than collisional activation because the latter requires a bath gas to be introduced into the ICR cell which must be pumped away prior to mass analysis.[24, 25]

Due to the constant 1.5×10^{-3} torr helium bath gas pressure present in the ECD_{LIT}, collision

induced dissociation (CID) is readily achievable in the LIT device. Thus, in the ECD_{LIT}, a parent can be resonantly excited which causes some of the kinetic energy gained by the ion during resonance excitation to be converted into internal, vibrational energy of the molecule resulting in dissociation of the parent ion. In the case of ECD, the parent to resonantly excite during CID would be the first charge-reduced species, $\mathbf{[M+nH]^{(n-1)+\bullet}}$.

By using CID to simultaneously aid ECD in the $ECD_{LIT,}$ a unique form of AI-ECD can be implemented. The ability to resonantly excite an ion to increase its kinetic energy allows the charge-reduced species ($\mathbf{[M+nH]^{(n-1)+\bullet}}$) to be activated via CID at the same time the parent ion ($\mathbf{[M+nH]^{n+}}$) is being irradiated with electrons for ECD. This process of simultaneously applying ECD and CID will be referred to as ECD+CID. Rather than activating the parent ion prior to or after irradiating it with electrons, the electron capture product is being activated as it is being formed. The ability to activate the charge-reduced species during ECD in the ECD_{LIT} makes it possible to improve the extent of parent ion dissociation, and thus peptide sequence coverage, compared to performing ECD alone.

5.1.2 *Difficulty associated with ECD product ion ambiguity*

Due to the rate of electron capture in the ECD_{LIT}, performing ECD on multiply charged parent ions results in multiple electron capture events under typical operating conditions. When a parent ion ($\mathbf{[M+nH]^{n+}}$) captures a low kinetic energy electron the charge-reduced species is formed ($\mathbf{[M+nH]^{(n-1)+\bullet}}$) which then dissociates into product ions. A significant percentage of this charge-reduced species does not dissociate following the first electron capture. If the charge state of the initial, even-electron parent ion is greater than two, the charge-reduced peak will be multiply charged; therefore if a second electron is captured the $\mathbf{[M+nH]^{(n-2)+}}$ species would form. In the case where the parent ion was doubly charged, the charge-reduced species resulting from electron capture would be singly charged ($\mathbf{[M+2H]^{+\bullet}}$). If a second electron is captured by $\mathbf{[M+2H]^{+\bullet}}$, all of the charge would be neutralized and thus undetectable by mass spectrometry.

With successive non-dissociative electron capture events, the charge is decreasing but the number of hydrogens remains constant. With each electron capture, a proton is being neutralized, resulting in the intact species containing one more hydrogen than if that same charge state would

have been formed directly from electrospray ionization (ESI). When the charge-reduced species containing additional hydrogens dissociates, the product ions would be observed at mass-to-charge ratios that differ from their theoretical values making spectral interpretation and sample identification complicated. The ambiguity in ECD product ion identification due to multiple electron capture events has been observed on the ECD_{LIT} instrument.[12]

ECD+CID can be used to reduce the occurrence of non-dissociative electron capture in the ECD_{LIT}. In Scheme 1, EC_1 and EC_2 represent first and second electron capture (but no dissociation) events and D_1 and D_2 indicate the dissociation channels that could follow each electron capture during ECD. If the parent ion ($\mathbf{[M+nH]^{n+}}$) were to capture one electron but not undergo dissociation, it would form the odd-electron, charge-reduced capture product ($\mathbf{[M+nH]^{(n-1)+\bullet}}$). The $\mathbf{[M+nH]^{(n-1)+\bullet}}$ ion could then capture a second electron to form $\mathbf{[M+nH]^{(n-2)+}}$ (EC_2), and so on. If the $\mathbf{[M+nH]^{(n-1)+\bullet}}$ ion undergoes dissociation to form product ions via the D_1 channel, product ions corresponding to typical ECD experiments would be observed. However, product ions formed from the D_2 pathway could contain neutralized protons. Product ions that contain neutralized protons would result in mass-to-charge ratios corresponding to the presence of additional hydrogen(s). Under conditions where the EC_1D_1 pathway is favored, the EC_2, and consequently the D_2, pathways would be disfavored. In ECD+CID (denoted by dashed line in Scheme 1) the charge-reduced ion ($\mathbf{[M+nH]^{(n-1)+\bullet}}$) is resonantly excited and dissociated at the same time the parent ion ($\mathbf{[M+nH]^{n+}}$) is being irradiated with low energy electrons. As a result, EC_1D_1 becomes the dominant reaction pathway over EC_2 and any subsequent processes, e.g. EC_2D_2, EC_x.

Scheme 1

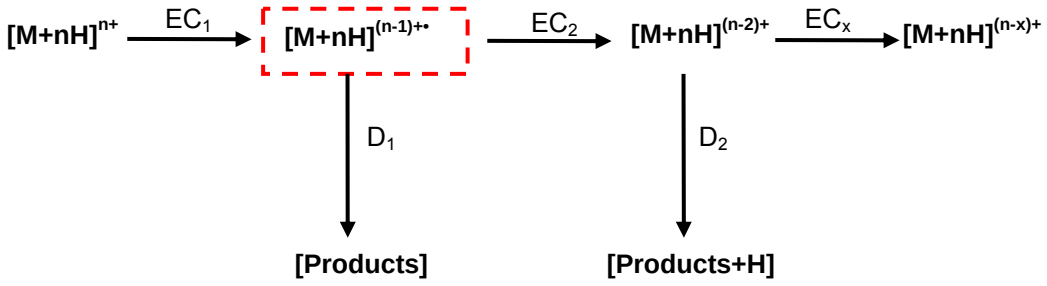

5.1.3 *Implementation of ECD+CID in the ECD_{LIT}*

In this chapter, the effect of simultaneously performing CID on the charge-reduced parent ion

during ECD (i.e., ECD+CID) to improve peptide sequence coverage over performing ECD alone is demonstrated using **[M+4H]$^{4+}$** melittin. In addition, the ability of ECD+CID to prevent multiple electron capture events in the ECD_{LIT} instrument and to aid in *de novo* peptide sequencing is presented. The effects of the combined electrodynamic and static magnetic fields on ion motion in the ECD_{LIT} are also discussed.

5.2 Experimental

5.2.1 *Samples*

The peptide melittin (GIGAVLKVLTTGLPALISWIKRKRQQ-NH_2; M_r: 2846.46) was purchased from Sigma-Aldrich, Inc. (St. Louis, MO) and used without further purification. An ESI peptide solution was made to a concentration of 5 μM in 50:50 v% methanol/water. Acetic acid (1% by volume) was added to the final sample mixture to aid in the electrospray process.

5.2.2 *ECD_{LIT} instrumentation and experimental parameters*

Mass spectrometry experiments were performed on a NanoFrontier LIT-TOF (Hitachi High Technologies).[12] Ions were generated using nanoelectrospray ionization (nESI). The basic operation of this mass spectrometer has been described in Chapter 1 and previously in the literature.[12] For the ECD+CID experiments, the ECD_{LIT} was modified so a supplemental ac waveform can be applied to one pair of the ECD_{LIT} quadrupole rod set. The supplemental ac waveform allows an ion of interest to be resonantly excited and thus undergo activation through collisions with the 7.5×10^{-4} torr of helium bath gas present in the ECD_{LIT}.

Two different ECD+CID experiments were performed. For the first experiment, ECD+CID was used to improve the extent of dissociation over that achieved using ECD alone. For ECD alone, melittin **[M+4H]$^{4+}$** was irradiated for 10 ms with 1.2 eV electrons. During this experiment an electron current of 0.33 μA was measured on the rods of the quadrupole ion guide located on the source side of the ECD_{LIT}.[12] For ECD+CID, melittin **[M+4H]$^{4+}$** was irradiated for 190 ms with 1.2 eV electrons while **[M+4H]$^{3+\bullet}$** (*m/z* 949.595, V_{rf} = 221 $V_{0\text{-}p}$) was resonantly excited with a 400 $mV_{0\text{-}p}$ supplemental ac waveform. During the ECD+CID an electron current of 0.33 μA was measured.

For the second experiment, ECD+CID was used to reduce the extent of non-dissociative electron capture during ECD in the ECD_{LIT}. For this experiment the instrumental parameters were

varied until the ECD and ECD+CID experiments displayed similar mass spectra. During ECD alone, melittin **[M+4H]$^{4+}$** was irradiated for 7.0 ms with 1.0 eV electrons. The measured electron current during this experiment was 0.85 μA. Under ECD+CID conditions, **[M+4H]$^{4+}$** was irradiated for 80 ms with 1.2 eV electrons while **[M+4H]$^{3+\bullet}$** (*m/z* 949.595, V_{rf} = 221 $V_{0\text{-}p}$) was resonantly excited with a 300 $mV_{0\text{-}p}$ supplemental ac waveform. The electron current measured during ECD+CID was 0.80 μA.

5.2.3 *Effect of the magnetic field on ion motion in the ECD_{LIT}*

In ECD+CID experiments, the parent ion **[M+nH]$^{n+}$** is irradiated with electrons while the odd-electron, charge-reduced ion, **[M+nH]$^{(n-1)+\bullet}$**, is simultaneously in resonance with a supplemental ac waveform of a sufficient amplitude to perform CID. To determine the resonance conditions for the supplemental ac waveform of a specific mass-to-charge ratio, the combination of the electrodynamic and static magnetic fields present in the ECD_{LIT} must be considered. By virtue of the magnetic field, there are two resonance frequencies for each mass-to-charge ratio as described by Equation 5.1:

$$\omega = \omega_q \pm \omega_c \quad \text{(Equation 5.1)}$$

where, ω is the observed frequency of radial motion for a given ion and ω_q and ω_c are the ion's secular and cyclotron frequencies, respectively. ω_q can be expressed in terms of experimental parameters following the procedure outlined by Douglas et. al.[26] The voltages applied to the ECD_{LIT} rods create the quadrupolar potential, φ(x,y,t):

$$\varphi(x, y, t) = \frac{(x^2 - y^2)}{r_0^2}(U - V_{rf}\cos\Omega t) \quad \text{(Equation 5.2).}$$

In Equation 5.2, x and y refer to the radial dimensions of the LIT; r_0 is the radius of the inscribed circle of the rod array; V_{rf} is the zero-to-peak amplitude of the drive rf voltage applied to the LIT, U is the dc potential applied to the LIT rod set which is typically 0 V, and Ω is the angular frequency of V_{rf}, at time t. From Equation 5.2 it can be shown that if U = 0 V, ω_q can be expressed as:

$$\omega_q \approx \frac{4\,z\,e\,V_{rf}}{2\sqrt{2}\,m\,\Omega\,r_0^2} \quad \text{(Equation 5.3).}$$

Independently, the effect of the magnetic field on the ion motion is described by the cyclotron equation:[27]

$$\omega_c = \frac{z\,e\,B}{m} \quad \text{(Equation 5.4).}$$

In Equation 5.4, B is the magnetic field strength present in the ECD_{LIT} in units of Tesla. Substituting Equations 5.3 and 5.4 into Equation 5.1 and solving for *m/z* results in:

$$\frac{m}{z} = \frac{\sqrt{2}\,e\,V_{rf}}{\Omega\,r_0^2\,\omega_0} \pm \frac{e\,B}{\omega_0} \quad \text{(Equation 5.5).}$$

where ω_0 is the frequency of the applied supplemental dipolar waveform. From Equation 5.5 it can be seen that for a constant set of experimental parameters (i.e., B, Ω, ω_0, and r_0), the zero-to-peak drive rf voltage amplitude (V_{rf}) can be scanned to find either or both resonance points associated with a supplemental dipolar waveform. Therefore, prior to performing each ECD+CID experiment the resonance points of the CID parent ion (e.g., **$[M+nH]^{(n-1)+\bullet}$**) were determined by holding all other variables constant (B = 150 mT, Ω = 467.3 kHz, ω_0 = 47.2 kHz, r_0 = 6.0 mm) and changing V_{rf} until the ion of interest is brought into resonance with the supplemental waveform.

5.3 Results and Discussion

5.3.1 *Determination of an ion's secular frequency resonance points*

The process of varying the drive rf amplitude to determine an ion's resonance points is demonstrated for the **$[M+4H]^{4+}$** charge state of melittin in Figure 5.1. The extracted ion current for **$[M+4H]^{4+}$** (*m/z* 712.196) is plotted as a function of V_{rf} in Figure 5.1A. Two resonance points were observed corresponding to V_{rf} values of 133 and 141 $V_{0\text{-}p}$, respectively. The reduction in **$[M+4H]^{4+}$** abundance at V_{rf} 133 and 141 $V_{0\text{-}p}$ is indicative of CID occurring, as evidenced by the detection of product ions at the resonance points. As V_{rf} is varied the parent ion is brought into resonance with the supplemental ac waveform. A supplemental ac waveform amplitude of 700 $mV_{0\text{-}p}$ was sufficient to cause dissociation. The difference between being on- and off-resonance with the supplemental ac waveform is demonstrated by the mass spectra in Figure 5.1B where the top (*) spectrum corresponds to the off-resonance condition indicated in Figure 5.1A. No dissociation is observed when the parent ion is not in resonance with the supplemental waveform. Conversely, the bottom (**) spectrum in Figure 5.1B was acquired when the parent ion was resonant with the supplemental ac waveform as indicated in Figure 5.1A. In such a case, the **$[M+4H]^{4+}$** parent ion is activated through

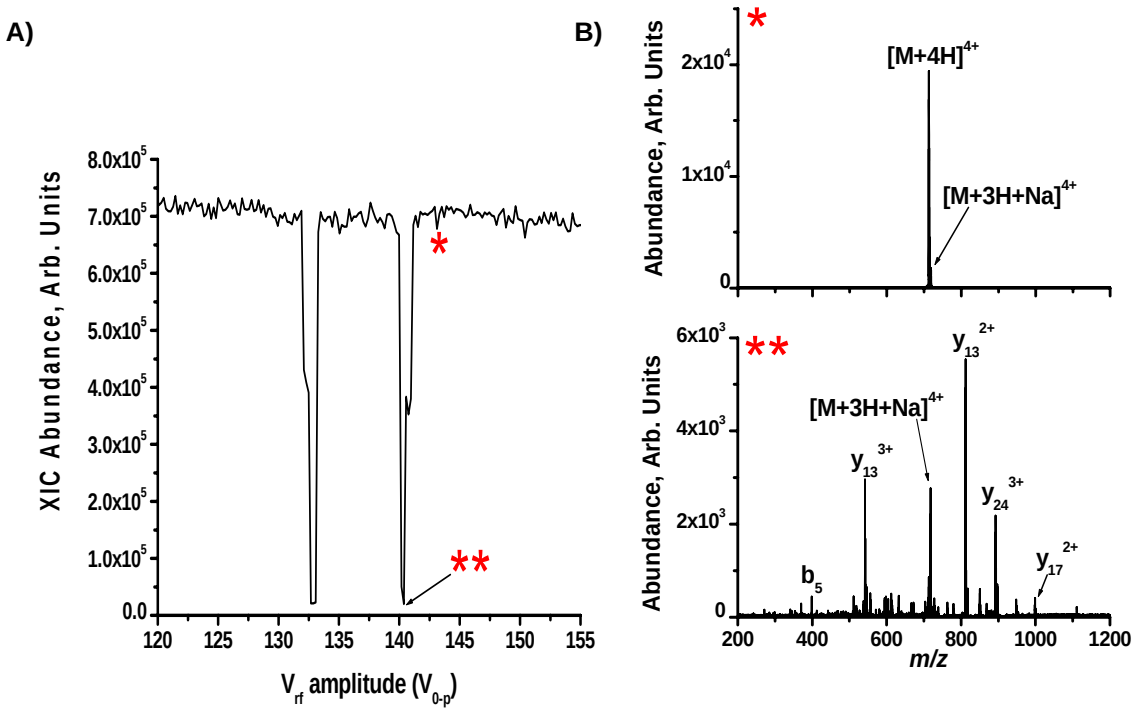

Figure 5.1 Determination of an ion's secular frequency resonance points due to the combined magnetic and electrodynamic fields in the ECD_{LIT}. A) Extracted ion current for **[M+4H]$^{4+}$** melittin (m/z 712.638) as a function of rf amplitude ($V_{0\text{-}p}$). Two resonance points are observed (at 133 and 141 $V_{0\text{-}p}$). B) Mass spectra acquired when the **[M+4H]$^{4+}$** parent ion was off- (*, top spectrum) and on- (**, bottom spectrum) resonance.

collisions with the helium bath gas and dissociates into product ions. The CID spectra acquired at both resonance points (i.e. V_{rf} = 133 and 141 $V_{0\text{-}p}$) were the same suggesting that the choice of which resonance point to use is not critical.

5.3.2 *ECD+CID for improved sequence coverage*

The use of ion activation with ECD does improve parent ion dissociation.[15, 17, 28] The ECD_{LIT} is capable of using CID for parent ion activation during the electron irradiation portion of an ECD experiment. In Figure 5.2, the benefit of using ECD+CID (top spectrum) to improve the extent of peptide dissociation compared to performing ECD alone (bottom spectrum) is demonstrated. When ECD is performed by itself under typical conditions, the most abundant product ion is the charge-reduced species (e.g., **[M+4H]$^{3+\bullet}$**). The dissociation of the **[M+4H]$^{3+\bullet}$** results in the formation of product ions in ECD. When the **[M+4H]$^{3+\bullet}$** ion remains intact, as shown in the bottom spectrum of Figure 5.2, a small amount of product ions are formed. In ECD+CID the dissociation of the **[M+4H]$^{3+\bullet}$**

ion is induced through collisional activation, thereby improving the peptide sequence coverage. The amino acid sequence of melittin given in the bottom of Figure 5.2 indicates the sites of backbone cleavage. A solid arrow represents cleavage observed under both ECD+CID and ECD alone conditions; a diagonally striped arrow indicates cleavage only observed in ECD alone; an open arrow represents cleavage from ECD+CID only. All charge states of a product ion associated with the same

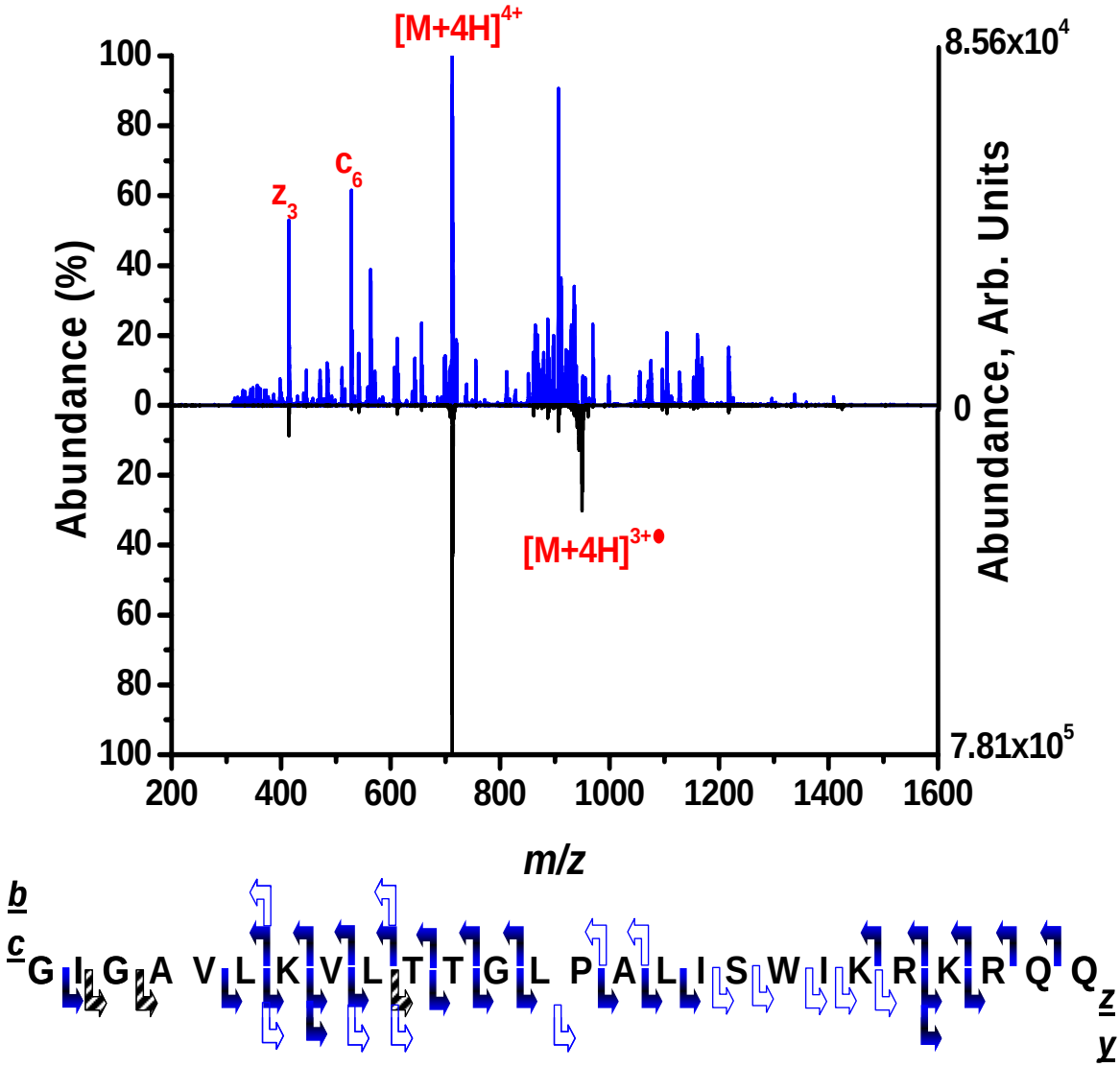

Figure 5.2 ECD+CID for improved peptide sequence coverage. ECD+CID spectrum (top) and ECD spectrum (bottom) of **[M+4H]$^{4+}$** of melittin. The amino acid sequence for melittin indicates sites of backbone cleavage. Solid arrows indicate product ions (**c** or **z**) that were observed in both dissociation experiments. Striped arrows represent backbone cleavages unique to the ECD alone experiment while the empty arrow indicates cleavage exclusive to the ECD+CID experiment.

N-C_α bond cleavage are represented by one arrow. The backbone cleavage results indicate that the sequence coverage achieved under ECD+CID was 88% compared to only 76% with ECD alone.

The ability to excite only the **$[M+4H]^{3+\bullet}$** ion during the ECD+CID experiment, rather than all first generation product ions, ensures that additional product ions gained from the CID event come from the charge-reduced species. As shown in Figure 5.2, examples of both amide and N-C_α bond cleavage unique to ECD+CID were observed. However, the only amide bond dissociation that contributed to the improved sequence coverage with ECD+CID was with the amide bond cleavage N-terminal to proline to generate the **y_{13}^{2+}** ion. Unlike ECD, with CID the amide bond N-terminal to proline is preferentially cleaved, which allows ECD+CID to provide complementary information to ECD alone. The additional product ions from amide cleavages (i.e., **b** / **y** ions) formed from ECD+CID does complicate the spectrum compared to when only ECD-related product ions (i.e., **c** / **z** ions) are observed. However, with ECD+CID the dominant dissociation pathway is still N-C_α bond cleavage, as seen in Figure 5.2. By identifying the c-series and z-series product ions based on the mass differences of the twenty common amino acids, **b**-ions can be differentiated from **c**-ions because of their 17.027 Da mass difference and **y**-ions can be identified from **c**-ions based on their 16.019 Da mass difference.[29]

The data in Figure 5.3 verifies that only the **$[M+4H]^{3+\bullet}$** ion was resonantly excited. The theoretical isotopic distribution and monoisotopic mass-to-charge value for the even electron **$[M+3H]^{3+}$** species when it is formed directly from ESI is given in Figure 5.3A. Under ECD+CID conditions, Figure 5.3B, the isotopomers associated with the odd-electron, charge-reduced species are no longer observed because the **$[M+4H]^{3+\bullet}$** ion was resonantly activated to undergo dissociation. The experimentally observed isotopic distribution for the **$[M+4H]^{3+\bullet}$** ion under ECD alone conditions is shown in Figure 5.3C. Note that compared to the distribution in Figure 5.3A, the distribution of Figure 5.3C is shifted to higher mass-to-charge values indicative of the additional hydrogen on **$[M+4H]^{3+\bullet}$** resulting from the neutralization of a proton.

Considering the amino acid sequence from Figure 5.2, it can be seen that the improved sequence coverage observed with ECD+CID is due to cleavage N-terminal to proline and the formation of **z_6**-**z_9** product ions. Shown in Figure 5.4 are the mass-to-charge regions associated with

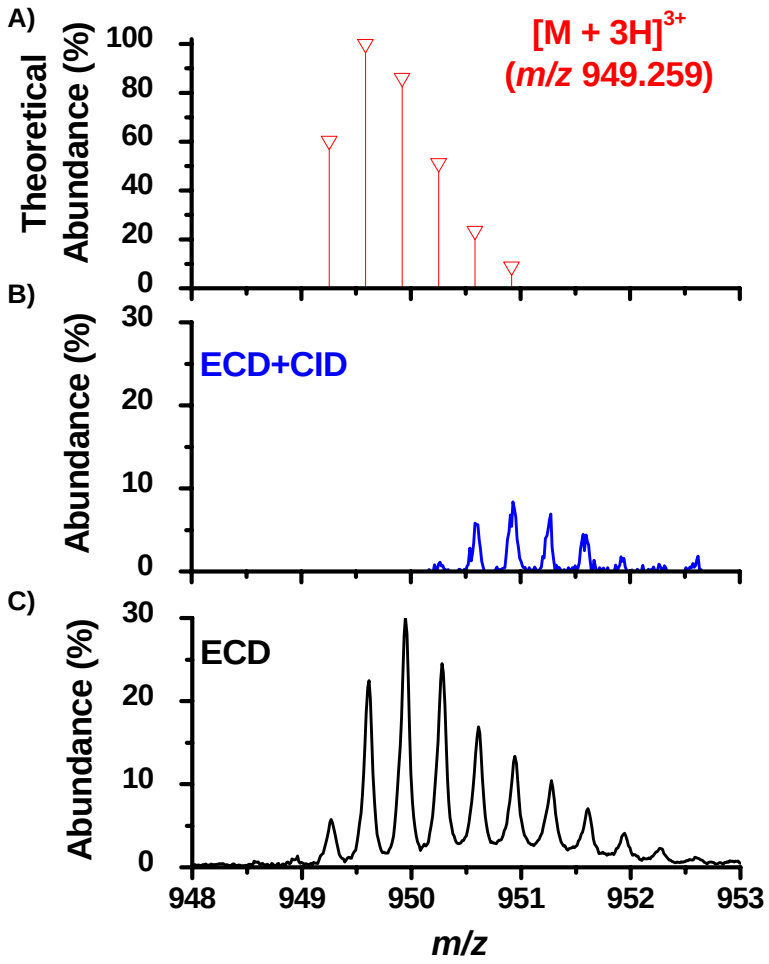

Figure 5.3 Expanded mass-to-charge regions around melittin **[M+4H]**$^{3+\bullet}$ from Figure 5.2. A) The theoretical isotopic distribution expected if the $[M+3H]^{3+}$ charge state were formed directly from ESI. B) The mass-to-charge region observed in the ECD+CID spectrum for **[M+4H]**$^{3+\bullet}$ demonstrating its removal due to resonance excitation. C) The mass-to-charge region observed in the ECD alone spectrum for **[M+4H]**$^{3+\bullet}$.

these **z**-ions. For each product ion the theoretical, monoisotopic mass-to-charge value is given, and the corresponding isotopomer is indicated with an arrow. The relative abundances within the isotopic distributions for the $\mathbf{z_7}^{+2}$ and $\mathbf{z_6}$ product ions differ from the relative abundances observed in the $\mathbf{z_8}^{+2}$ and $\mathbf{z_9}^{+2}$ distributions. The differences in the isotopic distributions are due to errors in the ion statistics associated with the detection of the lower abundant $\mathbf{z_7}^{+2}$ and $\mathbf{z_6}$ product ions. Regardless, the data in Figure 5.4 clearly show that the **z** ions in question are observed under ECD+CID conditions and not formed with ECD alone.

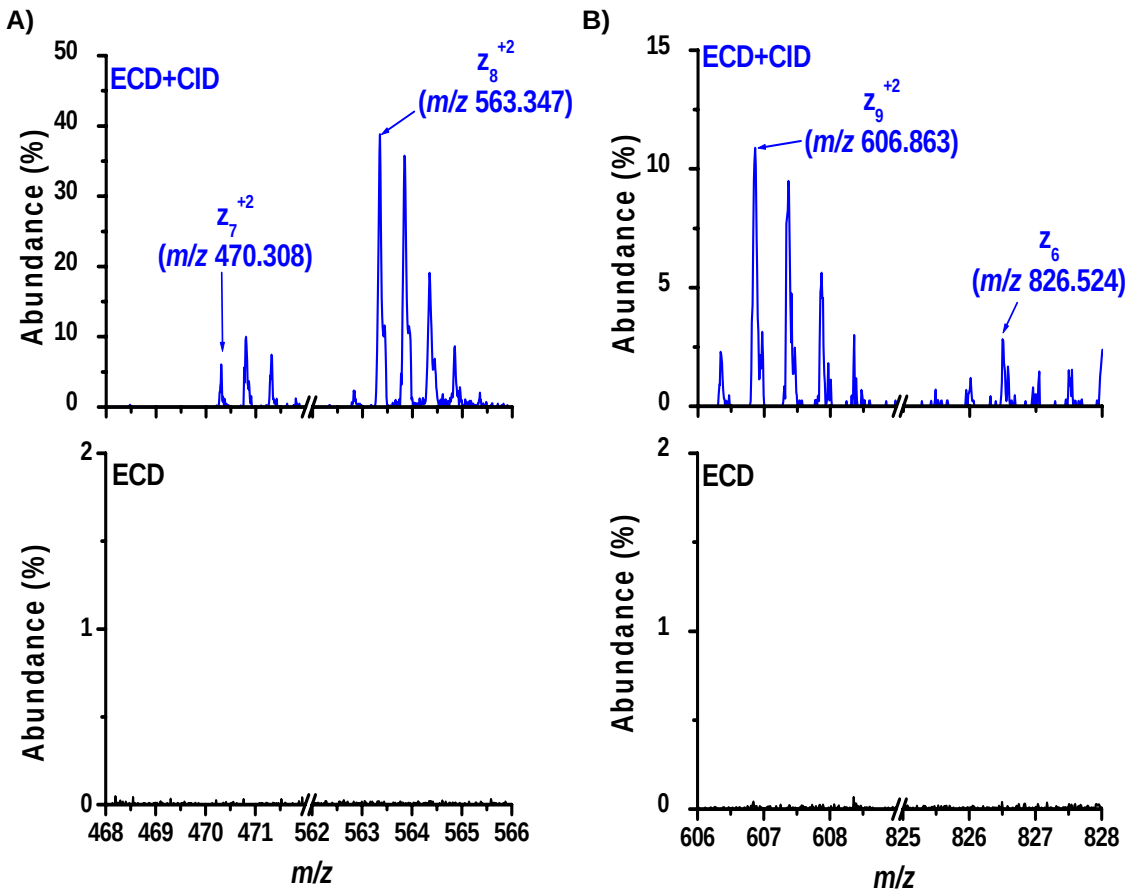

Figure 5.4 Expanded mass-to-charge regions around z_6-z_9 ions unique to ECD+CID in Figure 5.2. A) z_7^{+2} and z_8^{+2} ions are present in ECD+CID (top) experiment but absent under ECD alone conditions (bottom). B) z_9^{+2} and z_6 ions are present in ECD+CID (top) experiment but absent under ECD alone conditions (bottom).

The results in Figures 5.2 - 5.4 demonstrate the utility of ECD+CID for improving the sequence coverage for peptide ECD analyses. For the ECD+CID experiment, an ECD duration of 190 ms was required so the electron current passing through the ECD_{LIT} was the same as that produced in 10 ms with ECD alone. The duration of electron irradiation must be increased with ECD+CID due to the presence of the supplemental ac waveform. The supplemental waveform decreases the transmission of the electrons through the ECD_{LIT} by working against the radial focusing effect of the magnetic field and displacing the electrons from the LIT central axis. The supplemental waveform also increases the acceleration of the electrons to kinetic energies too large for efficient ECD.[11, 14, 30] Consequently, a longer ECD duration is needed under ECD+CID conditions to ensure a sufficient number of parent ions participate in ECD to produce enough product ions to be detected. However, the longer ECD duration required for ECD+CID does not necessitate a longer

spectral acquisition. Both spectra in Figure 5.2 were acquired for the same total amount of time, i.e., the same amount of sample was consumed to produce the ECD+CID and ECD spectra.

5.3.3 *ECD+CID for improved de novo sequencing*

Ion-electron reactions are an attractive set of MS/MS methods for peptide analyses because they can provide extensive sequence coverage and allow labile bonds (e.g., PTMs) to remain intact while only requiring the electron kinetic energy and flux to be tuned.[31] The data in Figure 5.2, where only ECD was performed (bottom spectrum), used electrons with kinetic energies optimized for maximum electron capture cross-section. However, it is intriguing to consider the benefit of increasing the electron flux under such conditions in an attempt to improve the extent of dissociation in ECD. To explore the possibility of higher electron flux improving peptide sequence coverage with the ECD_{LIT}, the voltage dropped across the electron filament was increased so the electron current measured on the quadrupole ions guide changed from 0.33 to 0.80—0.85 μA. Increasing the electron flux introduces a larger number of electrons to the ECD_{LIT}. When parent ions contain more than two protons, their charge-reduced species would still be multiply-charged and thus capable of capturing another electron. As described in Scheme 1, the second electron capture can lead to product ions with mass-to-charge values that differ from theory, making spectral interpretation difficult. By using ECD+CID the first charge-reduced species ($\mathbf{[M+nH]^{(n-1)+\bullet}}$) can be resonantly excited and dissociated thereby preventing a second electron capture and allowing the ambiguity introduced by multiple electron capture events (i.e., sequential proton neutralization) to be avoided.

ECD+CID with a measured electron current of 0.80 μA is shown in the top spectrum of Figure 5.5 where the parent ions for ECD and CID were the $\mathbf{[M+4H]^{4+}}$ and $\mathbf{[M+4H]^{3+\bullet}}$ species, respectively. The result of increasing the electron flux to a measured electron current of 0.85 μA and using only ECD is shown in the bottom spectrum of Figure 5.5. The parent ion was the $\mathbf{[M+4H]^{4+}}$ charge state of melittin. The two spectra appear similar which is due to the majority of the same peptide backbone sites being cleaved under both ECD+CID and ECD alone conditions. The amino acid sequence in the bottom of Figure 5.5 shows the locations of **c** / **z** ion formation; as with Figure 5.2, the arrows are used to represent which MS/MS method is responsible for each cleavage. Under the present experimental conditions, a larger number of N-C_α bonds are cleaved with ECD alone than for

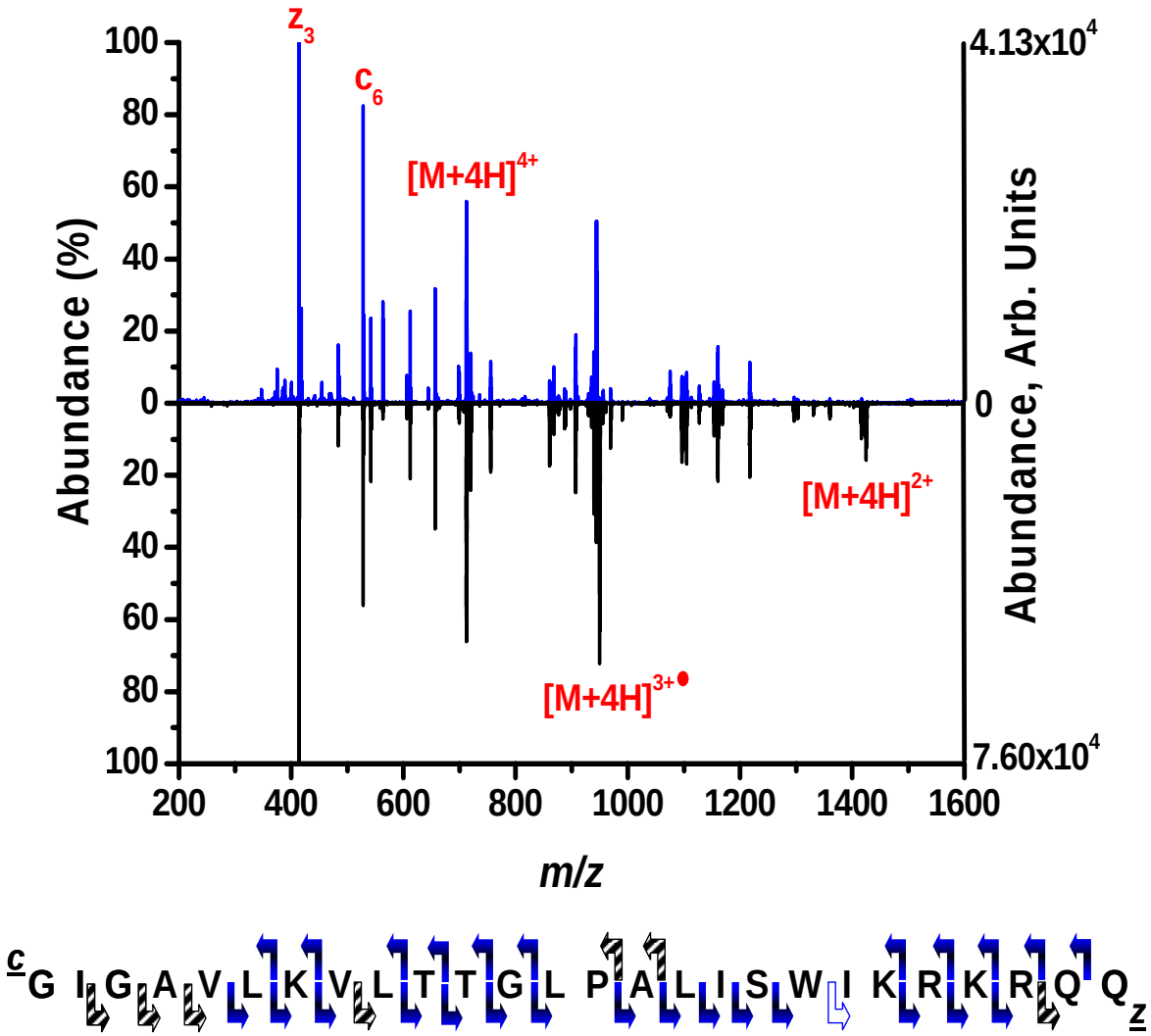

Figure 5.5 ECD+CID for improved *de novo* sequencing. ECD+CID spectrum (top) and ECD spectrum (bottom) of **[M+4H]$^{4+}$** of melittin. The method used to annotate the amino acid sequence for melittin indicates is the same as was used in Figure 5.2.

ECD+CID (84% vs. 76%). However, this improved sequence coverage is due only to the ability to annotate even those product ions which have mass-to-charge values different than what is theoretically expected because the amino acid sequence was known *a priori*.

Taking a closer look at Figure 5.5, some important differences between the ECD alone and ECD+CID spectra become apparent. Illustrated in Figure 5.6 are the theoretical isotopic distributions for the **[M+3H]$^{3+}$** and **[M+2H]$^{2+}$** melittin charge states generated directly from ESI (Figures 5.6A and 5.6D) and the corresponding mass-to-charge regions of the experimental ECD+CID and ECD alone

spectra from Figure 5.5. The vertical, dashed line in the left and right panels represents the monoisotopic mass-to-charge value for each charge state that would be expected in the absence of any neutralized protons. The mass-to-charge region around **[M+4H]$^{3+\bullet}$**, shown in Figures 5.6B and 5.6C, provides evidence for the successful application of ECD+CID. By applying CID on the **[M+4H]$^{3+\bullet}$** ion during ECD+CID, it is effectively removed from the ECD_{LIT} and thus its ability to capture a second electron has been reduced, as shown in Figure 5.6B. In contrast, the results from performing ECD alone, in Figure 5.6C, show that the **[M+4H]$^{3+\bullet}$** isotopic distribution is present with a significant abundance. From Figure 5.6C, it can be seen that the capture of one electron by **[M+4H]$^{4+}$** does result in a small amount of the even-electron **[M+3H]$^{3+}$** being formed; most likely due to a loss of

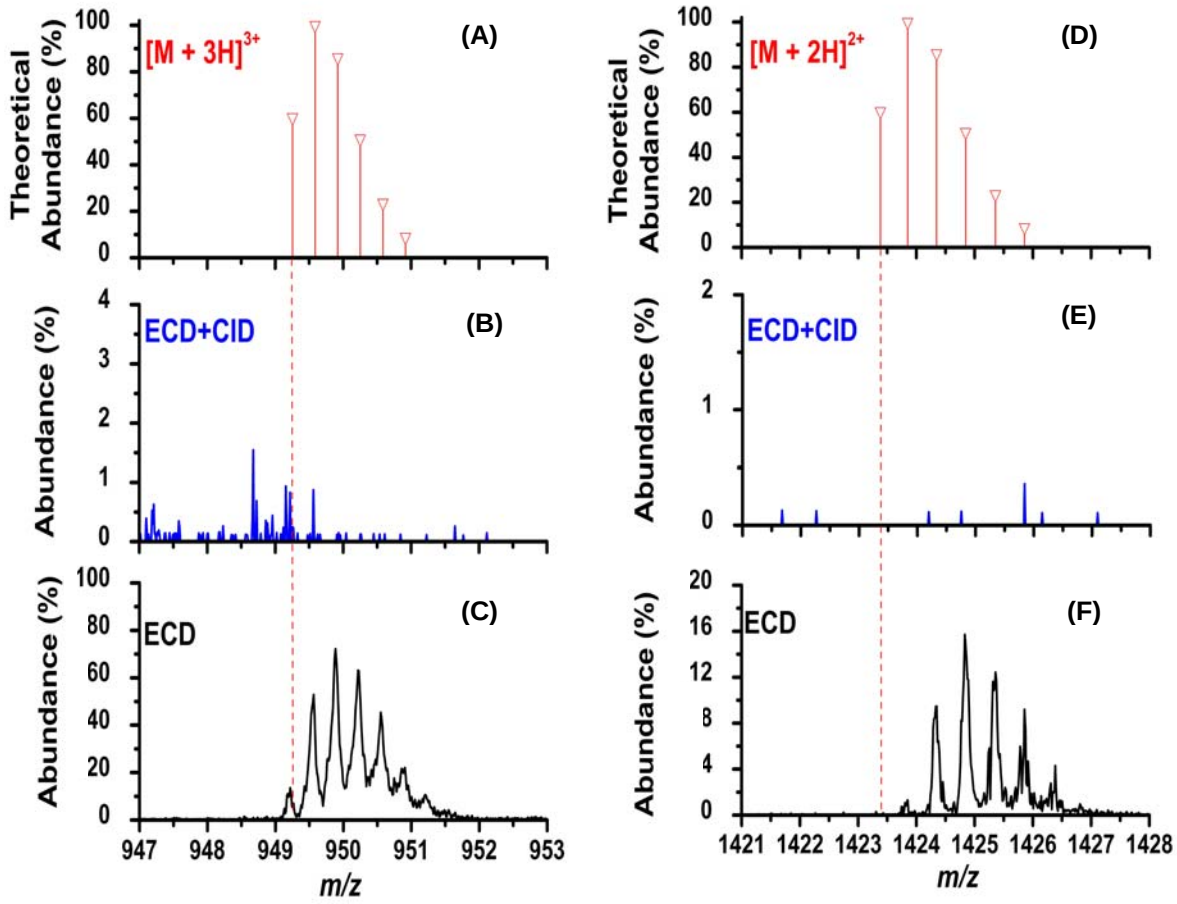

Figure 5.6 Expanded mass-to-charge regions around melittin **[M+4H]$^{3+\bullet}$** and **[M+4H]$^{2+}$** from Figure 5.5. The theoretical isotopic distributions expected if the charge states were formed directly from ESI are given for A) **[M+3H]$^{3+}$** and D) **[M+2H]$^{2+}$**. The mass-to-charge regions observed in the ECD+CID spectra are given for B) **[M+4H]$^{3+\bullet}$** and E) **[M+4H]$^{2+}$**. The mass-to-charge regions observed in the ECD alone spectra are given for C) **[M+4H]$^{3+\bullet}$** and F) **[M+4H]$^{2+}$**.

H• from **[M+4H]$^{3+\bullet}$**. Under ECD+CID conditions (Figure 5.6E), the **[M+4H]$^{2+}$** ion is not observed due to the resonance excitation of the **[M+4H]$^{3+\bullet}$** intermediate. Conversely, the **[M+4H]$^{2+}$** ion is present when ECD alone is performed, where the mass-to-charge values of the isotopic distribution indicate the presence of two neutralized protons with respect to **[M+2H]$^{2+}$** formed directly from ESI. The distribution for **[M+4H]$^{2+}$** in Figure 5.6F does show a small amount of **[M+3H]$^{2+\bullet}$**, most likely due to a loss of **H•** but this time from **[M+4H]$^{2+}$**. Because **[M+4H]$^{2+}$** is formed readily under typical ECD conditions in the ECD_{LIT}, the ability to perform ECD+CID is beneficial. The electron densities for the ECD+CID and ECD experiments were 1.0 and 1.1 μA/mm^2, respectively. By using approximately the same electron densities for both experiments, the effectiveness of ECD+CID can be observed directly from Figure 5.6. With an electron irradiation time of only 7 ms for the ECD control experiment, the high electron densities readily achievable within the ECD_{LIT} allow the sequential capture of electrons to occur. Therefore, even at short (i.e., 7 ms) irradiation times, it is necessary to minimize EC_2D_2 (see Scheme 1) when higher electron fluxes (i.e., 0.8 μA vs 0.33 μA) are used. Comparing Figures 5.6E and 5.6F clearly show the effectiveness of the ECD+CID process.

The ability of ECD+CID to reduce the amount of ambiguity in product ion identification resulting from sequential electron capture is demonstrated in Figure 5.7. The mass-to-charge values for the **z_{23}^{+2}** and **z_{24}^{+2}** melittin product ions from Figure 5.5 are shown in the left and right panels of Figure 5.7, respectively. The data in Figure 5.7 is presented in the same format as Figure 5.6, where the theoretical isotopic distributions are shown in Figures 5.7A and 5.7D while the ECD+CID and ECD alone results are shown in Figures 5.7B, 5.7E, 5.7C, and 5.7F, respectively. For both product ions under ECD alone conditions, it was observed that their experimental isotopic distributions were shifted corresponding to the presence of one neutralized proton (Figures 5.7C and 5.7F). Under ECD+CID conditions, the abundances of both product ions were reduced (Figures 5.7B and 5.7E). Therefore, the formation of the **z_{23}^{+2}** and **z_{24}^{+2}** product ions can be attributed to multiple electron capture events. The data from Figure 5.7 demonstrate the utility of ECD+CID for simplifying the spectra when multiple electron capture events can occur because the abundance of the mass-shifted product ions have been significantly reduced in the MS/MS spectrum.

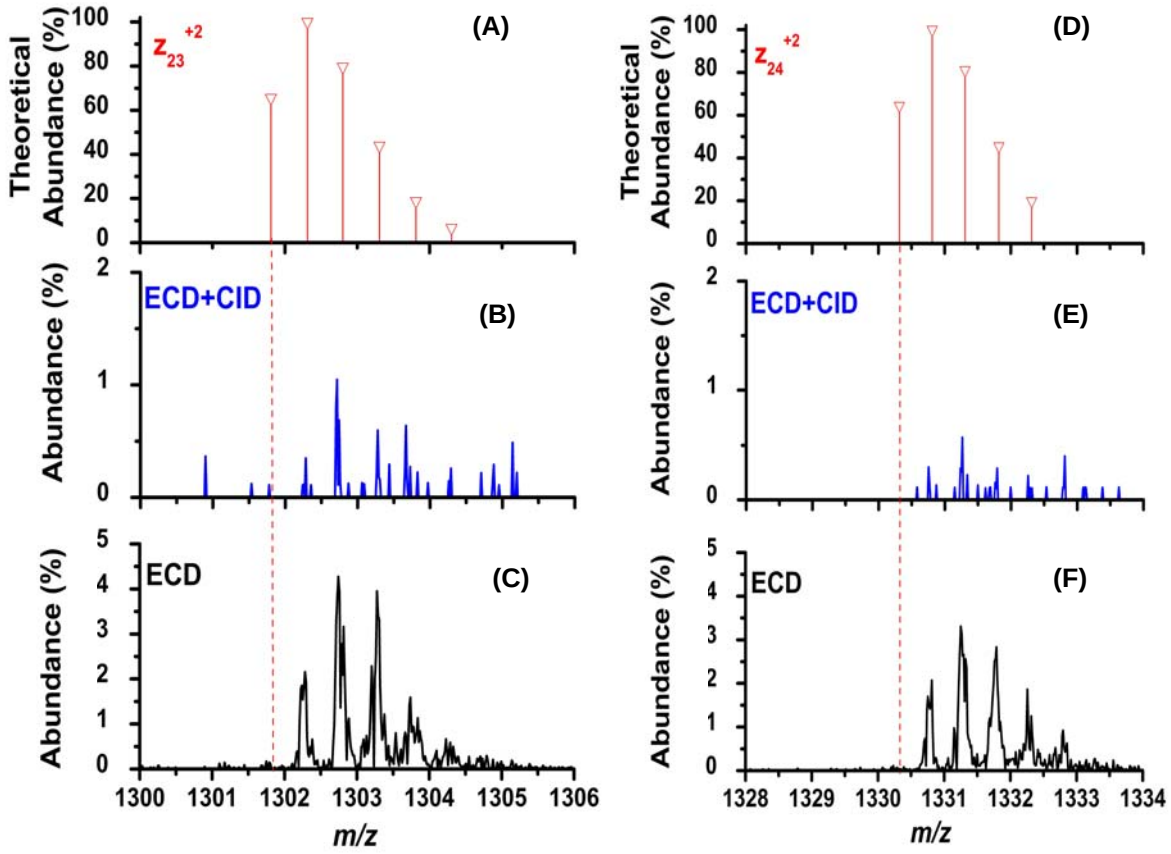

Figure 5.7 Mass-to-charge regions around z_{23}^{+2} and z_{24}^{+2} melittin product ions from Figure 5.5. The theoretical isotopic distributions are given for A) z_{23}^{+2} and D) z_{24}^{+2}. The mass-to-charge regions observed in the ECD+CID spectra are given for B) z_{23}^{+2} and E) z_{24}^{+2}. The mass-to-charge regions observed in the ECD alone spectra are given for C) z_{23}^{+2} and F) z_{24}^{+2}.

The spectra in Figure 5.8 serve as experimental evidence that product ions without neutralized protons are retained during ECD+CID and are observed at their expected mass-to-charge value. Shown in Figure 5.8 are the mass-to-charge regions around the z_{24}^{+3} and z_{15}^{+2} product ions from the results in Figure 5.5. The theoretical isotopic distributions for the z_{24}^{+3} and z_{15}^{+2} product ions are given in Figure 5.8A. The relative abundances of the isotopic distributions for the z_{24}^{+3} and z_{15}^{+2} product ions under ECD+CID and ECD alone conditions are given in Figure 5.8B and 5.8C, respectively. The isotopic distributions acquired from the ECD+CID experiment differ from the theoretical distributions seen in Figure 5.8A. Under ECD alone conditions, the relative abundances of the isotopic distributions are similar to the theoretically predicted values. The ECD+CID results show a greater discrepancy in their isotopic distributions compared to theory than the ECD alone results

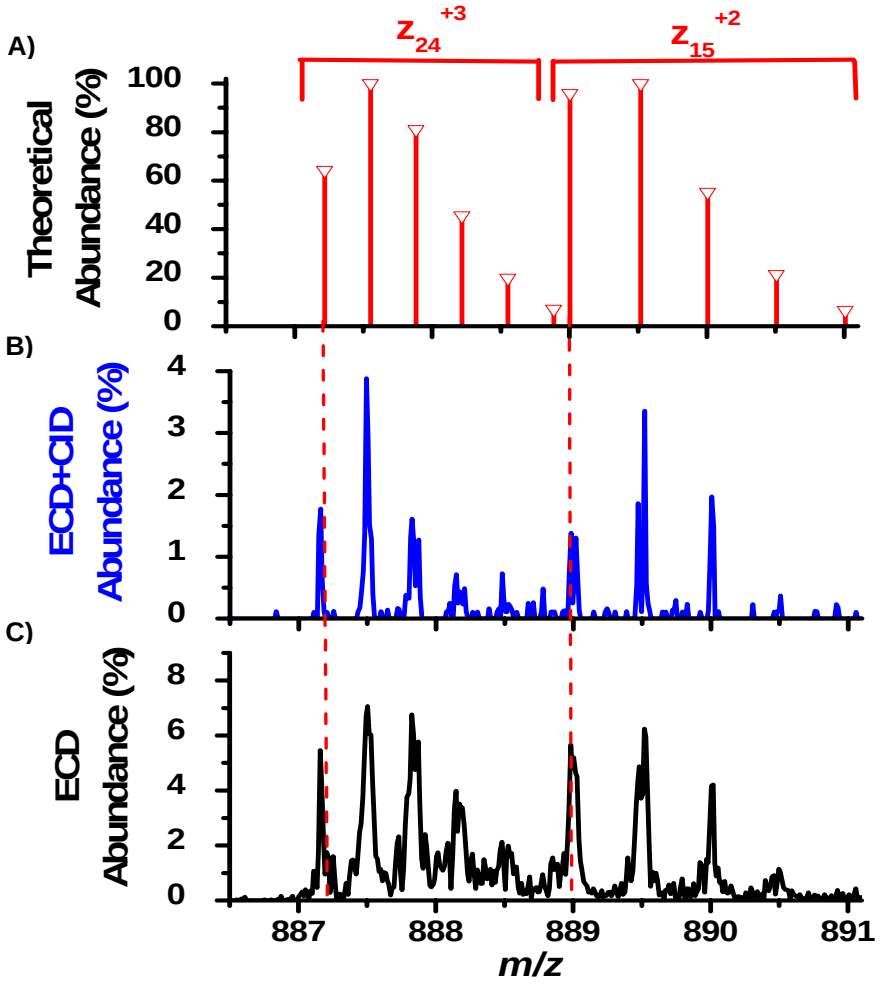

Figure 5.8 Mass-to-charge regions around z_{24}^{+3} and z_{15}^{+2} from Figure 5.5. A) The theoretical isotopic distributions for z_{24}^{+3} and z_{15}^{+2}. B) Product ion isotopic distributions under ECD+CID conditions. C) Product ion isotopic distributions under ECD alone conditions. Vertical, dashed lines represent the theoretical, monoisotopic mass-to-charge ratio.

due to the low abundance of the z_{24}^{+3} and z_{15}^{+2} product ions detected in the ECD+CID experiment. As a result, the ion statistics are better for the z_{24}^{+3} and z_{15}^{+2} product ions in the ECD alone experiment resulting in a better agreement to the theoretically predicted isotopic distributions.

The z_{24}^{+3} product ion can only form from the capture of one electron by the $[M+4H]^{4+}$ parent ion. Under both ECD+CID and ECD alone conditions, the z_{24}^{+3} product ion is detected at its theoretical mass-to-charge value. The results shown in Figure 5.8 thus support the previous discussion regarding Figures 5.7B and 5.7E that the z_{23}^{+2} and z_{24}^{+2} ions, respectively, were reduced in abundance due to ECD+CID. Specifically, the results from Figures 5.7B, 5.7E, and 5.8B demonstrate

that ECD+CID is effective at reducing the abundance of ions that result from the capture of more than one electron.

In Figure 5.8, the $\mathbf{z_{15}^{+2}}$ product ion was also detected at its theoretical mass-to-charge value under both experimental conditions. Because the $\mathbf{z_{15}^{+2}}$ product ion only has two protons remaining, it could contain at least one neutralized proton similar to the $\mathbf{z_{23}^{+2}}$ and $\mathbf{z_{24}^{+2}}$ product ions from Figure 5.7. However, considering Figures 5.8B and 5.8C, the $\mathbf{z_{15}^{+2}}$ product ion was not shifted therefore it does not contain any neutralized protons. Taking into account the amino acid sequence of melittin provided in Figure 5.5 and assuming the protons located on the peptide sequence reside at basic residues, the results presented in Figures 5.7 and 5.8 suggest that the neutralized proton observed under ECD conditions for $\mathbf{z_{23}^{+2}}$ and $\mathbf{z_{24}^{+2}}$ was located on the lysine residue closest to the N-terminal end. Thus, if the parent ion sequence is known, ECD+CID could be used to further study characteristics of non-dissociative electron capture such as factors that dictate the location of electron capture and charge reduction for peptides and proteins.

5.4 Conclusions

A new technique called simultaneous ECD, CID (ECD+CID) has been implemented on a recently developed ECD_{LIT} instrument. A brief discussion of the theory regarding ion motion was given to help describe the effect of the combined electrodynamic and static magnetic fields present in the ECD_{LIT} device. The ability to perform ECD+CID is unique to this ECD_{LIT} instrument; where a single mass-to-charge of interest can be resonantly activated through collisions with the ~7.5×10^{-3} torr helium bath gas. The resonant activation is achieved by applying a supplemental ac waveform to the ECD_{LIT} rod set.

The ability of ECD+CID to aid in peptide sequencing was demonstrated using melittin. By resonantly activating the charge-reduced species ($\mathbf{[M+4H]^{3+\bullet}}$) as it is formed from $\mathbf{[M+4H]^{4+}}$ undergoing a non-dissociative electron capture event, the amount of peptide sequence coverage observed was 88%, compared to 76% when only ECD was performed on the $\mathbf{[M+4H]^{4+}}$ charge state. Results have also shown that ECD+CID can reduce the occurrence of multiple electron capture events thereby simplifying MS/MS spectral interpretation under conditions of increased electron flux. The abundance of product ions observed at mass-to-charge ratios that are shifted from their expected

values under typical ECD conditions, due to the neutralization of protons, are reduced in the MS/MS spectrum via ECD+CID. It has also been demonstrated that information about the location of the neutralized proton inherent with electron capture can be obtained by comparing ECD+CID and ECD results.

5.5 References

1. Zubarev, R. A.; Kelleher, N. L; McLafferty, F. W. Electron Capture Dissociation of Multiply Charged Protein Cations. A Nonergodic Process. *Journal of the American Chemical Society*. **1998**, 120, p. 3265-3266.

2. Kruger, N. A.; Zubarev, R. A.; Horn, D. M.; McLafferty, F. W. Electron Capture Dissociation of Multiply Charged Peptide Cations. *International Journal of Mass Spectrometry*. **1999**, 185/186/187, p. 787-793.

3. Kruger, N. A.; Zubarev, R. A.; Carpenter, B. K.; Kelleher, N. L.; Horn, D. M.; McLafferty, F. W. Electron Capture versus Energetic Dissociation of Protein Ions. *International Journal of Mass Spectrometry*. **1999**, 1999, p. 1-5.

4. Syka, J. E. P.; Coon, J. J.; Schroeder, M. J.; Shabanowitz, J.; Hunt, D. F. Peptide and Protein Sequence Analysis by Electron Transfer Dissociation Mass Spectrometry. *Proceedings of the National Academy of Sciences, U.S.A.* **2004**, 101, p. 9528-9533.

5. Coon, J. J.; Ueberheide, B.; Syka, J. E. P.; Dryhurst, D. D.; Ausio, J.; Shabanowitz, J.; Hunt, D. F. Protein Identification using Sequential Ion/Ion Reactions and Tandem Mass Spectrometry. *Proceedings of the National Academy of Sciences, U.S.A.* **2005**, 102, p. 9463 - 9468.

6. Liang, X.; Hager, J. W.; McLuckey, S. A. Transmission Mode Ion/Ion Electron-Transfer Dissociation in a Linear Ion Trap. *Analytical Chemistry*. **2007**, 79, p. 3363 - 3370.

7. Kaplan, D. A.; Hartmer, R.; Speir, J. P.; Stoermer, C.; Gumerov, D.; Easterling, M. L.; Brekenfeld, A.; Kim, T.; Laukien, F.; Park, M. A. Electron Transfer Dissociation in the Hexapole Collision Cell of a Hybrid Quadrupole-Hexapole Fourier Transform Ion Cyclotron Resonance Mass Spectrometer. *Rapid Communications in Mass Spectrometry*. **2008**, 22, p. 271-278.

8. Hogan, J. M.; Pitteri, S. J.; Chrisman, P. A.; McLuckey, S. A. Complementary Structural Information from a Tryptic N-Linked Glycopeptide via Electron Transfer Ion/Ion Reactions and Collision-Induced Dissociation. *Journal of Proteome Research*. **2005**, 4, p. 628 - 632.

9. Baba, T.; Hashimoto, Y.; Hasegawa, H.; Hirabayashi, A.; Waki, I. Electron Capture Dissociation in a Radio Frequency Ion Trap. *Analytical Chemistry*. **2004**, 76, p. 4263-4266.

10. Silivra, O. A.; Kjeldsen, F.; Ivonin, I. A.; Zubarev, R. A. Electron Capture Dissociation of Polypeptides in a Three-Dimensional Quadrupole Ion Trap: Implementation and First Results. *Journal of the American Society for Mass Spectrometry*. **2005**, 16, p. 22 - 27.

11. Ding, L.; Brancia, F. L. Electron Capture Dissociation in a Digital Ion Trap Mass Spectrometer. *Analytical Chemistry*. **2006**, 78, p. 1995-2000.

12. Satake, H.; Hasegawa, H.; Hirabayashi, A.; Hashimoto, Y.; Baba, T.; Fast Multiple Electron Capture Dissociation in a Linear Radio Frequency Quadrupole Ion Trap. *Analytical Chemistry*. **2007**, 79, p. 8755-8761.

13. Bushey, J. M.; Baba, T.; Glish, G. L. *Electron Capture Dissociation in a radio frequency Ion Trap Versus a Fourier Transform Ion Cyclotron Resonance Mass Spectrometer*. in *The 56th ASMS Conference on Mass Spectrometry and Allied Topics*. 2008. Denver, CO.

14. Cooper, H. J.; Hakansson, K.; Marshall, A. G. The Role of Electron Capture Dissociation in Biomolecular Analysis. *Mass Spectrometry Reviews*. **2005**, 24, p. 201 - 222.

15. Horn, D. M.; Ge, Y.; McLafferty F. W. Activated Ion Electron Capture Dissociation for Mass Spectral Sequencing of Larger (42 kDa) Proteins. *Analytical Chemistry*. **2000**, 72, p. 4778-4784.

16. Sze, S. K.; Ge, Y.; Oh, H. B.; McLafferty F. W. Plasma Electron Capture Dissociation for the Characterization of Large Proteins by Top Down Mass Spectrometry. *Analytical Chemistry*. **2003**, 75, p. 1599 - 1603.

17. Tsybin, Y. O.; Witt, M.; Baykut, G.; Kjeldsen, F.; Hakansson, P.; Combined Infrared Multiphoton Dissociation and Electron Capture Dissociation with a Hollow Electron Beam in Fourier Transform Ion Cyclotron Resonance Mass Spectrometry. *Rapid Communications in Mass Spectrometry*. **2003**, 17, p. 1759-1768.

18. Oh, H. B.; McLafferty, F. W. A Variety of Activation Methods Employed in "Activated-Ion" Electron Capture Dissociation Mass Spectrometry: A Test Against Bovine Ubiquitin 7+ Ions. *Bulletin of the Korean Chemical Society*. **2006**, 27, p. 389 - 394.

19. Swaney, D. L.; McAlister, G. C., Wirtala, M.; Schwartz, J. C.; Syka, J. E. P.; Coon, J. J. Supplemental Activation Method for High-Efficiency Electron-Transfer Dissociation of Doubly Protonated Peptide Precursors. *Analytical Chemistry*. **2007**, 79, p. 477 - 485.

20. Xia, Y.; Han, H.; McLuckey, S. A. Activation of Intact Electron-Transfer Products of Polypeptides and Proteins in Cation Transmission Mode Ion/Ion Reactions. *Analytical Chemistry*. **2008**, 80, p. 1111-1117.

21. Tsybin, Y. O.; He, H.; Emmett, M. R. ; Hendrickson, C. L.; Marshall, A. G. Ion Activation in Electron Capture Dissociation to Distinguish between N-Terminal and C-Terminal Product Ions. *Anal. Chem.* **2007**, 79, p. 7596-7602.

22. Mihalca, R.; van der Burgt, Y. E. M.; McDonnell, L. A.; Duursma, M.; Cerjak, I; Heck, A. J. R.; Heeren, R. M. A. Combined Infrared Multiphoton Dissociation and Electron-Capture Dissociation using Co-Linear and Overlapping Beams in Fourier Transform Ion Cyclotron Resonance Mass Spectrometery. *Rapd Commun. Mass Spectrom.* **2006**, 20, p. 1838-1844.

23. O'Brien, J.T.; Prell, J. S.; Holm, A. I. S.; Williams, E. R. Effects of Electron Kinetic Energy and Ion-Electron Inelastic Collisions in Electron Capture Dissociation Measured Using Ion Nanocalorimetry. *Journal of the American Society for Mass Spectrometry*. **2008**, 19, p. 772 - 779.

24. Laskin, J.; Futrell, J. H. Activation of Large Ions in FT-ICR Mass Spectrometry. *Mass Spectrometry Reviews*. **2005**, 24, p. 135-167.

25. Amster, I. J. Fourier Transform Mass Spectrometry. *Journal of Mass Spectrometry*. **1996**, 31, p. 1325-1337.

26. Douglas, D. J.; Frank, A. J.; Mao, D. M. Linear Ion Traps in Mass Spectrometry. *Mass Spectrometry Reviews*. **2005**, 24, p. 1-29.

27. Marshall, A. G.; Hendrickson, C. L.; Jackson, G. S. Fourier Transform Ion Cyclotron Resonance Mass Spectrometry: A Primer. *Mass Spectrometry Reviews*. **1998**, 17, p. 1-35.

28. Håkansson, K.; Chalmers, M. J.; Quinn, J. P.; McFarland, M. A.; Hendrickson, C. L.; Marshall A. G. Combined Electron Capture and Infrared Multiphoton Dissociation for Multistage MS/MS in a Fourier Transform Ion Cyclotron Resonance Mass Spectrometer. *Analytical Chemistry*. **2003**, 75, p. 3256 - 3262.

29. Tsybin, Y. O.; He, H.; Emmett, M. R.; Hendrickson, C. L.; Marshall, A. G. Ion Activation in Electron Capture Dissociation to Distinguish between N-Terminal and C-Terminal Product Ions. *Analytical Chemistry*. **2007**, 79, p. 7596-7602.

30. Kjeldsen, F.; Haselmann, K. F.; Budnik, B.; Jensen, F.; Zubarev, R. A. Dissociative capture of hot (3-13 eV) electrons by polypeptide polycations: an efficient process accompanied by secondary fragmentation. *Chemical Physics Letters*. **2002**, 2002, p. 204-206.

31. Zubarev, R. A. Reactions of Polypeptide Ions with Electrons in the Gas Phase. *Mass Spectrometry Reviews*. **2003**, 22, p. 57 - 77.

Chapter 6

Electron Detachment Dissociation (EDD) in a Linear Ion Trap (LIT)

6.1 Introduction

6.1.1 *Analysis of acidic analytes*

Electron detachment dissociation (EDD) is the anionic complement to electron capture dissociation (ECD). Acidic analytes prefer to be ionized as anions. The use of EDD for the analysis of several types of anions has been demonstrated using Fourier transform ion cyclotron resonance mass spectrometers (FTICR-MS): peptides [1, 2], oligodeoxynucleotides [3], gangliosides [4], DNA sequences [5], glycosaminoglycans [6, 7], and oligosaccharides [8]. EDD has also been performed on peptide anions in a three-dimensional quadrupole ion trap mass spectrometer (QITMS).[9] These previous implementations showed promise for the use of EDD as a sequencing method. For example, several common post translational modifications (PTMs) increase the acidity of peptides even further, e.g. phosphorylation, sulfation, and glycosylation. Published results have shown that EDD can provide extensive sequence coverage of peptides while allowing PTMs to be retained.[9]

6.1.2 *Implementation of EDD in a LIT*

As described in Chapter 1, a hybrid linear ion trap (LIT)/time of flight (TOF) mass spectrometer has been developed that makes it possible to perform ion-electron reactions in a LIT.[10] The LIT where EDD takes place will be referred to as the EDD_{LIT} in this chapter. The work described in this chapter represents the first example of EDD performed using the LIT/TOF instrument. The optimal electron energy and irradiation time for performing EDD on peptide anions in the EDD_{LIT} have been determined. The electron density in the EDD_{LIT} device allows shorter electron irradiation times to be used during EDD experiments than on FTICR-MS instruments. Compared to

performing EDD on a QITMS, the LIT/TOF instrument offers better resolving power and higher mass measurement accuracy (MMA).

6.2 Experimental

6.2.1 *Samples*

The peptides FLEEV (M_r: 635.72) and insulin chain A (GIVEQCCASVCSLYQLENYCN, all cysteins are trioxidated (SO_3H), M_r: 2531.64) were purchased from Sigma-Aldrich, Inc. (St. Louis, MO). The peptides substance P (RPKPQQFFGLM, M_r: 1348.70) and cardiodilatin (NPMYNAVSNADLMDFK; 1-16, human, M_r: 1830.10) were purchased from the American Peptide Company (Sunnyvale, CA). All peptides were used without further purification and diluted to ~ 5 μM in 50:50 v% methanol/water or 50:50 v% acetonitrile/water. Ammonium hydroxide or ammonium acetate were added (1% by volume) to aid in anion formation during negative mode ESI. Chloroform (1% by volume) was also added in some instances to alleviate problems with electrical discharge occurring at the tip of the nESI sprayer.

6.2.2 *EDD_{LIT} Instrumentation*

The EDD_{LIT} is part of a hybrid LIT/TOF mass spectrometer (nano-Frontier, Hitachi High Tec., Japan) that utilizes a LIT before the EDD_{LIT} for parent ion accumulation and isolation.[10] The parent anions are sent to the EDD_{LIT} where they are irradiated with electrons of kinetic energies greater than 10 eV. The electrons are generated from a thoriated tungsten filament. The electron kinetic energy is defined by the potential difference between the filament (filament offset) and the dc offset applied to the EDD_{LIT} rods. A desired electron kinetic energy was achieved by holding the dc potential of the EDD_{LIT} rod set constant while the filament offset was made more negative. As a result, the axial trapping condition for parent ions in the EDD_{LIT} was not changed over the entire range of electron energies. To control electron injection, the gate electrode (see Figure 1.3 in Chapter 1) located between the electron filament and the back trapping electrode of the EDD_{LIT} blocks the passage of electrons when it is in the HI state (i.e., at a more negative voltage) and allows electrons to pass when it is held LO. The electron current passing through the EDD_{LIT} was measured on the rods of the ion guide located on the opposite end of the EDD_{LIT} with respect to the electron filament. Following EDD the product ions are sent to a reflectron-TOF for mass analysis.

The effects of electron kinetic energy and electron irradiation time on the EDD spectra of FLEEV were studied. For the electron energy dependence experiment, an electron irradiation time of 40 ms was chosen based on previous results. The electron kinetic energy was varied from 1.75 to 30.0 eV in 0.5 eV increments. Two spectra were acquired at each electron energy: one with the electron beam irradiating ions in the EDD_{LIT} and one without the electron beam. Operating the instrument in such a manner helps to ensure that the results of the measurement are due to differences in electron energy and not due to differences in parent ion abundance. The instrument was operated in a similar manner for the electron irradiation time dependence experiment. The electron kinetic energy was held constant at 28 eV, and the irradiation time was varied from 1 to 80 ms in 1 ms increments.

For the peptide EDD spectra, each peptide was irradiated with 28 eV electrons for 30 ms. The measured electron currents were 2.20, 2.27, 3.90, and 2.16 μA for FLEEV, cardiodilatin, substance P, and insulin chain A, respectively. The FLEEV and insulin chain A spectra were each acquired for 2.0 minutes, representing an accumulated signal from 1008 EDD_{LIT} fills. The substance P and cardiodilatin spectra were each acquired for 5.0 minutes, representing an averaged signal from 2520 EDD_{LIT} fills.

6.3 Results and Discussion

6.3.1 *First EDD spectrum (FLEEV)*

The EDD spectrum of FLEEV acquired using 28 eV electrons and 30 ms irradiation is shown in Figure 6.1. The most abundant peak in the spectrum is the remaining parent ion, $\mathbf{[M\text{-}2H]^{2-}}$. The spectrum also contains sequence specific product ions (i.e., $\mathbf{a_3}$, $\mathbf{a_4}$, $\mathbf{x_2}$, $\mathbf{x_3}$, and $\mathbf{x_4}$) and small neutral losses associated with the charge-reduced ion ($\mathbf{[M\text{-}2H]^{2-\bullet}}$). The results show that the most favored C_α-C cleavage occurs between the phenylalanine and leucine to generate the $\mathbf{x_4}$ ion. The reason for this is presumably due to the ability of the $\mathbf{x_4}$ product ion to stabilize the negative charge located on either of the glutamic acids more effectively than the smaller product ions (i.e., $\mathbf{x_2}$ and $\mathbf{x_3}$) or the radical product ions (i.e., $\mathbf{a_3}$ and $\mathbf{a_4}$). It has been reported previously that in vacuo charge stabilization is achieved through intramolecular charge solvation [9, 11].

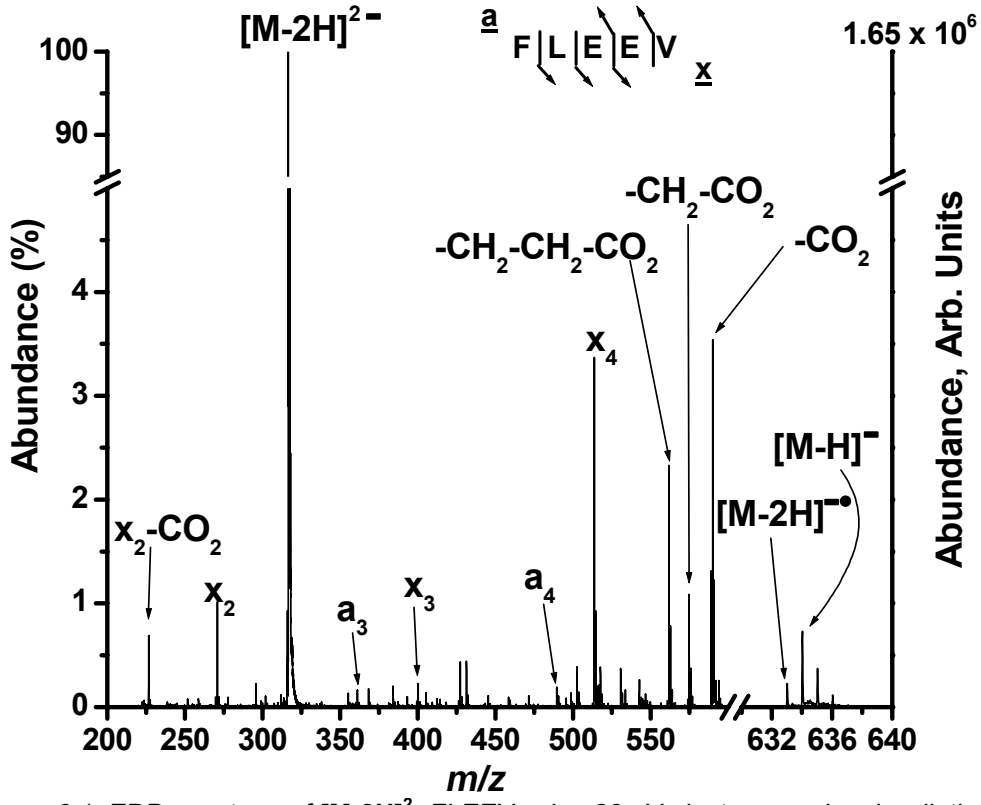

Figure 6.1 EDD spectrum of **[M-2H]**$^{2-}$ FLEEV using 28 eV electrons and an irradiation time of 30 ms.

The most abundant neutral loss corresponds to the loss of $\mathbf{CO_2}$ from one of three carboxylic acids present on FLEEV. Other neutral losses associated with cleavage of the glutamic acid side chains were also observed ($\mathbf{-CH_2\text{-}CO_2}$ and $\mathbf{-CH_2\text{-}CH_2\text{-}CO_2}$). The $\mathbf{CO_2}$ loss from the charge-reduced species was observed with greater abundance than the charge-reduced peak itself in Figure 6.1. This trend is in agreement with the facile loss of $\mathbf{CO_2}$ observed from EDD performed in a QITMS when the analyte contained carboxylic acids [9, 12].

6.3.2 *Electron kinetic energy dependence*

The operation of the EDD_{LIT} was characterized by plotting the extracted ion abundances of selected product ions as a function of electron kinetic energy and electron irradiation time. The effect of electron kinetic energy is illustrated in Figure 6.2. The stability of the ESI source and reproducibility of parent ion injection and storage in the EDD_{LIT} are indicated in Figure 2A, where the electron beam was off. When electrons were injected, the abundance of **[M-2H]**$^{2-}$ FLEEV remained constant up to an electron kinetic energy of 10 eV, as seen in Figure 2B. For electrons with kinetic

energies greater than 10 eV, the **[M-2H]$^{2-}$** abundance decreased linearly from 10 to 30 eV. The 10 eV electron kinetic energy threshold observed for electron detachment in the EDD_{LIT} is in good agreement with values reported for FTICR-MS instruments [2].

The extracted ion abundances for the charge-reduced ion (**[M-2H]$^{-\bullet}$**) and the loss of **CO_2** from **[M-2H]$^{-\bullet}$** are given in Figures 6.2C and 6.2D, respectively. The formation of both of these ions was negligible with electron kinetic energies less than 10 eV. The abundances of the charge-reduced and related ions increase with axial electron kinetic energies between 10 eV and 20 eV. At electron

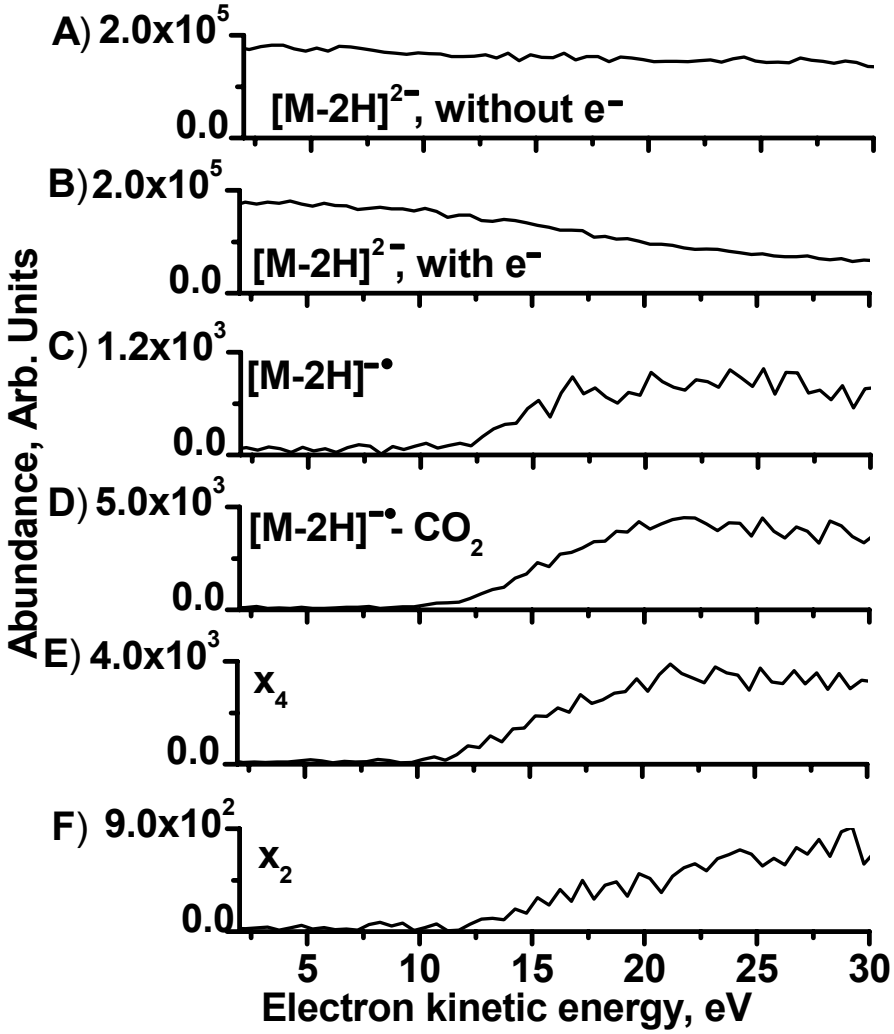

Figure 6.2 Ion abundance remaining after EDD as a function of electron kinetic energy using an electron irradiation time of 40 ms; (M = FLEEV). A) **[M-2H]$^{2-}$** without electrons injected into ECD cell, B) **[M-2H]$^{2-}$** with electrons injected into ECD cell, C) **[M-2H]$^{-\bullet}$**, D) **CO_2** loss from the **[M-2H]$^{-\bullet}$**, E) **x_4**, and F) **x_2**.

kinetic energies of 28 eV the abundances for the charge-reduced ion, its related **CO_2** loss ion, and the **x_4** product ion were still being detected at their maximum values, see Figure 6.2C-E. The abundance of the **x_2** product ion was still increasing at an electron kinetic energy of 28 eV. Accessing electron kinetic energies higher than 30 eV required changing the dc offset applied to the EDD_{LIT} rod set. Changing the ECD_{LIT} dc offset would have adversely affected the parent ion trapping so electron kinetic energies were kept below 30 eV. An electron energy of 28 eV is higher than those typically reported for EDD in FTICR instruments (e.g., 19 eV [7], 16-17 eV [3], 18 eV [2, 5]) but there are exceptions (20 to 30 eV) [8]. An electron energy of 28 eV is also larger than that reported for conducting EDD in the QITMS (10-20 eV) [9].

An electron kinetic energy of 28 eV results in the highest abundances for the EDD product ions plotted in Figure 6.2. From the data in Figure 6.3, the fragmentation efficiency is observed to increase as the electron kinetic energy approaches the 28 eV region. The collection efficiency decreases as the electron kinetic energy increases, showing the same trend as the **$[M-2H]^{2-}$** parent

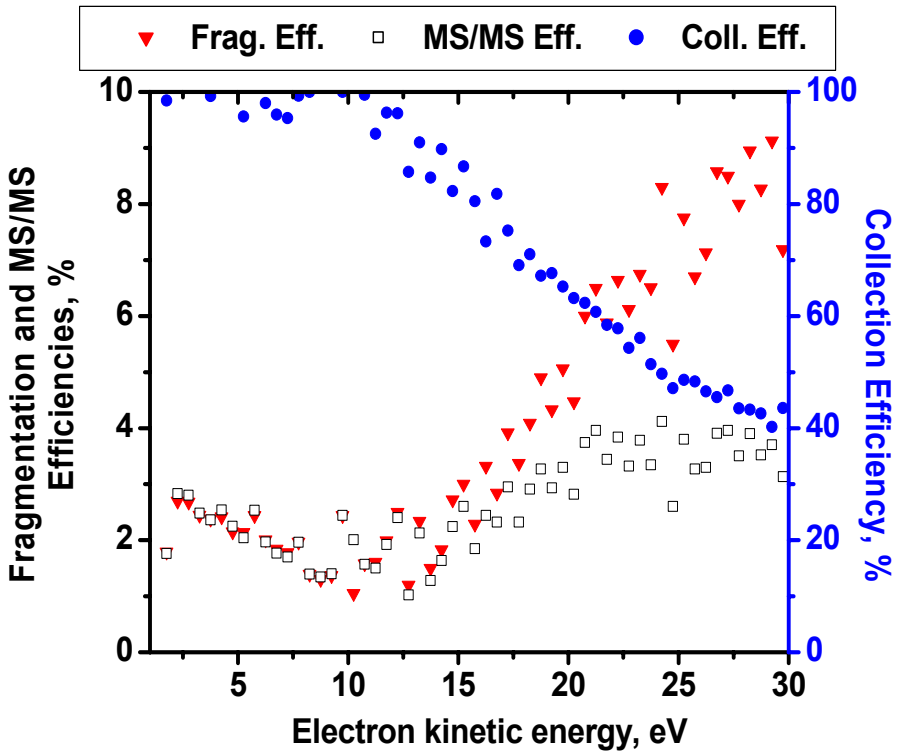

Figure 6.3 Fragmentation, collection, and MS/MS efficiencies for EDD as a function of electron kinetic energy.

ion abundance seen in Figure 6.2B. The trend of increasing fragmentation efficiency is reasonable because some product ions (e.g., $\mathbf{x_2}$ from Figure 6.2F) are still increasing in absolute abundance with 28 eV electrons. Because the fragmentation efficiency is at a non-minimal value and product ion abundance is either maintained at a maximum or is continuing to increase with 28 eV electrons, this electron kinetic energy was used for the remainder of the peptide EDD experiments described in this chapter.

6.3.3 *Electron irradiation time dependence*

The effect of electron irradiation time on EDD was measured using 28 eV electrons, the results are shown in Figure 6.4. The goal was to determine the shortest electron irradiation time that

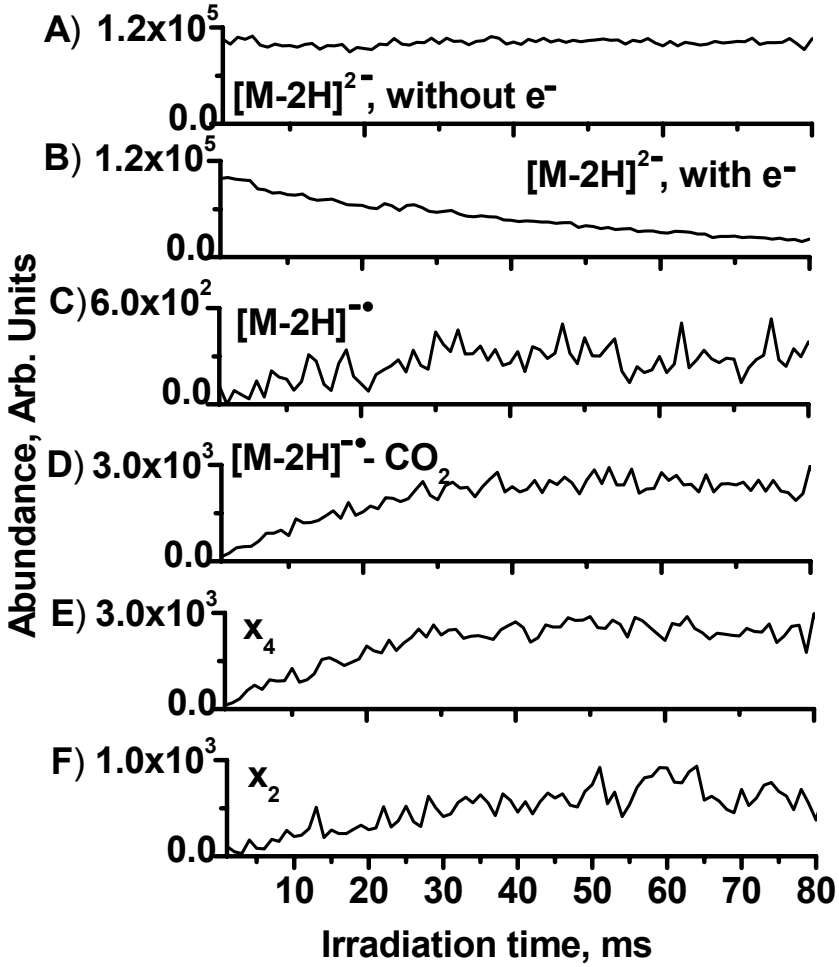

Figure 6.4 Ion abundance remaining after EDD as a function of electron irradiation time; (M = FLEEV) using 28 eV electrons. A) $\mathbf{[M\text{-}2H]^{2-}}$ without electrons injected into ECD cell, B) $\mathbf{[M\text{-}2H]^{2-}}$ with electrons injected into ECD cell, C) $\mathbf{[M\text{-}2H]^{-\bullet}}$, D) $\mathbf{CO_2}$ loss from the charge-reduced ion, E) $\mathbf{x_4}$, and F) $\mathbf{x_2}$.

provided maximum product ion abundance. The most abundant product ions from Figure 6.1 (i.e., $\mathbf{x_4}$ and the $\mathbf{CO_2}$ loss from the charge-reduced species) were used to indicate the preferred electron irradiation time. The extracted ion abundance for $\mathbf{[M\text{-}2H]^{-\bullet}\text{-}CO_2}$ and $\mathbf{x_4}$ are plotted as a function of irradiation time in Figure 6.4D and 6.4E, respectively. In both Figure 6.4D and 6.4E, the extracted ion abundance reaches a maximum at an irradiation time of 30 ms, which is shorter than any other mass analyzer. Electron irradiation times used for EDD experiments on the QITMS were reported to be between 200 and 400 ms.[9] For EDD experiments performed in ICR cells electron irradiation times of 150-170 ms [2] up to 1 s [7, 13] have been reported.

6.3.4 *Examples of EDD for* $\boldsymbol{[M\text{-}2H]^{2-}}$ *parent ions (cardiodilatin and substance P)*

To explore a larger peptide than FLEEV that contains aspartic instead of glutamic acid residues, EDD was performed on cardiodilatin. The results of this EDD experiment are shown in

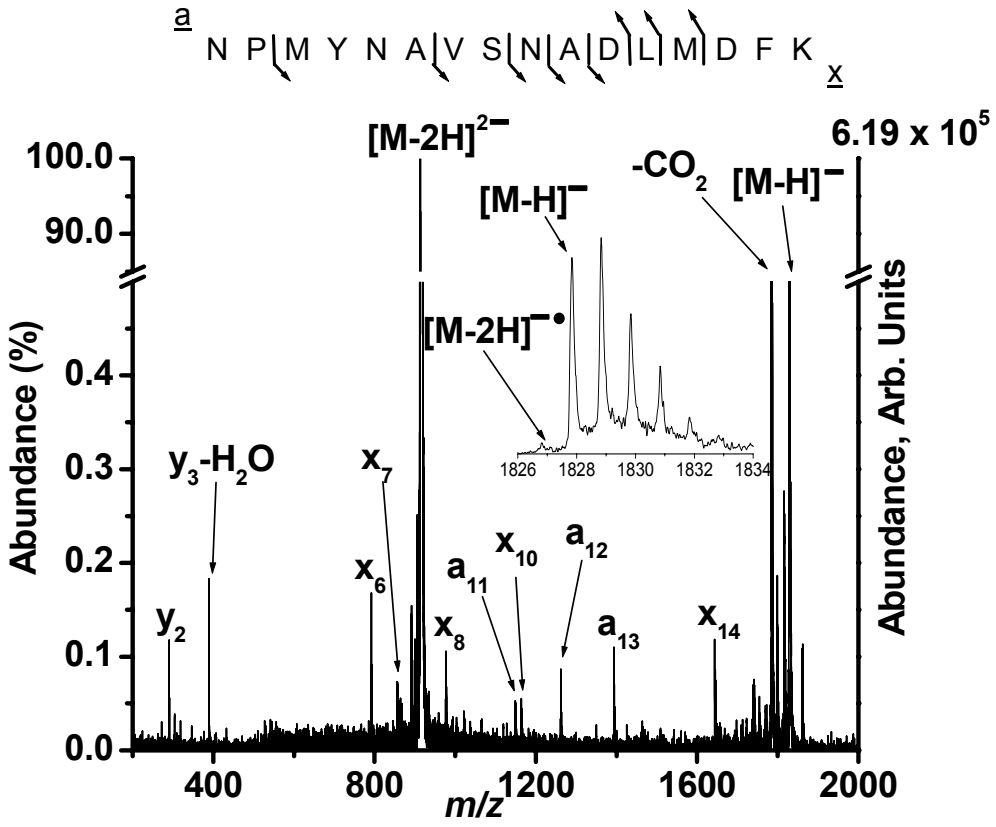

Figure 6.5 EDD spectrum of $\mathbf{[M\text{-}2H]^{2-}}$ cardiodilatin (1-16, human) using 28 eV electrons and an irradiation time of 30 ms. Inset: charge-reduced $\mathbf{[M\text{-}2H]^{-\bullet}}$ and $\mathbf{[M\text{-}H]^{-}}$.

Figure 6.5, where eight **a** / **x** and two **y** product ions were observed. Six of the eight C_α-C cleavages occur within three amino acid residues of the probable sites of deprotonation (i.e. the aspartic acids). This trend is in agreement with the idea that amino acid residues near the deprotonation site are expected to take part in charge solvation to a greater extent than residues remote from the charge site. As a result, C_α-C cleavage is expected to be favored near sites of deprotonation.[9] The charge-reduced ion is shown in the inset of Figure 6.5. Similar to FLEEV both odd- and even-electron oxidized ions were observed but the majority of the oxidized ion is comprised of the even electron **$[M-H]^-$** ion. This result suggests that the electron detachment efficiency for cardiodilatin is less than that of FLEEV or proton transfer to **$[M-2H]^{2-}$** of cardiodilatin from background cations is more preferred than for FLEEV. Because EDD proceeds through a radical ion intermediate, the lower relative abundance of the **$[M-2H]^{-\bullet}$** species for cardiodilatin explains the low product ion abundance.

Both ECD and EDD proceed through a radical ion intermediate, to evaluate the similarity of information gained between these two techniques EDD was performed on substance P, an ion commonly used in ECD studies. The result of performing EDD on the **$[M-2H]^{2-}$** charge state of substance P is given in Figure 6.6; both odd and even electron oxidized ions are observed in the inset. The only acidic site on the free-acid form of substance P is the carboxylic acid located at the C-terminus, thus the other site of deprotonation required to form **$[M-2H]^{2-}$** involved one of the hydrogens on an amide nitrogen.[9] Thus, the negative charge is not sequestered on a given side chain moiety. The resulting C_α-C cleavage produced an x-series of ions. The formation of an x-series during EDD is in contrast to the c-series that is characteristic of performing ECD on substance P. This difference is due to the location of the charged site on the radical ion intermediate. In negative ion mode, the negative charge is located on the C-terminal carboxylic acid thus an x-series of product ions is observed using EDD. The EDD results in Figure 6.6 indicate that for substance P the electron that gets detached by the high energy, incident electrons is preferentially the one not associated with the carboxylic acid moiety. Overall the spectrum in Figure 6.6 is comparable to the EDD of substance P results reported using a QITMS.[9] Like ECD, in EDD no peptide backbone bond cleavage is observed N-terminal to proline. Similar to the QITMS results, the

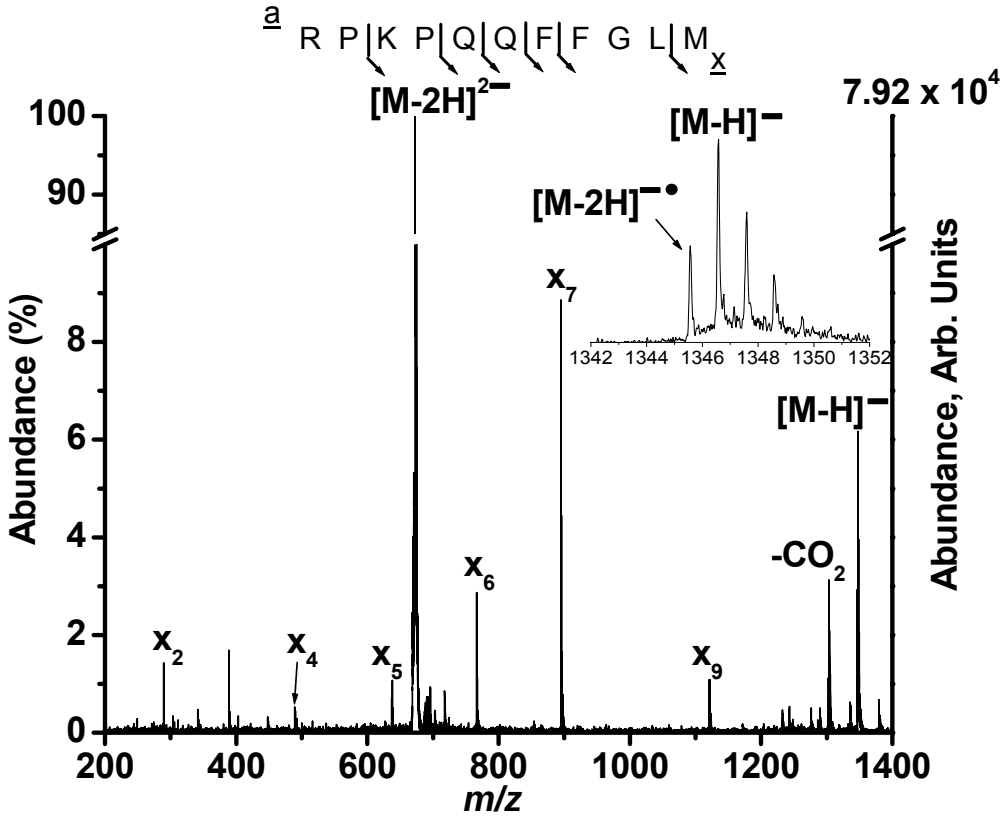

Figure 6.6 EDD spectrum of **[M-2H]$^{2-}$** substance P (free acid) using 28 eV electrons and an irradiation time of 30 ms. Inset: charge-reduced **[M-2H]$^{-\bullet}$** and **[M-H]$^{-}$**.

x_7 ion is the most abundant product ion and **CO_2** loss is prevalent. The abundant loss of **CO_2** from the charge-reduced ion is attributable to the presence of the C-terminal carboxylic acid. However, the relative abundance of **x_7** formation versus **CO_2** loss is greater in the EDD_{LIT} than in the QITMS.[9] According to reference [9] the lowest-energy channel for peptide backbone dissociation is C_α-C bond cleavage, which is in competition with decarboxylation. Decarboxylation has been calculated to be exothermic by 69 kJ mol^{-1} and the formation of **a•** and **x** product ions first requires the separation of the carboxy group from the peptide backbone, which is endothermic by 33 kJ mol^{-1}.[9] The observance of **CO_2** loss in both the EDD_{LIT} and the QITMS supports the idea that decarboxylation does compete with peptide backbone dissociation in both instruments. The larger relative abundance of the **x_7** ion for the EDD_{LIT} versus the QITMS data indicates that the 33 kJ mol^{-1} endothermic reaction barrier is more easily overcome in the EDD_{LIT} than in the QITMS. It may be easier to overcome the endothermic barrier for dissociation in the EDD_{LIT} versus the QITMS because more internal energy is

imparted to the parent ion during the electron detachment process in the EDD_{LIT} than in the QITMS. The use of higher electron kinetic energies on the ECD_{LIT} (28 eV) than on the QITMS (10-20 eV) support this idea, but more experiments are needed to study the differences in EDD between the two instruments.

6.3.5 *EDD of the* ***[M-6H]$^{6-}$*** *parent ion of insulin chain A*

All of the previous parent ions used for EDD experiments in this chapter have been doubly charged. Insulin chain A, when all of the cysteins are trioxidated, readily forms the **[M-6H]$^{6-}$** charge state under the nESI conditions described in the experimental section. Performing EDD on the **[M-6H]$^{6-}$** charge state resulted in the spectrum shown in Figure 6.7 where the fragmentation, collection, and MS/MS efficiencies are 84.7%, 99.1%, and 83.9%, respectively. EDD resulted in 75% of the C_α-C bonds being cleaved, see Figure 6.7A. Expanding the y-axis in Figure 6.8B reveals representative product ions and prominent losses of **CO_2** from the charge-reduced species, which is consistent with previous EDD data.

The relative abundance of the charge-reduced ions following EDD of insulin chain A is interesting and raises questions about the identity of these peaks. The isotopic distributions for the first and second charge-reduced species from EDD are plotted along with their respective charge states formed directly from nESI in Figure 6.8. The x-axis is broken so both charge states can be examined on one plot and the vertical, dashed line associated with each isotopic cluster represents the monoisotopic mass-to-charge ratio of the respective charge state if it were formed directly from nESI. In Figure 6.8, the **[M-6H]$^{5-\bullet}$** species generated from EDD of the **[M-6H]$^{6-}$** parent ion is deficient one hydrogen but has the same charge as the **[M-5H]$^{5-}$** species formed directly from nESI. Because the first charge reduced species (i.e., **[M-6H]$^{5-\bullet}$**) has the same hydrogen deficiency as the parent ion but has one less charge, the first charge reduced species must contain a free radical. In Figure 6.8, the **[M-6H]$^{4-}$** from EDD is deficient two hydrogens but has the same charge as the **[M-4H]$^{4-}$** species formed directly from nESI. With the **[M-6H]$^{4-}$** containing two fewer charges but the same hydrogen deficiency as the EDD parent ion, it is possible for the **[M-6H]$^{4-}$** species to contain two free radicals or a newly formed covalent bond created from the combination of the two radicals.

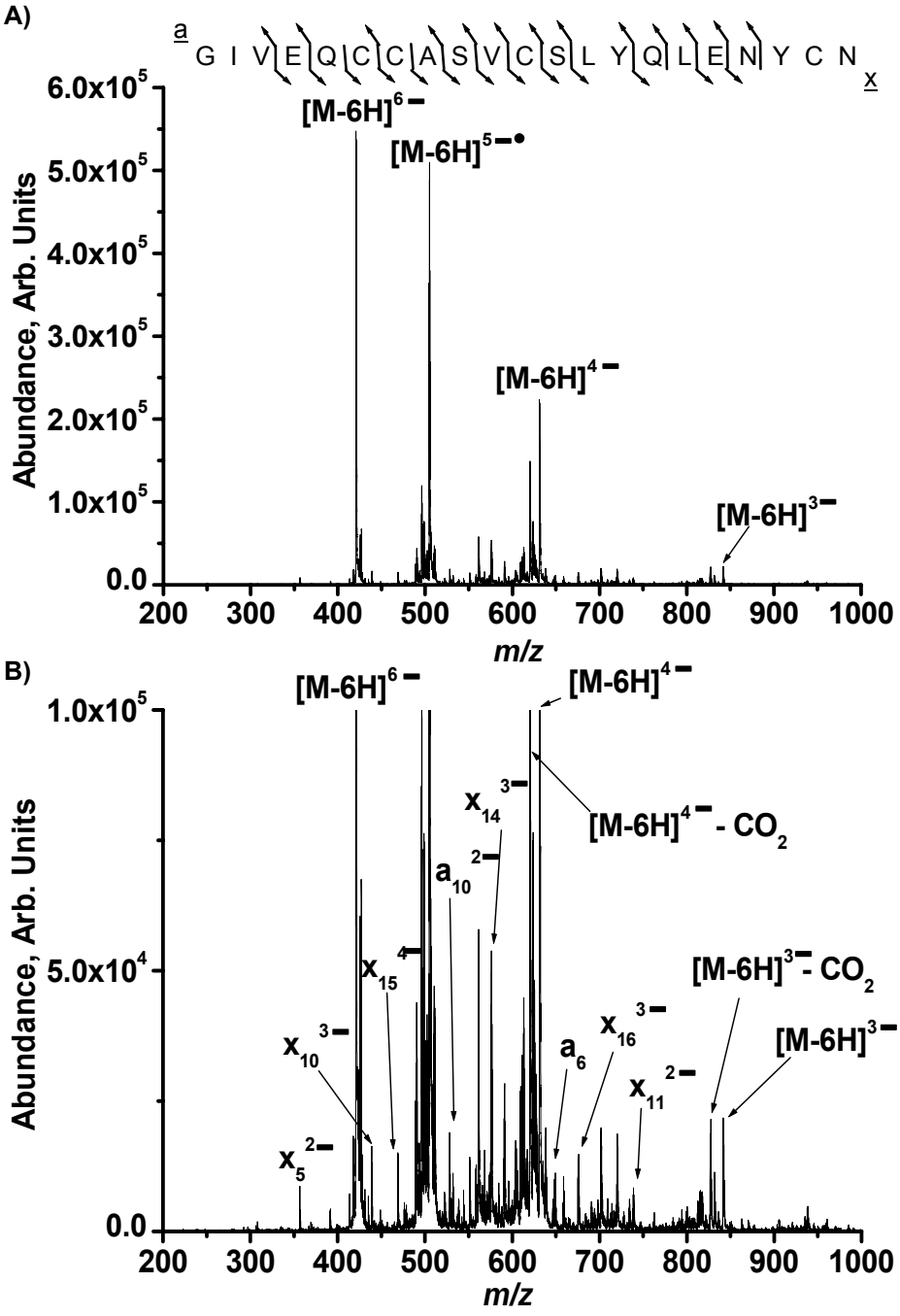

Figure 6.7 EDD of **[M-6H]$^{6-}$** insulin chain A. A) EDD spectrum showing sites of backbone cleavage for insulin chain A. B) Magnified view of EDD spectrum in A) showing the S/N of select product ions.

Attempts at identifying the radical nature of the charge-reduced species resulting from EDD have been made using gas-phase radical scavenger molecules (e.g., 7,7,8,8-tetracyanodiquinodimethane, TCNQ). The goal of the radical scavenger experiments was to

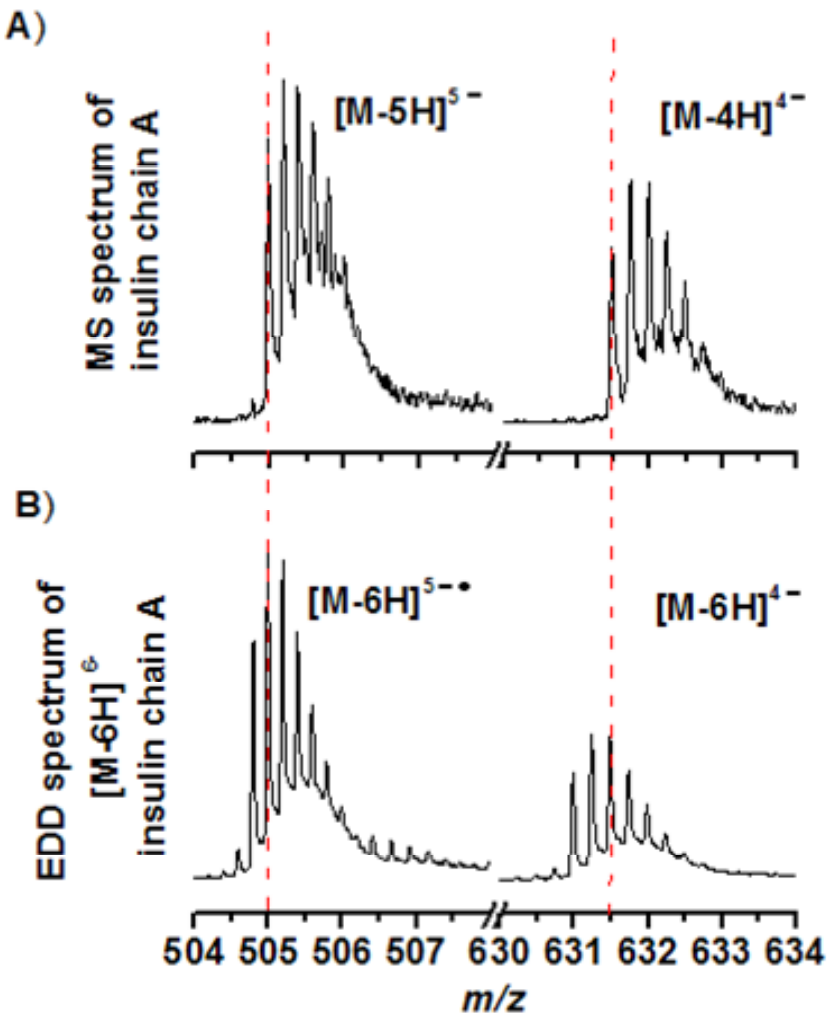

Figure 6.8 A) Isotopic distributions of the **[M-5H]$^{5-}$** and **[M-4H]$^{4-}$** charge states for insulin chain A formed directly from nESI. B) Isotopic envelopes of the **[M-6H]$^{5-\bullet}$** and **[M-6H]$^{4-}$** charge-reduced species formed from EDD of the **[M-6H]$^{6-}$** parent ion. The vertical line given for each charge state represents the theoretical, monoisotopic mass-to-charge ratio expected if that charge state was formed directly from nESI.

add one molecule of TCNQ to an ion for every free radical present on that ion.[14-16] The results from the radical scavenger experiments have not provided definitive answers due mainly to the difficulty associated with introducing the solid TNCQ into the EDD_{LIT}. At present, the radical nature of the charge-reduced species resulting from EDD is still unknown but the use of different reagents for radical ion-molecule scavenger reactions is being actively pursued in our group. Preliminary results have been promising and show potential for use in identifying the charge-reduced species produced from EDD.

6.3.6 *Explanation of proton transfer in EDD*

The formation of the **[M-H]$^-$** ion from electron detachment of FLEEV **[M-2H]$^-$** observed in Figure 6.1 is interesting. While the **[M-2H]$^{-\bullet}$** ion can be explained from electron detachment, the formation of the even electron **[M-H]$^-$** species cannot because it contains one proton more than its parent ion. This behavior has been noted before in EDD where it was proposed that proton-transfer reactions between the parent dianion and a radical cation formed by electron ionization (EI) or from **H•** transfer from neutral compounds are responsible for the **[M-H]$^-$** species.[1, 9] No experiments where performed to determine the actual mechanism of **[M-H]$^-$** formation in references [1, 9], rather the proposed mechanisms were offered only as an explanation for the observation of such peaks in EDD spectra. In an effort to study these two potential reaction pathways in the EDD_{LIT}, EI spectra of the EDD cell background were acquired in positive mode under two different trapping conditions. The results from the two background experiments are shown in Figure 6.9. In Figure 6.9A, a low mass cutoff sufficient to trap **$[H_2O]^{+\bullet}$** was used while 26 eV electrons irradiated residual gases within the ECD cell for 15 ms. Under such conditions a spectrum consistent with background air is observed with **$[H_2O]^{+\bullet}$** and **$[H_3O]^+$** along with **$N_2^{+\bullet}$** and **$O_2^{+\bullet}$**. The water could be a source of **H•** for transfer to **[M-2H]$^{-\bullet}$** thus producing the even electron **[M-H]$^-$** ion. Alternatively, **$[H_3O]^+$** could be a source of **H^+** for proton transfer to **[M-2H]$^{2-}$** which would also result in the formation of the **[M-H]$^-$** ion. However, for **$[H_3O]^+$** to react with the parent dianion, ions of opposite polarity and considerably different mass-to-charge values must be mutually stored in the EDD cell. Such a situation is unlikely under the conditions used to acquire the FLEEV EDD spectrum in Figure 6.1.

Increasing the low mass cutoff to a value compatible with trapping FLEEV and irradiating the EDD_{LIT} background in positive mode with 26 eV electrons for 15 ms resulted in the spectrum shown in Figure 6.9B. While several ions were detected the peak at *m/z* 149 corresponds to protonated phthalic anhydride (PPA), which is universal to the EI spectra of the phthalate class of compounds. A peak representative of protonated phthalic acid (*m/z* 167) is also indicative of phthalates. Comparing the spectra in Figure 6.9, the abundance of PPA is ~100 times greater than the abundance of **$[H_3O]^+$**, suggesting that phthalates are present in the EDD_{LIT} at a higher number density than background water. Efforts to identify the specific phthalate present in the system have proven unsuccessful but

performing CID on *m/z* 292 generates product ions at *m/z* 149 and 167, suggesting that *m/z* 292 is also a phthalate-related ion.

Regardless of the identity of the phthalate present, the available proton on protonated phthalic acid or PPA would react with **[M-2H]$^{2-}$** to form the observed **[M-H]$^{-}$** ion because the proton affinity (PA) of PPA or protonated phthalic acid is less than that of **[M-2H]$^{2-}$**. The proton affinity for the phthalic anhydride is considered to be < 195 kcal mol^{-1} [17]. The proton affinities of the neutral,

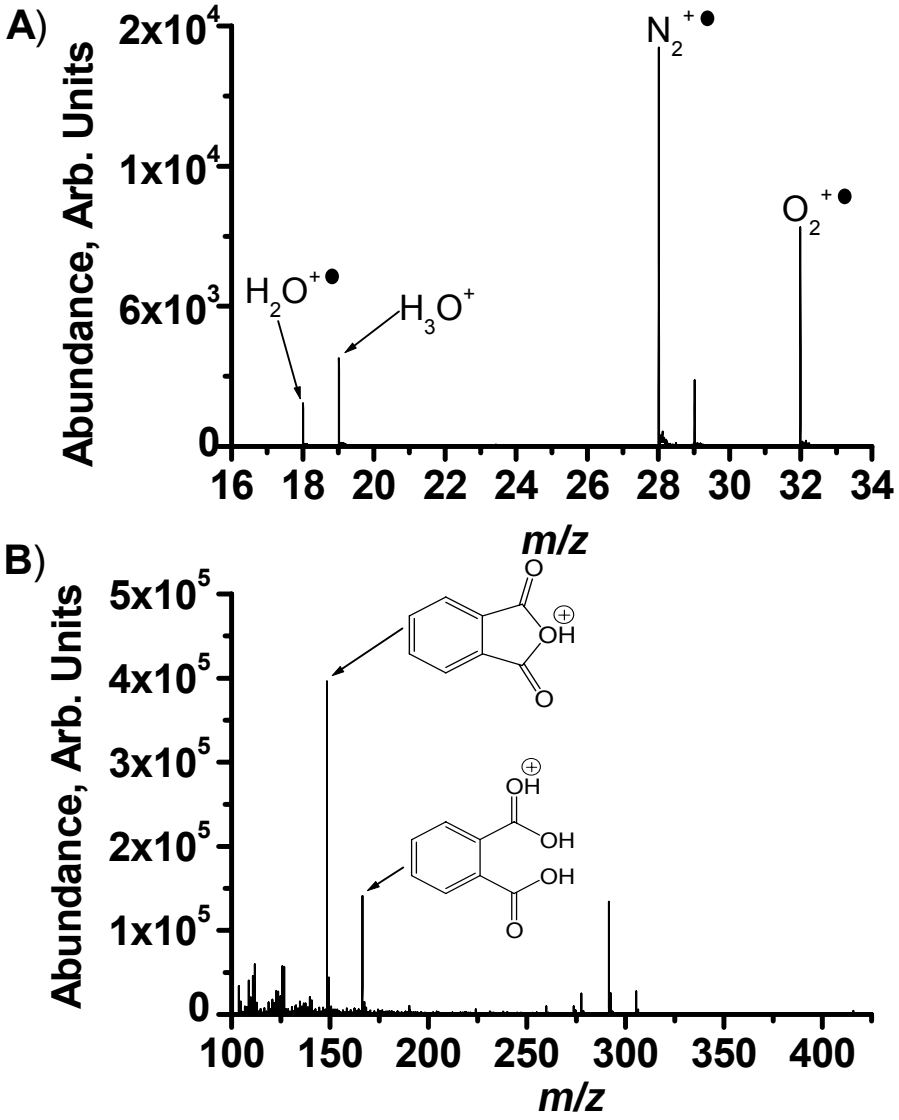

Figure 6.9 Background spectra of EDD_{LIT} residual gas in positive ion mode under A) conditions to trap *m/z* 18 and B) conditions to trap *m/z* 149.

20 common amino acids have been reported to be within the range 210.0 to > 243.2 kcal mol^{-1}[18], which would make the proton affinity of a dianion even larger than 243.2 kcal mol^{-1}. For example, the proton affinity of carboxylate moiety is 345.9 kcal mol^{-1}.[19] Thus the transfer of a proton from PPA to a multiply charged peptide anion would be thermodynamically favorable. Furthermore, it has been suggested by both theoretical and experimental evidence that if the electron affinity of an anionic reagent is greater than 60-70 kcal mol^{-1} proton transfer is favored over electron transfer [19]. In the present case, the peptide anion can be considered the anionic reagent. The negative sites on FLEEV are the carboxylic acids; their carboxylate forms have electron affinities of approximately 77.4 kcal mol^{-1} [19]. Thus proton transfer from PPA would be favored over electron transfer from the $\mathbf{[M\text{-}2H]^{2-}}$ parent ion. However, as with $\mathbf{[H_3O]^+}$, phthalate cations would have to be mutually trapped with the parent anion in the EDD_{LIT} for proton transfer to occur. Creating the same trapping potential typically used for EDD experiments (i.e., the same relative potentials used to trap anions were applied to the EDD_{LIT} front and back trapping electrodes) and irradiating the vacuum chamber background with 26 eV electrons for 15 ms (spectrum not shown) resulted in the phthalate cation at *m/z* 292 being trapped. Therefore, it is possible that during EI of background gases could form cationic phthalate ions which are able to undergo proton transfer reactions to the $\mathbf{[M\text{-}2H]^{2-}}$ parent anions resulting in the formation of $\mathbf{[M\text{-}H]^-}$ during EDD experiments within the EDD_{LIT}.

The insulin chain A results showed that performing EDD on the $\mathbf{[M\text{-}6H]^{6-}}$ parent ion does not produce ions that correspond to the transfer of a proton from phthalate cations present in the EDD_{LIT} to the peptide anion (see Figure 6.8). For the insulin chain A used in this work, all of the cysteins were in their trioxidated state. The electron affinity for the trioxidated cystein side chains ($\mathbf{SO_3^{-\bullet}}$) could not be found in the literature, but electron affinities for $\mathbf{O_3^{-\bullet}}$ and $\mathbf{SO_2^{-\bullet}}$ moieties are 49.7 kcal mol^{-1} and 27.2 kcal mol^{-1}, respectively.[19] These electron affinities are within the range (< 60-70 kcal mol^{-1}) where electron transfer from the insulin chain A peptide to the phthalic anhydride would be favored over proton transfer from the phthalic anhydride to the peptide. As a result, the isotopic distributions of the charge-reduced species for insulin chain do not contain more hydrogens than the parent ion, as seen in Figure 6.8.

6.4 Conclusions

Electron detachment dissociation has been demonstrated for the first time in a EDD_{LIT} device. EDD spectra similar to those reported previously using a QITMS were observed but were acquired with superior mass resolving power due to the TOF mass analysis. It was demonstrated that EDD can be successfully performed on both acidic and basic peptides in the EDD_{LIT}. The effect of electron kinetic energy and irradiation time on EDD operation was also characterized. Electron energies of 28 eV and an irradiation time of 30 ms were found to be optimal for the peptides studied.[12] The irradiation time of 30 ms allows EDD to be performed in the EDD_{LIT} faster than in any other mass analyzer presently available. Finally, experiments were carried out to explain the formation of **$[M-H]^-$** during EDD of **$[M-2H]^-$** parent ions. The results support the idea that phthalate present as a neutral in the vacuum chamber is being ionized by EI during the EDD process. When the charge on the peptide anion is localized around a carboxylate moiety, the cationic phthalate transfers a proton to the anionic parent ion. If the charge on the peptide anion is localized around a trioxidated moiety, an electron from the anionic parent is transferred to and results in the neutralization of the cationic phthalates.

6.5 References

1. Budnik, B. A.; Haselmann, K. F.; Zubarev, R. A. Electron Detachment Dissociation of Peptide Di-Anions: an Electron-Hole Recombination Phenomenon. *Chemical Physics Letters*. **2001**, 342, p. 299-302.

2. Kjeldsen, F.; Hørning, O. B.; Jensen, S. S; Giessing, A. M. B.; Jensen, O. N. Towards Liquid Chromatography Time-Scale Peptide Sequencing and Characterization of Post-Translational Modifications in the Negative-Ion Mode Using Electron Detachment Dissociation Tandem Mass Spectrometry. *Journal of the American Society for Mass Spectrometry*. **2008**, 19, p. 1156-1162.

3. Yang, J.; Mo, J.; Adamson, J. T.; Hakansson, K. Characterization of Oligodeoxynucleotides by Electron Detachment Dissociation Fourier Transform Ion Cyclotron Resonance Mass Spectrometry. *Analytical Chemistry*. **2005**, 77, p. 1876-1882.

4. McFarland, M.A.; Marshall, A. G.; Hendrickson, C. L.; Nilsson, C. L.; Fredman, P.; Mansson, J. E. Structural Characterization of the GM1 Ganglioside by Infrared Multiphoton Dissociation, Electron Capture Dissociation, and Electron Detachment Dissociation Electrospray Ionization FT-ICR MS/MS. *Journal of the American Society for Mass Spectrometry*. **2005**, 16, p. 752-762.

5. Mo, J.; Hakansson, K. Characterization of Nucleic Acid Higher Order Structure by High-Resolution Tandem Mass Spectrometry. *Analytical and Bioanalytical Chemistry*. **2006**, 386, p. 675-681.

6. Wolff, J.J.; Amster, I. J.; Chi, L.; Linhardt, R. J. Electron Detachment Dissociation of Glycosaminoglycan Tetrasaccharides. *Journal of the American Society for Mass Spectrometry*. **2007**, 18, p. 234-244.

7. Wolff, J.J.; Chi, L.; Linhardt, R. J.; Amster; I. J. Distinguishing Glucuronic from Iduronic Acid in Glycosaminoglycan Tetrasaccharides by Using Elecctron Detachment Dissociation. *Analytical Chemistry*. **2007**, 79, p. 2015-2022.

8. Adamson, J.T.; Hakansson, K. Electron Detachment Dissociation of Neutral and Sialylated Oligosaccharides. *Journal of the American Society for Mass Spectrometry*. **2007**, 18, p. 2162-2172.

9. Kjeldsen, F.; Silivra, O. A.; Ivonin, I. A.; Haselmann, K. F.; Gorshkov, M.; Zubarev, R. A. C_{α}-C Backbone Fragmentation Dominates in Electron Detachment Dissociation of Gas-Phase Polypeptide Polyanions. *Chemistry - A European Journal*. **2005**, 11, p. 1803-1812.

10. Satake, H.; Hasegawa, H.; Hirabayashi, A.; Hashimoto, Y.; Baba, T. Fast Multiple Electron Capture Dissociation in a Linear Radio Frequency Quadrupole Ion Trap. *Analytical Chemistry*. **2007**, 79, p. 8755-8761.

11. Liu, D. F.; Wyttenbach, T.; Carpenter, C. J.; Bowers, M. T. Investigation of Noncovalent Interactions in Deprotonated Peptides: Structural and Energetic Competition between Aggregation and Hydration. *J. Am. Chem. Soc.* **2004**, 126, p. 3261 - 3270.

12. Haselmann, K. F.; Budnik, B. A.; Kjeldsen, F.; Nielsen, M. L.; Olsen, J. V.; Zubarev, R. A. Electronic Excitation gives Informative Fragmentation of Polypeptide Cations and Anions. *European Journal of Mass Spectormetry*. **2002**, 8, p. 117 - 121.

13. Kalli, A.; Hakansson, K. Preferential Cleavage of S-S and C-S Bonds in Electron Detachment DIssociation and Infrared Multiphoton Dissociation of Disulfide-Linked Peptide Anions. *International Journal of Mass Spectrometry*. **2007**, 263, p. 71-81.

14. McEwen, C. N.; Rudat, R. A. Radical Trapping in a Mass Spectrometer Ion-Source. 1. *Journal of the American Chemical Society*. **1981**, 103, p. 4343-4349.

15. McEwen, C. N.; Rudat, M. A. Gas-Phase Radical Structures - Radical Trapping. 2. *Journal of the American Chemical Society*. **1981**, 103, p. 4349-4354.

16. McEwen, C. N.; Rudat, M. A. Isomerization of Gas-Phase Hydrocarbon Ions - Raical Trapping. 3. *Journal of the American Chemical Society*. **1981**, 103, p. 4355-4359.

17. Jarvis, M. J. Y.; Koyanagi, G. K.; Zhao, X.; Covey, T. R.; Bohme, D. K. Scrubbing Ions with Molecules: Kinetic Studies of Chemical Noise Reduction in Mass Spectrometry Using Ion-Molecule Reactions with Dimethyl Disulfide. *Analytical Chemistry*. **2007**, 79, p. 4006 - 4012.

18. Gorman, G. S.; Speir, J. P.; Turner, C. A.; Amster, I. J. Proton Affinities of the 20 common Amino Acids. *Journal of the American Chemical Society*. **1992**, 114, p. 3986-3988.

19. Gunawardena, H. P.; He, M.; Chrisman, P. A.; Pitteri, S. J.; Hogan, J. M.; Hodges, B. D. M.; McLuckey, S. A. Electron Transfer versus Proton Transfer in Gas-Phase Ion/Ion Reactions of Polyprotonated Peptides. *Journal of the American Chemical Society*. **2005**, 127, p. 12627-12639.

Chapter 7

Activated Ion Electron Capture Dissociation (AI-ECD) in a Linear Ion Trap (LIT)

7.1 Introduction

7.1.1 *Ion activation for the improvement of ECD*

As described in Chapter 1, several methods of ion activation exist that cover a range of energies and result in the formation of different types of product ions.[1] With the application of mass spectrometry to the field of proteomics, there has been a drive toward developing an activation method that can provide complete sequence coverage of intact proteins thereby allowing *de novo* sequencing. Electron capture dissociation (ECD) is an activation method used in MS/MS experiments that comes closest to providing complete protein sequence coverage while allowing labile bonds to remain intact.[2-4]

In addition to preserving labile bonds, ECD has demonstrated the ability to cleave the protein backbone while not disrupting non-covalent, intramolecular interactions.[5] While the propensity for keeping non-covalent interactions intact has allowed ECD to be used to study changes in gas phase ion structure [6], the retention of non-covalent interactions can be detrimental to the goal of acquiring complete protein sequence coverage because they prevent product ion separation and thus detection. By disrupting the intramolecular interactions through vibrational excitation, the amount of dissociation from ECD increases.[7] Several methods have been used for disrupting the intramolecular interactions before, during, or after ECD, and they include infrared multiphoton dissociation (IRMPD), sustained off-resonance irradiation collision induced dissociation (SORI-CID) and blackbody infrared radiative dissociation (BIRD).[8] IR activation is the most widely used method due to practical considerations. For example, with IRMPD no collision gas is required which is not the case for CID where the gas must be pumped away after CID and prior to mass analysis with FTICR-MS.

7.1.2 *Use of infrared (IR) radiation for ion activation*

Due to the low energy of a single IR photon, multiple photons must be absorbed to accumulate a sufficient amount of vibrational energy to overcome the critical energy for dissociation at which point cleavage of the bonds with lowest activation energy is observed.[9, 10] Because multiple photons must be absorbed to overcome the dissociation threshold, the use of IR activation has been implemented primarily on ion trapping instruments (i.e., quadrupole ion traps and FTICR-MS instruments).[11-17] IRMPD has also been incorporated into a rf-only hexapole external to an ICR cell[18] and a quadrupole collision cell (q) that was part of a hybrid quadrupole time-of-flight (QqTOF) mass spectrometer.[19]

7.1.3 *Development of AI-ECD*

Ion activation used in conjunction with ECD has been given the name activated ion ECD (AI-ECD).[7] To-date, all AI-ECD experiments have been performed in FTICR-MS instruments. AI-ECD has been developed to increase the amount of product ion information acquired in one MS/MS experiment and thus improve confidence in the identification of the parent ion. The extent of protein ion dissociation observed from ECD depends on the amino acid sequence and the higher order structure of the protein.[2, 20] AI-ECD has shown the ability to produce different amounts of protein ion dissociation than ECD alone by disrupting non-covalent bonds that maintain parent ion higher order structure and hold non-separated product ions together.[21] Other results have shown that applying IR radiation to the charge-reduced species following ECD of proteins results in extensive sequence coverage comprised mainly of **c** and **z** ions.[22] AI-ECD has also been used to probe parent ion internal energy during the ECD process.[21, 23] ECD and IRMPD were first used independently to study a glycosolated peptide,[24] but no attempt was made to perform ECD on an IR-activated ion because the orientation of the CO_2 laser and electron filament precluded their simultaneous use. To achieve simultaneous ECD and IRMPD, other researchers have moved the path of the CO_2 laser beam off-axis with respect to the electron beam.[25] Results from this work demonstrated that the number of product ions formed increased when ECD was being performed simultaneously with IR-heating relative to ECD alone. By incorporating a dispenser cathode an IR laser could be aligned along the axis of the hollow electron beam thereby increasing the interaction

volume of activated ions with the incident electron beam.[25] With the hollow electron beam, performing ECD and IRMPD consecutively and simultaneously did increase the sequence coverage of the peptide defensin, but ECD of IR-activated ions only occurred when the activated ions overlapped with the area of the hollow electron beam. Recently, work has been published where the IR and electron beams are introduced through opposite ends of the ICR cell (i.e., axial trapping electrodes).[26] This method has demonstrated improved overlap of the IR and electron beams. Due to the improved overlap, increased sequence coverage for substance P and melittin was reported when ECD and IRMPD were performed simultaneously over performing each MS/MS method individually.

As described in the Introduction Chapter, a hybrid mass spectrometer [27] consisting of a linear ion trap (LIT) located orthogonally to a TOF mass analyzer was introduced in 2007 that was capable of performing ECD. This instrument has been modified to allow IR activation to be performed in the LIT where ECD occurs, which will be referred to as the ECD_{LIT} for clarity. As in Ref. [26], the IR laser and electron beams are introduced through opposite ends of the ECD_{LIT}. By incorporating IR activation, it became possible to conduct AI-ECD experiments in the ECD_{LIT} for the first time. Results from performing AI-ECD experiments on the $\mathbf{[M+7H]^{7+}}$ charge state of ubiquitin and the $\mathbf{[M+32H]^{32+}}$ charge state of carbonic anhydrase will be discussed. Also, practical considerations about aligning the CO_2 laser on the ECD_{LIT} system will be addressed, and the effect of bath gas pressure will be described.

7.2 Experimental

7.2.1 *Samples*

Leucine enkephalin (YGGFL, M_r: 555.62), substance P (RPKPQQFFGLM; free acid, M_r: 1348.70), angiotensin I (DRVYIHPFHL, M_r: 1296.48), bovine ubiquitin (M_r: 8.6 kDa), and bovine carbonic anhydrase (M_r: 29 kDa) were purchased from Sigma-Aldrich, Inc. (St. Louis, MO) and used without further purification. nESI solutions were made for each analyte by diluting the appropriate aqueous stock solution to a concentration of 5 μM in either 50:50 v% methanol/water or 50:50 v% acetonitrile/water. Acetic acid (1% by volume) or formic acid (1% by volume) was added to the final sample mixture to aid in the electrospray process.

7.2.2 *Laser / instrument orientation and alignment*

AI-ECD experiments were performed on a NanoFrontier LIT/TOF (Hitachi High Technologies) mass spectrometer.[27] The instrument was modified with a 38 mm I.D., 118 mm O.D. zero-length reducer flange (MDC Vacuum Products, LLC) for securing a 85% IR transmissive, 50 mm O.D. BaF_2 window (Edmund Optics). A 25 W CO_2 laser (Synrad Inc.) was secured to a vibrationally isolated laser table located adjacent to the LIT/TOF instrument. As shown in Figure 7.1, two gold mirrors were used to direct the IR radiation along the radial axis of the ECD_{LIT}. The IR beam was focused to the axial center of the ECD_{LIT} by passing through a 25.4 mm O.D., 38 cm focal length zinc selenide lens (Lambda Research Optics, Inc.). Both the ZnSe lens and the gold mirror located immediately before it were mounted on magnetic optic bases which were used to secure both optical elements to the nanoFrontier instrument housing. The gold mirror was fastened to a translational stage that allowed positioning of the mirror in the x-direction. The ZnSe lens was secured to a translational stage that provided movement in the y-direction.

Alignment of the IR beam was achieved by using a green-emitting diode. The silver mirror shown in Figure 7.1 allows the green diode beam to be oriented collinearly with the IR laser beam,

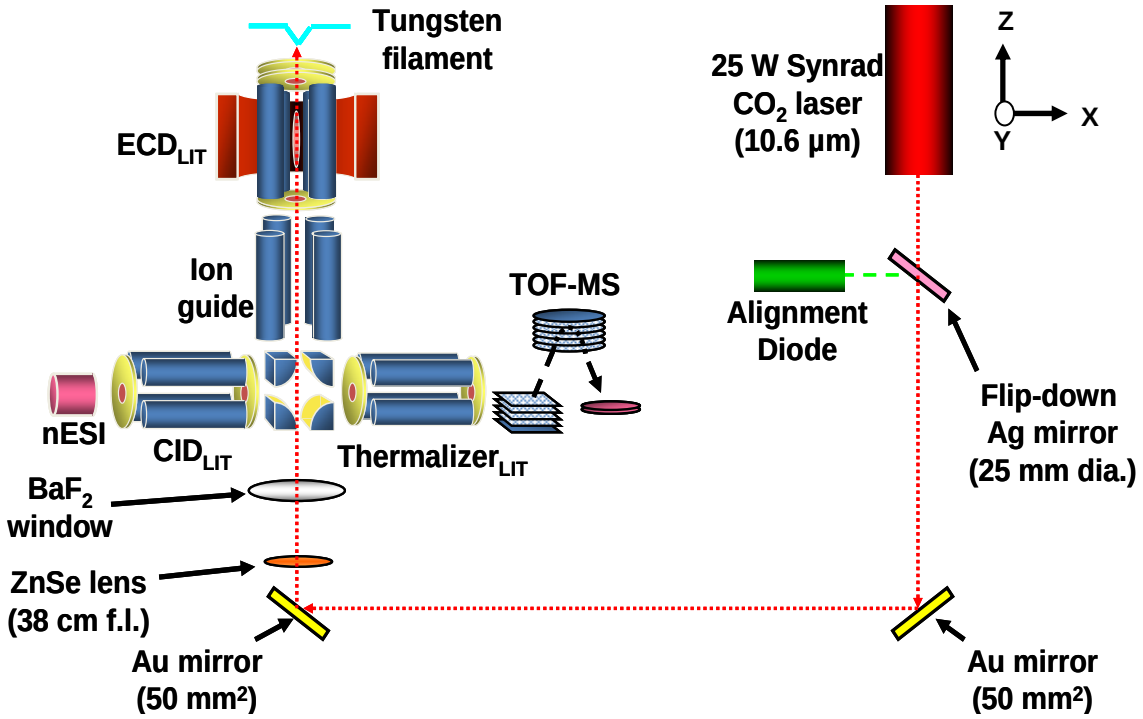

Figure 7.1. Simplified diagram showing the optical components and orientation associated with the CO_2 laser and nanoFrontier mass spectrometer. The diagram is not to scale.

and the mirror can also be flipped down parallel to the laser table to allow the IR beam to pass unobstructed after alignment is complete. IR-sensitive paper was used to ensure the green diode and IR beam were aligned at each optical component shown in Figure 7.1. At this stage of alignment (i.e., visual alignment using the green diode) the position and angles of the two gold mirrors were adjusted until two conditions were met. First, the back reflectance of the green diode off of the BaF_2 window and ZnSe lens was collinear with the incident diode beam. Second, the green diode beam was centered through a 5 mm I.D. hole in the Einzel lens of the quadrupole bender located in the vacuum chamber of the mass spectrometer.

With the IR and diode beams collinear and visually aligned to the radial center of the ECD_{LIT} axis, fine positioning of the IR beam can be performed. Optical alignment can not be used for this purpose because there is no path the IR beam could take to exit the instrument past the tungsten filament which is used to generate free electrons for ECD. The tungsten filament is located in the radial center of the ECD_{LIT} because it is centered on the back flange of the ECD device. When the IR beam is aligned properly it should be incident upon the tungsten filament resulting in an increase in the filament's temperature. An increase in the filament temperature would increase the number of free electrons generated from the filament surface. Therefore, alignment of the IR beam can be done by monitoring the electron current emitted from the filament. To make monitoring changes in electron current as sensitive as possible, the ECD_{LIT} conditions are set for maximum electron transmission. Using a rf amplitude of 0.0 $V_{0\text{-}p}$, high kinetic energy electrons (~ 11 eV) are used to generate a low baseline level of electron current (0.05 μA). With the IR laser triggered, the y-position of the ZnSe lens and the x-position of the gold mirror located immediately before the ZeSe lens are adjusted until a maximum in the electron current is measured.

7.2.3 *Implementation of AI-ECD*

Ions are generated using nESI and accumulated in the CID_{LIT} (see Figure 7.1). Parent ions are then isolated in the CID_{LIT} and transferred to the ECD_{LIT} where they can be irradiated with electrons or IR photons. The control software for the ECD_{LIT} is written in LabVIEW code (National Instruments Inc.) and provides the user the ability to perform ECD or IR activation by themselves, simultaneously, or sequentially (either ECD then IR activation or vice versa). The specific operating

conditions used to acquire the data presented in this chapter will be provided during the discussion of the appropriate figures and results. Following ECD, IR activation, or a combination of both (e.g., AI-ECD) the product ions and any remaining parent ions are sent to the reflectron TOF for mass analysis.

7.3 Results and Discussion

7.3.1 *Optimization of ECD_{LIT} trapping conditions for IRMPD*

Final alignment of the IR beam is achieved by monitoring the extent of IRMPD observed using leucine enkephalin with the goal of achieving maximum fragmentation efficiency. The first spectra acquired from performing IRMPD in the ECD_{LIT} are shown in Figure 7.2. The abundance of the isolated, protonated molecule can be observed in Figure 7.2A. Using the laser alignment obtained by monitoring the emitted electron current, the IRMPD spectrum shown in Figure 7.2B is acquired with 30 ms of IR irradiation time and a rf amplitude of 17.7 $V_{0\text{-}p}$. The depth of the Dehmelt pseudopotential well is proportional to the rf amplitude. A larger rf amplitude indicates a deeper trapping well depth

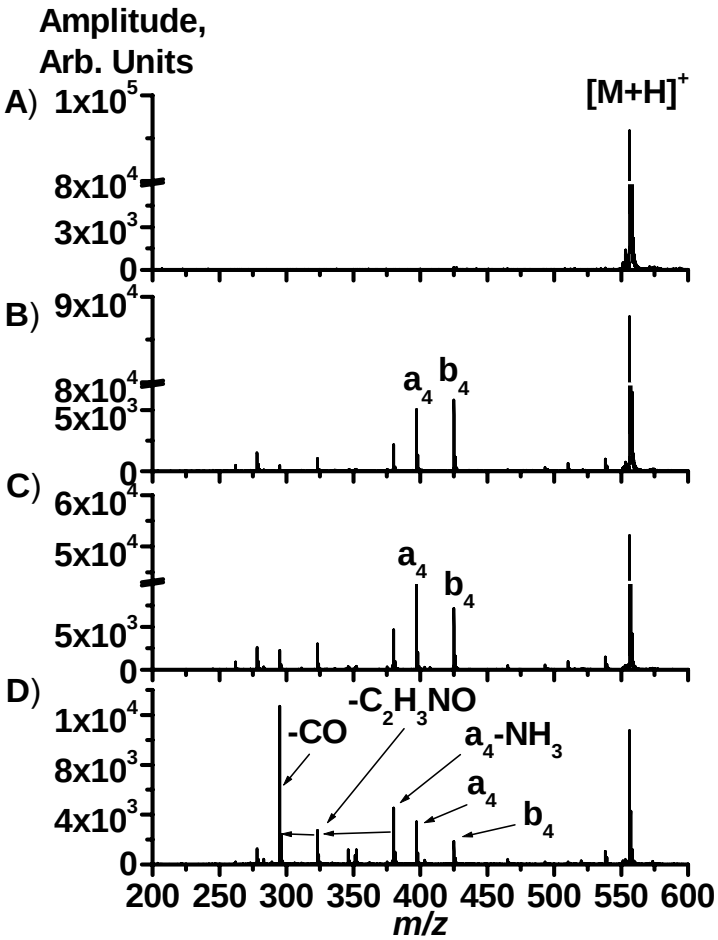

Figure 7.2 Optimization of ECD_{LIT} parameters for IRMPD. A) Isolation of $[M+H]^+$ YGGFL in the ECD_{LIT}. B) The first IRMPD spectrum acquired on the ECD_{LIT} instrument (IR irradation time = 30 ms, rf ampitude = 17.7 $V_{0\text{-}p}$). C) IRMPD spectrum acquired after re-positioning the ZnSe lens and gold mirror, all other parameters were the same as in B). D) IRMPD spectrum using the same laser alignment as in C) but the helium bath gas pressure was decreased to 1.5×10^{-4} torr and the rf amplitude was increased to 59.0 $V_{0\text{-}p}$.

which confines the ions closer to the radial center of the ECD_{LIT}. Because minimal dissociation of the **$[M+H]^+$** parent ion was observed in Figure 7.2B, the ZnSe lens and gold mirror translatable in the x-direction were repositioned until the maximum amount of dissociation was achieved, as shown in Figure 7.2C. With the laser aligned, the fragmentation efficiency in Figure 7.2C is still < 50%. The results in Figure 7.2C highlight the difficulty of performing IRMPD in the linear quadrupole ion trap due to their inherently high bath gas (typically helium) pressures (~$1.5x10^{-3}$ torr).

The helium bath gas provides the benefit of improving the sensitivity and resolution of three-dimensional and linear quadrupole ion traps [28], where ion kinetic and internal energy are transferred to the helium molecules through collisions.[29] However, this collisional cooling occurs at the detriment of IRMPD, if the rate of ion internal energy dissipation due to collisions occurs faster than internal energy deposition from the absorption of IR photons then limited dissociation will be observed (as seen in Figure 7.2C). To decrease the rate of internal energy loss by collisional cooling and thus improve dissociation from IRMPD, the temperature of the He bath gas can be increased in a process referred to as thermally assisted (TA)-IRMPD.[30] Unfortunately heating the ECD_{LIT} to temperatures higher than those produced from the tungsten electron filament is not an option due to concerns about the temperature stability of the neodymium permanent magnet used to house the ECD_{LIT}.[27] Another option is to pulse in the bath gas to aid in parent ion trapping, pump it away before IR activation to reduce the extent of internal energy loss by collisional cooling, then reintroduce the bath gas for improved product ion trapping and detection.[31] Because no pulse valve could be readily configured to the ECD_{LIT} the most straightforward method to reduce the rate of internal energy loss by collisional cooling is to decrease the helium bath gas pressure. By decreasing the helium bath gas pressure in the ECD_{LIT} to $1.5x10^{-4}$ torr and increasing the rf amplitude to 59.0 $V_{0\text{-}p}$, the amount of dissociation during IRMPD is increased, as illustrated in Figure 7.2D. Increasing the rf amplitude radially compresses the ion cloud thereby improving the overlap of the IR photons and the trapped ions. It was found that only increasing the rf amplitude did not improve the amount of dissociation significantly and that the greatest improvement was found by also lowering the helium bath gas pressure. The fragmentation efficiency of the spectrum in Figure 7.2D is 60%, and the

product ions observed are consistent with dissociation of YGGFL by vibrational excitation in a three-dimensional ion trap.[32]

7.3.2 *Optimization of ECD_{LIT} parameters for ECD and IR activation*

A tradeoff exists between the optimal bath gas pressures for performing IR activation versus ECD. Through collisional cooling, the bath gas radially focuses the ions to the center of the ECD_{LIT}. The radial focusing improves the overlap of the ion cloud with the incident electron and IR beams, which are aligned collinear to the ECD_{LIT} axis. The improved overlap is beneficial for parent ion electron capture and IR activation. In addition to radial focusing, collisional cooling also reduces the vibrational internal energy of ions as they undergo collisions with the bath gas, i.e., the ions are deactivated. Because ECD does not rely on the excitation of vibrational modes for dissociation, deactivation is not an important factor. Conversely, IRMPD produces product ions by increasing the ion internal energy until the critical energy for dissociation is overcome. Deactivation brought about by collisional cooling removes internal, vibrational energy gained by the parent ion through the absorption of IR photons. For the absorption of IR photons to cause dissociation, the rate of ion activation must be greater than the rate of ion deactivation. The rate of deactivation can be decreased by lowering the pressure of the helium bath gas. Thus the helium bath gas pressure must be decreased until a compromise in ECD and IRMPD performance is reached to allow AI-ECD to be performed.

The choice of which bath gas pressure to operate the ECD_{LIT} at is determined by the type of dissociation that is preferred. In the case of AI-ECD experiments, the type of dissociation desired is brought about by electron capture processes and IR radiation is used only to activate the parent ion rather than induce dissociation. The effect of bath gas pressure on performing IRMPD and ECD, but not together, is shown in Figure 7.3. Reducing the bath gas pressure to 7.5×10^{-5} torr resulted in an ECD fragmentation efficiency of 4.6%, as illustrated in Figure 7.3A. At the same pressure, the extent of dissociation due to the absorption of IR photons is also small as evidenced by the fragmentation efficiency of 5.9% in Figure 7.3B. Increasing the pressure by a factor of two, to 1.5×10^{-4} torr, increased the ECD fragmentation efficiency to 23.1% (Figure 7.3C). The increase in bath gas pressure resulted in a concomitant decrease in the IRMPD fragmentation efficiency, as shown in

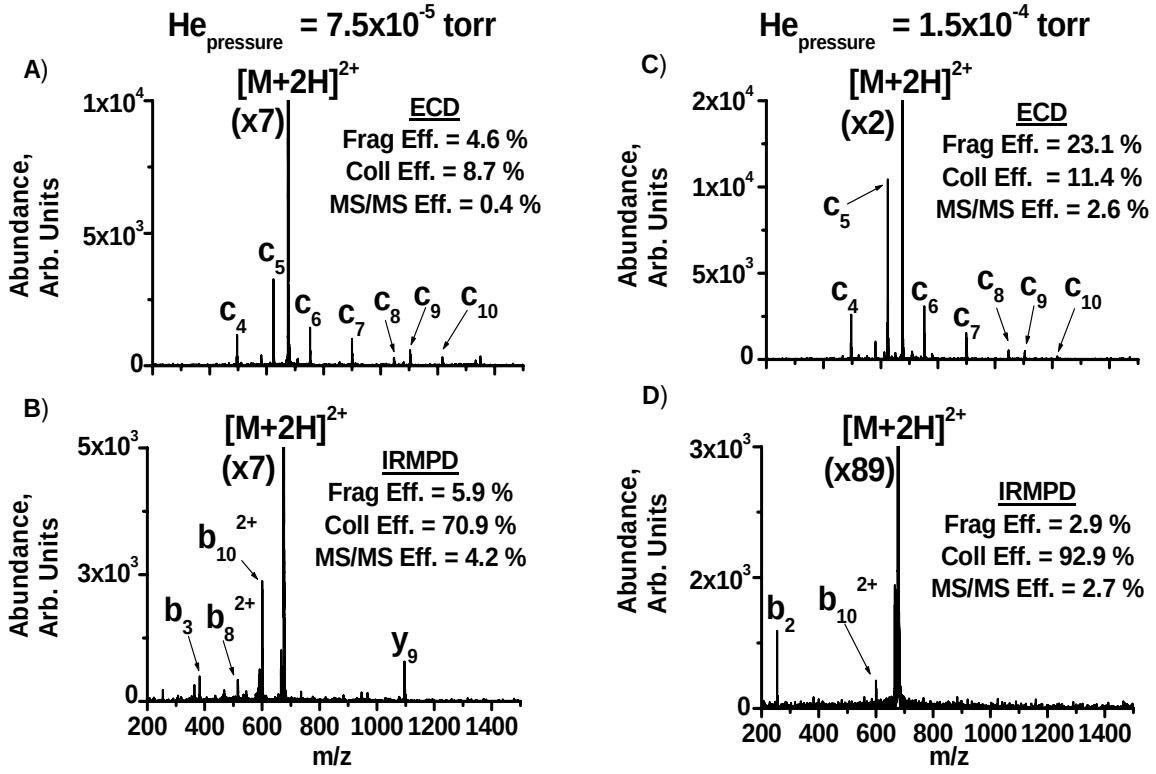

Figure 7.3. ECD and IRMPD at reduced pressures in the ECD_{LIT}. A) ECD of $\mathbf{[M+2H]^{2+}}$ substance P at a bath gas pressure of $7.5x10^{-5}$ torr. B) IRMPD of $\mathbf{[M+2H]^{2+}}$ substance P at a bath gas pressure of $7.5x10^{-5}$ torr. C) ECD of $\mathbf{[M+2H]^{2+}}$ substance P at a bath gas pressure of $1.5x10^{-4}$ torr. D) IRMPD of $\mathbf{[M+2H]^{2+}}$ substance P at a bath gas pressure of $1.5x10^{-4}$ torr. For all spectra, an irradiation time of 10 ms (IR photons or electrons) was used. The amount the y-axis had to be expanded to view the product ions is given in each spectrum underneath the remaining parent ion abundance (e.g., (x7) in Figure A). This same notation is used throughout this chapter.

Figure 7.3D. The only IRMPD product ions observed at a bath gas pressure of $1.5x10^{-4}$ torr were the $\mathbf{b_2}$ and $\mathbf{b_{10}}^{2+}$ ions. Increasing the bath gas to pressures greater than $1.5x10^{-4}$ torr resulted in no dissociation of the parent ion, presumably because the rate of internal energy loss by collisional cooling was faster than the rate of increasing parent ion internal energy from IR absorption.

Overall, to ensure that the internal energy imparted to the parent ion by the IR activation process is not completely dissipated by collisional cooling, the IR irradiation time and helium bath gas pressures are varied until a minimal amount of product ions are observed. The extent to which IRMPD occurs is consciously limited because the goal is to use IR radiation to activate, not dissociate, parent ions. By limiting the amount of dissociation due to IR activation, the primary dissociation channel should be the formation of **c** / **z** ions related to ECD which will aid in spectral interpretation.

For the AI-ECD experiments discussed in this chapter, a helium bath gas pressure of ~1.5x10^{-4} torr was used.

7.3.3 *AI-ECD of* ***[M+7H]$^{7+}$*** *ubiquitin*

The electron capture cross-section in ECD increases linearly with the square of the parent ion charge state.[33] Ubiquitin is a 76 amino acid residue protein (M_r = 8.6 kDa) that, under the nESI conditions used here, forms parent ion charge states of +7 to +13. Results from performing ECD alone on the +7 charge state (**[M+7H]$^{7+}$**) with an ECD duration of 5 ms are shown in Figure 7.4A. The major result of electron capture is the formation of the odd-electron, charge reduced ion (**[M+7H]$^{6+\bullet}$**). The limited dissociation results in a fragmentation efficiency of only 7.2%. Increasing the ECD duration to 30 ms in an attempt to increase the amount of time ions and electrons interact resulted in the spectrum shown in Figure 7.4B. While the fragmentation efficiency improved to 29.8%, the increase is attributable to the formation of the intact, charge-reduced species. Consequently, little

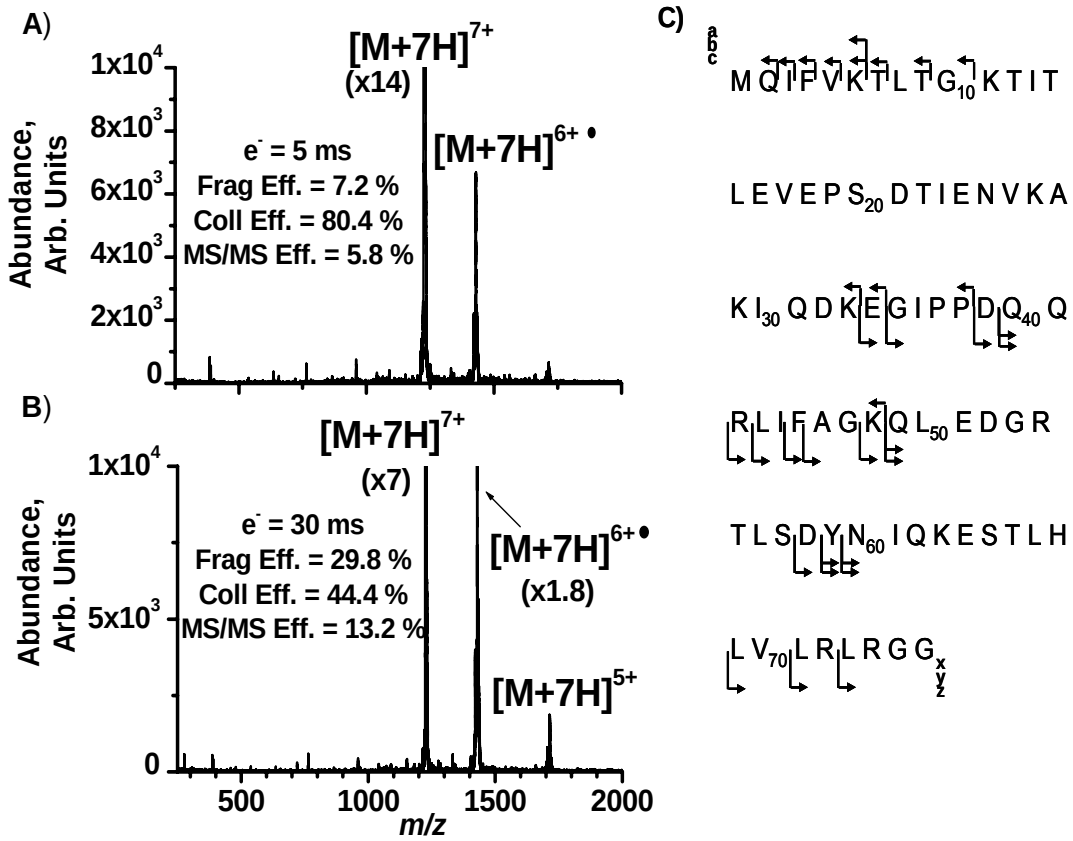

Figure 7.4. A) ECD of **[M+7H]$^{7+}$** ubiquitin, ECD duration = 5 ms. B) ECD of **[M+7H]$^{7+}$** ubiquitin, ECD duration = 30 ms. C) Annotation of ECD spectrum from B). Electron kinetic energy = 1.2 eV.

sequence information is acquired from performing ECD alone. Shown in Figure 7.4C is the annotation of the ubiquitin amino acid sequence determined from the MS/MS spectrum in Figure 7.4B. The majority of the peptide cleavage that is observed is due to N-C_α bond scission to generate **c** and **z** ions, but the sequence coverage is only 32%. Large gaps in sequence coverage exist that would make it difficult to sequence and accurately identify this protein from the MS/MS spectrum in Figure 7.4B. The results in Figure 7.4 clearly demonstrate the need for a method to increase the amount of dissociation and thus information gained from one MS/MS experiment.

The IR irradiation time required to activate but not dissociate the parent ion will depend upon the choice of helium bath gas pressure, the amount of overlap between the ion cloud and the IR beam with a given laser alignment, and the laser power. Before attempting AI-ECD on **[M+7H]$^{7+}$** ubiquitin, the appropriate amount of IR radiation had to be determined that would activate but not

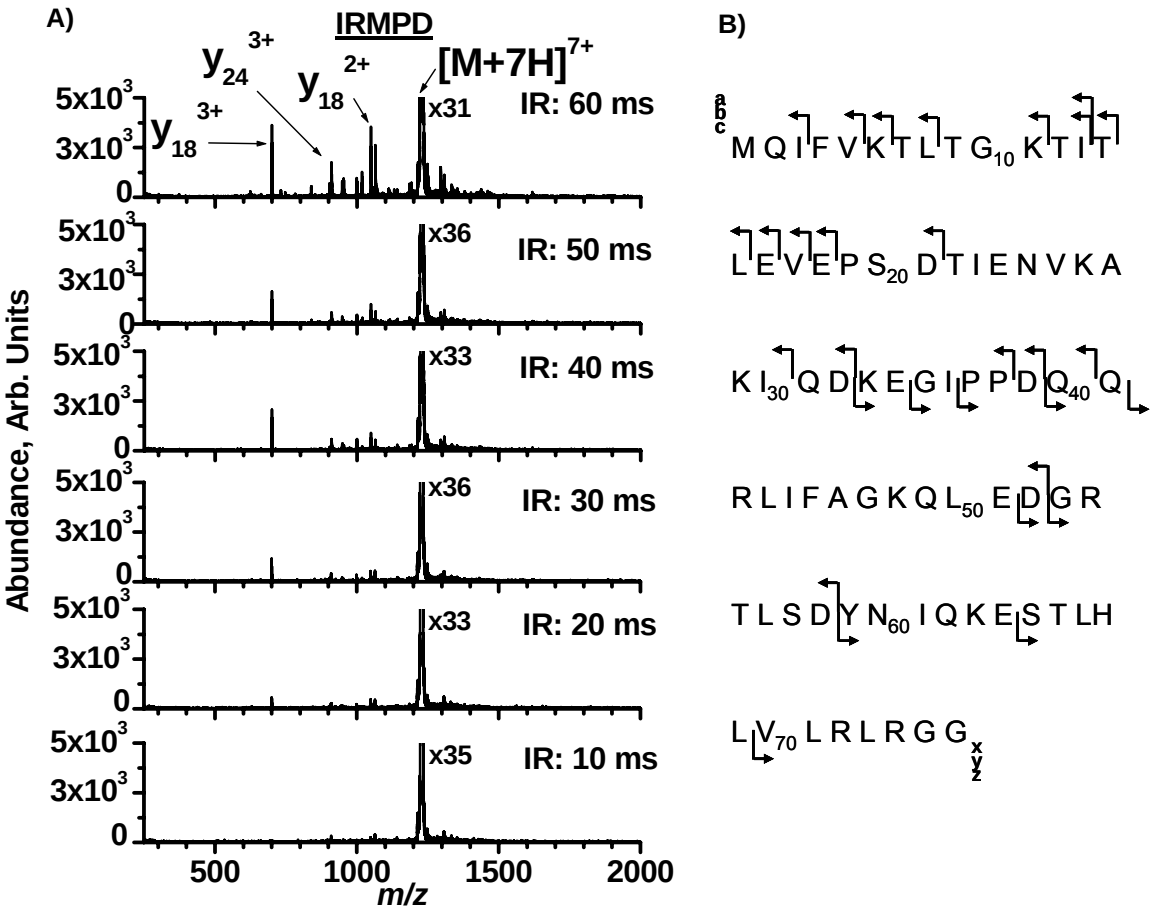

Figure 7.5. A) IRMPD spectra of **[M+7H]$^{7+}$** ubiquitin as a function of IR irradiation time. B) Annotation of the IRMPD spectrum in A) with an IR irradiation time of 60 ms.

dissociate the parent ion. The effect of varying the IR irradiation time on the IRMPD spectra of **[M+7H]**$^{7+}$ ubiquitin is demonstrated in Figure 7.5. An IR irradiation time of 10 ms (Figure 7.5) was not sufficient to cause dissociation. Increasing the irradiation time to 60 ms did increase the product ion abundance, as shown in Figure 7.6 for selected product ions. The extent of parent ion dissociation was still relatively small (5.7% fragmentation efficiency). As mentioned previously, for AI-ECD the IR radiation is desired only to activate the ion. Shown in Figure 7.5B is the annotation of the IRMPD spectrum acquired with 60 ms of IR radiation. The extent of product ion formation with 60 ms of IR irradiation show that minimal dissociation due to IR activation is occurring. The sequence coverage achieved here with IRMPD was 33%, which is similar to what was achieved with ECD (i.e., in Figure 7.4B the sequence coverage was 32%). In Figure 7.5B, except for one **a** ion all other product ions were **b** or **y** ions. It will be of interest to study which types of product ions are formed during AI-ECD where both IR activation and ECD are employed.

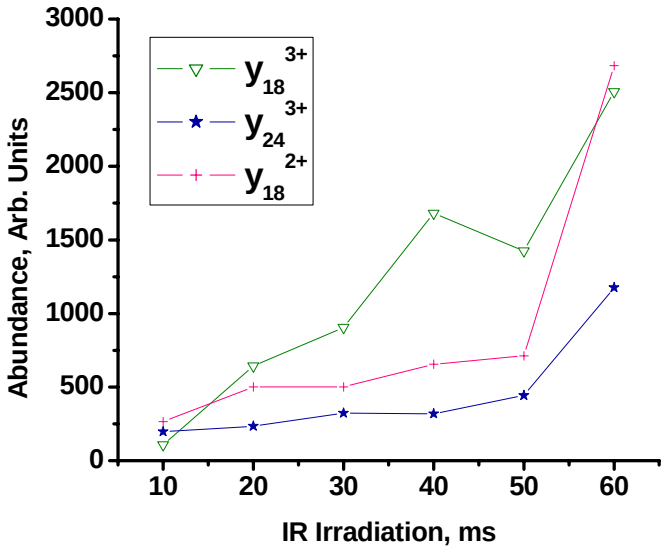

Figure 7.6 Extracted ion abundance for selected product ions as a function of IR irradiation time. Data from Figure 7.5.

7.3.3.1 *IR → ECD*

Ion activation prior to ECD is believed to induce a conformational change (i.e., protein unfolding). Ideally the unfolded conformation will allow access to a greater number of dissociation channels for ECD than are available when the protein is in a more compact state. In an unfolded state the non-covalent intramolecular interactions that may prevent fragment ion separation have been disrupted. The loss of internally energy by collisional cooling associated with the ECD_{LIT} may cause the denatured protein to refold prior to undergoing electron capture resulting in a decreased amount of parent ion dissociation compared to performing ECD on the unfolded protein.[21] The

extent to which protein refolding occurs can be monitored by varying the delay between IR activation and ECD. However, the best conditions for IR activation followed by ECD with no delay must first be determined. For clarification the AI-ECD process where IR activation is used prior to ECD will be denoted as IR→ECD.

The result of performing IR→ECD at various IR irradiation times is shown in Figure 7.7. The electron irradiation time was held constant at 5 ms while the IR irradiation time was varied from 10 to 60 ms. As the amount of IR radiation increases the abundance of product ions also increases. The most abundant product ions are ECD-related ions (i.e., **c** or **z** ions), but other types of backbone cleavage are observed. The annotated ubiquitin sequence shown in Figure 7.7B corresponds to the top spectrum in Figure 7.7A (i.e., IR irradiation of 60 ms, electron irradiation of 5 ms). The sequence

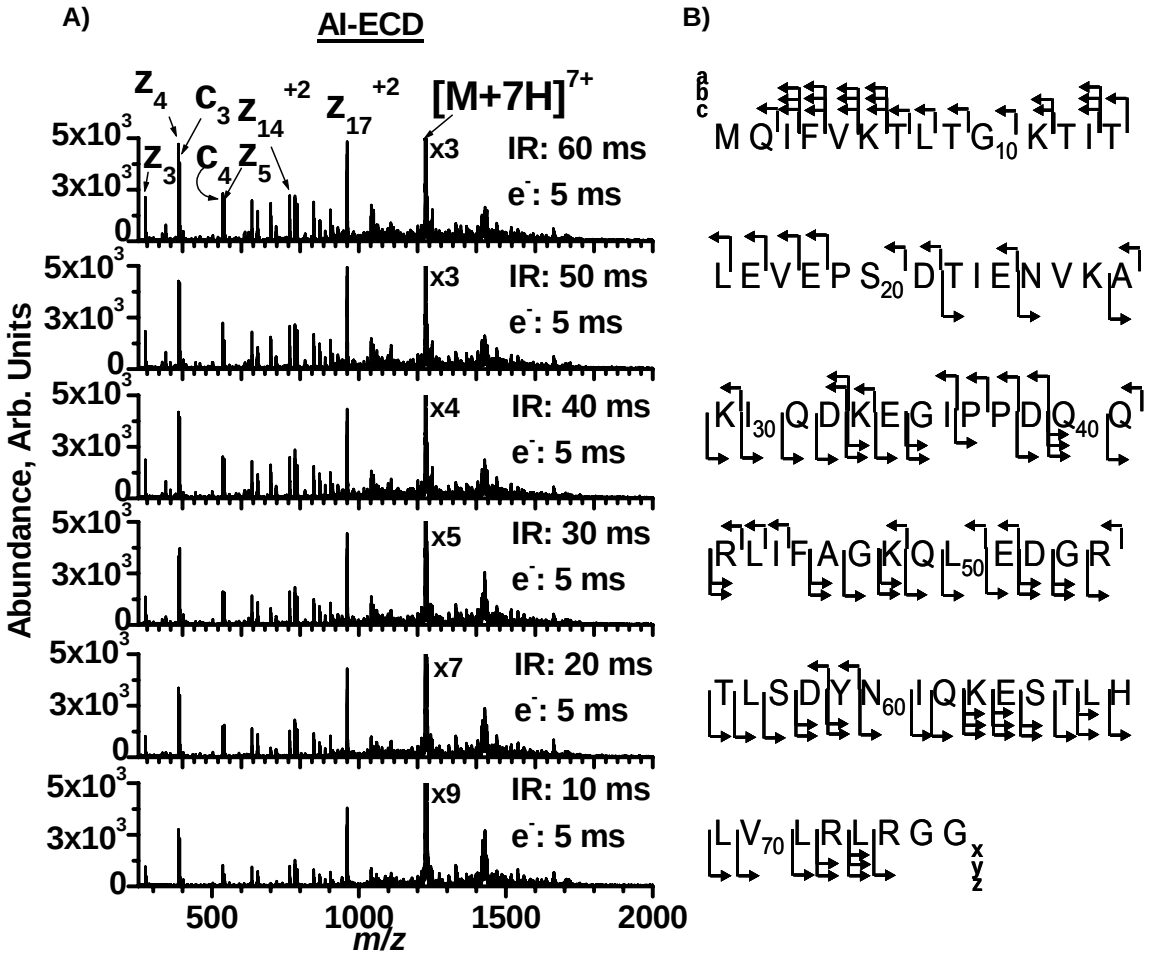

Figure 7.7 A) IR→ECD for ubiquitin as a function of IR irradiation time. No delay was used between IR activation and ECD. B) Annotation of top spectrum in A), i.e., IR: 60 ms, e^-: 5 ms. Electron kinetic energy = 1.2 eV.

coverage, considering all product ions, illustrated in Figure 7.7B is 87%. When only **c** and **z** ions are considered the sequence coverage is 73% compared to 39% and 11% when only **b** / **y** and **a** / **x** ions, respectively, are considered. The 39% sequence coverage attributable to **b** / **y** ions from IR→ECD is similar to the 33% sequence coverage due to **b** / **y** ions formed when only performing IRMPD (see Figure 7.5). These results show that AI-ECD does increase the amount of N-C_α bond cleavage over ECD alone. The sites of backbone cleavage unique to the AI-ECD experiment in Figure 7.7B are shown in Figure 7.8. Figure 7.8 represents the same annotation as in Figure 7.7B, but the backbone cleavages that were observed for ECD only (Figure 7.4B) and for IRMPD only (Figure 7.5B) have been removed so the increased dissociation provided by AI-ECD is apparent. The results in Figure 7.8 show that AI-ECD has improved the total sequence coverage but the spectral complexity has also increased due to the variety of product ion types formed. The primary dissociation channel associated with ECD is **c** / **z** ion formation, but a secondary channel exists when the neutralized H-atom is captured by an amide nitrogen resulting in **a** / **y** ions.[3] The presence of **b** ions in Figure 7.7B was not unexpected due to their presence in the 60 ms IRMPD spectrum from Figure 7.5. However, **x** ion formation is still unexplained. It should also be noted that only **c'** and no **c•** ions were observed in the spectra of Figure 7.7, indicating that no H-atom transfer between pieces of an undissociated **[c'+z•]** complex was detected. When the **c'** ion transfers an **H•** to the **z•**, what remains is a **c•** ion at a mass-to-charge ratio less than the expected **c'** product ion and a **z'** ion which would be overlaid with the ^{13}C isotopomer of the expected **z•** ion. The lack of H-atom transfer is most likely due to a decreased **[c'+z•]** complex lifetime because of IR activation prior to ECD disrupting intramolecular interactions holding the

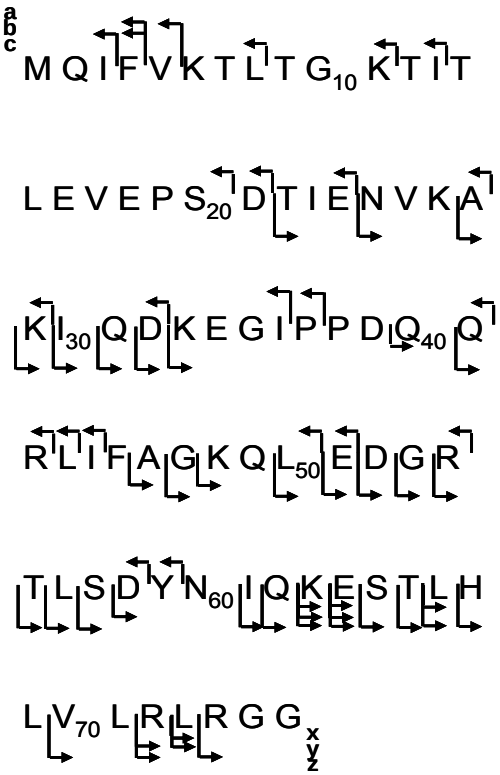

Figure 7.8 Annotation of ubiquitin showing backbone cleavages unique to the AI-ECD results in Figure 7.7B.

complex together. This observation is consistent with the literature.[21]

The results from Figure 7.7 show that several types of product ions are formed during AI-ECD. In an effort to study the extent of preferential ion formation at a given set of conditions, the abundances of selected product ions were plotted as a function of IR irradiation time in Figure 7.9. At each IR irradiation time, the abundance for a selected product ion was normalized to the abundance of the remaining parent ion (**[M+7H]**$^{7+}$). In Figure 7.9, the data points at zero IR irradiation are from the results in Figure 7.4 where only ECD was performed. The data in Figure 7.9 for IR irradiation times of 10-60 ms are from the IR→ECD results in Figure 7.7. The results in Figure 7.9 show that the use of IR activation prior to ECD increases the relative abundance of the charge-reduced species and

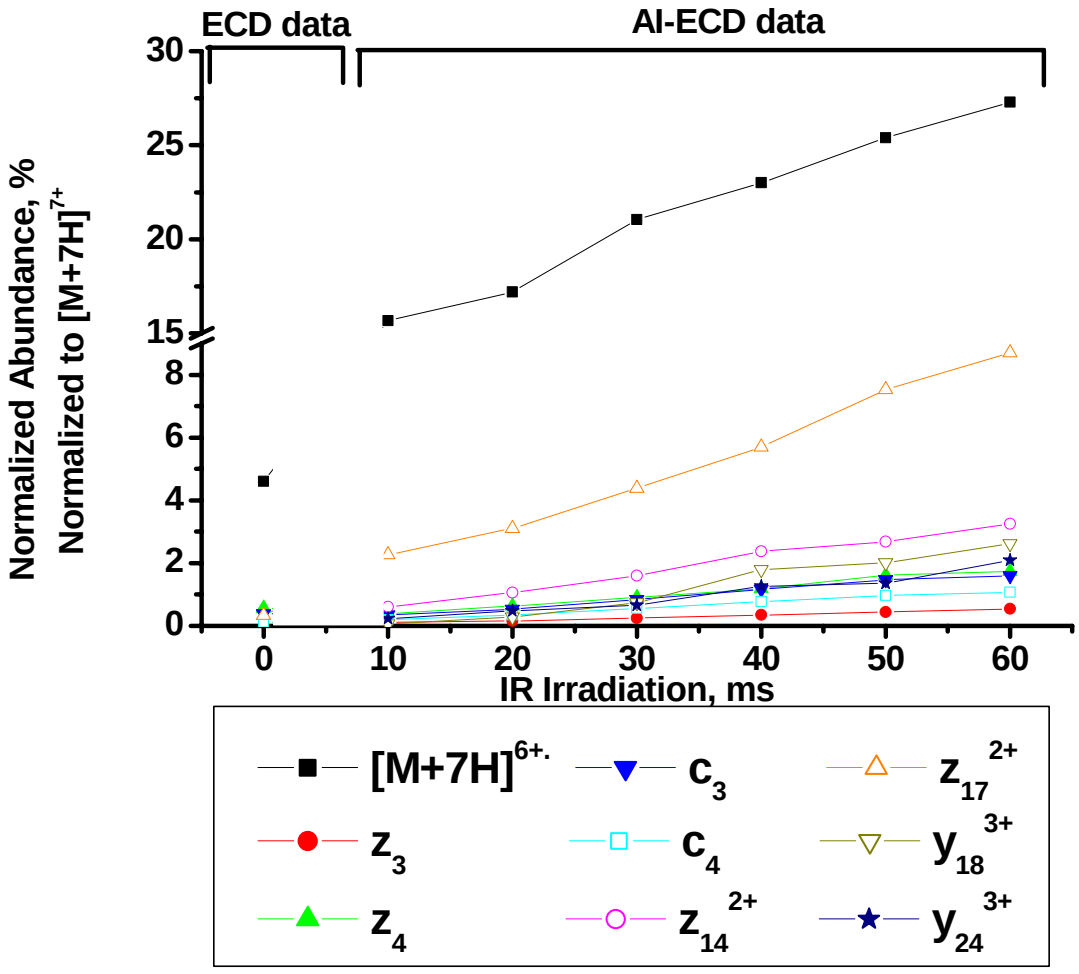

Figure 7.9 Normalized abundances for selected ions formed during ECD alone (Figure 7.4) and as a function of IR irradiation time from the IR→ECD experiments in Figure 7.7.

product ions compared to performing ECD alone. As the amount of pre-ECD IR activation increases (i.e., > 10 ms) the relative abundances of $\mathbf{[M+7H]^{6+\bullet}}$, the **c** / **z** ions, and the $\mathbf{y_{18}^{3+}}$ and $\mathbf{y_{24}^{3+}}$ ions also increase. The increase in relative abundances with IR irradiation time could be due to a decrease in the $\mathbf{[M+7H]^{7+}}$ abundance remaining after ECD, as shown in Figure 7.7, rather than an increase in product ion abundance.

The absolute abundances for the product ions and charge-reduced species as a function of IR irradiation time for the IR→ECD experiments in Figure 7.7 are plotted in Figure 7.10. The abundance of the $\mathbf{[M+7H]^{6+\bullet}}$ species decreases but the **c** / **z** and **y** product ion abundances increase with increasing IR irradiation time. The data in Figure 7.10 support the idea that in AI-ECD, as the IR irradiation time increases, the excitation of internal vibrational modes due to IR absorption changes the $\mathbf{[M+7H]^{7+}}$ parent ion conformation. Thus, the IR activation could be forming parent ion

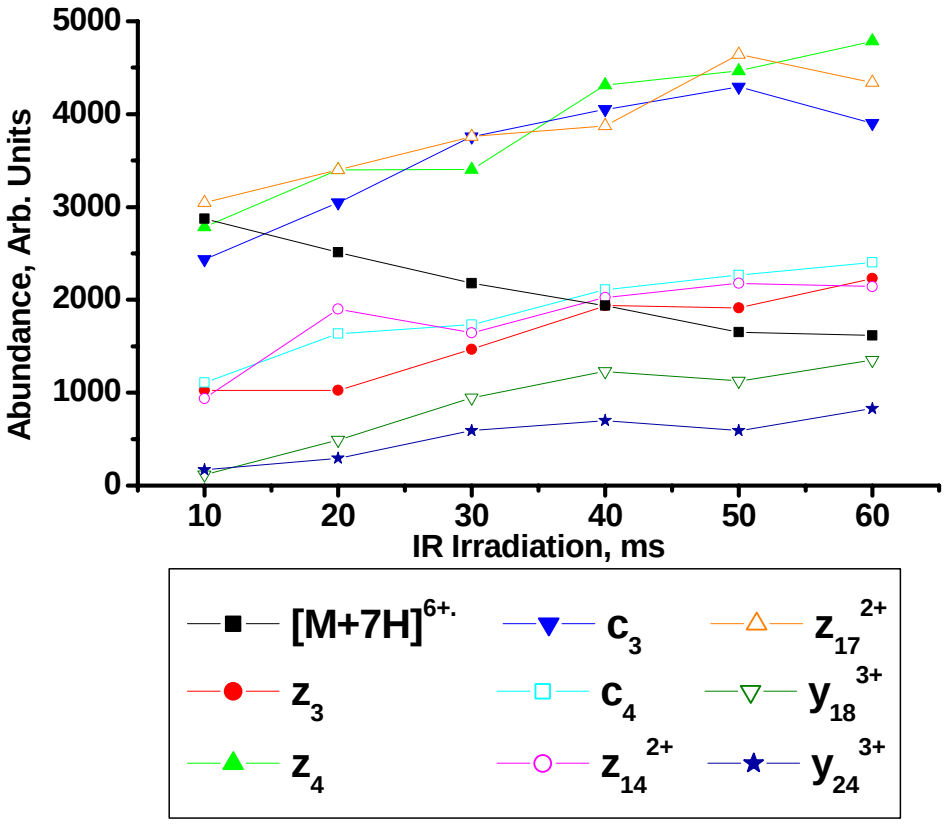

Figure 7.10 Absolute abundances of selected product ions as a function of IR irradiation time from the IR→ECD experiments shown in Figure 7.7.

conformations that have higher electron capture cross-sections. As the IR irradiation time increases, more parent ions can adopt conformations that more efficiently capture electrons.

Plotted in Figure 7.11 are the product ion abundances normalized to the total abundance of those product ions at a given IR irradiation time from Figure 7.9. The results in Figure 7.11 show that as the IR irradiation time increases the relative abundances of the ECD product ions, when normalized to the sum of the product ion abundance, do not increase. The approximately constant relative abundances of the **c** / **z** ions in Figure 7.11 show that the trends observed in Figures 7.9 and 7.10 are due to more parent ions having conformations with higher electron capture cross-sections. In Figure 7.11, the small increase in relative **y**-ion abundance is consistent with using longer IR activation times and is in agreement with the results in Figure 7.6. Overall, The results from Figures 7.7-7.11 support the idea that IR activation prior to ECD induces a conformational change (i.e., protein unfolding) of the parent ion. The IR→ECD results for **[M+7H]**$^{7+}$ ubiquitin show that the

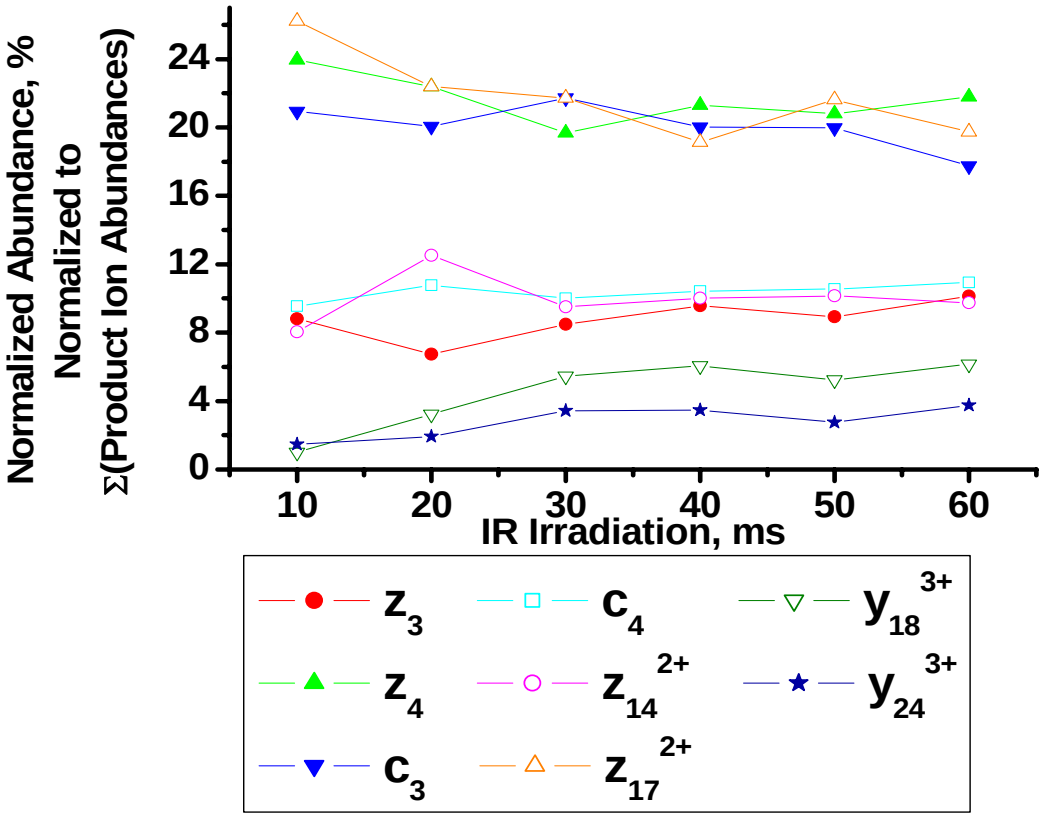

Figure 7.11 Product ion abundances from Figure 7.9, normalized to the sum of those product ion abundances at a given IR irradiation time.

conformational change works to increase the electron capture cross-section of the parent ion which increases the total number of products formed, rather than increasing the abundance of only certain product ions.

Another way of studying the effect of IR activation prior to ECD involves providing a delay time between the IR activation and ECD while keeping the IR and electron irradiation times constant. The results of the IR→ECD delay experiment are shown in Figure 7.12. As the delay time increases the extent of dissociation also decreases and the abundance of the charge-reduced species remains constant at delay times longer than 20 ms. The data for the charge-reduced species in Figure 7.12 indicates that the parent ion continues to unfold for 20 ms after irradiation then does not refold at longer times but loses internal energy that that can lead to dissociation. Also, because the relative abundances in Figure 7.12 at delay times greater than 20 ms are different from those observed when performing ECD alone (see ECD Data in Figure 7.9) the unolded conformation may be different than

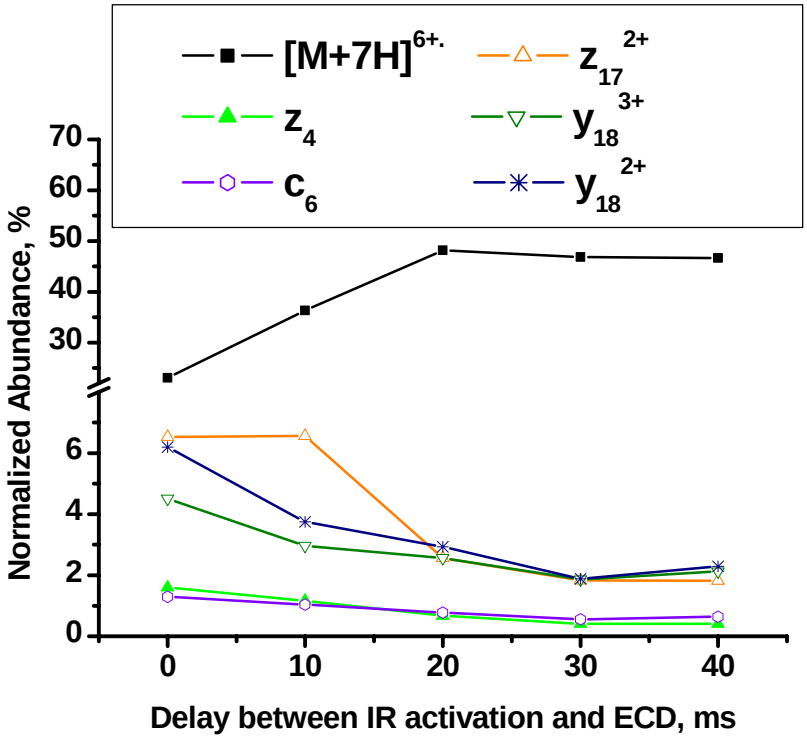

Figure 7.12 IR→ECD at different delay times between IR activation and ECD. Extracted ion abundances at different delay times, normalized to the residual parent ion ($[M+7H]^{7+}$) abundance. IR irradiation = 50 ms, electron irradiation = 5 ms, electron kinetic energy = 1.2 eV.

the initial conformation formed from nESI.. The results from Figure 7.12 support the idea that IR activation does increase the parent ion internal energy, however the internal energy is dissipated within 20 ms under the conditions used for the experiment.

7.3.3.2 *ECD → IR*

Ion internal energy gained through IR activation can be lost through collisions with the helium bath gas in the ECD_{LIT} if there is a delay between the IR activation and ECD. However, the amount of structural information from performing ECD on proteins can be increased by using IR activation after electron capture to dissociate intact, charge-reduced species. It has been demonstrated that dissociating the charge-reduced species (**$[M+nH]^{(n-1)+\bullet}$**) with IR irradiation results in extensive dissociation into **c** / **z** type ions.[25] The process of post-ECD IR activation will be referred to as ECD→IR.

Given the previously mentioned problems with collisional cooling in the ECD_{LIT}, ECD→IR is perhaps the more attractive form of AI-ECD for this device. If an intact **[c'+z•]** complex is formed from electron capture IR radiation can be used to disrupt the intramolecular interactions holding the complex together, essentially performing IRMPD. Even if internal energy of the **[c'+z•]** complex is lost through collisions with the helium bath gas, as long as the amount of IR activation is sufficient to break apart the **[c'+z•]** complex, the individual **c** and **z** ions will not re-combine. The effect of varying the duration of IR irradiation following ECD in ECD→IR is shown in Figure 7.13. With 1 ms of irradiation time the most abundant product ion is the charge-reduced species, but as the IR irradiation time increases the $\mathbf{z_{17}}^{2+}$ ion becomes the most abundant product ion. With 60 ms of IR irradiation the most abundant product ions are **c** and **z** ions, as indicated in Figure 7.13A and on the annotated sequence in Figure 7.13B. The sequence coverage demonstrated in Figure 7.13B is 67%, which is better than the 32% observed in Figure 7.4. The results in Figure 7.13 also suggest that the preference for increasing the amount of N-C_α bond cleavage over other forms of protein backbone cleavage is greater for ECD→IR than IR→ECD (i.e., Figure 7.7). For the ECD→IR results in Figure 7.13, the sequence coverage associated with just **c** / **z** ions is 66% while for just **b** / **y** and **a** / **x** ions coverage is only 17% and 3%, respectively. Compared to IR→ECD, **b** / **y** ions are less likely to be formed in ECD→IR. ECD→IR also shows a slight decrease in **c** / **z** ion formation compared to

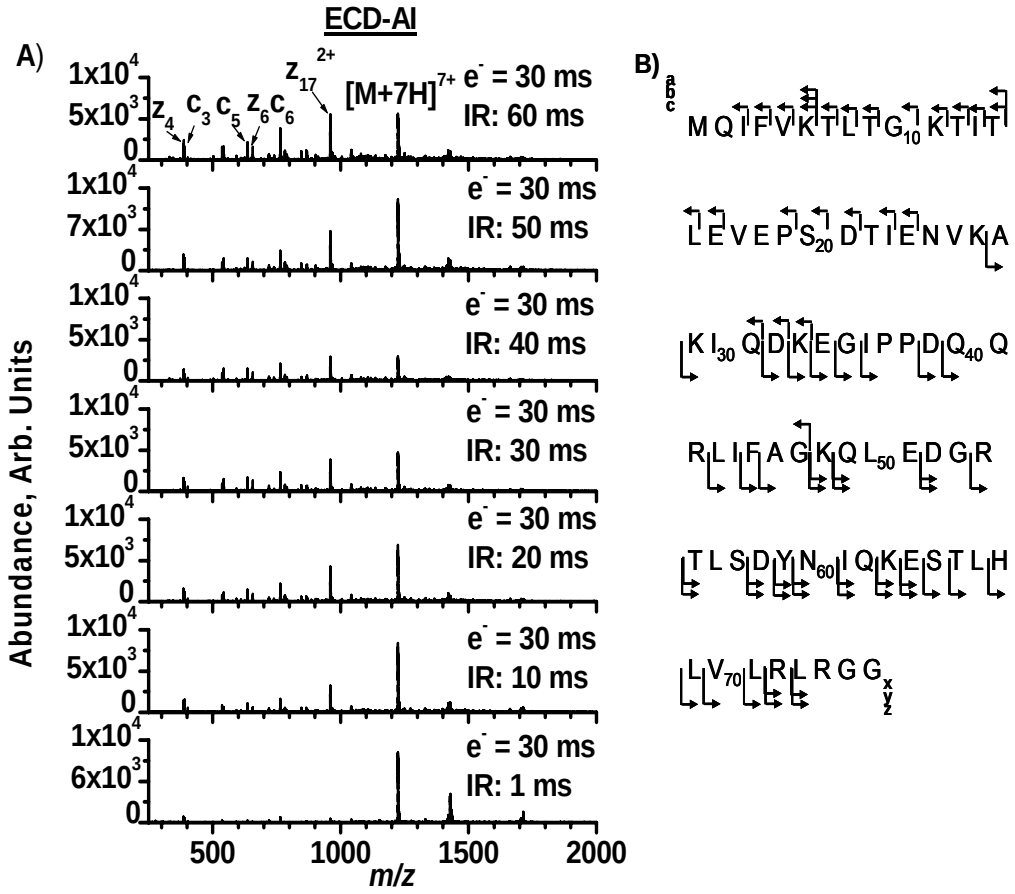

Figure 7.13 ECD→IR of **[M+7H]$^{7+}$** ubiquitin A) ECD→IR as a function of IR irradiation time. B) Annotation of the top spectrum in A (i.e. e- = 30 ms, IR: 60 ms). Electron irradiation = 30 ms, electron kinetic energy = 1.2 eV.

IR→ECD. The ratio of **c** / **z** ions to **b** / **y** ions is 66% : 17% for ECD→IR versus 73% : 39% for IR→ECD.

To determine which IR irradiation time produces the most parent ion dissociation under ECD→IR conditions, the fragmentation, collection, and MS/MS efficiencies are plotted as a function of the duration of IR radiation in Figure 7.14. The data using 1 ms IR irradiation time was not included as it was previously determined that a minimum of 10 ms of IR activation was required to begin parent ion dissociation under the current set of conditions (see Figure 7.5). The effect of IR irradiation times longer than 60 ms could not be studied under the experimental set of conditions used to acquire the data for Figure 7.14 because the total duration of electron and IR irradiation had to be kept equal to or less than 90 ms. For ion isolation and accumulation in the CID_{LIT} (see Figure 7.1) an accumulation time of 100 ms resulted in reaching the space charge limit for the CID_{LIT}. The

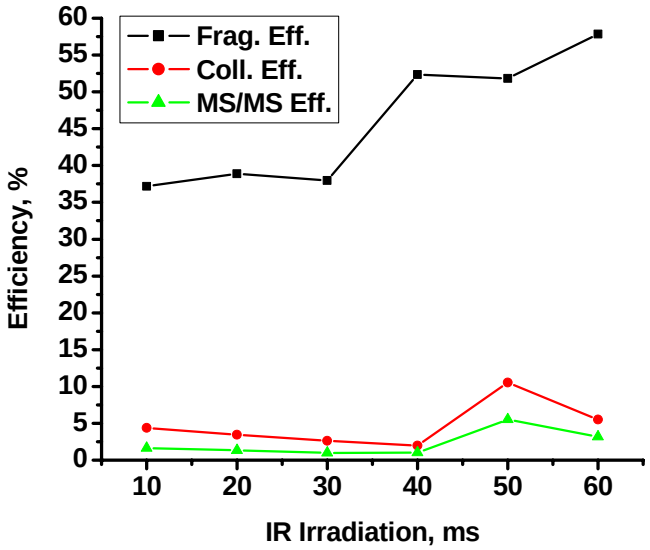

Figure 7.14 Dissociation efficiencies for ECD→IR as a function of IR irradiation time. Electron irradiation = 30 ms, electron kinetic energy = 1.2 eV.

CID_{LIT} accumulation time determines the total amount of time available to perform experiments in the ECD_{LIT}. In addition to the electron and IR irradiation times, there are delays required for ion injection into and ejection out of the ECD_{LIT} that must considered in the 100 ms of available experiment time. As a result, with an electron irradiation time of 30 ms, the maximum IR irradiation time that could be studied was 60 ms. The results in Figure 7.14 indicate that of the IR irradiation times studied, 60 ms produces the highest fragmentation efficiency. This observation is in agreement with a visual inspection of the spectra in Figure 7.13A. The results in Figure 7.14 show that the IR activation successfully improves the extent of parent ion dissociation. The dissociation efficiency data may also provide information about the stability of the **[c'+z•]** complex, if the amount of internal energy imparted to the parent ion during the electron capture process is not dissipated prior to IR activation. The **[c'+z•]** complex that forms following electron capture is proposed to consist of non-separated **c'** and **z•** species held together by non-covalent interactions. By changing the IR irradiation time or laser power used to irradiate the **[c'+z•]** complex, information about the non-covalent interactions could be studied which may ultimately provide information on what the gas phase structure of the parent ion was when electron capture occurred.

The capture of an electron by a multiply protonated polypeptide is exothermic by an energy equal to the recombination energy of this process, the proposed energy is 4 – 7 eV.[34] Because dissociation in ECD occurs in less than 10^{-12}s[35] there is not enough time to redistribute any of the excess recombination energy into vibrational modes of the parent ion. As a result, negligible amounts of internal energy are imparted to the parent ion during ECD and varying the delay time between ECD

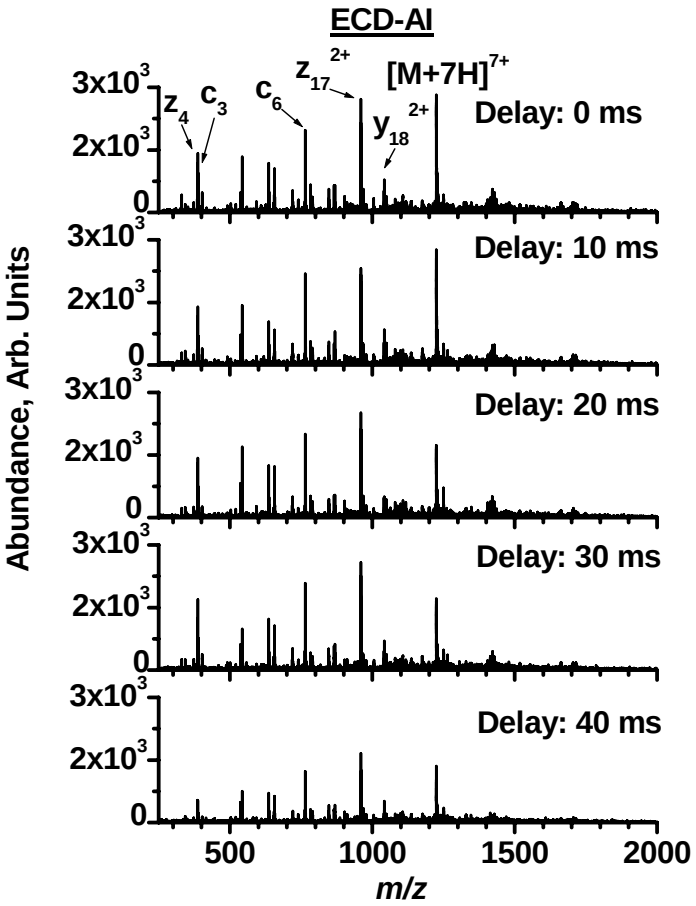

Figure 7.15 ECD→IR as a function of delay time between ECD and post-ECD IR activation. Electron irradiation = 30 ms, IR irradiation = 60 ms, electron kinetic energy = 1.2 eV.

and post-ECD IR activation should show no change in dissociation. The result of varying the delay time ECD and IR activation is shown in Figure 7.15. As the delay time changes, the relative abundances in the spectra remain mostly unchanged. For example, the fragmentation efficiencies when the delay time was 0 and 40 ms are 44 and 45 %, respectively. Overall, the fragmentation, collection, and MS/MS efficiencies for the data in Figure 7.15 are 50 ± 6%, 5 ± 2%, and 2 ± 1%, respectively. The results in Figure 7.15 support the idea that there is no excess internal energy remaining in the product ions following ECD. There is still a question about where the excess recombination energy goes following parent in dissociation if it does not go into internal energy of the product ions. One hypothesis is that the excess recombination goes into the kinetic energy of the product ions, but further work is needed to test this hypothesis.

7.4 Conclusions

Activated ion ECD (AI-ECD) can be performed in the ECD_{LIT}. Results support the idea that the use of IR activation prior to ECD (IR→ECD) induces a conformational change of the parent ion into a conformation with a higher electron capture cross-section. The higher cross-section improves the amount of parent ion dissociation. Results also show that the **$[M+7H]^{7+}$** parent ion of ubiquitin continues to unfold for 20 ms after IR irradiation but then does not refold at longer times. Data from

experiments where IR activation was used after ECD (ECD→IR) indicate that there is no excess internal energy remaining in the product ions following ECD, because no change in fragmentation efficiency was observed as the delay between ECD and post-ECD IR activation was varied.

The use of IR→ECD and ECD→IR both improved the sequence coverage of **[M+7H]**$^{7+}$ ubiquitin compared to performing ECD alone. Using ECD alone and an electron irradiation time of 30 ms, 32% sequence coverage was achieved. For IR→ECD, with no delay between the IR activation and ECD, a total sequence coverage of 87% was acquired. When only **c** / **z** ions are considered, a sequence coverage of 73% was observed. Under ECD→IR conditions, the total sequence coverage was 67% and when only **c** / **z** ions considered, a sequence coverage of 66% was acquired.

7.5 References

1. Sleno, L.; Volmer, D. A. Ion Activation Methods for Tandem Mass Spectrometry. *Journal of Mass Spectrometry*. **2004**, 39, p. 1091-1112.

2. Zubarev, R. A.; Kelleher, N. L.; McLafferty, F. W. Electron Capture Dissociation of Multiply Charged Protein Cations. A Nonergodic Process. *Journal of the American Chemical Society*. **1998**, 120, p. 3265-3266.

3. Zubarev, R. A.; Horn, D. M.; Fridriksson, E. K.; Kelleher, N. L.; Kruger, N, A.; Lewis, M. A.; Carpenter, B. K.; McLafferty, F. W. Electron Capture Dissociation for Stuctural Characterization of Multiply Charged Protein Cations. *Analytical Chemistry*. **2000**, 72, p. 563-573.

4. Ge, Y.; Lawhorn, B. G.; ElNaggar, M.; Strauss, E.; Park, J. H.; Begley, T. P.; McLafferty, F. W. Top Down Characterization of Larger Proteins (45 kDa) by Electron Capture Dissociation Mass Spectrometry. *Journal of the American Chemical Society*. **2002**, 124, p. 672-678.

5. Zubarev, R. A.; Haselmann, K. F.; Budnik, B.; Kjeldsen, F.; Jensen, F. Towards an Understanding of the Mechanism of Electron-Capture Dissociation: A Historical Perspective and Modern Ideas. *European Journal of Mass Spectrometry*. **2002**, 8, p. 337-349.

6. Breuker, K.; Oh, H.; Horn, D. M.; Cerda, B. A., McLafferty, F. W. Detailed Unfolding and Folding of Gaseous Ubiquitin Ions Characterized by Electron Capture Dissociation. *Journal of the American Chemical Society*. **2002**, 6407-6420.

7. Horn, D. M.; Ge, Y.; McLafferty, F. W. Activated Ion Electron Capture Dissociation for Mass Spectral Sequencing of Larger (42 kDa) Proteins. *Analytical Chemistry*. **2000**, 72, p. 4778-4784.

8. Oh, H. B.; McLafferty, F. W. A Variety of Activation Methods Employed in "Activated-Ion" Electron Capture Dissociation Mass Spectrometry: A Test against Bovine Ubiquitin 7+ Ions. *Bulletin of the Korean Chemical Society*. **2006**, 27, p. 389 - 394.

9. Bomse, D. S.; Woodin, R. L.; Beauchamp, J. L. Molecular Activation with Low-Intensity CW Infrared Laser Radiation. Multiphoton Dissociation of Ions Derived from Diethyl Ether. *Journal of the American Chemical Society*. **1979**, 101, p. 5503-5512.

10. Jockusch, R. A.; Paech, K.; Williams, E. R. Energetics from Slow Infrared Multiphoton Dissociation of Biomolecules. *Journal of Physical Chemistry*. **2000**, 104, p. 3188-3196.

11. Louris, J. N.; Brodbelt, J. S.; Cooks, R. G. Photodissociation in a Quadrupole Ion Trap Mass Spectrometer Using a Fiber Optic Interface. *International Journal of Mass Spectrometry and Ion Processes*. **1987**, 75, p. 345-352.

12. Little, D. P.; Speir, J. P.; Senko, M. W.; O'Connor, P. B.; McLafferty, F. W. Infrared Multiphoton Dissociation of Large Multiply Charged Ions for Biomolecule Sequencing. *Analytical Chemistry*. **1994**, 66, p. 2809-2815.

13. Goolsby, B. J.; Brodbelt, J. S. Tandem Infrared Multiphoton Dissociation and Collisionally Activated Dissociation Techniques in a Quadrupole Ion Trap. *Analytical Chemistry*. **2001**, 73, p. 1270-1276.

14. Dunbar, R. C. Photodissociation of Trapped Ions. *International Journal of Mass Spectrometry*. **2000**, 200, p. 571-589.

15. Drader, J. J.; Hannis, J. C.; Hofstadler, S. A. Infrared Multiphoton Dissociation with a Hollow Fiber Waveguide. *Analytical Chemistry*. **2003**, 75, p. 3669-3674.

16. Laskin, J.; Futrell, J. H. Activation of Large Ions in FT-ICR Mass Spectrometry. *Mass Spectrometry Reviews*. **2005**, 24, p. 135-167.

17. Gardner, M. W.; Vasicek, L. A.; Shabbir, S.; Anslyn, E. V.; Brodbelt, J. S. Chromogenic Cross-Linker for the Characterization of Protein Structure by Infrared Multiphoton Dissociation Mass Spectrometry. *Analytical Chemistry*. **2008**, 80, p. 4807-4819.

18. Hofstadler, S. A.; Sannes-Lowery, K. A.; Griffey, R. H. Infrared Multiphoton Dissociation in an External Ion Reservoir. *Analytical Chemistry*. **1999**, 71, p. 2067-2070.

19. Raspopov, S. A.; El-Faramawy, A.; Thomson, B. A.; Siu, K. W. M. Infrared Multiphoton Dissociation in Quadrupole Time-of-Flight Mass Spectrometry: Top-Down Characterization of Proteins. *Analytical Chemistry*. **2006**, 78, p. 4572-4577.

20. Robinson, E. W.; Leib, R. D.; Williams, E. R. The Role of Conformation on Electron Capture Dissociation of Ubiquitin. *Journal of the American Society for Mass Spectrometry*. **2006**, 17, p. 1470 - 1480.

21. Lin, C.; Cournoyer, J. C.; O'Connor, P. B. Probing the Gas-Phase Folding Kinetics of Peptide Ions by IR Activated DR-ECD. *Journal of the American Society for Mass Spectrometry*. **2008**, 19, p. 780 - 789.

22. Tsybin, Y. O.; Witt, M.; Baykut, G.; Kjeldsen, F.; Hakansson, P. Combined Infrared Multiphoton Dissociation and Electron Capture Dissociation with a Hollow Electron Beam in Fourier Transform Ion Cyclotron Resonance Mass Spectrometry. *Rapid Communications in Mass Spectrometry*. **2003**, 17, p. 1759-1768.

23. Tsybin, Y. O.; He, H.; Emmett, M. R.; Hendrickson, C. L.; Marshall, A. G. Ion Activation in Electron Capture Dissociation to Distinguish between N-Terminal and C-Terminal Product Ions. *Analytical Chemistry*. **2007**, 79, p. 7596-7602.

24. Hakansson, K.; Cooper, H. J.; Emmett, M. R.; Costello, C. E.; Marshall, A. G.; Nilsson, C. L. Electron Capture Dissociation and Infrared Multiphoton Dissociation MS/MS of an N-Glycosylated Tryptic Peptide To Yield Complementary Sequence Information. *Analytical Chemistry*. **2001**, 73, p. 4530-4536.

25. Håkansson, K.; Chalmers, M. J.; Quinn, J. P.; McFarland, M. A.; Hendrickson, C. L.; Marshall, A. G. Combined Electron Capture and Infrared Multiphoton Dissociation for Multistage MS/MS in a Fourier Transform Ion Cyclotron Resonance Mass Spectrometer. *Analytical Chemistry*. **2003**, 75, p. 3256 - 3262.

26. Mihalca, R.; van der Burgt, Y. E. M.; McDonnell, L. A.; Duursma, M.; Cerjak, I.; Heck, A. J. R.; Heeren, R. M. A. Combined Infrared Multiphoton Dissociation and Electron-Capture Dissociation using Co-Linear and Overlapping Beams in Fourier Transform Ion Cyclotron Resonance Mass Spectrometery. *Rapid Communications in Mass Spectrometry*. **2006**, 20, p. 1838-1844.

27. Satake, H.; Hasegawa, H.; Hirabayashi, A.; Hashimoto, Y.; Baba, T. Fast Multiple Electron Capture Dissociation in a Linear Radio Frequency Quadrupole Ion Trap. *Analytical Chemistry*. **2007**, 79, p. 8755-8761.

28. Stafford, G. C. J.; Kelley, P. E.; Syka, J. E. P.; Reynolds, W. E.; Todd, J. F. J. Recent Improvements in and Analytical Applications of Advanced Ion Trap Technology. *International Journal of Mass Spectrometry and Ion Processes*. **1984**, 60, p. 85-98.

29. Goeringer, D.E.; McLuckey, S. A. Evolution of Ion Internal Energy During Collisional Excitation in the Paul Ion Trap: A Stochastic Approach. *Journal of Chemical Physics*. **1996**, 104, p. 2214-2221.

30. Payne, A. H.; Glish, G. L. Thermally Assisted Infrared Multiphoton Photodissociation in a Quadrupole Ion Trap. *Analytical Chemistry*. **2001**, 73, p. 3542-3548.

31. Boué, S.M.; Stephenson, J. L.; Yost, R. A. Pulsed Helium Introduction into a Quadrupole Ion Trap for Reduced Collisional Quenching During Infrared Multiphoton Dissociation of Electrosprayed Ions. *Rapid Communications in Mass Spectrometry*. **2000**, 14, p. 1391-1397.

32. Vachet, R. W.; Bishop, B. M.; Erickson, B. W.; Glish, G. L. Novel Peptide Dissociation: Gas-Phase Intramolecular Rearrangement of Internal Amino Acid Residues. *Journal of the American Chemical Society*. **1997**, 119, p. 5481-5488.

33. Cooper, H. J.; Hakansson, K.; Marshall, A. G. The Role of Electron Capture Dissociation in Biomolecular Analysis. *Mass Spectrometry Reviews*. **2005**, 24, p. 201 - 222.

34. Leib, R. D.; Donald, W. A.; Bush, M. F.; O'Brien, J. T.; Williams, E. R. Internal Energy Deposition in Electron Capture Dissociation Measured Using Hydrated Divalent Metal Ions as Nanocalorimeters. *Journal of the American Chemical Society*. **2007**, 129, p. 4894-4895.

35. Zubarev, R. A. Reactions of Polypeptide Ions with Electrons in the Gas Phase. *Mass Spectrometry Reviews*. **2003**, 22, p. 57 - 77.

Chapter 8

Conclusions and Future Directions

8.1 Summary

The work described in the previous chapters involved the development of methods aimed at improving the information content from tandem mass spectrometry experiments. The use of IAM on a Q-FTICR-MS instrument was shown to increase the number of parent ions that could be studied using MS/MS over a given amount of time. The operation of ECD on a Q-FTICR-MS and a ECD_{LIT}/TOF was compared. Results demonstrated that the information provided by ECD on both instruments is very similar, suggesting that the benefits of ECD can be realized on non-FTICR mass spectrometers. A new method, referred to as ECD+CID, was developed to improve the quality of the data acquired from the ECD_{LIT} instrument. The first examples of EDD and AI-ECD performed in a LIT were also characterized using the ECD_{LIT}. All of these topics have shown promise for improving MS/MS analyses. The results of these studies are summarized here and potential areas for continued research are discussed.

8.2 Pulsed nESI

The ability to convert nESI into a pulsed ionization method allows sample consumption to be reduced. By using a flared inlet capillary, more than one nESI sprayer can be positioned in front of the mass spectrometer sampling orifice. Using a high voltage pulsing circuit, pulsed nESI operation has been demonstrated from a dual-sprayer source. The desired mode of operation (e.g. pulsing or continuous) can be realized solely by controlling the voltage applied to each sprayer. Limited instrument modification is required to interface the dual-sprayer source to a mass spectrometer with an atmospheric sampling orifice.

8.2.1 *Expanding the number of sprayers*

At present, two nESI sprayers have been used with the flared inlet capillary. The use of two sprayers has proven beneficial for introducing analyte from one sprayer and a calibrant from another to improve mass measurement accuracy. Improved mass measurement accuracy is beneficial in the spectral interpretation, elemental composition determination, and identification of unknowns. By using two nESI sprayers the calibrant and analyte can be introduced to the mass spectrometer at the same time, this process is referred to as internal calibration. For internal calibration, mass-to-charge ratios for the calibrant in a spectrum are used to calibrate that spectrum. Without a dual nESI source the calibrant and analyte would have to be analyzed separately, which is referred to as external calibration. For external calibration, the calibrant mass-to-charge ratios from a spectrum are used to calibrate a different spectrum. The introduction of an internal calibrant offers one method of improving mass measurement accuracy, especially for trapping mass analyzers, because the analyte and calibrant can be exposed to the same trapping fields and space charge effects.

Due to the symmetry of the flared inlet capillary, more than two sprayers could be positioned for sampling by the mass spectrometer source. A similar idea has been implemented with conventional ESI sprayers where a mechanical barrier was used to control which sprayer was being sampled by the instrument.[1] By using high voltage to control which sprayer is sampled rather than a mechanical system, nESI can be used instead of conventional ESI, faster switching times can be achieved, sample loss can be reduced, and you have the option of using more than one sprayer at a time.

One goal behind the development of a multi-sprayer ESI source was to utilize chromatographic separation (e.g., HPLC) before each sprayer, allowing the benefits of LC-MS to be realized in a multiplexed fashion. An obstacle associated with connecting a LC system to each sprayer that must be overcome is the fact that the mobile phase of each LC system is constantly moving through the sprayer. Even if the sprayer is not being sampled by the mass spectrometer, analyte will be eluting from the LC separation. This scenario is more critical when high voltage switching is used to control the nESI operation of each sprayer. When no spray potential is applied to a given sprayer the LC eluate will continue to come through the sprayer, resulting in a droplet at the sprayer tip. The droplet could clog the nESI tip, change the potential needed to initiate electrospray,

or drop off the end of the sprayer tip before it can be analyzed. The challenge lies in deciding what to do with the continuous influx of sample when using a pulsed nESI process.

8.2.2 *Source design compatible with a range of instruments*

One of the biggest advantages of the pulsed, dual-sprayer source is its ability to be coupled to any mass spectrometer with an atmospheric sampling orifice without the need for extensive instrument modification. With the present popularity of ESI, most commercially available mass spectrometers have the ability to sample ions generated from a ESI (or nESI) source. Using the proof-of-principle design introduced in Chapter 2 as a starting point, a modular device could be constructed that would allow the dual-sprayer source to be interfaced with a variety of mass spectrometers. The main requirement for the successful operation of the dual-sprayer source is the ability to obtain a trigger from the mass spectrometer that corresponds to the ion accumulation or sampling period that could initiate electrospray. The access to such a trigger will vary from instrument to instrument.

8.3 IAM

The implementation of IAM on a Q-FTICR-MS resulted in obtaining MS/MS spectra for six analytes in two MS/MS experiments while characteristic resolving power and mass measurement accuracies were maintained. Through the use of a "ratiogram" product-parent ion correlations are graphically represented where each product ion is encoded with a ratio unique to the parent ion from which it was formed.

8.3.1 *Benefit of IAM considering the time scale of FT detection*

The mass analysis step associated with FTICR-MS instruments is inherently long (up to 1.0 s).[2] The direct benefit of performing IAM on such an instrument is the ability to obtain more parent ion information in less time (i.e., fewer MS/MS spectra). With the specific Q-FTICR-MS used for the work described in Chapter 3, the ICR must perform a mass analysis step on a packet of ions before a different set of ions can be passed by the mass-selective quadrupole. The ability to mass analyze an ion packet in the ICR cell while externally accumulating the next ion packet has allowed hybrid FTICR-MS instruments to reach duty cycles close to 100%.[3, 4] With the appropriate modifications to the instrument software used to control the Q-FTICR-MS described in this dissertation, one packet

of ions could be mass analyzed in the ICR cell while the next round of ion encoding is occurring in the external hexapole. Such a software modification would allow an even greater time savings to be realized with the IAM technique.

8.3.2 *Obstacles to increasing the number of parent ions encoded*

One way to improve the IAM technique is to increase the number of parent ions that can be encoded. As shown in Chapter 3, MS/MS experiments were performed on six parent ions by acquiring two MS/MS spectra. Because the generation of a ratiogram requires that two MS/MS spectra be acquired, each with a different set of relative accumulation times for the parent ions, the time savings provided by IAM is equal to half the number of parent ions encoded. The largest number of parent ions that have been used for IAM experiments on the Q-FTICR-MS instrument thus far have been six. It would be beneficial to determine how many parent ions the IAM technique is capable of encoding. The major limitation to the number of parent ions that can be encoded is the space charge limit associated with the external hexapole. As the space charge limit is reached, a non-linear signal response to ion accumulation time is achieved which is not conducive for the IAM encoding procedure. Also, as the amount of charge accumulated in the collision hexapole increases, ion flight times to the ICR cell following ejection from the hexpole begin to be effected.[5] While the signal response to accumulation time and effect of space charge on ion flight time could be calibrated for specific charge densities in the collision hexapole, such a strategy is not conducive to on-line analyses. Also, as demonstrated in Figure 3.3 of Chapter 3, the accumulation time at which the space charge limit of the external hexapole is reached will vary depending on the parent ion charge state.

Another obstacle to increasing the number of parent ions that can be encoded in an IAM experiment is the external accumulation time needed to detect each parent ion (and their associated product ions) with an adequate signal-to-noise ratio. Each analyte will have a characteristic minimal accumulation time in order to be detected and that accumulation time will depend on, among other things, the concentration and ionization efficiency of each analyte. Therefore, one way to proceed in trying to increase the number of parent ions able to be encoded via IAM is to use analytes with similar

ionization efficiencies that are present in the sample mixture at equal concentrations. However, it is unlikely for these conditions to occur with real-world samples.

The final obstacle that must be overcome in order to increase the number of parent ions that can be encoded is minimizing the uncertainty in the ratiogram. Because two spectra are required to generate the ratiogram, any uncertainty in the acquisition of either spectrum will increase the ambiguity of the IAM results. As the number of parent ions to encode increases, the difference between the ratios in the ratiogram will decrease due to the space charge limits imposed by the external, collision hexapole. With smaller differences between the ratios an even greater amount of certainty will be required in the acquisition of both spectra. The electrospray process itself introduces some level of uncertainty into the measurement. However, the most critical areas of uncertainty that need to be addressed are related to the ion ejection from the collision hexapole, ion trapping in the ICR cell, and how changes in charge density within the collision hexapole have an effect on both of these processes.

8.4 ECD in a LIT vs. Q-FTICR-MS

The comparison of ECD between the ECD_{LIT}/TOF and Q-FTICR-MS mass spectrometers resulted in the acquisition of very similar MS/MS spectra from each instrument for representative peptides and the protein ubiquitin.

8.4.1 *Operational advantages to doing ECD in a LIT*

As described in Chapter 4, the largest difference between performing ECD in the ECD_{LIT} versus the FTICR-MS instrument is how straightforward it is to perform ECD in the ECD_{LIT}. The helium bath gas present in the ECD_{LIT} and the quadrupolar potential that exists in the radial dimension help focus the ion cloud to the center of the rod array. The electron filament is centered with respect to the rod array and the presence of a magnetic field created by a neodymium permanent magnet helps confine the free electrons to the radial center of the ECD_{LIT}. As a result, a good overlap of the focused ion cloud and electron beam is realized within the ECD_{LIT}.

The alignment of the ion cloud and electron beam within the ICR cell of the Q-FTICR-MS instrument is more difficult. The angle at which the ions enter the ICR cell will determine the central axis of their cyclotron orbit. As a result, the center of an ions' cyclotron orbit might not be the radial

center of the ICR cell. The electron source (an indirectly heated, hollow dispenser cathode as described in Chapter 1) is aligned with the radial center of the ICR cell. Thus, tuning of the ion optics on the source side of the ICR cell is required for good overlap of the ion cloud and electron beam. Also, the voltages applied to the ends of the ICR cell to axially trap the ions result in the ions being pushed away from the center of the ICR cell. Because there is no bath gas typically used within the ICR cell, there is no collisional cooling to help focus the ions back to the center of cell. Consequently, the act of axially trapping the ions in the ICR cell can result in the misalignment of the ion cloud and electron beam. For these reasons, it is more straightforward to perform ECD in the ECD_{LIT} than in the Q-FTICR-MS.

8.4.2 *Very similar product ions despite different background pressures*

Similar spectra were acquired from performing ECD in the ECD_{LIT} and Q-FTICR-MS instruments, despite there being a six-order of magnitude difference in background pressure between the ECD_{LIT} and the ICR cell. As the ions undergo collisions with the helium bath gas in the ECD_{LIT} ion kinetic and internal energy can be transferred to the bath gas. As a result, the pressure difference had been assumed to be the cause of greater parent ion dissociation from ECD in FTICR instruments compared to the ECD_{LIT} (e.g., the lack of a $\mathbf{c_4}$ product ion from ECD of $\mathbf{[M+2H]^{2+}}$ substance P).[6] However, the results from Chapter 4 showed that the parent ions dissociated to a similar extent when ECD was performed in both instruments. The spectral similarities are presumably a result of the parent ions having comparable internal energies in both systems before electron capture. Similar parent ion internal energies could arise due to the use of parent ion accumulation in a higher pressure ($\sim 1.5 \times 10^{-3}$ torr) region in both instruments prior to being irradiated with electrons.

It would be interesting to study the parent ion internal energies in both the ECD_{LIT} and Q-FTICR-MS instruments during ECD. Nanocalorimetry experiments have been used for this purpose.[7, 8] In nanocalorimetry, the internal energy deposited into a hydrated cluster (the charge carrier is typically calcium) due to electron capture can be determined from the number of water molecules lost by the cluster. Initial attempts to perform this experiment on the ECD_{LIT} instrument have been unsuccessful because of difficulties associated with injecting hydrated clusters into the ECD_{LIT}. Specifically, because the CID_{LIT} used for parent ion accumulation and isolation is heated to

120ºC, water evaporates off of the clusters preventing clusters of appropriate size for the nanocalorimetry experiments (e.g., 32 water molecules) from surviving to the ECD_{LIT}. The 120ºC set-point for the CID_{LIT} is not a user controlled parameter on the LIT/TOF instrument, making it difficult to reduce the temperature.

It could also be argued that the initial internal energy of the parent ion may be irrelevant because the fragmentation associated with ECD occurs fast enough after electron capture that there is no time for collisional cooling. Because collisional cooling could not occur to dissipate ion internal energy, the bath gas in the ECD_{LIT} would have little effect on the dissociation following electron capture. Thus, similar ECD spectra would be expected from the ECD_{LIT} and the FTICR-MS instruments. The results from Chapter 4 are in agreement with this idea but more experiments are needed to test this hypothesis.

8.5 ECD+CID

As described in Chapter 5, ECD+CID has demonstrated the ability to improve the sequence coverage for melittin over performing ECD alone (i.e., from 76% to 88%). In addition, ECD+CID can be used to reduce the extent of non-dissociative electron capture observed with performing ECD in the ECD_{LIT} instrument under certain conditions.

8.5.1 *Advantages of selectively exciting only the charge-reduced ion*

ECD+CID allows the charge-reduced ion ($\mathbf{[M+nH]^{(n-1)+\bullet}}$) to be activated via collisions with the helium bath gas at the same time the parent ion ($\mathbf{[M+nH]^{n+}}$) is being irradiated with electrons. Because of the helium bath gas in the ECD_{LIT}, vibrational excitation can be performed without having to pulse in a bath/collision gas or use CO_2 lasers to generate IR radiation. The use of ECD+CID increases the sequence coverage resulting from the MS/MS experiment compared to performing ECD alone. In addition, by resonantly exciting only the $\mathbf{[M+nH]^{(n-1)+\bullet}}$ species, product ions that correspond to N-C_α bond cleavage (i.e., **c** / **z** ions) dominate the MS/MS spectrum, as shown in Chapter 5. These results are in agreement with the literature, where the preferential formation of **c** / **z** ions resulted from the vibrational excitation of the $\mathbf{[M+nH]^{(n-1)+\bullet}}$ ion through the use of IR activation.[9]

8.5.2 *The Future of ECD+CID*

Given the ability of ECD+CID to improve sequence coverage, it would be advantageous to perform ECD+CID in an on-line, data-dependent manner following a chromatographic separation. For example, consider a tryptic digest of a protein sample. Because trypsin cleaves on the C-terminal side of lysine and arginine residues, the resulting tryptic peptides contain two basic sites which can readily form doubly charged ions. It has been shown that the use of ion-electron interactions for the dissociation of doubly charged parent ions often does not provide extensive sequence coverage.[10] By using a data-dependent algorithm to identify the doubly charged parent ions during a LC-MS run, ECD+CID could be applied to increase the amount of information acquired for those parent ions.

8.6 EDD

The EDD results in Chapter 6 were the first example of EDD being performed in a LIT (i.e., the EDD_{LIT}). It was determined that EDD could be performed with an electron irradiation time as short as 30 ms. The irradiation time of 30 ms for the LIT is significantly shorter than that typically used for EDD experiments performed on FTICR-MS instruments (e.g., 150 ms to 1 s).

8.6.1 *Fast EDD in a LIT*

The ability of the EDD_{LIT} to use the previously mentioned electron irradiation time of 30 ms for EDD experiments has led our group to perform EDD on the LC-time scale. As the procedure for performing LC-EDD on the EDD_{LIT} instrument becomes more refined, the method has great potential for the on-line analysis of proteins that contain PTMs. Because several common PTMs increase the acidity of the peptide/protein analytes to which they bind, ionization and subsequent MS/MS (i.e., EDD) in the negative ion mode may become the method of choice for their characterization.

8.6.2 *Charge-reduced (multi)radical stability*

An unexpected result came from performing EDD of the $\mathbf{[M-6H]^{6-}}$ parent ion of insulin chain A in the LIT. The relative abundances of the charge-reduced species are larger than expected. The abundance of these ions suggests they are rather stable against dissociation. Comparing the isotopic distributions for the charge-reduced species (i.e., $\mathbf{[M-6H]^{5-\bullet}}$, $\mathbf{[M-6H]^{4-}}$, $\mathbf{[M-6H]^{3-}}$, etc.) to the isotopic distributions for the same charge state generated directly from nESI confirmed the hydrogen deficiencies of the species formed as a result of EDD. In an effort to explain the relative abundance and apparent stability of the second and third charge-reduced species (i.e., $\mathbf{[M-6H]^{4-}}$ and $\mathbf{[M-6H]^{3-}}$) it

is of interest to determine if these ions contain multiple radicals or if the radicals formed from EDD have recombined to form a new covalent bond resulting in an even-electron ion.

One method that could be used as a screen for the presence of radicals are ion-molecule reactions between post ion-electron product ions and radical scavenger molecules. Initial attempts using 7,7,8,8-tetracyanodiquinomethane (TCNQ) as a radical scavenger have been unsuccessful.[11] At the time this dissertation was written, work was being actively pursued in our group to study the utility of different ion-molecule reactions as a method for determining the identity of charge-reduced species and product ions in both EDD and ECD experiments..

8.7 AI-ECD

As discussed in Chapter 7, AI-ECD is typically performed using IR radiation as the method of ion activation, due largely to all initial ECD experiments being performed on FTICR-MS instruments which precludes the straight forward use of collisional activation. Collisional activation could be used in the ECD_{LIT} to perform AI-ECD, but the implementation of collisional activation changes the ion trapping conditions and introduces a low-mass-cut-off (LMCO) that is approximately one-third the mass-to-charge ratio of the parent ion being activated. Any product ions with mass-to-charge ratios below the LMCO are not trapped and thus are not detected. The use of IR activation does not require any change in the ion trapping parameters therefore IR activation was used for the AI-ECD studies described in Chapter 7 as a way to probe the internal energy imparted to the parent ion during ECD.

8.7.1 *Practical benefits of AI-ECD on LIT/TOF versus FTICR-MS*

The practical benefits of performing AI-ECD with IR activation in the ECD_{LIT} compared to the FTICR-MS are the same as those that were given when discussing the benefit of performing ECD in the ECD_{LIT}. In the same way that collisional focusing of the ion cloud and radial trapping provided by the quadrupolar field aid in ion-electron overlap, they also aid in ion cloud-IR beam overlap when the IR laser beam is aligned along the radial center of the ECD_{LIT}. As described in Chapter 7, the procedure used to align the CO_2 laser ensures that the IR beam is in the radial center of the ECD_{LIT} rod array and thus collinear with the electron beam. Because the electron and IR beams are introduced through opposite ends of the ECD_{LIT}, neither the overlap of the IR nor electron beam with the trapped ion cloud must be compromised.

8.7.2 *Relative energetics between ECD→IR and IR→ECD experiments*

IR activation prior to ECD (IR→ECD) induces a conformational change of the parent ion into a conformation with a higher electron capture cross-section. The higher cross-section improves the amount of parent ion dissociation. Results also show that the **$[M+7H]^{7+}$** parent ion of ubiquitin continues to unfold 20 ms after being irradiated with IR photons but does not refold at longer times. Data from experiments where IR activation was used after ECD (ECD→IR) indicate that there is no excess internal energy remaining in the product ions following ECD, because no change in fragmentation efficiency was observed as the delay between ECD and post-ECD IR activation was varied.

The AI-ECD data taken with the ECD_{LIT} has been done with the protein ubiquitin (~8 kDa). It would be useful to try both IR→ECD and ECD→IR on a large protein (e.g., carbonic anhydrase) relatively low charge state (i.e., < 10 +). As the parent ion mass-to-charge increases, the benefit of using AI-ECD should become more apparent.

8.8 Conclusions

The work described in this dissertation demonstrated improvements in the information content of MS/MS experiments. The implementation of IAM on the Q-FTICR-MS improved parent-product ion correlations allowing MS/MS experiments to be performed on several parent ions simultaneously. ECD+CID was demonstrated to increase the amount of information acquired about the parent ion(s) compared to performing ECD alone. Also, ECD+CID showed the ability to reduce the extent of non-dissociative electron capture when ECD is performed in the ECD_{LIT}, thereby improving the content of the MS/MS results. Implementing EDD and AI-ECD on a LIT device for the first time has made it possible to study these reactions on a non-FTICR-MS instrument. By comparing ECD results from the ECD_{LIT} and Q-FTICR-MS instruments, a better understanding of the advantages and disadvantages of performing ECD on each instrument has been developed.

8.9 References

1. Leclercq, L.; Delatour, C.; Hoes, I.; Brunelle, F.; Labrique, X.; Castro-Perez, J. Use of a Five-Channel Multiplexed Electrospray Quadrupole Time-of-Flight Hybrid Mass Spectrometer for Metabolite Identification. *Rapid Communications in Mass Spectrometry*. **2005**, 19, p. 1611-1618.

2. Marshall, A. G.; Hendrickson, C. L.; Jackson, G. S. Fourier Transform Ion Cyclotron Resonance Mass Spectrometry: A Primer. *Mass Spectrometry Reviews*. **1998**, 17, p. 1-35.

3. Senko, M. W.; Hendrickson, C. L.; Emmett, M. R.; Shi, S. D. H.; Marshall, A. G. External Accumulation of Ions for Enhanced Electrospray Ionization Fourier Transform Ion Cyclotron Resonance Mass Spectrometry. *Journal of the American Society for Mass Spectrometry*. **1997**, 8, p. 970-976.

4. Belov, M. E.; Nikolaev, E. N.; Anderson, G. A.; Udseth, H. R; Conrads, T. P.; Veenstra, T. D.; Masselon, C. D.; Gorshkov, M. V.; Smith, R. D. Design and Performance of an ESI Interface for Selective External Ion Accumulation Coupled to a Fourier Transform Ion Cyclotron Mass Spectrometer. *Analytical Chemistry*. **2001**, 73, p. 253-261.

5. van Agthoven, M.A.; Hendrickson, C. L; Beu, S. C.; Blakney, G. T.; Quinn, J. P.; Marshall, A. G. *Optimal Event Sequences for Octopole-Quadrupole-Octopole External Ion Introduction for Fourier Transform Ion Cyclotron Resonance Mass Spectrometry*. in *The 55th ASMS Conference on Mass Spectrometry and Allied Topics*. 2007.

6. Satake, H.; Hasegawa, H; Hirabayashi, A.; Hashimoto, Y.; Baba, T. Fast Multiple Electron Capture Dissociation in a Linear Radio Frequency Quadrupole Ion Trap. *Analytical Chemistry*. **2007**, 79, p. 8755-8761.

7. Leib, R. D.; Donald, W. A.; Bush, M. F.; O'Brien, J. T.; Williams, E. R. Internal Energy Deposition in Electron Capture Dissociation Measured Using Hydrated Divalent Metal Ions as Nanocalorimeters. *Journal of the American Chemical Society*. **2007**, 129, p. 4894-4895.

8. O'Brien, J. T.; Prell, J. S.; Holm, A. I. S.; Williams, E. R. Effects of Electron Kinetic Energy and Ion-Electron Inelastic Collisions in Electron Capture Dissociation Measured Using Ion Nanocalorimetry. *Journal of the American Society for Mass Spectrometry*. **2008**, 19, p. 772 - 779.

9. Håkansson, K.; Chalmers, M. J.; Quinn, J. P.; McFarland, M. A.; Hendrickson, C. L.; Marshall, A. G. Combined Electron Capture and Infrared Multiphoton Dissociation for Multistage MS/MS in a Fourier Transform Ion Cyclotron Resonance Mass Spectrometer. *Analytical Chemistry*. **2003**, 75, p. 3256 - 3262.

10. Swaney, D. L.; McAlister, G. C.; Wirtala, M.; Schwartz, J. C.; Syka, J. E. P.; Coon, J. J. Supplemental Activation Method for High-Efficiency Electron-Transfer Dissociation of Doubly Protonated Peptide Precursors. *Analytical Chemistry*. **2007**, 79, p. 477 - 485.

11. McEwen, C. N.; Rudat, M. A. Radical Trapping in a Mass Spectrometer Ion-Source. 1. *Journal of the American Chemical Society*. **1981**, 103, p. 4343-4349.

Chapter 9

Appendices

The information contained in the following sections is meant to provide specific details about two electronic circuits and a LabVIEW program that may be of use to the next generation of Glish lab students. In Appendix 9.1 the electronic components and layout are provided, along with a representative output voltage profile, for the circuit used to control the pulsing of the dual nESI source described in Chapter 2. The user interface of the LabVIEW program used for the IAM project is given in Appendix 9.2. Appendix 9.3 contains the circuit used to measure the electron kinetic energies on the Q-FTICR-MS instrument as discussed in Chapter 4.

Appendix 9.1 Pulsed nESI circuit

The general operation of the pulsed nESI circuit was described in the Experimental section of Chapter 2. The strategy behind the circuit was to use a trigger from the mass spectrometer scan function, which corresponds to the accumulation of ions by the instrument, to independently control the operation of two nESI sprayers. The design used for the work described in this dissertation is given in Figure 9.1.

The scan function trigger from the mass spectrometer is inverted before being used as the clock signal for the J-K flip flop. It is necessary to invert the trigger signal from the instrument because the J-K flip flop only transfers data from the Q2 and Q2-bar outputs on the falling edge of the clock pulse. Because the goal is to have the nESI sprayers operate while the instrument trigger signal is HI (i.e., ions are only being generated while they can be sampled and accumulated for subsequent mass analysis) the change in the outputs of Q2 and Q2-bar of the J-K flip flop must correspond with the rising edge of the instrument trigger (i.e., the J-K flip flop clock signal). By inverting the trigger signal, the rising edge at the inverter input 2A becomes the falling edge at the

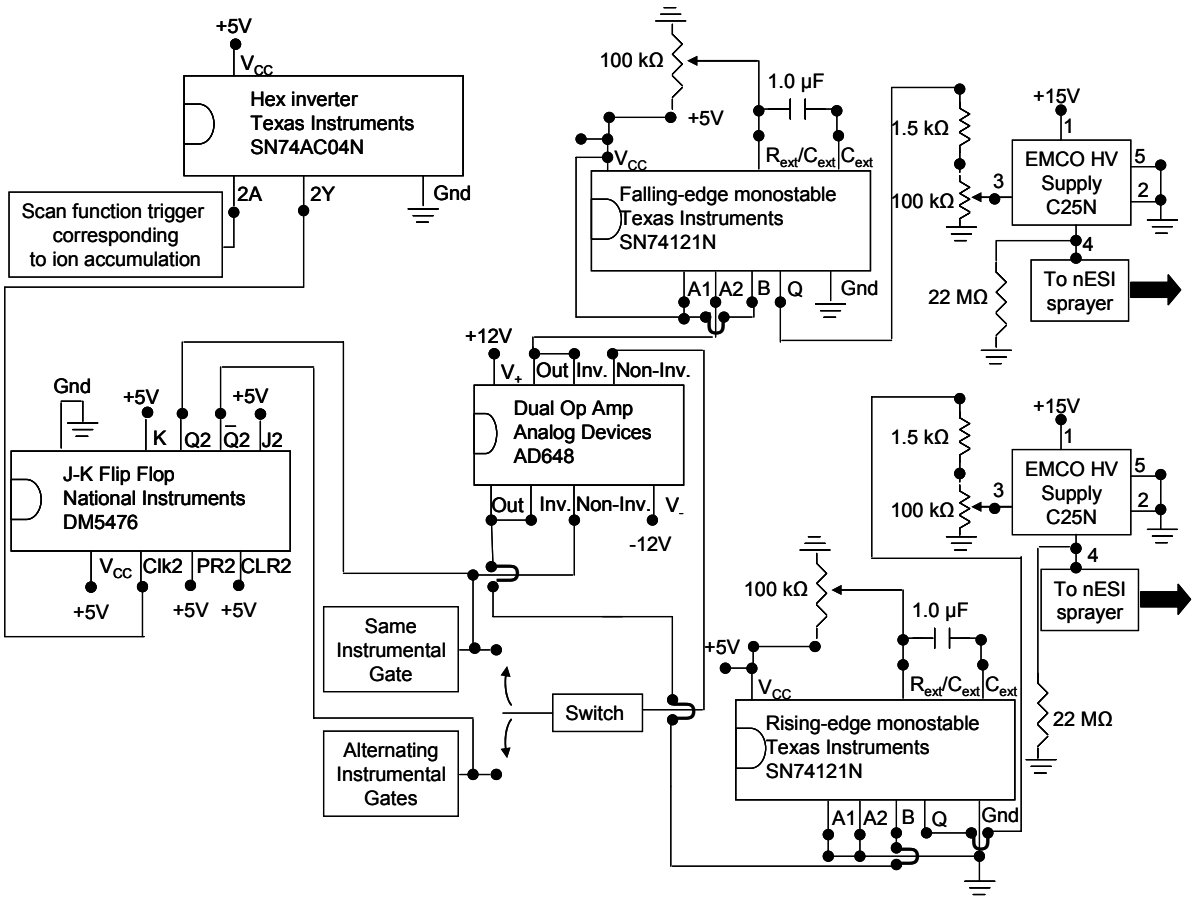

Figure 9.1 Schematic of the electronic circuit used for the high voltage pulsing of the dual-nESI source.

inverter output 2Y. The inputs of the J-K flip flop are held at a high logic level to allow the Q2 and Q2-bar outputs to toggle at the frequency of the clock signal. With the setup shown in Figure 9.1, the outputs of the J-K flip flop (i.e., Q2 and Q2-bar) remain at their respective logic level for the duration of the instrument scan function and not just for the duration of the ion accumulation portion of the scan function (see Chapter 2, Figure 2.1) because each output only responds to one transition in logic level, either HI→LO or LO→HI.

The Q2 and Q2-bar outputs of the J-K flip flop are then sent through a toggle switch which allows the user to decide in which mode the two nESI sprayers will operate, i.e., on alternating instrument scans or together on every instrument scan. For example, by moving the switch to the "Same Instrumental Gate" position, the circuit diagram shows that the Q2 output from the J-K flip flop will be used to control both monostables resulting in both sprayers operating simultaneously. If the switch is set to the "Alternating Instrumental Gates" position, one monostable will be controlled by

the Q2 output from the J-K flip flop while the other will be controlled by the Q2-bar output, resulting in the sprayers operating 180º out-of-phase with each other (i.e., on alternating instrument scans).

Regardless of the switch position, the outputs from the J-K flip flop are sent through voltage followers before arriving at the monostables. The Analog Devices AD648 contains two op-amps in one integrated circuit chip that could be wired to create two identical voltage followers. It was empirically determined that without the use of the voltage followers the output pulse widths of the monstables could not be independently controlled.

Two identical monostables were used for the pulsed circuit. By wiring the inputs appropriately one monostable could be triggered on the rising edge of the J-K output while the other is triggered on the falling edge. In this manner, when the switch is set in the "Alternating Instrumental Gates" position each sprayer operated on every other instrument scan. The pulse width of the monostable output is determined by an external network of resistors and capacitors (RC network). The relevant equation that describes the effect the resistance and capacitance values have on the output pulse width is given in Chapter 2. As mentioned, to operate the monostables with output pulse widths on the same time scale as the instrument trigger, a 1.0 μF capacitor is used while the output pulse width is varied by changing the resistance of the 100 kΩ variable resistor in the external RC network.

The output of the monostables is either in a HI (5 V) or LO (0 V) state. The percentage of the maximum output of the EMCO HV supplies is determined by the magnitude of the programming voltage applied to pin 3 of the supplies. As shown in Figure 9.1, a voltage divider is used to control the magnitude of the monostable output (when the monostable output is 5V) that is applied to pin 3 of the EMCO supplies. By using a 100 kΩ variable resistor, the high voltage that is applied to the nESI sprayer can be controlled. The output of the EMCO supplies is provided on pin 4, to which a 22 MΩ load resistor has been added in parallel for each supply. As described in Chapter 2, the use of this load resistor decreased the fall time of the output voltage by 16.4 ms (a 9 % improvement).

The high voltage measured on the nESI sprayers under the conditions used for the source stability experiment in Chapter 2 (see Figure 2.5) is displayed in Figure 9.2. The voltage traces for the sprayer containing YGGFL and AAA are shown in Figures 9.2A and 9.2B, respectively. In each

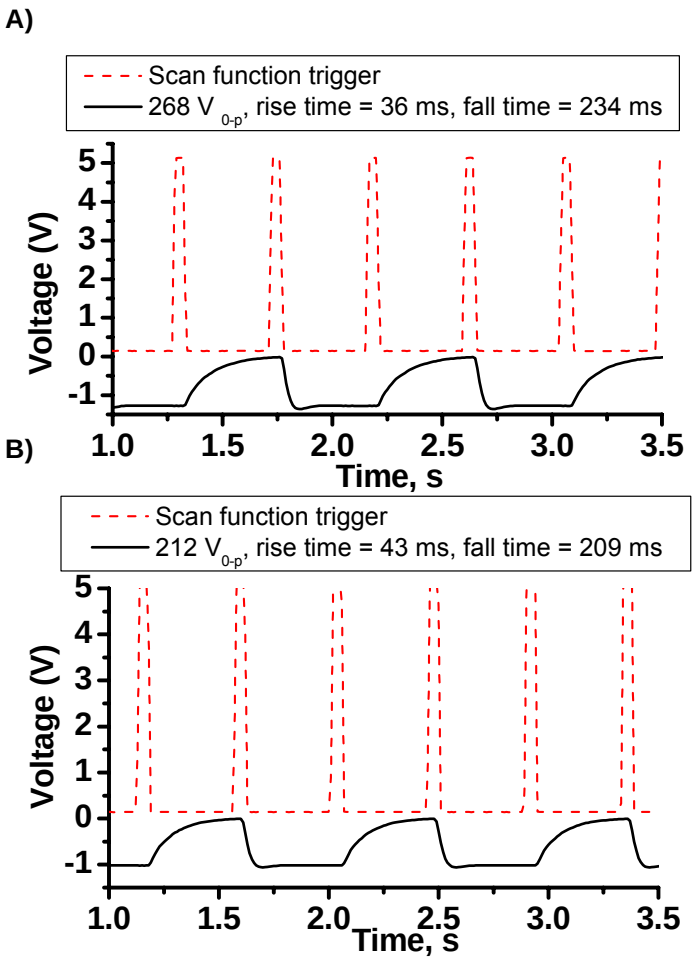

Figure 9.2 Plots of the high voltage outputs from the circuit shown in Figure 9.1. A) The voltage traces for the sprayer containing YGGFL. B) The voltage traces for the sprayer containing AAA. For the solid (black) traces, the values shown in the figure need to be multiplied by 200 to obtain the actual voltages (see text).

plot, the dashed line represents the scan function trigger that corresponds to ion accumulation. The solid lines are the voltages measured on the nESI sprayers. The specific EMCO supplies used in the circuit from Figure 9.1 provide output voltages from 0 to -2500 V. To measure the applied voltages, a 1000x voltage probe was used. However, when that probe was interfaced with the oscilloscope used to make the measurements shown in Figure 9.2, the observed voltage attenuation was not 1000 but 200. As a result, the applied voltages corresponding to the nESI sprayers shown in Figure 9.2 (i.e., the solid, black traces) must be multiplied by 200 to obtain the absolute voltages, thus a voltage of -1.2 V for the solid line represents a measured voltage of -240 V. The voltage scale for the scan function trigger in Figure 9.2 was measured using a 1x voltage probe. Because the

transfer capillary of the mass spectrometer is held at -1500 V, to stop electrospray a negative voltage must be applied to the nESI sprayer to reduce the 1500 V potential difference between the sprayer and transfer capillary. Thus, in Figure 9.2 electrospray is occurring when the nESI voltage traces approach 0.0 V. The nESI sprayer voltages in Figure 9.2 show that a given sprayer is only operating on every other instrument scan. The acquisition of each plot in Figure 9.2 was performed independently and no effort was made to have t = 0 correspond to the same part of the scan function trigger period.

Appendix 9.2 IAM LabVIEW control program

The step-by-step operation of the IAM LabVIEW program was given in Chapter 3. Provided here are images of the LabVIEW front panel and a description of the parameters that are used in performing IAM experiments on the Q-FTICR-MS instrument. The file name of the LabVIEW program is Qh_Control_for_IAM.vi. The LabVIEW program provides the same control over the Qh interface as the Bruker Apex software. Without using the IAM option in the program, the LabVIEW program can be used to operate the quadrupole in rf-only mode or in isolation mode, where the mass-to-charge ratio to be isolated ("Q1 Mass Command") can be set as well as the mass-to-charge window ("Resolution") to be used during isolation. To switch to isolation mode simply click the "DC Off" button until it changes to red and says "DC On."

Shown in Figure 9.3 are the parameters that were used to acquire Spectrum I of the peptide IAM-CID results discussed in Chapter 3. By choosing the "IAM Subvi" position of the toggle switch, the IAM process described in Chapter 3 begins. With the "IAM Subvi" option chosen, the "Q1 Mass Command" becomes irrelevant and the "DC On" Boolean appears as shown in Figure 9.3. The quadrupole changes which mass-to-charge it will pass according to the values listed in the "Q1 Mass" array. The amount of time each mass-to-charge ratio is allowed to pass through the quadrupole, and thus accumulated in the collision hexapole, is determined by the corresponding times set in the "Accumulation Time (ms)" array. The other parameters shown in Figure 9.3 are not associated with the IAM experiment. The "Q1 Pole DC Reverse" Boolean allows the communication between the PXI machine that is running the Qh_Control_for_IAM.vi. program and the Extrel QC150 quadrupole power supply to be verified. Clicking the "Q1 Pole DC Reverse" Boolean should product

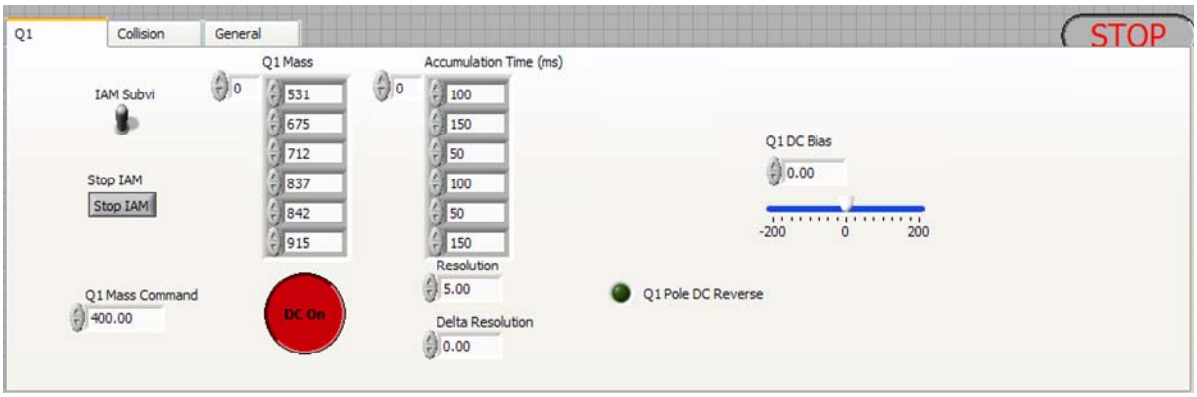

Figure 9.3 LabVIEW front panel of the Qh_Control_for_IAM.vi showing the IAM parameters used for the parent ion accumulations listed for Spectrum I from Chapter 3 (see Table 3.1).

an audible "beep" when communication is established. The "Q1 DC Bias" control allows the dc potential applied to the entire rod array of the quadrupole to be set. Typically this value is kept at 0.0 V.

To perform CID of the parent ions as they are isolated by the quadrupole, the potential difference between the hexapole in the Apollo II source and the collision hexapole must be set to a negative value (for positive ions). A unique collision voltage can be specified for each parent ion, as shown in Figure 9.4. The order in which the "Collision Voltage" array values are entered corresponds to the order in which the parent ion mass-to-charge ratios were entered into the "Q1 Mass" array. The values shown in Figure 9.4 are the same that were used for the IAM-CID experiments described in Chapter 3. The "Collision DC Bias Trap" value has no meaning when the IAM experiment is being performed. If the Qh_Control_for_IAM.vi is being run without the IAM

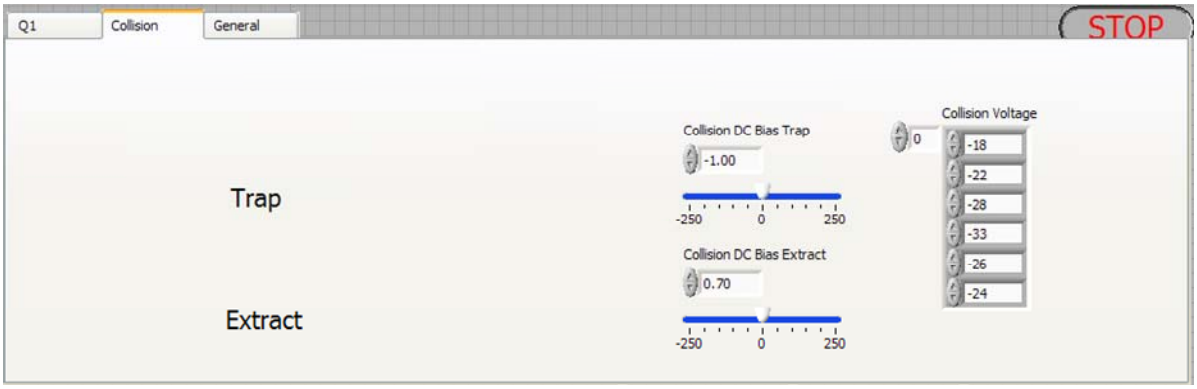

Figure 9.4 LabVIEW front panel of the Qh_Control_for_IAM.vi showing the incorporation of CID into the IAM program.

functionality enabled, the “Collision DC Bias Trap” sets the potential difference between the source and collisions hexapoles. The “Collision DC Bias Extract” is the dc potential applied to the collision hexapole rod array when ions are ejected from the hexapole and sent to the ICR cell for mass analysis. The “Collision DC Bias Extract” voltage is used both with and without the IAM process running. In general, it is best to tune for the optimum “Collision DC Bias Extract” voltage when a low ion density is trapped in the collision hexapole.

Appendix 9.3 FTICR-MS electron energy measurement circuit

The circuit used to measure the electron kinetic energy as a function of ECD Bias on the Q-FTICR-MS instrument is shown in Figure 9.5. In practical terms, the circuit was used to measure stopping curves for the electrons during ECD experiments. Ideally to make the type of measurement described here the stopping potential would be applied through a picoammeter, but because a suitable picoammeter was unavailable, the circuit in Figure 9.5 was constructed.

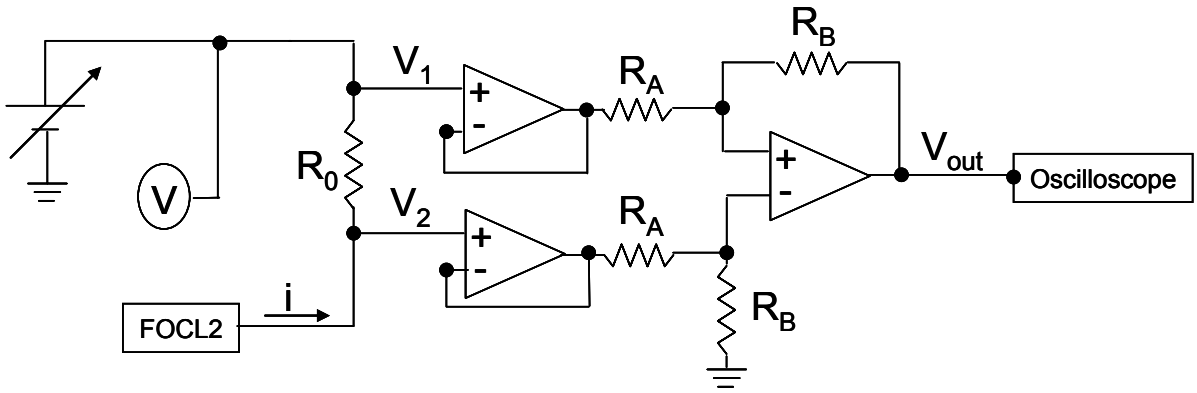

$$V_{out} = \frac{R_B}{R_A}(V_2 - V_1) = \frac{R_B}{R_A}(iR_0)$$

$$i = \frac{\left(\frac{R_B}{R_A}\right)V_{out}}{R_0}$$

Figure 9.5 Circuit used to generate electron stopping curves for the determination of electron kinetic energy as a function of ECD Bias in the Q-FTICR-MS instrument.

By removing the BNC cable connected to the voltage feedthrough for FOCL2 on the mass spectrometer, the circuit in Figure 9.5 could be connected to the feedthrough (represented by FOCL2 in the figure). At a given ECD bias, a variable negative potential is applied to FOCL2 until zero current is detected on FOCL2. The potential being applied to FOCL2 by the variable dc power supply was monitored using a voltmeter. To measure the current on FOCL2 as sensitively as possible, the current was converted to a voltage difference (V_2-V_1) by using two voltage followers and a differentiator circuit to measure the voltage drop across the load resistor (R_0). The resulting voltage (V_{out}) was measured using an oscilloscope and is related to the current measured on FOCL2 by the equations provided in Figure 9.5. The resistances used for R_A and R_B were 10 kΩ and 100 kΩ, respectively, providing a gain of 10 for the measurement of V_{out}.